Λ and K^0_S production in Pb–Pb and pp collisions with ALICE at the LHC

Luke David Hanratty

A thesis submitted to
The University of Birmingham
for the degree of

DOCTOR OF PHILOSOPHY

School of Physics and Astronomy
University of Birmingham
June 13, 2014

UNIVERSITY OF BIRMINGHAM

University of Birmingham Research Archive

e-theses repository

Abstract

In this work, the transverse momentum spectra of Λ and K^0_S measured with the ALICE experiment at the LHC are discussed. Measurements are presented for colliding systems of protons, at centre of mass energies 2.76 TeVand 7 TeV, and for lead ions at a centre of mass energy of 2.76 TeV per nucleon.

The spectra are discussed within a theoretical framework of a thermally equilibrated, hydrodynamically evolving system, which serves to explain the shape of the spectra for $p_T < 2$ GeV/c. For $p_T > 6$ GeV/c jet quenching is evident, but no evidence of particle species dependance in jet quenching is observed.

The Λ/K^0_S ratio shows an enhancement for $2 < p_T < 6$ GeV/c, peaking at 1.5 for the 5% most central Pb–Pb collisions compared to 0.6 for pp. This is discussed in terms of a coalescence model. It cannot be explained purely by enhanced baryon production, but must also involve a redistribution of particles within p_T. This supports the hydrodynamical picture of hadron production. A brief comparison to the results presently available in p–Pb collisions at the LHC is also given.

Author's Contribution

For the duration of my PhD, I have been working as part of the ALICE collaboration. Consequentially, this work bears a huge debt to the talented team of scientists and engineers involved in building and running both ALICE and the LHC, as well as those responsible for developing and maintaining the computer systems used in this analysis. I have spent time performing shifts in the ALICE control room, and on shift for the trigger systems, but for the bulk of my time with ALICE I worked within the 'BMPR' paper group, studying the Λ/K_S^0 ratio in Pb–Pb collisions (found in Appendix A [1]). Within that group, I studied the cut selection, fitting of the data, differences between pure and injected Monte Carlo, and preliminary studies of the systematic errors, and presented the results at the SQM2013 conference [2]. However, the entirety of the analysis presented here has been repeated & refined by me; to ensure consistency and to extend the study of Λ and K_S^0 production to pp collisions.

At the beginning of the analysis, the studies were based on the ESD file type, prepared by the ALICE offline team. As the work progressed, it switched to the reduced AOD format, and finally to TTrees produced by David Chinellato. At each of these switchovers, the code had to be entirely rewritten, with the result that all code used in the final analysis, save the broad selection used to select initial V0 candidates for the TTrees, was written by me and extensively debugged. Parallel codes were used by other members of the group, and served as a valuable crosscheck of the results, but all final results for the inclusive Λ and K_S^0 spectra in Pb–Pb and pp collisions, and any errors, in this work are mine.

Comparisons are made to other work done within the ALICE collaboration, and outside, and referenced as appropriate. In particular, the Λ and K_S^0 integrated yields are incorporated into the thermal fit by J. Stachel et al. [3], and the results for Λ and K_S^0 in Jet and Bulk analyses and in p–Pb collisions have been undertaken by other members of the ALICE collaboration.

For my wife, Holly.
Tota rerum statu in calido et densum.

Acknowledgements

My first thanks must go to my supervisors, Professor Peter Jones and Dr. Lee Barnby. Peter has supported me from the very beginning of my PhD; teaching me the basics of QGP theory, helping me to settle in at CERN, suggesting textbooks and, not least, patiently answering my often naive and convoluted questions. I have been privileged to work closely with Lee within the ALICE collaboration, both within my paper group and under him as PAG and PWG convener. He has supported me throughout the analysis, and has patiently sat through many long sessions to talk out bugs in the analysis.

I must also offer thanks to the rest of the ALICE team at Birmingham. David Evans, Roman Lietava, Gron Tudor-Jones and Orlando Villalobos-Baillie have all offered support and inspiration for my work, as have my fellow students; Didier Alexandre, Graham Lee, Arvinder Palaha, Plamen Petrov and Patrick Scott. Further thanks go to the Birmingham Nuclear Physics group, where I have worked for the past 4 years. They have always been happy to offer help with computing problems, an outsiders eye on the work or a cup of coffee and a chance to switch off.

My thanks go to all my family and friends who have supported me throughout. My wife, Holly, has tolerated the stresses and strains of producing this work much better than I, and has always been on hand to look over a paragraph or solve an equation.

Lastly, my parents; Rick and Jan. They have always believed in me and driven me to achieve my best, and, after 26 years of support, I owe this work to them. Thank you.

Contents

List of Figures

List of Tables

1

Introduction

To current knowledge, the universe experienced around us consists mainly of quarks and leptons, interacting via the four fundamental forces. Of these, gravity and the electromagnetic force are the most immediately obvious on macroscopic scales; pulling objects down towards the planet, and allowing us to lift objects against gravity. The weak force is the cause of various radioactive decays, and is now considered to be intimately related to the electromagnetic force [5]. The strong nuclear force is responsible for the binding of quarks into baryons and mesons, and further for binding baryons into atomic nuclei.

As such, the strong nuclear force is ubiquitous and yet subtle; it is acting all around us, responsible for the stable matter observed around us, and yet hidden away within nuclei. The particles which interact with the strong force; the quarks, are even more hidden, tightly bound inside nucleons as valence quarks, or appearing only in quantum vacuum fluctuations, generally referred to as sea quarks. This picture of the nucleon as formed of quarks was proposed by Gell-Mann [6], and has been well established through deep inelastic scattering experiments [7].

This aspect of the strong force; that it holds charges so tightly together that a 'naked' charge is never observed, is known as confinement. While it appears to be true for all everyday matter, it is natural to wonder about regimes where it might not hold. In particular, it is expected that at very high energies or short distances, the strong force

will drop off in strength - this is known as asymptotic freedom [8]. Thus, at very high temperatures or high densities, quarks could be expected to behave as though they were free. Interestingly, under the big bang theory of cosmology, the early universe would have satisfied both these conditions, and so studying the behaviour of matter under these conditions could help to understand the evolution of the universe.

Studying such a system of free quarks is exceptionally challenging. Once made, there is no known way to confine it for long term study, and the timescales on which it evolves prohibit direct observation of its evolution. Attempts have been made to reach the required energy densities in particle colliders such as Brookhaven's Relativistic Heavy Ion Collider (RHIC) [9] or CERN's Large Hadron Collider (LHC) [10], but measurements of the material created can only be performed after confinement has returned. Practically speaking, this means that what is detected in such experiments is largely hadrons, although electroweak probes may also be studied, largely to understand the initial collisions, but also to study the thermal evolution of the medium.

From studying the hadrons produced, much can be learnt about how matter behaves under deconfinement. Theoretical predictions of the behaviour of deconfined matter predict that the distribution of hadrons in position and momentum space will be different from that produced in elementary hard collisions. Further differences are expected between different quark and particle species, and so studying different hadronic distributions can help us to identify and analyse deconfined matter.

In this work, the production of two such particles, the Λ baryon and the K_S^0 meson, in Pb–Pb collisions at the LHC are described and discussed, as observed in ALICE (A Large Ion Collider Experiment). These are the lightest hadrons containing a strange quark, created either in the initial collision or the medium as there are no strange valence quarks in the colliding nuclei. The distributions of these particles are measured as a function of momentum relative to that produced in pp collisions at a similar centre of mass energy ($\sqrt{s}$). Particular attention is paid to the 'baryon anomaly': an apparent enhancement in the production of Λ relative to K_S^0 at certain momenta when comparing heavy ion

collisions to proton-proton collisions.

1.1 Confinement

The theory generally used to describe the strong force is Quantum Chromo-Dynamics (QCD), analogous to the QED theory of electromagnetic interactions. Where QED is based on a $U(1)$ group, QCD comes from the $SU(3)$ group [11], and as such has 3 charges (commonly referred to as colour). Further, as this group is non-abelian [12] the force carriers of QCD, the gluons, themselves carry colour. This is a marked source of difference between QCD and QED, where the photon carries no charge. As two quarks move apart, the gluons self interact, with the energy put into the field materialising as additional gluons and pulling the gluon field lines together, as shown schematically in Figure 1.1. Phenomenologically, this indicates a change in behaviour from a 'Coulomb-like' force ($F \propto \frac{1}{r^2}$) to a constant 'string-like' force. The potentials for these two forces can be seen in Figure 1.2. For a pure Coulomb force, the attraction between two charges tends towards zero as infinite separation is approached, while the QCD force shows a constant force between the charges - and a potential energy that is, theoretically, increasing towards infinity. This QCD potential may be written as

$$V_{\mathrm{QCD}} = -\frac{4}{3}\frac{\alpha_S}{r} + kr, \tag{1.1}$$

where r is the separation between two quarks, α_S is the strong coupling constant and k an effective string constant for the long distance force.

In nature, the potential energy will not tend to infinity with increasing separation. Eventually, the increasing energy will be realised as the creation of a quark-antiquark pair from the gluon field; the string breaks, leaving two separate string segments, each with a quark or antiquark at each end, such that the total colour charge of each segment is zero. Hence, the force exhibits confinement: no matter how much energy is put into the field, the quarks will never be separated into coloured states.

3
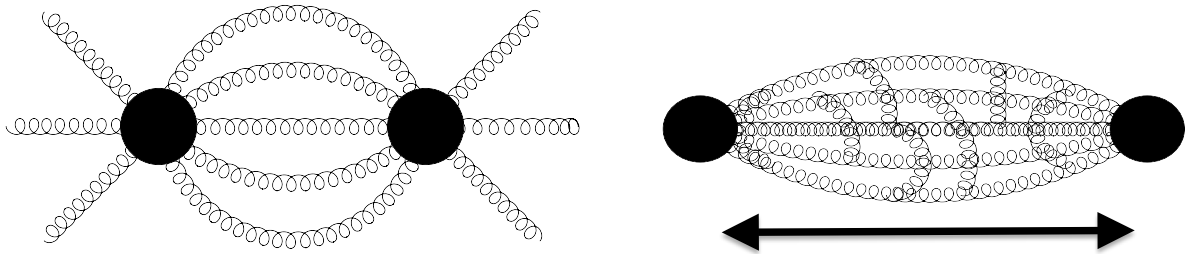
Figure 1.1: Schematic of Quark-Gluon Interactions - Schematic indicating gluon field lines as two quarks are separated.
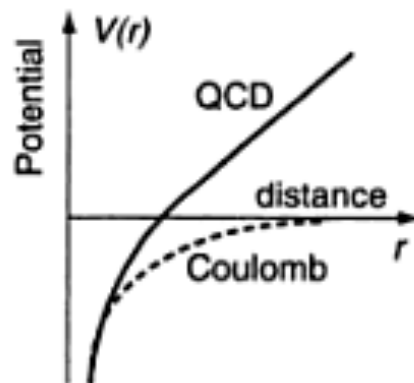
Figure 1.2: QCD and Coulomb Potentials - Potential between a quark and an anti-quark as a function of their separation in QCD (solid line) compared with the Coulomb potential (dashed line). [12]

1.2 Deconfinement

1.2.1 Asymptotic Freedom

The coloured force carriers of QCD theory also allow for deconfinement. Any 'bare' quark would be surrounded by a cloud of gluons and quark-antiquark pairs, borrowing energy from the vacuum as allowed by the Heisenberg uncertainty principle. We can consider the analogous case of screening in QED; any real electron will be surrounded by a cloud of electrons and positrons. These will be polarised slightly by the electric field of the electron, so that the virtual positrons will lie closer than their partners to the real electron. As a result, the magnitude of the electric field is reduced and the apparent charge of the electron is screened. As a test charge moves closer to the electron, however, the screening effect will be less, and the apparent charge of the electron will be higher, approaching the bare charge.

This is typically expressed in terms of a coupling strength α; the square of the weighting of a vertex in a Feynman diagram. The strength of any electromagnetic interaction is dependant on the distance scales of the interaction. This, in turn, is related to the momentum transfer of an interaction; high momentum transfer requires a virtual exchange particle with a very short wavelength. As such, the coupling strength is usually described in terms of the square of the four momentum transferred in an interaction, Q^2.

In QCD, we must also consider the effect of the charged gluons. These have the opposite effect to the virtual quark-antiquark pairs; the apparent charge at any distance is increased by gluon loops. The balance between these effects can be calculated [13], and gives a relationship to first order for the coupling 'constant' of

$$\alpha(Q^2) = \frac{\alpha(\mu_0^2)}{1 + \frac{11N_C - 2n_f}{12\pi}\alpha(Q_0^2)\ln(Q^2/Q_0^2)}.$$

(1.2)

This formula allows a value for the coupling constant for some scale Q^2 to be extrapolated from that measured at another scale Q_0^2. It depends on the number of charges, N_C, carried

5

by the gluons (3 for QCD) and the number of flavours, n_f, of quark (6 for QCD). Thus, for QCD, the anti-screening effect of the gluons overpowers the screening of the quarks. The closer one approaches the quark, or equivalently the higher Q^2, the less charge would apparently be contained within the region identified as the quark. This running of the QCD coupling has been measured, for example at DELPHI [14].

Figure 1.3 shows schematically how the coupling strength of the QCD and QED forces vary with increasing four-momentum transfer; equivalently with increasing energy or decreasing distance. As high enough energies are reached, the coupling strength becomes low enough for perturbative QCD to be accurate, and so cross sections in colliders such as the LHC can be calculated [15]. The assumptions used to calculate these are discussed briefly in Section 2.4.1.
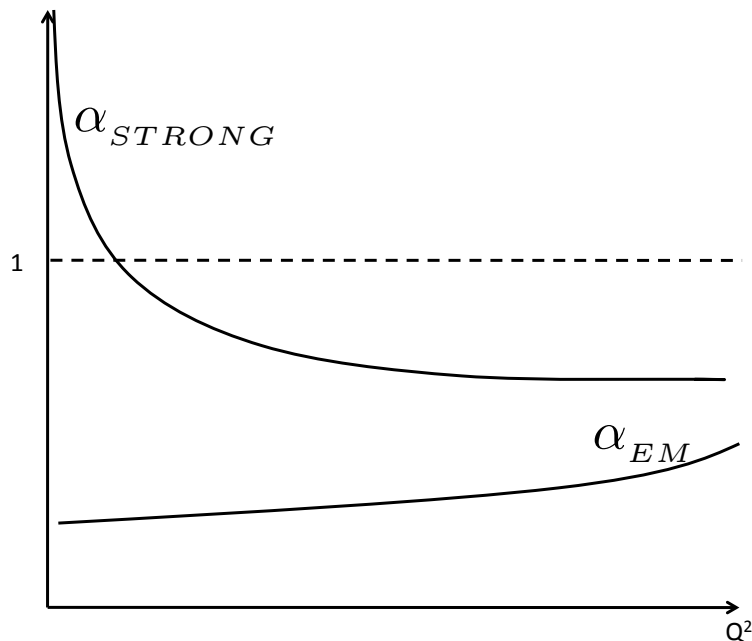
Figure 1.3: Coupling Strength of QCD and QED - Strength of QCD and QED coupling against four-momentum transfer Q^2. Large four-momentum transfer corresponds to high collision energies or short distance scales.

If this trend is continued up to hypothetically infinite energies or particle densities, we would expect the QCD force to become negligible, and so the quarks and gluons to behave as if free. However, such asymptotic freedom would only be valid for exceptionally high four-momentum transfers ($Q^2 >> 10^{26}$ GeV), and so is not achievable with current

heavy ion colliders [16].

1.2.2   Debye Screening

An alternative way to reach deconfinement in a bulk system is through the phenomenon of Debye Screening. In a system with a high density of mobile charges - a plasma - the force between any two charges will be screened by the polarised charges separating them. The effect of this Debye screening on the QCD potential, V_S, in the Coulomb-like region, is

$$V_S \sim -\frac{\alpha_S}{r} e^{-\frac{r}{r_D}}, \tag{1.3}$$

where r is the separation between the quarks, and r_D is the Debye screening length. As the density of charges in the plasma increases, through heating or compression the screening length will decrease. When this drops below the radius of a given hadron, that hadronic state will melt into the medium. The hadron is no longer bound in any meaningful sense, and instead the quarks will move throughout the plasma, interacting strongly with many other charges, but not being bound to any. As the quarks, and indeed gluons, within the medium are still able to interact strongly, this is qualitatively different from asymptotic freedom, and as such may demonstrate hydrodynamic behaviour.

As a phenomenological way of envisaging this, consider a gas of pions. As the temperature of the gas increases, the system can create new pions from the QCD vacuum, and the density of the system increases. Similarly, if the gas is compressed, the pions will, on average, be forced closer together. Eventually, a point is reached where the pions are overwhelmingly overlapping. At this point, it no longer makes sense to consider a given quark as belonging to a given pion; it may have multiple neighbouring quarks or antiquarks closer to it than its notional partner. This system is a quark-gluon plasma or QGP. As a whole it is still colour-neutral, but at the micro-scale the colour charges are diffusing throughout the medium.

1.3   The MIT Bag Model

While the above is qualitatively valid, it is useful to have more quantitative predictions to examine. Specifically, a prediction of the temperature where a phase change would be expected between hadronic matter and the quark-gluon plasma would be instructive in assessing the viability of producing this matter.

One way of approaching this is the MIT bag model [17], a simple model of hadrons from 1974 which nonetheless contains the essential physics. In this model, the valence quarks of a given hadron are considered to be localised within a region of space referred to as a bag. The quarks have no interaction potential within the bag; instead the confining force is represented by an external pressure B. The parameter B can be fixed by comparing the predictions of the model against the measured hadron mass spectra, and comes out at around $B^{\frac{1}{4}} \sim 200$ MeV [18].

While this model might seem overly simplistic, it offers one major advantage: as the quarks in the bag are defined as non-interacting particles, they can be approximated as behaving as an ideal gas. Similarly, on the scales of the strong force, a gas of hadrons can be approximated as non-interacting. From [12], the pressure and energy density of an ideal massless gas are given by

$$P = g\frac{\pi^2}{90}T^4, \qquad \epsilon = 3g\frac{\pi^2}{90}T^4, \tag{1.4}$$

where P and ϵ are the pressure and energy density of a gas of temperature T, and g is the number of degrees of freedom. The number of degrees of freedom will vary with temperature, as different hadronic states or quark flavours become accessible, but will initially be taken as the 3 pions for the hadron gas. For a QGP, there are 8 bosonic gluons, with 2 spin states for each, and 2 flavours of interest of fermionic quark, each with 3 colour states, 2 spin states and an antiparticle. The total number of degrees of freedom for a QGP is thus

$$g_{\text{QGP}} = 2 \times 8 + \frac{7}{8}\left(2 \times 3 \times 2 \times 2\right) \sim 37, \tag{1.5}$$

where the factor of $\frac{7}{8}$ reflects the Fermi-Dirac statistics of the quarks [12].

For the QGP the bag pressure must also be taken into account; this reduces the overall pressure and increases the energy density by B. In a mixed state, the state with the higher pressure will crowd out the other state, and so an approximation is reached for the transition temperature between the hadron gas (HG) and QGP phases by setting

$$P_{\text{HG}} = P_{\text{QGP}}, \tag{1.6}$$

$$3\frac{\pi^2}{90}T^4 = 37\frac{\pi^2}{90}T^4 - B. \tag{1.7}$$

This is shown graphically in Figure 1.4. The temperature at which the two curves cross gives us the critical temperature for the phase transition, T_{c}, and occurs at approximately 150 MeV. Note that this temperature justifies our limiting of the degrees of freedom for the hadron gas to the three pions. It is also of the same order as the bare strange quark mass; including this raises the number of degrees of freedom of the QGP slightly, and lowers the critical temperature slightly but does not notably change the physics. Its effect can be seen more clearly through Lattice QCD studies, as discussed below.
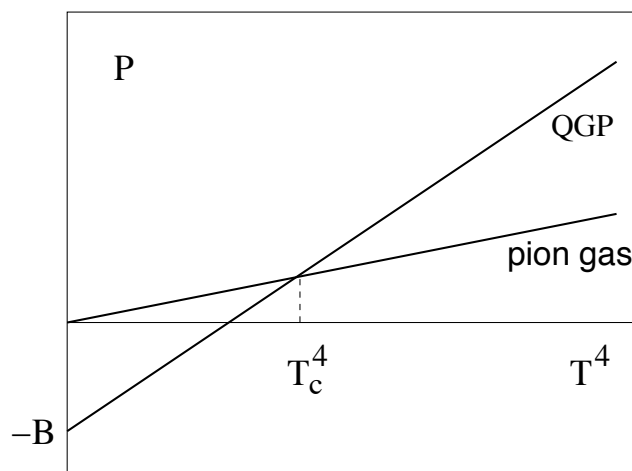
Figure 1.4: Pressure of the Hadron Gas and Quark-Gluon Plasma - Schematic of the pressure-temperature relationship for the Hadronic Gas and Quark-Gluon Plasma phase, using the MIT bag model. [18]

1.4   Lattice QCD Predictions

While the MIT bag theory can give us a feel for the order of magnitude of the transition temperature, and the mechanism involved, the approximations make it hard to say how much confidence can be placed in the result. Another approach is to examine the results obtained through lattice QCD calculations.

In lattice QCD, the Lagrangian associated with the theory is discretised onto a finite space-time grid. This procedure is described in detail in [19], from which Figure 1.5 is taken, showing the energy density prediction from these calculations as a function of temperature. The precise details of the prediction depend on the number of light quarks considered, but for a reasonable model of 2 light quarks and a strange quark with mass ~ 170 MeV, the critical temperature comes out at around 170 MeV. It should firstly be noted that this is surprisingly close to the prediction from the crude model of the previous section. The energy density at this temperature shows a sharp increase, compatible with a phase transition to a state with far higher degrees of freedom: a transition to a QGP state.

The energy density prediction from the ideal gas model, ϵ_{SB} is also indicated. The system should tend towards this value when the temperature is sufficiently high that the interaction forces are essentially overwhelmed. This does not appear to be the case within an order of magnitude of the transition temperature, and would suggest that truly free QCD behaviour requires temperatures much higher than those achievable in modern experiments. Any QGP created in the laboratory would have residual interactions, opening up the possibility of hydrodynamic-type behaviour.

The energy densities measured at several accelerators are indicated on the diagram, as well as the equivalent temperatures this theory would predict. These represent fixed target experiments at the Super Proton Synchrotron (SPS) at CERN, and higher energy collider experiments at RHIC. A prediction is also shown for the LHC. The energy density is estimated using the Bjorken formula [20], which relates the energy density at thermalisation to the transverse energy density in the detector.

10
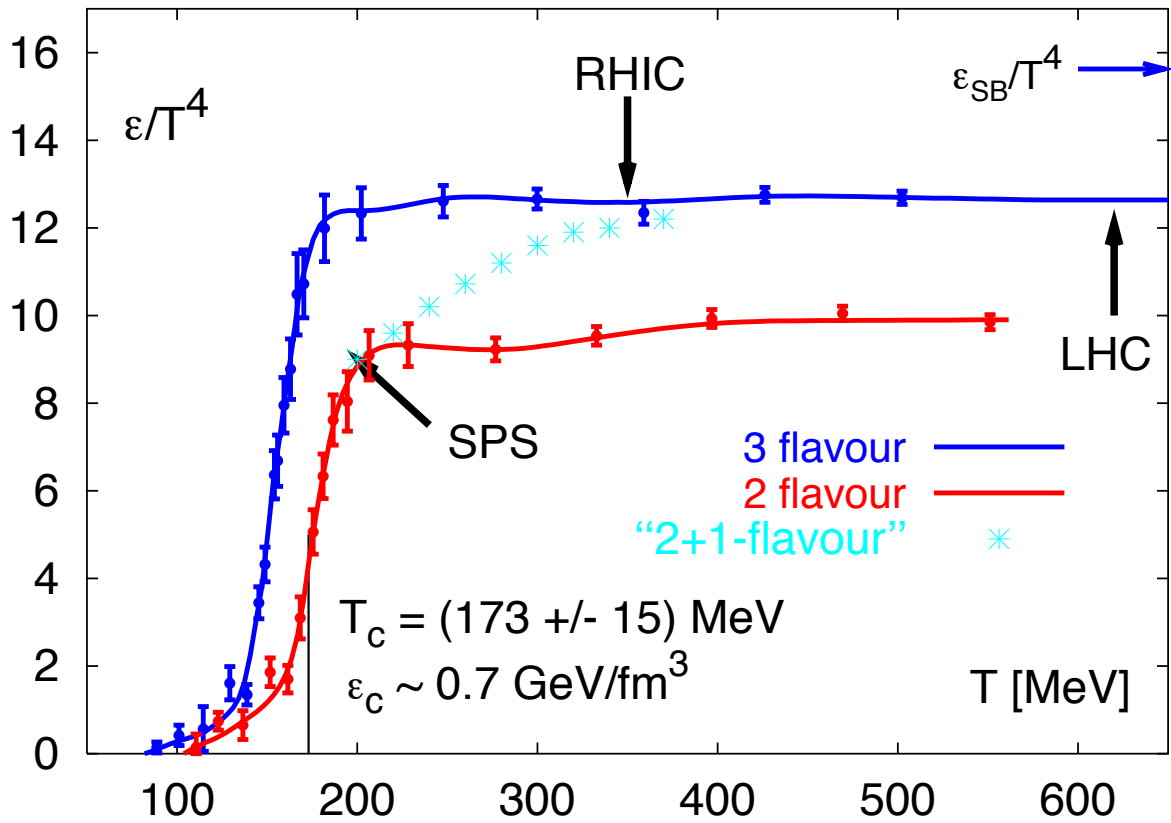
Figure 1.5: Lattice Predictions of Energy Density - Energy density of QCD medium as calculated with Lattice QCD. Also shown is the prediction from the ideal gas model, ϵ_{SB}. The critical temperature depends slightly on the number of light quark flavours considered. [19]

Overall, the lattice QCD calculations suggest, firstly, that a phase transition at around $T_c \sim 170$ MeV is to be expected, and that collisions of heavy ions at RHIC, and particularly at the LHC, should reach temperatures well over this transition point. As such, QGP production through Debye screening is expected in Pb–Pb collisions at $\sqrt{s_{NN}} = 2.76$ TeV in ALICE.

Another important Lattice QCD prediction is that the mass of quarks in a QGP is effectively lower than in the QCD vacuum [21]. As low energy QCD is non-perturbative, it is impossible to approximate through perturbation theory the gluon clouds surrounding any real quark. Instead, the theory is renormalised: fundamental parameters are expressed in terms of experimentally measured properties. This leads to effective quark masses in the vacuum known as dynamical masses; approximately 300 MeV for up and down quarks, and around 500 MeV for strange quarks [22]. As the strong coupling drops, the effective quark masses also drop, and in a QGP they reach their bare masses; a few MeV for the up and down quarks and around 100 MeV for the strange quark [23]. This is important for the behaviour of QGP, as it may speed chemical equilibrium; the statistically most likely distribution of quark flavours in the medium. Particularly, as the strange quark mass is now of the order of the QGP phase transition, strangeness equilibrium should be reached quicker in a QGP than in a hadron gas [24], as discussed in Section 1.8.

1.5   QGP in Colliders

It is useful to introduce the concept of rapidity when describing the behaviour of QGP in collider experiments. This is defined as:

$$y = \frac{1}{2} \ln \frac{E + p_z}{E - p_z}, \tag{1.8}$$

where E and p_z are the energy and momentum along the beamline axis respectively. Rapidity is additive under Lorentz boosts. Thus describing the geometric distribution of particles with respect to this variable allows simple comparisons between symmetric,

asymmetric and fixed-target colliders. In a symmetric collider, such as the LHC, particles travelling at right angles to the beam would appear at $y = 0$, while the highest rapidity a particle can have is that of the beam. For the LHC, operating at centre of mass energy $\sqrt{s_{\text{NN}}} = 2.76$ TeV, the beam rapidity is 7.9.

Intuitively, colliding nuclei might be expected to coalesce into a stationary 'fireball', with little memory of the initial beam momenta. This initially hot and dense fireball would then expand isotropically, cooling as it does so. When it cools back past the critical temperature, it would hadronise, and an isotropic distribution of hadrons would be observed.

However, in order for this image to hold, the colliding (Lorentz-contracted) nuclei would need to lose all of their kinetic energy over the length of the opposite nucleus. At the LHC, this would require an average energy loss per unit length of

$$\left\langle \frac{\mathrm{d}E}{\mathrm{d}x} \right\rangle = \frac{\sqrt{s_{\text{NN}}}/2}{2R/\gamma} \sim 150 \text{ TeV fm}^{-1}, \tag{1.9}$$

for each nucleon, where R is the radius of a lead nucleus in its rest frame, and γ the usual relativistic scale factor for the nucleus. Typical QCD scales of energy loss, such as the string tension, are of the order of 1 GeV fm^{-1} per string, which would clearly be insufficient to absorb the kinetic energy of the nuclei during the collision.

Bjorken argued that the presence of low fractional-momenta partons, with typical momenta given by the characteristic energy scale of QCD, $\Lambda_{QCD} \sim 200$ MeV would imply a minimal size to the nucleus of around 1 fm, due to the uncertainty relation between size and momentum. Under these conditions, the rate of energy loss would be

$$\left\langle \frac{\mathrm{d}E}{\mathrm{d}x} \right\rangle = \frac{\sqrt{s_{\text{NN}}}/2}{1\text{fm}} \sim 1.38 \text{ TeV fm}^{-1}, \tag{1.10}$$

which would still be significantly higher than the rate of energy loss due to QCD. Thus, to a certain extent the nuclei appear transparent, and will largely pass through each other. This will result in a large excess of baryon number appearing near the beam rapidity in

the detector.

As they pass through each other, however, the abundant low fractional momenta partons will interact, creating a rope of colour strings stretching between the two nuclei. It is these colour strings which are the source of the high energy densities required for QGP creation, forming a long thin fireball with initial momenta predominantly along the beampipe. This approximation is known as Bjorken Scaling, and is commonly used in hydrodynamical models of the system's evolution [20]. It is this assumption which allows the calculation of the Bjorken energy density, used to estimate the energy density within colliders in Figure 1.5.
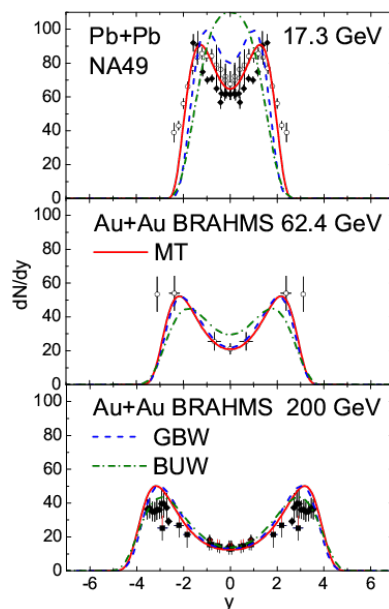
Figure 1.6: Baryon Transport at RHIC and the SPS - Net baryon number as a function of rapidity as measured in $\sqrt{s_{NN}} = 17.3$ GeV Pb–Pb collisions at the SPS, and $\sqrt{s_{NN}} = 62.4$ GeV and 200 GeV Au–Au collisions at RHIC [25].

Within this model, the incoming baryon number excess would be localised near the beam rapidity, while the central rapidity region will, on average, have no baryon number, as quarks and antiquarks must be created in pairs within it, naturally described by string breaking. Figure 1.6 shows the baryon number measured at SPS and RHIC as a function of rapidity. The baryon number is peaked around the beam rapidities, and is lower at central rapidity for higher energy collisions. However, in the case of total nuclear stopping, the baryon number would peak at $y = 0$ in the centre of mass frame. If Bjorken scaling

holds firmly, the rapidity distribution of particles produced far from the beam rapidity will be flat, and the baryon number distribution at central rapidity would be zero. This is not achieved at RHIC, but is a reasonable approximation, and will be closer still at LHC energies.

1.6 Time Evolution of the QGP

How is this plasma expected to evolve? By referring to it as a plasma, and describing it by its temperature, there is an implicit assumption that it has had time to thermalise locally. This will not happen instantaneously; there will be some time before it reaches this stage. After the initial collisions, particles emerge from the QGP vacuum, and appear after some time characteristic of the force, τ_{QGP}. With time dilation, this means that slower moving particles form first, at the centre of the system, while those particles at the edge of the system, or further from the centre of the collision, take longer to resolve.

These particles take some further time to thermalise, creating new particles as they do so in a parton cascade. It is the matter so formed that is referred to as the Quark Gluon Plasma. This is hot and dense, and so will be expected to expand into the surrounding vacuum. Its temperature will drop as it does so, mostly driven by its longitudinal expansion. Eventually its temperature will drop below the critical temperature, and the plasma will hadronise. The hadrons can still interact and so, until the mean free path of hadrons rises above the transverse size of the plasma, they will continue to thermalise. As time passes, and the density of the hadron gas drops, first inelastic and then elastic collisions will become sufficiently rare that the hadronic populations, and then the momentum distributions become fixed. These stages are referred to as chemical and thermal freezeout respectively, and the hadrons can thereafter be considered to be free-streaming particles, which will be observed in the detectors.

During this expansion process, a number of particles are created which will escape the medium, acting as probes to diagnose the properties of the medium. In the initial

15

hard collisions, high momenta electroweak probes (γ, W and Z) are created and, because they don't experience the strong force, they will escape the coalescing medium, carrying information about the initial collisions. Particularly hard partons can also be created in the initial collision with enough energy to escape the medium; these will leave energy within the medium, but cannot themselves be considered part of the medium. Photons will be emitted in a thermal spectrum by the thermalised medium, and can theoretically be detected to resolve the temperature of the medium. Unfortunately, this is experimentally difficult as the signal will be contaminated with photons emitted by the decay of (thermally distributed) pions, and the temperature of the system is in any case constantly evolving. Finally, the medium itself will break up into hadrons, which can be detected by experiments.

1.7   State of the Medium

Many measurements of the material produced in heavy ion collisions have been made, leading CERN in 2000 to announce that *"We now have evidence of a new state of matter where quarks and gluons are not confined"* [26]. Since then, experiments at RHIC, and at CERN have identified several parameters of the medium created. Measurements of the charged particle multiplicity at ALICE put the Bjorken energy density at greater than 10 GeV/fm^3 [27], approximately an order of magnitude over the critical energy density estimated from Lattice QCD [19]. Measurements of the flow of direct photons suggest that the times for thermal and chemical equilibrium are relatively short, at around 0.35 fm/c and 1.5 fm/c respectively [28], while the time to hadronisation is placed at around 11 fm/c from pion correlation measurements [29]. The medium appears to evolve hydrodynamically, with a particularly low shear viscosity to entropy ratio of ~ 0.2 [30]. All measurements appear consistent with production of QGP; high p_T strongly interacting particles are quenched while electroweak probes are not[31], heavy quarkonia states are sequentially suppressed [32], while lighter states show evidence of regeneration [33].

A particularly interesting, although experimentally challenging, measurement is that of thermal photon emission which, at RHIC, suggests a system evolving from initial temperatures of > 250 MeV to around 150 MeV with an intermediate QGP phase [34]. Further results from the LHC heavy ion programme are anticipated to add more detail to this picture.

1.8 Strangeness in Heavy Ion Collisions

Historically, strangeness has often been linked to studies of the quark gluon plasma. The existence of, and behaviour of, the QGP phase transition is linked to the mass of the strange quark [35]. As its dynamical mass is somewhat higher than the QGP phase transition temperature, and its bare mass somewhat below [22, 23], it plays a key role in determining the behaviour of the system close to the phase boundary, as seen in Figure 1.5.

Strangeness enhancement was first postulated as a signature of QGP by Rafelski et. al. in 1980 [36]. As there are no strange valence quarks in the incoming beam, net strangeness of the system must be zero, and any strange quarks must be created with an accompanying strange antiquark. The dominant production process in nucleon nucleon collisions will be

$$N + N \rightarrow N + \Lambda + K^+, \tag{1.11}$$

or similar processes involving a Σ particle in place of the Λ, or a K^0 in place of the K^+ [37]. The energy threshold for this process is relatively high; $m_N + m_\Lambda + m_K - 2m_N \sim 670$ MeV.

1.8.1 Strangeness Equilibrium in a Hadron Gas

More favourable processes for thermal production in a hadron gas, particularly one rich in pions are

$$N + \pi \rightarrow \Lambda + K^+, \tag{1.12}$$

$$\pi + \bar{\pi} \to K + \bar{K}, \tag{1.13}$$

with threshold energies of ~ 540 MeV and ~ 710 MeV respectively. Accompanied by strangeness exchange processes of the type

$$\Lambda + \bar{\mathrm{K}} \to \pi + \Xi, \tag{1.14}$$

absolute chemical equilibrium of strange hadronic species could eventually be achieved in a hot hadron gas. However, considering the comparatively low temperatures (extrapolated from thermal photon spectra), the timescales required are rather long. At a temperature $T = 160$ MeV, Rafelski et. al. find that the equilibration of strange hadrons takes roughly 1000 fm/c, in the case of zero baryon stopping [24]. For the case where baryon stopping is non-negligible, particularly true at SPS energies as seen in Figure 1.6, the multi-strange antibaryons $\bar{\Xi}$ and $\bar{\Omega}$ are only at roughly 10% of their equilibrium values after this time has passed.

Rafelski et. al. also calculate a distinct difference between the time evolution of multi-strange baryons and antibaryons in the case of non-zero net baryon number, despite the strangeness being created in quark-antiquark pairs. The reason for this lies in the processes responsible for redistributing strangeness in the hadron gas. As the production of multiple strange quark-antiquark pairs in one reaction will be suppressed, the majority of (multi)-strange antibaryons are created in exchange reactions [24] such as

$$\bar{N} + \mathrm{K} \to \bar{\Lambda} + \pi, \tag{1.15}$$

$$\bar{\Lambda} + \mathrm{K} \to \bar{\Xi} + \pi, \tag{1.16}$$

$$\bar{\Xi} + \mathrm{K} \to \bar{\Omega} + \pi. \tag{1.17}$$

Thus, the evolution of (multi)-strange antibaryons is dependant on the density of antinucleons, and so will be slower in a baryon-rich hadron gas.

Estimates of the lifetime of the fireball at LHC energies using pion correlations place it at the order of 10 fm [29], with earlier experiments at lower energies accordingly shorter lived. Thus it was predicted that strange hadrons cannot reach equilibrium through thermal rescattering processes in a hadron gas alone [38].

1.8.2   Strangeness Equilibrium in a QGP

Initially, from studies by Biro et. al., it was believed that the same was true of a QGP, as the reaction rates for $q + \bar{q} \rightarrow s + \bar{s}$ were too slow to reach equilibrium in the predicted QGP fireball lifetimes [39]. However, this neglected to include the contribution of gluons; a significant degree of freedom in the QGP phase, with a thermalisation time around a quarter that of the quarks [40]. With these included, the lowest order QCD Feynmann diagrams for strangeness production are those shown in Figure 1.7: $gg \rightarrow s\bar{s}$ and $q\bar{q} \rightarrow s\bar{s}$.
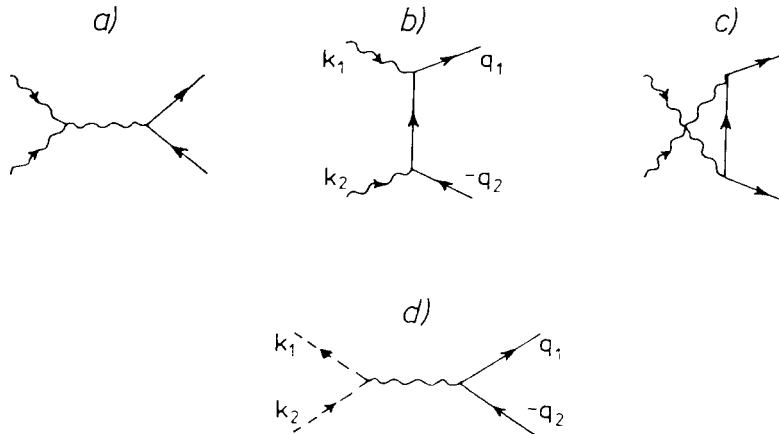
Figure 1.7: Lowest Order QCD Diagrams for $s\bar{s}$ Production - Feynman diagrams for (a-c) $gg \rightarrow s\bar{s}$ and (d) $q\bar{q} \rightarrow s\bar{s}$ [24].

All of these are annihilation processes, and so the threshold energy is simply twice the bare mass of a strange quark. When Rafelski proposed his original paper, this was thought to be of the order of 300 MeV [41], but has since been reduced to roughly 100 MeV, strongly favouring thermal production in a system believed to have temperature $T > 150$ MeV.

The impact of Pauli blocking can change the equilibration times slightly. As quarks

are fermions, they are subject to Pauli exclusion [42], which states that two fermions cannot be in the same quantum state. This has little effect in pp collisions, but in heavy ion collisions where the quark densities are higher, production can be suppressed as the available energy levels fill up. Hwa and Yang have shown that this causes around 6% of quark-antiquark pairs to be created as strange quarks rather than light quarks when comparing the initial stages of a heavy ion collision to a pp collision, slightly speeding the early stages of strange quark equilibration [43]. At higher temperatures, where strange quarks rapidly reach equilibrium, Pauli blocking of strange quarks can increase equilibrium time by around 10% [24].

For a strange quark mass of 200 MeV Rafelski et. al. find a QGP equilibration time of $1 - 10$ fm/c, dropping sharply as a function of QGP temperature [37]. This is similar to the expected QGP lifetime, and so chemical equilibrium of strangeness is predicted for QGP production in SPS, RHIC and LHC. Indeed, as the equilibration time is shorter for higher temperatures, any QGP produced may be over-saturated with strangeness at hadronisation, as the system has cooled over its evolution [44].

1.8.3 Experimental Evidence for Strangeness Enhancement

The consequence of the above discussions is that strangeness production will be enhanced in heavy ion collisions over that observed in pp collisions, and that it will be higher should a QGP phase be reached. The distinction should be particularly strong for multi-strange anti-baryons: in particular, the $\bar{\Omega}$ particle may be enhanced by a factor of 10^3 in a QGP compared to a Hadron Gas [37].

Disentangling this signature of QGP from experimental data is not straightforward. In the absence of a thermalised system, reactions such as those given in Equations 1.12 and 1.14 will enhance the strangeness production in heavy ion collisions relative to a pp baseline through rescattering. Figure 1.8 (left) shows the charged kaon to pion ratios measured in STAR as a function of beam energy. It can be seen that, at low energy, the K^+/π^+ ratio is significantly higher than the K^-/π^- ratio, with the two becoming
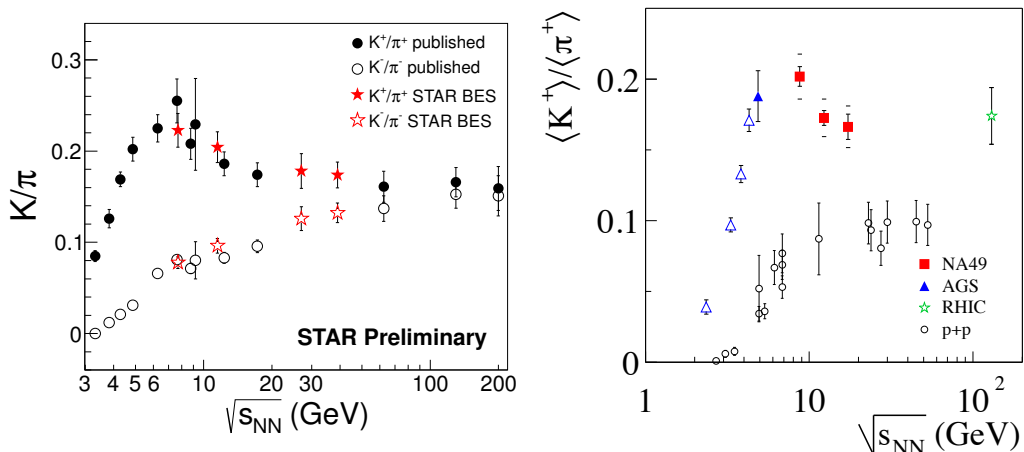
Figure 1.8: K/π **Ratio at SPS, AGS and RHIC** - Left: charged kaon to pion ratios measured by STAR at RHIC as a function of beam energy [45]. Right: charged K^+/π^+ ratio as a function of beam energy measured in Pb–Pb and pp collisions at SPS, AGS and RHIC [46]

consistent for centre of mass energies above ~ 50 GeV. This is linked to the baryon-antibaryon asymmetry in the colliding system; as K^+ is initially produced in conjunction with Λ, while K^- is produced with a $\overline{\Lambda}$, there is an enhancement of K^+ over K^- for systems with significant baryon stopping. This effect must be considered for any potential signal of baryon enhancement.

The right hand plot of Figure 1.8 shows a similar measurement with data recorded in pp collisions included. As the beam energy increases, the pp baseline also increases, while at the higher beam energies, the ratio in heavy ion collisions appears more constant. This would appear to imply that the heavy ion systems have achieved strangeness equilibrium, suggesting the presence of a QGP phase. The increase in the ratio measured in pp collisions has been linked to a suppression of strangeness production in low energy pp collisions, when compared to e^+e^- collisions [47]. Where QCD string energies are low compared to the mass of a given hadron, it has been suggested that the limited phase space available for particle production suppresses their creation. However, when the string energy is much higher than the hadron mass, phase space is saturated, and so particle production appears thermal, and particle ratios do not change strongly with further increases in beam energy.

21

ALI-PREL-72168
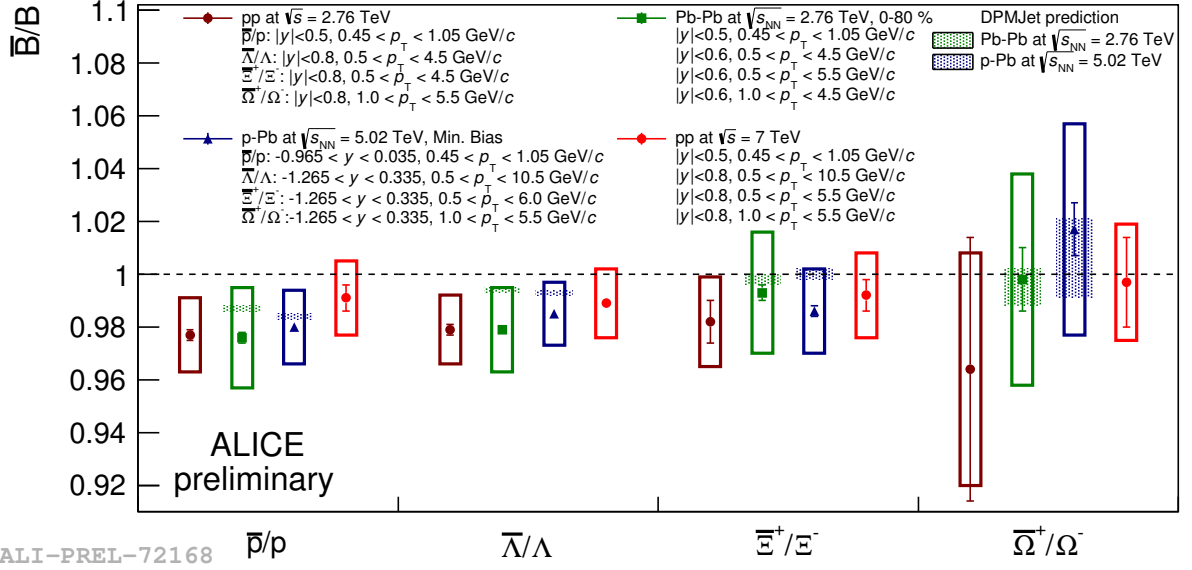
Figure 1.9: Antibaryon to Baryon Ratios at ALICE - Midrapidity antibaryon to baryon ratios as measured in pp, p–Pb and Pb–Pb collisions with ALICE at the LHC [48, 49]
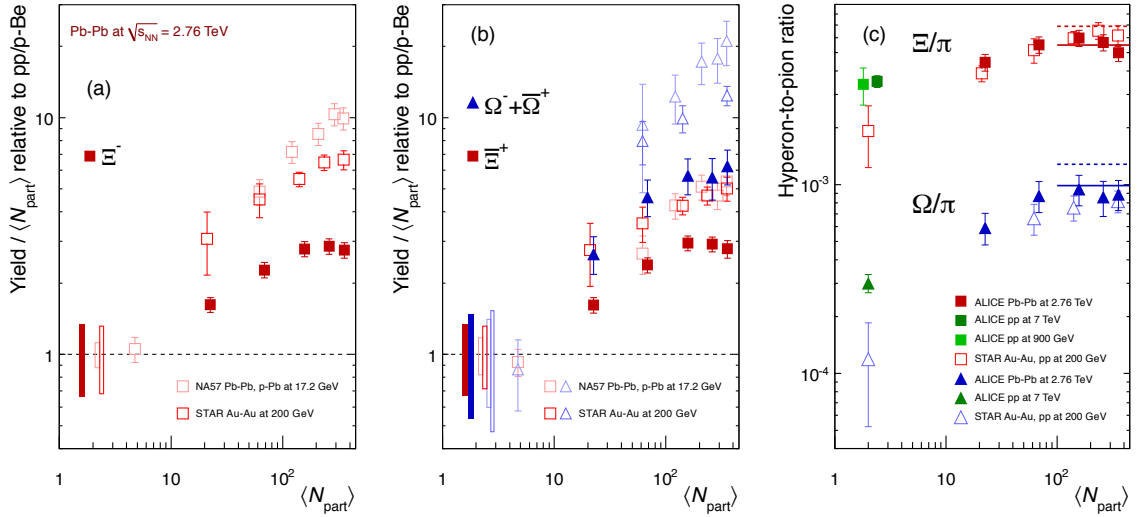
Figure 1.10: Enhancement of Strange Nucleon Production in ALICE - a,b: Relative yield of (multi)-strange baryons in heavy ion collisions, normalised to baseline pp/p-Be collisions and number of participant nucleons. c: ratio of multistrange baryons to pions for A-A and pp collisions at LHC and RHIC energies. Lines indicate thermal model predictions. [50]

By LHC energies, differences between the yield of baryons and antibaryons (at mid rapidity) are sufficiently small to be considered negligible, as seen in Figure 1.9. The K/π ratio does not change from RHIC energies [51], further supporting the idea that kaons, at least, reach thermal equilibrium in heavy ion collisions for $\sqrt{s_{\rm NN}} > \sim 50$ GeV.

Figure 1.10 (a,b) shows the apparent enhancement of multi-strange baryon production in heavy ion collisions relative to pp collisions (p-Be for NA57) for centre of mass energies ranging from 17.2 GeV $\leq \sqrt{s_{\rm NN}} \leq 2.76$ TeV. This is calculated by dividing the mid-rapidity yield of strange baryons measured in a heavy ion collision by the baseline measurement, and then further by the approximate number of nucleons involved in the collision. The points clearly lie above 1, and show dependance upon the number of nucleons involved, and the energy of the collision. The enhancement is greater for the Ω (sss) than the Ξ (ssd), as would be expected from the strangeness contents, and the effects of baryon-antibaryon asymmetry can be seen in the RHIC and SPS results. The enhancement increases with the number of participants, suggesting that the size of the system affects the time required for equilibration of strangeness. More interestingly, the magnitude of the enhancement appears to decrease with collision energy, with the LHC results appearing to also saturate with system size. This decrease with energy can be explained with referral to plot (c), which shows the ratio of the multi-strange baryon yields to that of the pions in each collision system. In the heavy ion collisions, these ratios show a weak dependance on the number of participant nucleons but no energy dependance; suggesting that although the system size may vary, the fraction of strange hadrons does not - they are fully chemically equilibrated. For the pp collisions, however, the situation is different. Not only is the ratio lower, the lower energy RHIC points are significantly below the LHC points. Rather than strangeness in heavy ion collisions being less enhanced as we go from RHIC to LHC energies, it appears that strangeness in pp collisions is less *suppressed*. Interestingly, there is no significant difference in the Ξ/π ratio between the two LHC energies given of $\sqrt{s} = 900$ GeV and 7 TeV, suggesting that strangeness in pp collisions at the LHC may no longer be suppressed. When the LHC begins running at

full operational energy, a conclusive answer to this problem may become available.

1.9 The Baryon Anomaly

Although the enhancement due to strangeness content of singly-strange Λ and kaons is relatively weak at RHIC and LHC energies ($K/\pi \sim 1.5$ in Pb–Pb collisions, ~ 1.3 in pp collisions [52]), further physics can be extracted from their behaviour.

When RHIC first started running Au–Au collisions at $\sqrt{s_{\mathrm{NN}}} = 130$ GeV, it was noticed that the yield of baryons approached that of mesons around $p_{\mathrm{T}} = 2$ GeV/c [53, 54]. Measurements of the p/π and $\bar{p}/\pi$ ratio were used to quantify this, as shown in Figure 1.11. These ratios clearly indicate a growth in the ratio for the p_{T} region $1 < p_{\mathrm{T}} < 2$ GeV/c. The PHENIX results (left and centre) show a clear increase compared to the ratio measured in lower energy pp collisions, and also highlight that although there is significant baryon-antibaryon asymmetry, there is a growth in both ratios. The STAR results (right) indicate that it is a centrality related effect; more head on collisions, with a larger system volume, show a greater increase in the ratio at a given p_{T}. Unfortunately the statistics and p_{T} limits of these measurements make it hard to derive many more substantive statements. At higher p_{T}, does the ratio continue to infinity, as implied by some hydrodynamic models [55], return to pp like behaviour, or settle at some fixed level of baryon enhancement? Do the less central collisions reach the same level of enhancement as the central collisions?

In order to answer these questions, the $\Lambda/\mathrm{K}_{\mathrm{S}}^0$ ratio was studied. As these particles are both singly strange, any strangeness enhancement should cancel out in the ratio, hopefully revealing the same behaviour as the p/π ratio. As the Λ and $\mathrm{K}_{\mathrm{S}}^0$ are the lightest strange baryon and meson respectively, they can only decay through the weak interaction. This leads both to have distinctive decay topologies, separated from the original collision point, allowing relatively clean experimental identification over a wide range of p_{T}.

The $\Lambda/\mathrm{K}_{\mathrm{S}}^0$ ratio measured by STAR is shown in Figure 1.12 [58]. At low and high p_{T}
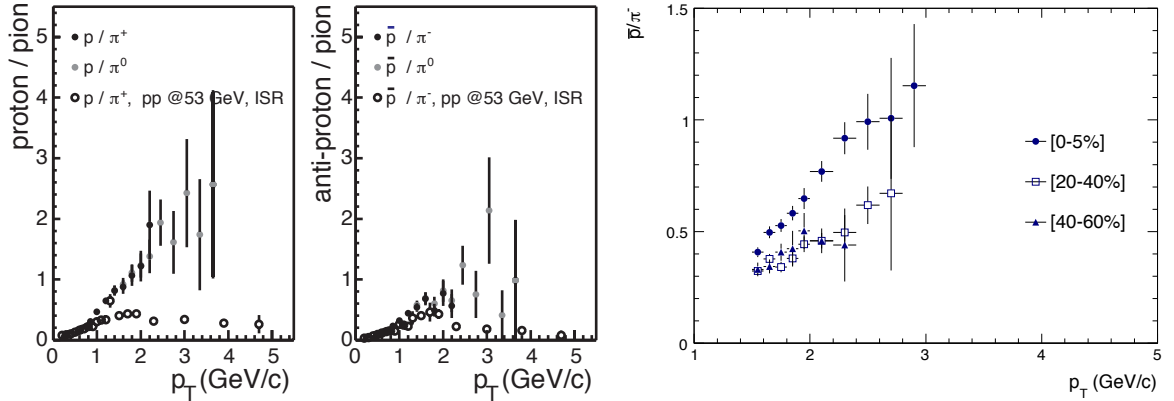
Figure 1.11: $p(\bar{p})/\pi$ **Ratio at RHIC** - (Anti-)proton to pion ratio measured in Au–Au collisions at RHIC. Left and Centre: p/π and $\bar{p}/\pi$ ratio measured by PHENIX in 0-10% most central $\sqrt{s_{\mathrm{NN}}} = 130$ GeV Au–Au collisions [56]. Also shown are similar measurements in pp collisions at $\sqrt{s} = 53$ GeV. Right: $\bar{p}/\pi$ ratio measured by STAR in $\sqrt{s_{\mathrm{NN}}} = 200$ GeV Au–Au collisions for a selection of centralities [57].
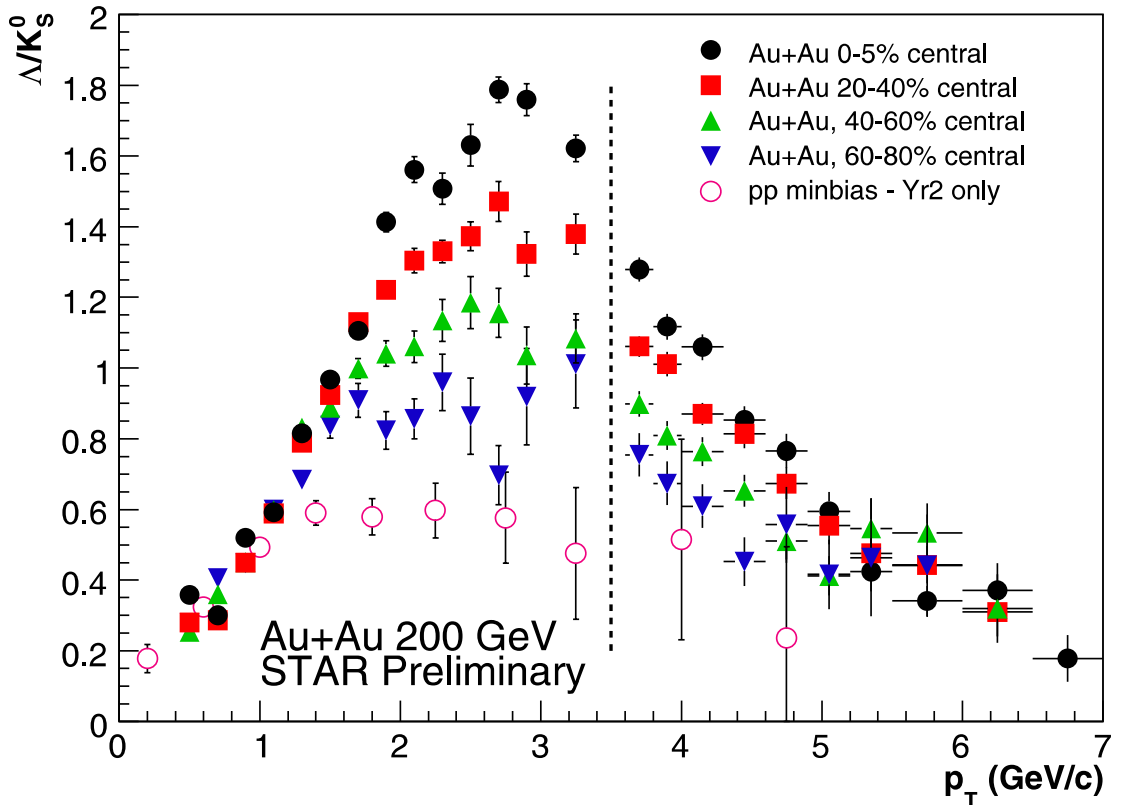
Figure 1.12: The Λ/K_S^0 Ratio Measured at STAR - The Λ/K_S^0 ratio as measured in $\sqrt{s_{\mathrm{NN}}} = 200$ GeV Au–Au collisions at STAR [58]. Results to the right of the dotted line have had their statistics improved by including the 2004 Au–Au run.

all centralities appear to be consistent, as does the pp reference. In the intermediate p_T region $1.5 < p_T < 5$ GeV/c, however, there is a distinctive increase in the ratio in Au–Au collisions when compared to the pp reference, which increases for more central collisions. Qualitatively, the low p_T region can be understood in terms of a hydrodynamical model, although this must be less important as we reach higher p_T in order for the ratio shape to turn over. At the highest p_T shown, the particle spectra are usually considered to be similar to those generated in pp, although suppressed by passage through the QGP [59]. This would predict that the Λ/K_S^0 ratio is identical to that in pp as we continue to higher p_T. In the intermediate p_T region, where the enhancement and separation between centralities can be resolved, recombination models can reproduce the data [60]. These models postulate that hadronisation of a QGP occurs by the coalescence of co-moving constituent quarks within the plasma. As such, baryons would be created with 3 times the typical momentum of a quark, while mesons would form with only twice the typical quark momenta, leading to an apparent enhancement of the baryon to meson ratio. This effect is bolstered by the relative ease of creating a baryon through quark coalescence when compared to string fragmentation. These theoretical ideas required to describe the full p_T range of the ratio will be discussed in detail in the next chapter.

Despite this improvement in p_T-reach and statistics of the baryon to meson ratio, some questions remain. How consistent are the heavy-ion and pp ratios at high and low p_T? Is there a sharp change in behaviour between pp and peripheral heavy-ion collisions? Answering these questions is one of the prime motivations for attempting to improve this measurement at the LHC. By extending the p_T reach and improving the statistics of the measurement, it should be possible to clearly resolve all differences between the ratio in pp and Pb–Pb collisions. Further, by repeating the measurement at LHC energies, we can answer other questions. Is the effect energy dependant; or will it appear to saturate as seen for the K/π ratio in Figure 1.8? By making this measurement differential in energy as well as centrality, the theoretical models believed to explain the ratio are tested, and our understanding of the underlying physics improved.

1.10 Outline

The remainder of this thesis will be devoted to the measurement of the Λ and K_S^0 spectra, leading to the Λ/K_S^0 ratio, in Pb–Pb and pp collisions with ALICE at the LHC. Chapter 2 goes into more detail on the theory considered most important at each p_T region of the Λ/K_S^0 spectra; hydrodynamics at low p_T, jet quenching at high p_T and coalescence in the intermediate p_T region where the enhancement is expected. Chapter 3 details the experimental apparatus used to perform this measurement; ALICE and the LHC. Chapter 4 describes the analysis techniques used to extract Λ and K_S^0 candidates from the collected data, and correct them to reach an estimate of the true spectra produced in the collisions. Details of crosschecks on the spectra, and estimations of the systematic uncertainties of the measurements will also be given. Finally, Chapters 5 and 6 will discuss the results of this analysis, in the context of the theoretical models introduced in Chapter 2 and complementary measurements from RHIC and the LHC, and highlight the areas in which further research is needed.

2

Theory

In this chapter, several theoretical concepts which have implications for the p_T spectra of the Λ and K_S^0 are discussed. At low momentum, particle production is expected to be entirely due to the evolution of the thermalised QGP, which is discussed in terms of a hydrodynamical model. A slight variation on this is to allow coalescence of quarks which are close together in phase space within the medium, a phenomenon which potentially enhances baryon production and gives a higher average momenta to baryons than mesons. At the highest reaches of momentum studied, particle production will be dominated by the initial hard collisions of the nuclei, but interactions with the medium can still cause discrepancies between production rates measured in Pb–Pb and pp collisions.

2.1   Thermal Production of Particles

The Quark Gluon Plasma is defined as a thermalised state of matter. As such, it must exist long enough for a (local) temperature to be well defined. Unlike the simplest models of an ideal gas, this medium has the potential to change the relative abundances of its constituents, and in full thermal equilibrium it will be described by the Grand Canonical Ensemble.

A hadron gas could also follow this model, if in contact for long enough to reach thermal and chemical equilibrium. This is not the only way to reach a hadron gas described by

the Grand Canonical ensemble; when hadrons are formed from the Quark Gluon Plasma, they are effectively in contact with a thermal and chemical bath, and so should be formed in a state of thermal and chemical equilibrium. Thermal models predict the overall abundances of particles by assuming the presence of a hadron gas in thermal and chemical equilibrium. Typically, the three lightest quarks (up, down and strange) are considered to be in equilibrium as described in Section 1.8, for example as in the work of A. Andronic et. al. [61]. Some models, however, include a fugacity factor γ to allow for some part of the system being out of equilibrium, for example to allow strangeness to be depleted or oversaturated, as in the models of Rafelski et. al. [41].

The distribution of hadrons in full thermal and chemical equilibrium is calculated from the Grand Canonical partition function Z. For a particle species i, the number density n_i is given by

$$n_i = -\frac{T}{V}\frac{\partial \ln Z_i}{\partial \mu} = \frac{g_i}{2\pi^2}\int_0^\infty \frac{p^2 \, \mathrm{d}p}{exp[(E_i - \mu_i)/T] \pm 1}, \tag{2.1}$$

where g_i is the degeneracy due to spin, T the temperature of the system and V the volume [61]. E_i and μ_i are the energy and chemical potential of a hadron species respectively, and the $\pm$ is $+$ for fermions and $-$ for bosons. The integral is taken over all momenta p. The chemical potential can be expanded out into separate chemical potentials for baryon number B, isospin I_3 and strangeness S:

$$\mu_i = \mu_B B_i + \mu_{I_3} I_{3i} + \mu_S S_i, \tag{2.2}$$

where the individual chemical potentials can generally be fixed by insisting on conservation laws, such as zero net strangeness in the collision. As a result, the only parameters taken from fitting to data (in the simplest thermal equilibrium models) are the temperature T and the baryon chemical potential μ_B.

Figure 2.1 shows the results of thermal fits to SPS and RHIC data. The left plot shows a simultaneous fit to a selection of particle ratios in $\sqrt{s_{NN}} = 200$ GeV collisions at RHIC. The three resonances K^{*0}, Λ^* and Δ^{++} are not included in the fit as the resonances can

potentially decay during the hadron gas phase, leading to a suppression of their observed yields as their decay products rescatter [41]. Disregarding these, it is notable how well the fit simultaneously describes all other particle ratios. This suggests, firstly, that the hadronic system is in fact thermalised, and secondly that all particles were produced at the same temperature. This suggests that the breakup of the hadronic gas is rapid, as otherwise there would be an observable relationship between the inelastic cross sections of a hadron and the temperature at which its yield is fixed.
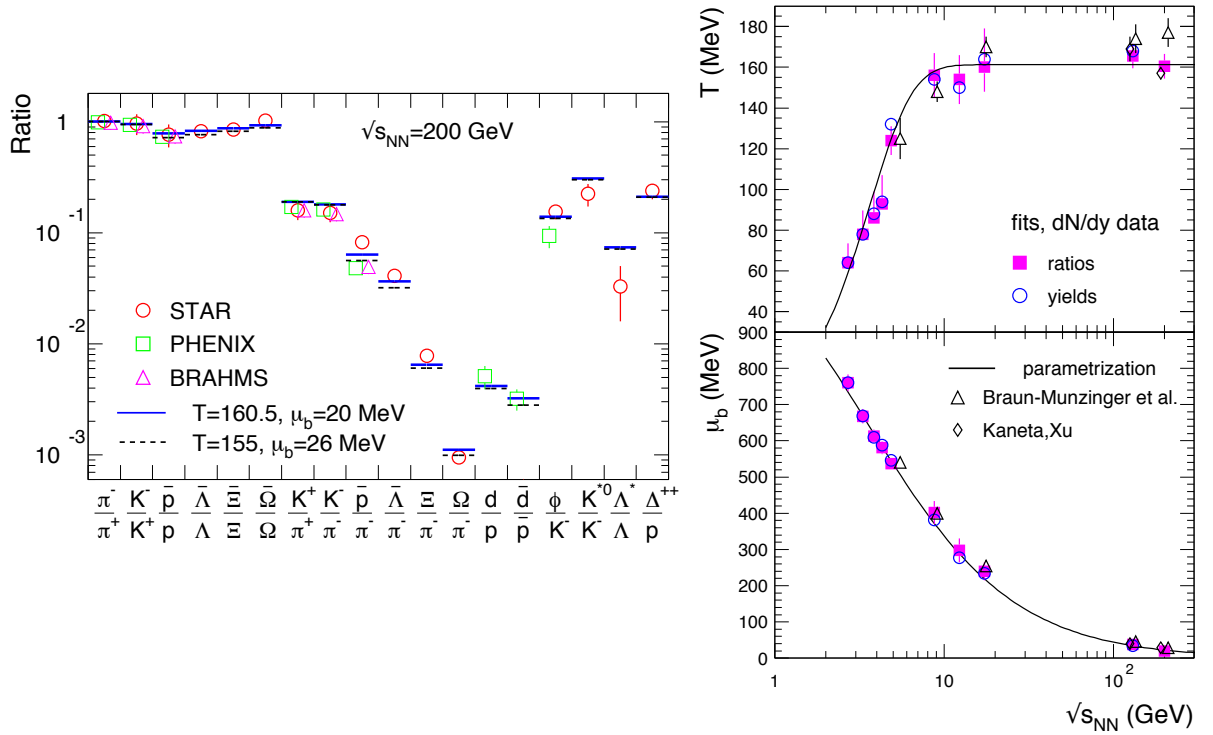
Figure 2.1: Results of Thermal Fits in Heavy Ion Experiments - Left: results of a thermal fit to particle ratios measured at RHIC, for Au–Au collisions at $\sqrt{s_{NN}} = 200$ GeV. Right: Temperature and Baryon Chemical Potential extracted from thermal fits for a selection of SPS and RHIC collision energies. [61]

The right hand side of Figure 2.1 shows the evolution of the temperature and baryon chemical potential extracted from these fits. As expected from Figure 1.6, the baryon chemical potential drops significantly with increasing $\sqrt{s_{NN}}$, as less of the incoming baryon number remains in the mid-rapidity region. The temperature however shows a much more interesting feature: at low centre of mass energy, it increases with the incoming

energy density, until it reaches a plateau. Recalling that this is the temperature of the hadronic gas phase, rather than any potential QGP, it strongly supports the idea of a phase transition with a critical temperature of around 160 MeV. It is possible, from the data points shown, to suppose that this plateau is rising slightly rather than flat; results from thermal fits of ALICE data will clarify this, and are discussed in Section 5.6.

While these results are consistent with a QGP to hadron gas transition, as expected in collisions of heavy ions, they could also be explained in terms of a thermalised hadron gas. This would naturally have a thermal distribution of hadrons, and if the energy required for the phase transition is high, it would plateau at the critical temperature. However, predictions of thermalisation times for hadrons [62] make this model implausible, as described in Section 1.8.1. It is worth noting, however, that particle yields from pp collisions are already close to a thermal distribution; see for instance [63]. In such a system, the number of hadrons produced is sufficiently low to make rescattering implausible. Werner et. al. explain this observation as due to a phase space distribution in a string breaking model [47]. This predisposition to a thermal-like distribution could make thermalisation times shorter, both for a Quark Gluon Plasma and for a hadron gas.

2.1.1   Chemical and Kinetic Freezeout Points

The evidence for chemical equilibrium implies the existence of kinetic equilibrium as well. The chemical distribution can only be changed by specific inelastic collisions, while the distribution of particles momenta may be statistically distributed through all collisions, including the more common elastic interactions. Thus, the point of kinetic freezeout may lie at a lower temperature than chemical freezeout [62]. As the particle density drops below the point where chemical thermalisation can be realised, kinetic thermalisation can continue, until the density of the system is so low that rescattering becomes negligible. As such, the kinetic temperature distribution will be 'frozen' at a lower temperature than the chemical one. This can be seen in Figure 2.2, where the blue kinetic freezeout points are systematically below the red chemical freezeout measurements.

Several other general properties of hadron production can be drawn from this plot. Firstly, the various freezeout points for collisions at SPS and AGS collisions follow a line of fixed entropy per baryon, consistent with an adiabatic expansion of the medium [62]. Kinetic freezeout appears to occur at a constant particle density, where rescattering is no longer significant. Chemical freezeout, however, appears to occur at a energy per particle of 1 GeV, which is comparable to the predicted energy of the phase transition at zero baryon chemical potential [64]. This is the case even for e^+e^- collisions at LEP, where no rescattering is expected to occur. Heinz thus argues that the apparent chemical equilibrium of particle yields is due to a maximisation of entropy in particle production, rather than explicit thermalisation [62].

2.2 Initial Conditions

While the thermal models discussed above can provide accurate predictions for overall particle yields, for more detailed descriptions of the particles measured in heavy ion collisions it is necessary to consider the initial conditions of the evolving system.

2.2.1 The Glauber Model

The Glauber Model (discussed in historical depth in [65]) allows a comparison between nucleon-nucleon collisions and nucleus-nucleus collisions. As such it allows identification of behaviour which is qualitatively different in the two systems, and not merely scaled up from one binary collision to (for example) 1500.

It rests on several approximations; that the cross section for collisions of nucleons is identical in vacuum and within nuclei, and further that the cross section will not change following a collision. More specifically, collisions are not considered to change the properties of the nucleons at all; they are entirely transparent. The approximation of transparency is good at the high collision energies used in modern colliders [66], while the assumption of a vacuum-like cross section is unlikely to be true, and so will show up in
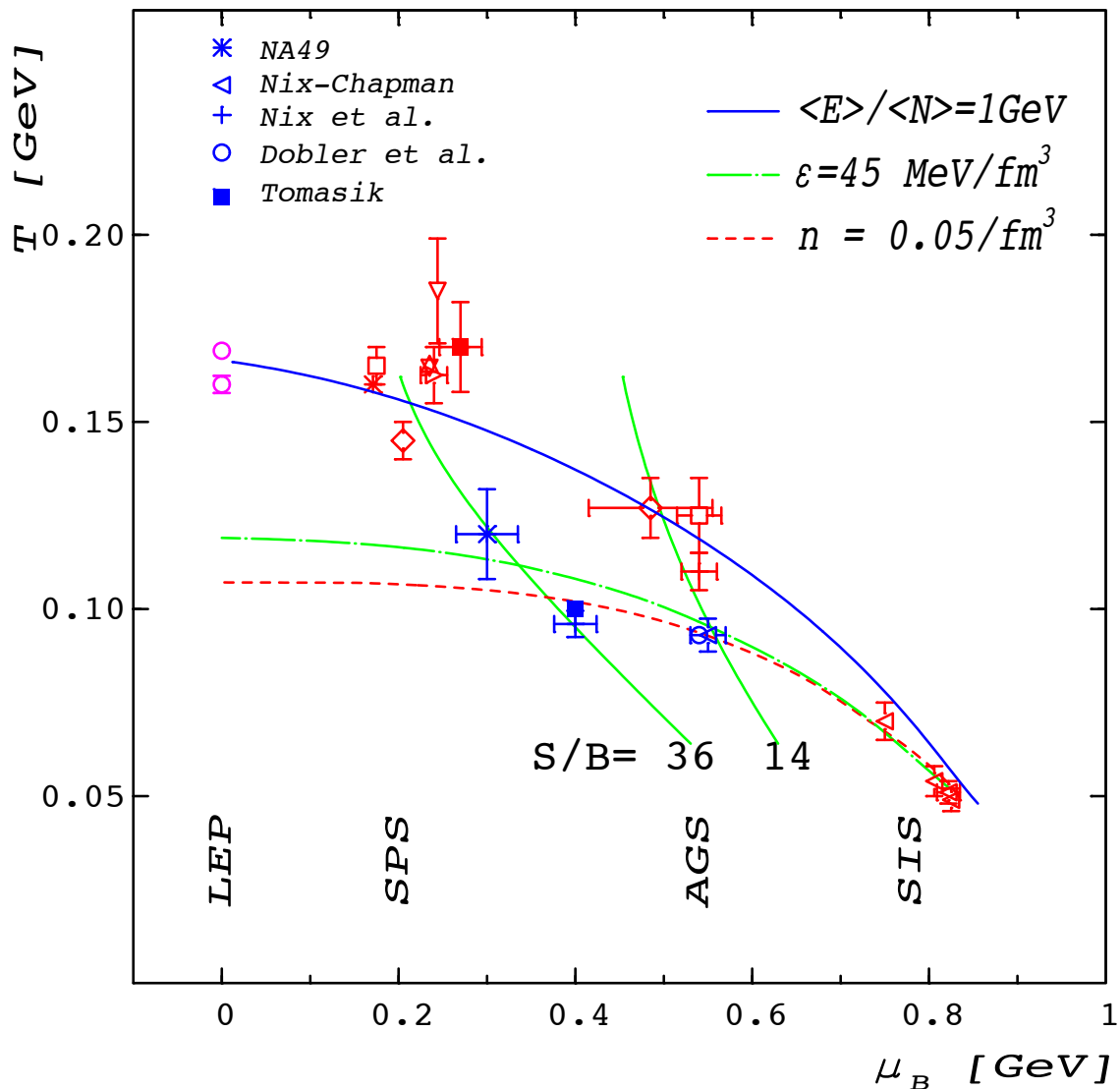
Figure 2.2: Chemical and Kinetic Freezeout Measurements - Chemical and Kinetic Freezeout calculations from SPS and AGS data. The upper red points, and solid fit line indicated chemical freezeout measurements. The lower blue points and dotted lines indicate kinetic freezeout. [64]

any comparison between theory and data.
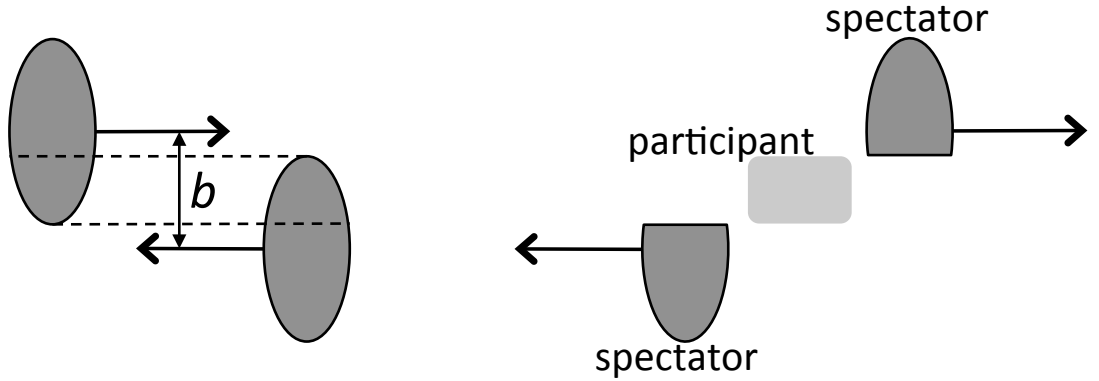
Figure 2.3: Impact Parameter of Colliding Nuclei - Geometry of colliding nuclei with impact parameter **b** indicated on the left hand diagram. This determines the 'participant' and 'spectator' nuclei for the collision, as shown on the right hand side.

Under these approximations, a prediction can be made for the number of nucleons which will be involved in a collision between two nuclei with impact parameter **b**, where the impact parameter is defined as the separation between the two nuclei's centres transverse to the beam, as indicated in Figure 2.3. While nuclei passing close to each other with an impact parameter larger than twice the nuclear radius may undergo electromagnetic interactions, strong interactions should occur only when the nuclei physically overlap, due to the short range nature of the force. This distance, d_{inel} is then calculated from the inelastic nucleon-nucleon cross section [4]:

$$d_{\mathrm{inel}} = \sqrt{\sigma_{NN}^{\mathrm{inel}}/\pi}. \tag{2.3}$$

Two approaches may then be taken to estimate the number of nucleon-nucleon collisions in a nucleus-nucleus collisions. In the optical limit, the nucleus is described by some smooth density function $\rho(r)$, and a thickness function, $T_A(\mathbf{s})$, of a nucleus A, travelling in the z direction can be defined:

$$T_A(\mathbf{s}) = \int \mathrm{d}z \rho_A(z, \mathbf{s}). \tag{2.4}$$

A reasonable (non-discrete) approximation for the nucleon density is the phenomenological

34

Saxon-Woods parameterisation [67]:

$$\rho_A(r) = \frac{\rho_{\mathrm{nm}}}{1 + \exp((r - R_A)/a)}, \tag{2.5}$$

where ρ_{nm} and R_A are the overall density and radius of the nuclei, typically extracted from lepton-nuclei scattering experiments [68], and a represents a skin depth of the nucleus.
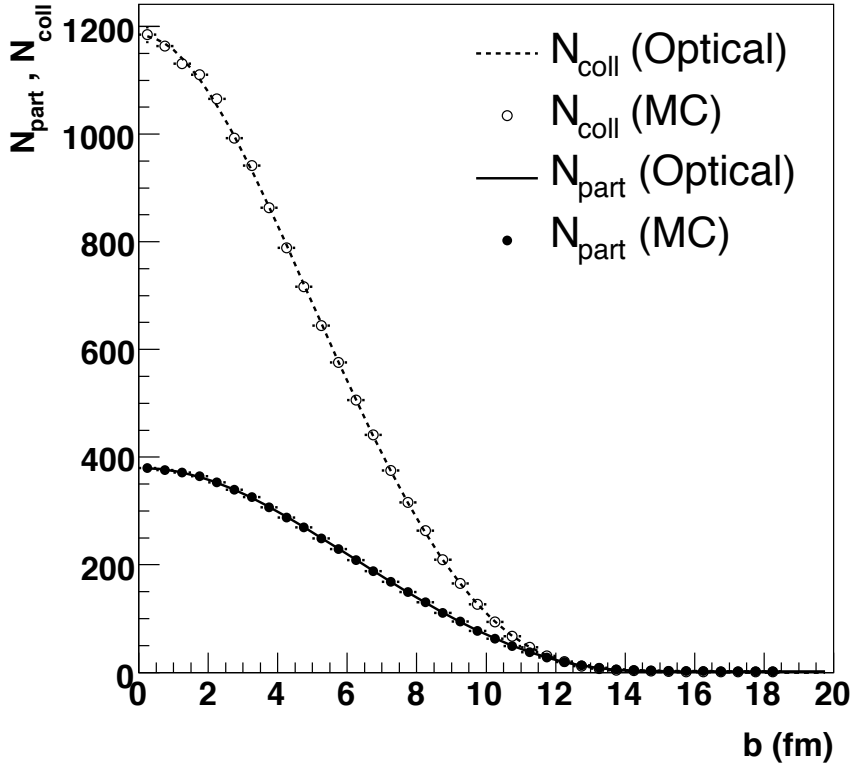
Figure 2.4: Glauber Model Predictions - Glauber model predictions for the number of participants N_{part} and binary collisions N_{coll} in Au–Au collisions against impact parameter. The optical (smooth density) approximation and Monte Carlo methods are notably similar. Calculated with $\sigma_{NN}^{\mathrm{inel}} = 42$ mb, and thus $d_{\mathrm{inel}} = \sqrt{\sigma_{NN}^{\mathrm{inel}}/\pi} = 1.2$ fm [65].

Using such a parameterisation, the number of participant nucleons, N_{part}, or the number of binary collisions between nucleons, N_{coll}, can be calculated as a convolution of the two nuclei's thickness functions. More practically, however, it is commonly done using Monte Carlo simulations which can more realistically model the discrete distribution of nucleons within the nucleus. The nucleons are distributed stochastically within the nucleus using the above potential [4]. Collisions are usually considered to have occurred

if two nucleons pass within d_{inel} of each other. Figure 2.4 shows the predictions for the number of participants and collisions reached using both these techniques; the techniques give highly similar results for a wide range of impact parameter.

Calculating the number of nucleon-level participants and collisions in a nucleus-nucleus collision is useful, as it has direct bearing on what will be observed in the detectors. Intuitively, it is expected that a peripheral collision will not reach the energy densities required to create the QGP, while more head-on collisions might do so. More accurately, it is observed that lower energy particles are produced at a rate proportional to N_{part} [69, 70], while higher energy particles are produced at a rate proportional to N_{coll} [71, 72]. However, there is no way of directly measuring the impact parameter of two colliding nuclei, particularly not at an event-by-event level. Instead, what is commonly used is the definition of centrality. The centrality of a collision with a given impact parameter is that percentage of the total cross section which occurs with a higher impact parameter; that is:

$$c = \frac{\int_0^b \mathrm{d}\sigma/\mathrm{d}b' \, \mathrm{d}b'}{\int_0^\infty \mathrm{d}\sigma/\mathrm{d}b' \, \mathrm{d}b'} = \frac{1}{\sigma_A A} \int_0^b \frac{\mathrm{d}\sigma}{\mathrm{d}b'} \, \mathrm{d}b'. \tag{2.6}$$

This is essentially just a redistribution of the impact parameter, in a way that is less experiment specific, but has the advantage of also being more intuitive; it is easier to understand that 0-5% corresponds to the most central 5% of events for example, rather than an impact parameter of 0-3.5 fm (in Pb–Pb collisions in ALICE). The energy distribution at central rapidity and the particle multiplicity distribution should increase monotonically when heading to more central events, as both N_{part} and N_{coll} do so. Similarly, the energy of the spectator nucleons should decrease for more central events (as this will be inversely correlated with N_{part}). Thus, the centrality distribution can be mapped to any of these observables; for instance the 0-5% most central events will correlate to events with the top 5% of charged particle multiplicity at mid-rapidity.

Measurements from RHIC and the LHC are typically given in a centrality bin calculated in this manner, often with appropriate scalings to N_{part} or N_{coll}, in order to give a comparison to a series of independent nucleon-nucleon collisions. Where such scalings are

undertaken in this thesis, they will be indicated. It is important to note that, although such scalings account for the multiplicity of primary collisions in moving from a pp to a Pb–Pb system, they do not account for other nuclear effects such as rescattering. In particular, physical processes such as the Cronin effect [73] cannot be explained in terms of independent nucleon-nucleon collisions.

2.2.2   Pre-equilibrium Models

More complex models must be used to bridge the gap between the initial hard collisions, described by the Glauber model, and the thermally equilibrated system we identify as a QGP (or even a hadron gas). Such models must take account of the multiple rescattering processes which will occur, and are used to set initial conditions for models which describe the evolution of the thermal system, such as the hydrodynamic models discussed below. Typically, the models are either entirely perturbative or phenomenological, due to the difficulties in describing QCD over a wide range of Q^2 [74].

A perturbative approach often used is the Parton Cascade model [75]. In this model, the incoming nuclei are considered as a cloud of real and virtual partons, described by the measured parton distribution functions and nuclear structure functions. Interactions between the partons are described by pQCD, as they would be in a theoretical description of a pp collision, and the partons so produced are allowed to fragment. Unlike pp collisions, however, the partons are allowed to reinteract, through $2 \rightarrow 2$ scattering processes, and $2 \rightarrow 1$ fusions. The distributions of energy and entropy (identified with the number of particles) can then be used as an input to hydrodynamic models. Due to the range of applicability of pQCD, these models are typically using minijet production; allowing high p_T partons to fragment into a softer p_T distribution. This assumption may be justified, particularly at LHC energies, as the majority of the p_T of the system can be generated in this way [76]. The HIJING Monte Carlo generator is an example of a parton cascade model [77].

Phenomenological approaches are complementary to perturbative models as they in-

herently contain the non-perturbative QCD behaviour [74]. A typical example is a String Breaking model. In such models, the Glauber model is used to identify wounded nucleons, which will act as a source of colour strings connecting the two nuclei. These strings will then split into gluon-gluon or quark-antiquark pairs, in a QCD equivalent of the Schwinger mechanism [78], and the quarks and gluons so formed taken as the origin of the QGP, and allowed to interact following classical kinetic theory [79]. Such a method breaks down at high collision energies, where the high density of strings produced leads to an overlapping of strings. Several approaches can be considered to resolve this; for instance allowing strings to combine into colour ropes, leading to enhanced strangeness and baryon production from the higher string tension [80], or considering the strings to form a coherent colour field [12].

An alternative non-perturbative approach is that of the Colour Glass Condensate. This model rests on two key concepts. Firstly, that the abundance of gluons within the proton carrying a low fraction of the momenta (x) rises strongly for $x \rightarrow 0$ [81]. Secondly, that this cannot continue to infinitely small x; by the uncertainty principle, a gluon with increasingly small momentum has increasingly large size, and eventually the gluons will overlap and interact with each other, saturating the gluon abundances [82]. These gluons can be described as a classical field, and the nucleus-nucleus collision is then described by an interaction between these fields [83]. The final coloured field gives an entropy distribution which can be used as the initial conditions for hydrodynamic evolution.

2.3   Hydrodynamics

While thermal models can accurately reproduce overall hadron production, in order to understand the p_{T} distribution of hadrons, it is necessary to have a model of the systems evolution. There are, as yet, no models which can completely describe the evolution of a heavy ion collision [84]; from the initial hard collisions, through a pre-equilibrium phase with multiple rescatterings, to a thermal evolution and finally hadronisation and

freeze out. Hydrodynamical models describe the thermal evolution of the system and, while limited by the uncertainties in the pre-equilibrium freeze out phases, reproduce well several experimental observables, particularly the low p_T and azimuthal distributions of identified hadrons [85, 86].

2.3.1 Elliptic Flow

As described in Section 2.2.1, the impact parameter of a collision affects the number of nucleons participating in a given collision, usually parameterised as the centrality of the collision. In addition, the impact parameter will also change the geometry of a collision. Referring back to the Bjorken picture of nucleus-nucleus collisions [20], the cross section of the long, thin plasma will be given by the overlap of the two nucleons. As seen in Figure 2.5, in the case where the collision is not perfectly head on, the cross section of the plasma will not be perfectly symmetric; in general it will be approximately elliptical. More complicated geometries are also possible, particularly due to the stochastic nature of the nucleon distribution, as shown in the right hand plot.

Elliptic flow   Triangular flow
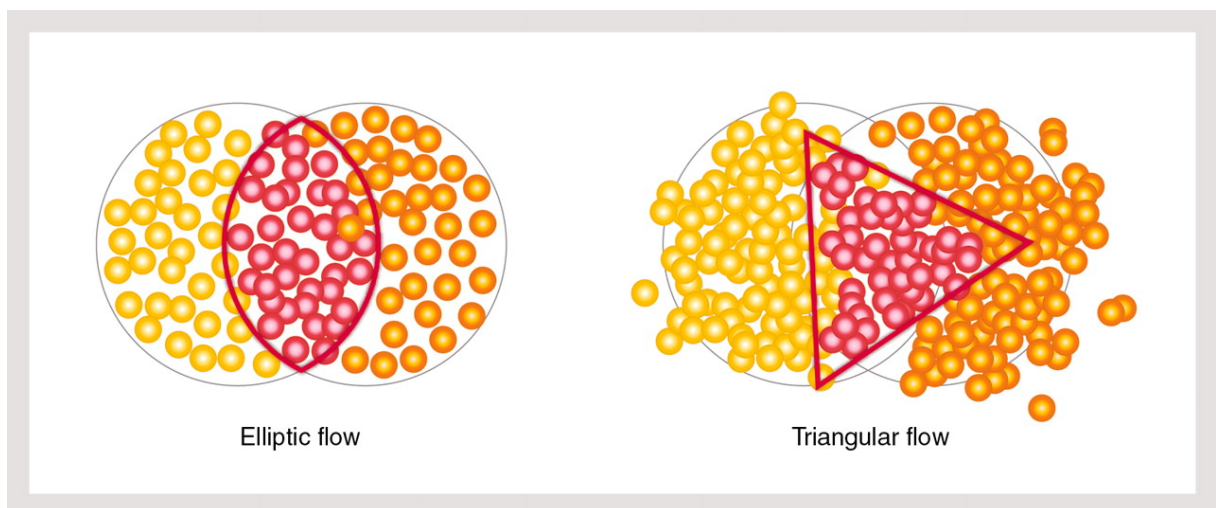
Figure 2.5: Elliptic And Triangular Flow - Schematic of the profile of colliding nuclei, indicating the prevalent flow distribution [87].

For such cases, the anisotropy of the parton distribution leads to an anisotropy of the final momentum distribution. For a parton created in an elliptical system, more collisions will occur if it travels along the long axis than along the short [84]. For a thermalised

system, such phenomena can be theoretically modelled using hydrodynamics, which approximates the system as continuous, and described by currents of energy, momentum and charge [88]. In this picture, elliptical flow emerges as a consequence of the pressure gradients: the pressure at the centre and the edge of the system is identical for each orientation, and thus the shorter path length has a higher pressure gradient, leading to a higher momentum flow in that direction; visible as an azimuthal (ϕ) anisotropy in the distribution of measured hadrons in the detector. This flow will cease when the mean free path of the partons is greater than the system size, and so scattering of the partons no longer occurs.

Elliptic flow, predicted as a signature of collective flow by Ollitrault [89], has been experimentally measured at the AGS [90], SPS [91], RHIC [92] and more recently at the LHC [93]. It is a challenging measurement, as the orientation of the ellipse with respect to an experimental set up changes with each collision, and so averaged over many events there will not be any azimuthal anisotropy in the detector.

If the orientation of the collision can be estimated, for instance by identifying an approximate plane of symmetry [94], then the strength of the anisotropic flow can be quantified by calculating the Fourier coefficients of the azimuthal particle distribution [95]. The elliptic flow is then given by the second Fourier coefficient, ν_2. Historically, this technique has been refined by measuring the correlations of particles with respect to each other, rather than a plane of symmetry, [94], although this can be distorted by non-flow correlations, such as 2-particle decays. The effect of these is minimised by combining multi-particle correlations into Cumulants [96], and this is commonly done in ALICE.

Figure 2.6 shows the magnitude of ν_2 as a function of p_{T}, measured at ALICE for various particle species and compared to a viscous hydrodynamic prediction, VISH2+1, which is discussed in more detail in Section 2.6. The result is clearly not consistent with zero, as would be expected for the case of no rescatterings between particles [94]. The Monte Carlo predictions follow the behaviour of the particles well, suggesting that their assumptions of low shear viscosity and rapid thermalisation are correct [88]. Shear
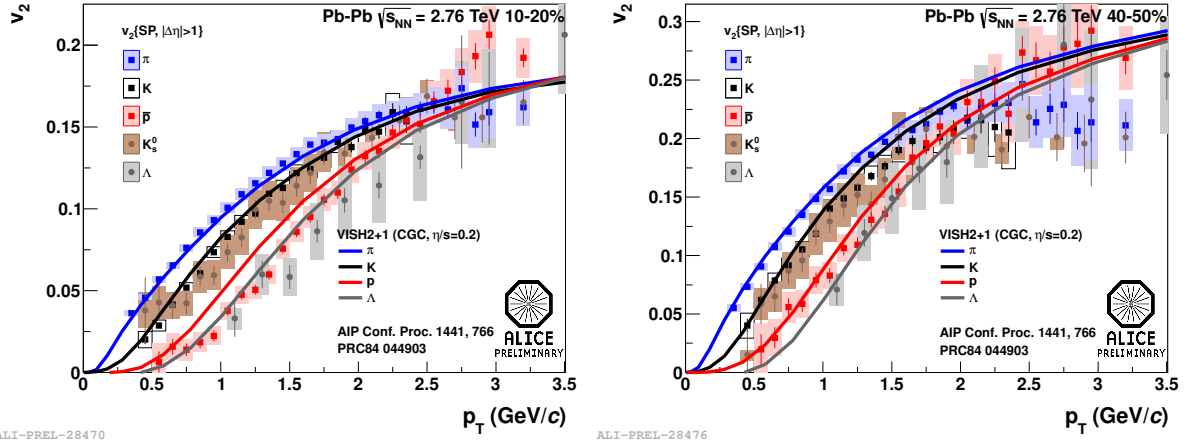
Figure 2.6: ν_2 Measured in ALICE - Elliptic flow as measured by ALICE for various particle species, along with model predictions [97].

viscosity will tend to lower the anisotropy, and extended evolution of the system before thermalisation could also reduce the initial anisotropy before it can be translated to flow. However, while these conclusions are plausible, the interplay between the two effects can reduce their significance. Dependant on the choice of initial conditions (for example, whether the Glauber or Colour-Glass-Condensate models are used) the measurement of the shear viscosity can vary by 100% [88]. For particularly anisotropic initial conditions, the pre-equilibrium phase can last as long as 2 fm/c, and still give good hydrodynamic predictions of the elliptic flow [84]. Further, the shear viscosity is not expected to remain constant over the evolution of the fireball; it should vary as a function of temperature [88], and could rise sharply at hadronisation [85].

Despite these reservations, the results certainly seem to indicate strong elliptic flow, and are reproduced well by a Monte Carlo model based on hydrodynamic behaviour with a low viscosity. There is separation of the particles by mass, indicating that the origin of this behaviour is due to a collective velocity. Overall, this measurement provides strong motivation for modelling the medium produced in heavy ion collisions as a fluid, at least for the production of low p_T hadrons, below around 3 GeV/c.

2.3.2 Radial Flow

The presence of collective flow in the system will affect the transverse momentum (p_T) distribution of particles. Local thermal production of hadrons, in common with production of low p_T hadrons in high energy pp collisions [12], is well described by

$$E\frac{\mathrm{d}^3\sigma}{\mathrm{d}^3p} \sim \exp -m_T/T, \qquad (2.7)$$

where m_T is given by $m_T = \sqrt{p_T^2 + m^2}$. The inverse slope parameter T is associated with the temperature for thermal production but such an interpretation is less clear for e^+e^- or pp collisions.

The introduction of flow changes this distribution: the particles are thermally distributed in a frame comoving with the flow. As a result, the distribution observed in the lab frame is Lorentz boosted, and the momentum distribution is blueshifted. In general, the form of the transverse momentum distribution will be complex, but in the ultrarelativistic case, where $p_T > m$, it can be described as a thermal distribution with an effective temperature given by (from [98])

$$T_{observed} = T_{freezeout}\sqrt{\frac{1 + v_T}{1 - v_T}}, \qquad (2.8)$$

where v_T is the average radial flow velocity. At lower momenta, however, the p_T-distribution is dependant on the distribution of radial flow and on the mass on the particles, as one might expect for a flow of constant velocity rather than momentum. For example, where the flow velocity profile is linear and the density distribution of the plasma is Gaussian the effective temperature will be (from [98])

$$T_{observed} = T_{freezeout} + \frac{1}{2}mv_T^2. \qquad (2.9)$$

The key observation here is that the observed temperature of the p_T distribution is greater for more massive particles. Thus, at low p_T, the heavier Λ particles will be boosted

to higher p_{T} than the lighter K_S^0, while at higher p_{T} they should give the same observed 'temperature'. A more complete description of the boosted thermal distribution, known as a blastwave distribution, is used to describe the particles' p_{T} more completely, and this is described in Section 5.6. However, it is not possible to fully describe them even with this form, as the highest p_{T} particles may escape the medium before being fully thermalised. This phenomena will be discussed further in Section 2.4.

2.4 Jet Quenching

In the preceding discussion, the concept of thermalisation was used; that multiple interactions between partons would distribute energy and momentum statistically, giving rise to collective phenomena such as pressure and temperature. However at higher momenta of hadrons, this picture is not necessarily correct. A parton with high momentum from a nucleon-nucleon collision on the periphery of the system may escape before the onset of thermalisation. Moreover, even those highly energetic partons which do traverse the thermalised medium may not become fully thermalised; although they undergo many interactions, they may keep the main part of their momentum, and so eventually escape the medium [85]. Fries et. al. show that the p_{T} distribution of thermal partons drops off much more quickly with p_{T} than the spectrum produced in pp collisions [99]. As such, the process of (incomplete) thermalisation will tend to lower the momentum of high p_{T} partons. At high p_{T}, it becomes increasingly likely that an observed hadron has escaped the medium before becoming fully thermalised, rather than being generated through thermal processes.

Thus in considering high p_{T} hadron spectra it cannot be assumed that it will be fully described by thermal processes. Instead, perturbative QCD, studied extensively for pp collisions, can be used to try and understand the differences imparted by the thermalised medium onto the hard partons.

2.4.1 Hard Processes in Vacuum

The calculation of cross sections in QCD depends on the concept of factorisation. Using pQCD, parton level cross sections such as $\sigma^{u+\bar{u}\to d+\bar{d}}$ are calculable for large momentum transfer by utilising the fact that the strong coupling constant is small at high Q^2 (Section 1.2). Such calculable scatterings are referred to as hard. However, experimentally, this is not a process which can be cleanly created; due to confinement, quarks are held within hadrons. At the LHC protons are collided, and the end results of interactions are observed which are, most often, between the sea quarks or gluons associated with the protons. This leads to an unavoidable element of incalculable non-perturbative QCD in any collision; the sea quarks are dominantly formed at very low momentum exchange. The assumption of factorisation is that the distribution of these sea partons relative to a proton will be process independent, and so can be factorised out of the cross section. For example the cross section for $p + p \to u + \bar{u} + X$ would instead become

$$\sigma^{p+p\to u+\bar{u}+X} = \sum_{i,j,k} f_{i/p}(x_1, Q^2) * f_{j/p}(x_2, Q^2) * \sigma^{i+j\to u+\bar{u}+k}, \tag{2.10}$$

where Q gives the momentum transferred in the interaction, and x is the fraction of the proton's momentum associated with a particular parton [100]. As such, $f_{i/p}$ gives the probability distribution for a parton i within a proton to have a given fraction of the protons momentum. These functions, referred to as parton distribution functions (PDFs), can be extracted from deep inelastic lepton-proton scattering experiments [101].

2.4.2 Jets

This methodology appears to work well for predictions of cross sections at the LHC, although the large energy increase over colliders measuring the PDFs, such as DESY [102], means that the measured PDFs must be extrapolated to lower x and higher Q^2. It is possible to calculate parton production cross sections in this way, however hadrons are observed in the detectors.

The process of hadron formation is typically described as fragmentation, where a colour string stretched between the two hadrons formed in the initial hard collision repeatedly breaks, forming a collection of colour-neutral hadrons. This model is implemented in various Monte Carlo Generators as the Lund String Model [103], and its success in describing pp collisions suggests that it is a suitable picture of the process.

Analogous to the preceding discussion, fragmentation functions can be introduced to describe this process. Again the factorisation assumption is used; that partons, a long way from the interaction, will fragment independently of the process which created them. This leads to an overall cross section for hadron production in a pp collider of

$$\sigma^{p+p\rightarrow h+X} = \sum_i \sigma^{p+p\rightarrow i+Y} * D_{i\rightarrow h}(z, \mu_F^2), \tag{2.11}$$

where z is the fraction of parton i's momentum eventually carried by the hadron of interest h, and μ_F^2 gives an energy scale used for renormalisation of the QCD formalism [100]. Again, these can be studied in collisions such as $e^+ + e^- \rightarrow h + X$, where the initial hard collision is well understood.

This process complicates studies of the hard partons of interest. As with the hadronisation, which conceals the distribution of partons in QGP, the fragmentation of partons to hadrons in vacuum can hide information about the behaviour of the parton within the medium. Most notably, there is not one hadron to associate with the parton.

In order to define an object which is theoretically calculable and also experimentally measurable, the concept of jets is used. Roughly speaking, a jet is defined theoretically as a hard parton and all soft radiation associated with it, and experimentally as a spatial cluster of energy. More precisely, any jet definition must be collinear (two partons close together in position and momentum should not appear different to a single parton) and infrared safe (the perturbatively incalculable process of soft gluon emission should not alter the jet). Using these definitions, it is possible to ally theoretical predictions on a parton level to experimental observations at a hadronic level. For further information on

the algorithms used to define jets, the reader is directed towards [100] and [104].

2.4.3   In-Medium Interactions

Quenching of jets produced in the initial collisions was first suggested by Bjorken to be a signature of QGP [105]. In a coloured medium, the hard coloured partons will lose energy in a manner analogous to the Bethe-Bloch formulation, whereby electrically charged particles lose energy when passing through a medium. For electrically charged particles at reasonably low energies, energy is passed to the medium through photon mediated interactions, reducing the energy of the particle but otherwise leaving it unchanged [106]. For more energetic particles, the photons produced can undergo pair production, resulting in an electromagnetic shower effect as the produced electron-positron pairs emit photons which can themselves pair produce.

Similar processes can occur in the coloured medium; elastic collisions can pass energy to the thermal partons of the medium [105], and inelastic collisions or gluon radiation can distribute that energy into new partons within the medium [107, 108]. The first impact of these processes will be that the overall energy of the parton is lowered; the typical energy of the medium partons is lower than the hard partons under consideration, and so collisions will tend to redistribute energy from the jet into the medium. The energy loss is predicted to rise with the energy of the parton [107, 108], and so jet suppression can be significant for very high p_T. Another potential effect is that the jet could broaden due to large angle gluon radiation [109]. These effects are referred to as 'Jet Quenching'; a hypothetical in-vacuum jet may have its energy lowered and its shape broadened due to its presence in the medium.

Several examples of jet quenching have been observed. Observations at RHIC [110], and more recently with ALICE [111] have used two-particle correlations to demonstrate the effects of jet quenching; there is a clear suppression of the yield of high p_T hadrons azimuthally opposite to a triggered high p_T hadron in central Pb–Pb collisions relative to peripheral Pb–Pb or pp collisions. Studies using jet finding algorithms at ATLAS [112]

and CMS [113] have also shown an asymmetry in jet energy. These experiments indicate that the jets are still largely back to back, but energy is distributed around the detector. Significant jet broadening has not been observed however [114].

2.4.4 Hadronic Suppression

As explained above, the process of fragmentation means that the observed objects most closely corresponding to initial partons are jets, rather than individual hadrons. This complicates theoretical predictions for the effect of jet quenching on individual hadron spectra, and it is in general not possible to make a model-independent prediction. However, certain general features are understood; at low p_T the hadron spectra should be described by a boosted thermal distribution, while this will under-predict the yield at higher p_T. In this region, the dominant mode of hadron production will be fragmentation of hard partons, driven by a leading parton which may have undergone energy loss in the medium. While some models predict the onset of fragmentation in the medium [115], assuming that it will not begin until the parton is in vacuum (as would be implied by a simple interpretation of the string breaking model) gives a picture similar to the pp collision case, save that every parton is moved down in p_T by some unknown amount. The p_T distribution of hard hadrons tends to fall off with a power law behaviour and so, in the region where fragmentation dominates, there will be fewer hadrons at any given p_T.

Suppression of high p_T hadrons is typically demonstrated using the nuclear modification factor, R_{AA}, defined as a ratio of hadron yields in Pb–Pb collisions to that measured in pp events, scaled by the estimated number of binary collisions from the Glauber Model. Thus, should a Pb–Pb collision simply behave as an incoherent sum of nucleon-nucleon collisions, the ratio would be 1. The ratio can be affected by cold nuclear matter effects such as Cronin multiple scattering [73] or nuclear shadowing [116] as well as the hot jet-quenching effect of interest.

Figure 2.7 shows the results for R_{AA} as measured by CMS. Firstly, the electroweak
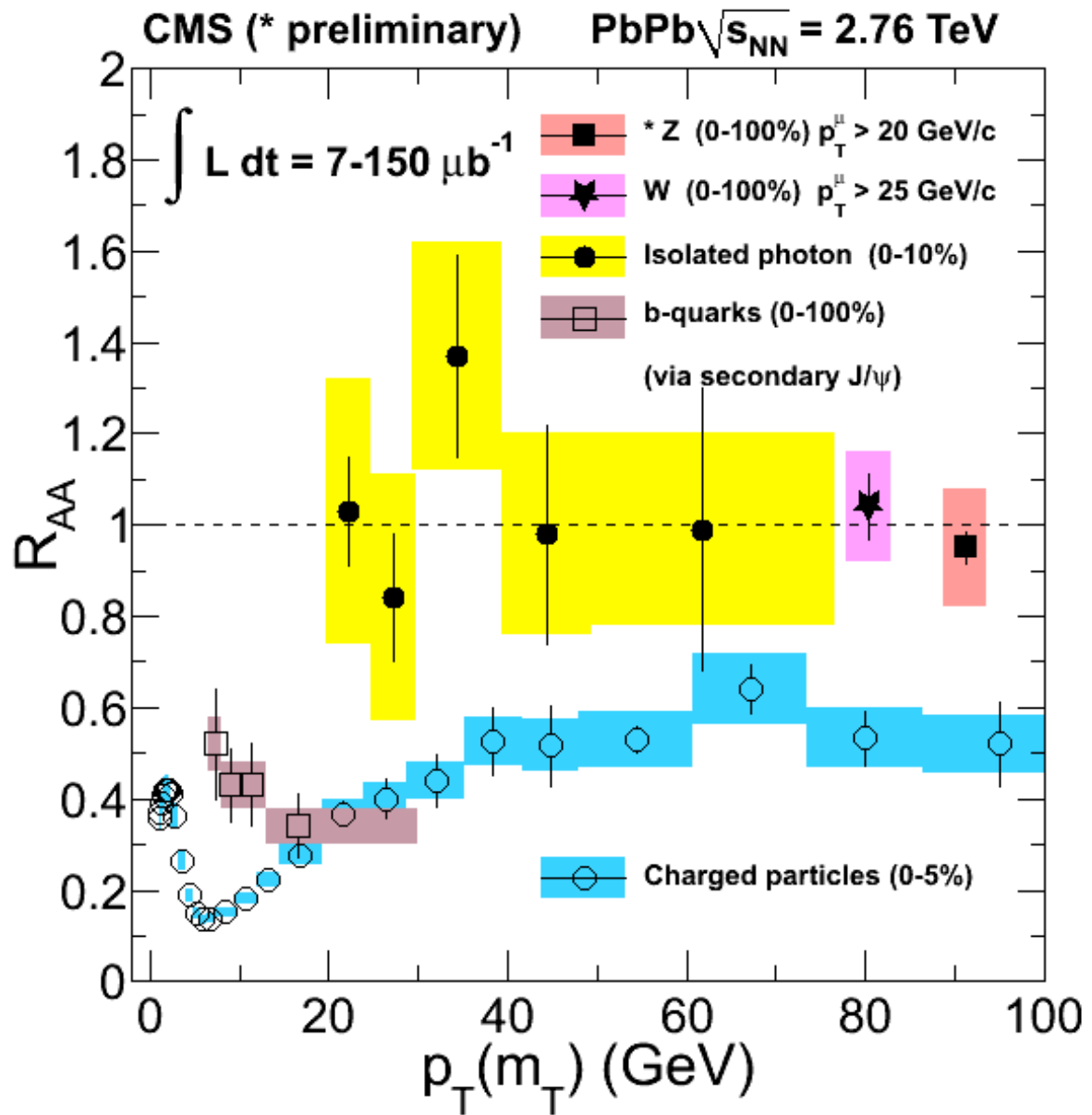
Figure 2.7: R_{AA} **as Measured in CMS** - R_{AA} of charged particles in central collisions at CMS along with electroweak probes. [31]

probes (shown in yellow, pink and red) are clearly consistent with an R_{AA} of 1. This suggests that there are no issues with the Glauber model assumptions used to construct this ratio; as the electroweak probes do not interact strongly, one expects them to behave as if produced by an incoherent set of nucleon-nucleon collisions. The charged hadrons however are distinctly different. At low p_T, the behaviour will be complicated by the switch-over from thermal behaviour to fragmentation, but at higher $p_T > \sim 5$ GeV/c there is clear evidence of suppression of the hadronic yields, which never reach a value higher than 0.5. These values can be used to constrain models of jet quenching, see for instance [117].

2.4.5 Effect on Strange Hadrons

It is possible that the suppression will be different for different hadron species; it can be seen in Figure 2.7 that hadrons containing b-quarks do not appear to follow the same general trend, although their p_T reach is insufficient to make any definitive statements. Following the argument made above, if different partons lose their energy equally within the medium, and do not start to fragment until they reach the vacuum then there is no reason to suppose a dependance on hadro-chemistry in the suppression of high p_T hadrons. However, several models do predict a hadro-chemistry dependant suppression, which can then be studied by comparing results for high p_T Λ and K^0_S to other hadrons, such as protons and pions. A selection of such models are discussed here.

It is generally assumed that the boost of a high p_T parton means that it will typically have escaped the medium before the onset of fragmentation. However, Bellwied and Markert argue that, while true hadrons might not be formed until later, the 'pre-hadron' may become colour-neutral on a shorter timescale, significantly reducing interactions with the medium [118]. As the fragmentation function to different hadrons varies, so should the production time of the colourless pre-hadrons; and so there should be a difference in suppression between protons, pions, kaons and lambda particles above $p_T \sim 6$GeV/c.

Aurenche and Zakharov, however, suggest that the production of baryons in QGP

may be enhanced, as interactions with the medium may carry away the colour imbalance [119]. Thus, rather than creating a baryon-antibaryon pair, fragmentation need only create a baryon, as the anti baryon is dispersed into the medium. This again would suggest a difference between the R_{AA} observed for baryons and mesons persisting to high p_T, although the relative contribution of the effect may be small.

Finally, Wiedemann and Sapeta consider several possible origins of jet hadrochemistry changes in [115]. Firstly, that any gluon interaction with the medium may change the invariant mass distribution of the jet, and so the hadronic distribution, and also that exchanges between the medium and the jet may lead to the jet becoming more thermal in its distribution. They predict that the proton to pion ratio may increase by 100%, even out to p_T as high as $O(100\mathrm{GeV}/c)$, which would lead to distinct differences in the R_{AA} of baryons and mesons. It is notable that this model relies only on medium-induced branching of the parton shower; the hadronisation stage of fragmentation may occur entirely outside of the medium, and hadrochemical differences would still be observed within this model.

2.5 Coalescence

The low p_T region of hadron spectra can be described well by assuming thermal production of hadrons at a fixed temperature. The highest p_T regions can be understood, at least qualitatively, as a pp-like production process with jet energies quenched by in-medium interactions. To understand the intermediate p_T region, a method for moving from one regime to the other is needed. One of the most effective models for doing so is Coalescence [99, 120, 121], which describes a microscopic process potentially underlying the thermal production at low p_T.

Coalescence offers a new mode of hadronisation. Unlike fragmentation, where a single parton splits to form a number of colour-neutral hadrons, the key concept behind coalescence is that several partons close together in phase space can combine to form a hadron.

Most models use an instantaneous projection of the parton distributions into hadrons, and so the model is only suitable for $p_T > 1$ GeV/c, containing $\sim 5\%$ of the partons. Below this level, consideration must be given to energy and entropy conservation, and naive $2 \to 1$ and $3 \to 1$ images of quark to hadron transformation are no longer appropriate. As an alternative approach to this problem, Ravagli and Rapp take a dynamical scattering approach rather than an instantaneous projection of quarks onto hadrons [122].

Experimental support for this model comes from the quark number scaling for elliptic flow shown in Figure 2.8. When plotted as a function of the transverse kinetic energy, shown on the right hand side of the left panel of Figure 2.8, baryons display a common ν_2, as do mesons. Further, if scaled to show the ν_2 and kinetic energy per valence quark, as in the right hand panel of Figure 2.8, all particles appear to follow a common trajectory [123]. In the coalescence model, this is a natural consequence of the flow of light quarks in the QGP phase [60]. The breakdown of this scaling at low p_T when ν_2 is plotted as a function of p_T, shown in the left hand plots, indicates strong flow in the hadronic phase of the system.
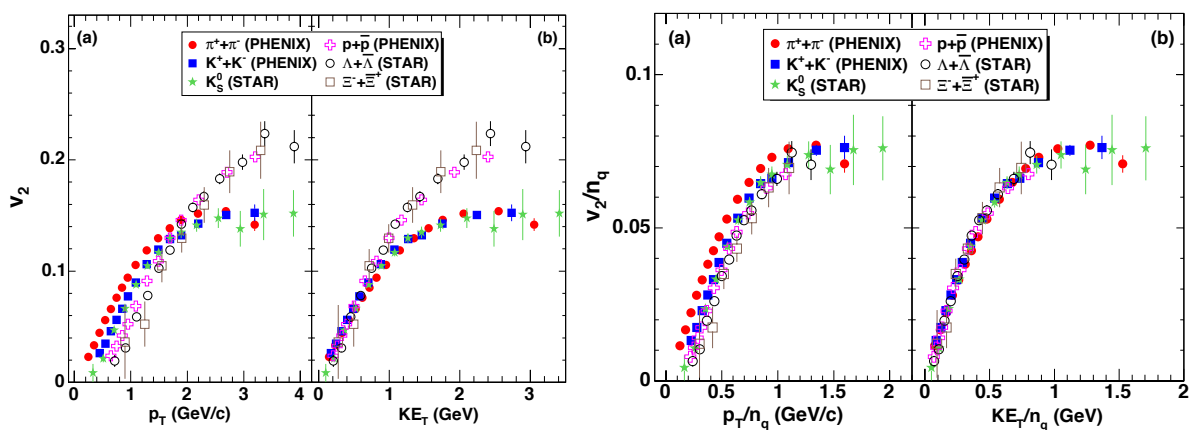
Figure 2.8: ν_2 **Measured in RHIC** - Elliptic flow as measured in $\sqrt{s_{\mathrm{NN}}} = 200$ GeV Au–Au collisions at RHIC for various particle species [123]. Within each panel, the left plot is shown as a function of p_T and the right as a function of transverse kinetic energy. The right panel has been scaled to the number of valence quarks.

At low p_T Fries et. al. predict a thermal exponential distribution of quarks ($e^{-p_T/T}$), while at high p_T pQCD gives a power law spectrum ($(p_T/\mu)^{-\alpha}$, $\alpha > 0$) [99]. The drop off in yield as a function of p_T can favour recombination; fragmentation can only produce a

hadron at lower p_T than the initial hadron, while coalescence can combine several partons to reach a higher p_T. However, one parton can create several hadrons through fragmentation, while coalescence can produce at most one hadron for every quark-antiquark pair. Fries et. al. estimate the ratio of hadrons produced by recombination, R, to those produced by fragmentation, F, for the two different distributions [99]. For the exponential distribution, the ratio is

$$\frac{R}{F} \propto e^{-\frac{p_T}{T}\left(1 - \frac{1}{\langle z \rangle}\right)}, \tag{2.12}$$

and for the power law

$$\frac{R}{F} \propto \left(\frac{p_T \langle z \rangle}{\mu}\right)^{-\alpha}, \tag{2.13}$$

where $\langle z \rangle$ is the average fraction of the initial partons momentum carried by a fragmented hadron. Thus, at high p_T, coalescence will dominate for a thermal spectrum, and fragmentation for pQCD. For the expected spectrum in heavy ion collisions, thermal at low p_T, but described by a power law spectrum at high p_T, the contribution of coalescence would be greatest at intermediate p_T, where the two spectra meet.

Coalescence of a thermal distribution of partons by instantaneous projection gives rise to a thermal distribution of hadrons [60]. This supports the concept that this process underlies the production of thermalised hadrons from a QGP, potentially even lower in p_T, where the formalism used is unreliable [94]. It also produces both baryons and mesons with the same thermal distribution, unlike fragmentation which favours mesons over baryons due to the necessity to conserve baryon number. Thus, if there is an entirely thermal distribution of partons at all p_T, the ratio of Λ to K_S^0 yields would increase with p_T. A more realistic parton spectra would lead to an enhancement in the ratio at mid p_T, as observed in measurements at RHIC (Section 1.9).

In order to accurately describe the p_T distribution of hadrons produced, coalescence between the thermal and pQCD spectra, as well as within them, must be considered. Greco et. al. approach this by having a cutoff at 2 GeV/c; below this point the partons have a thermal distribution, while above it they take a power law [120]. Such relatively low

p_T power law parton showers arising from pQCD are referred to as minijets. By allowing coalescence between partons in minijets and thermal partons in the medium, coalescence effects persist to intermediate p_T. For example, the excess of baryons over mesons would continue to around 6 GeV/c, rather than the 5 GeV/c seen at RHIC energies.

Greco also shows that there is significant interplay between flow effects and coalescence; baryons may be formed at intermediate p_T through coalescence, and pushed to yet higher p_T by the collective flow. This interplay can complicate interpretation of experimental results, however it is only through a model such as coalescence that the gradual switch-off of flow effects as we return to (quenched) vacuum-like behaviour at high p_T can be understood.

Some variations of the coalescence model make distinctive predictions for the behaviour of the Λ/K_S^0 ratio at LHC energies. For example, Hwa et. al. treat fragmentation as two separate processes; fragmentation into partons followed by coalescence into hadrons [124]. Within this model the interplay between minijets and medium naturally arises, and gives similar results to Greco. However, Hwa also argues that this model of fragmentation should give rise to the possibility of coalescence occurring between partons arising from separate minijets [121]. At RHIC energies this process was negligible, but should it occur at LHC energies it is predicted that it could lead to enhanced baryon to meson ratios extending as far as 20 GeV/c. This model would also predict differences in the hadrochemistry of jets, as baryon number and quark flavour would naturally be exchanged between jets and medium.

2.6 Theoretical Models

When interpreting experimental results in the light of these theories, it is instructive to compare to predictions from the models. Two models are referred to extensively in this work, as they highlight the behaviour of the Λ/K_S^0 ratio.

The first is a Hydrodynamical model, Vish2+1, [125, 126, 127]. This model treats the

expansion of the colliding system as a viscous fluid, with a boost-invariant description longitudinally, but a full 2-dimensional description radially, as per Bjorken Scaling. The Glauber Model is used to generate an initial energy density, and the model then evolves with a shear viscosity to entropy ratio $\eta/s = 0.2$. The final particle spectra are given by a kinetic thermal distribution when the system expands to a defined freezeout temperature of 130 MeV. These particles then no longer interact, and give the p_T spectra for comparison with data. The reduced temperature compared to expectations for the phase transition simulates the presence of hydrodynamical flow in the early stages of the hadronic phase, but does not account for any differences in viscosity in this phase.

The second model is EPOS 2.17v3, [128, 129]. This model aims to reproduce particle behaviour in Pb–Pb collisions across all p_T scales, by modelling the interactions between hard jet-like constituents and softer hydro-like partons. The initial partons are created using the string-breaking approach, where flux tubes connect nearby partons, and can break to give a new quark-antiquark pair. A core-corona approach is then used to define the fluid region of the system, and slow strings, or those deep in the medium, are treated as part of the medium, and allowed to evolve hydrodynamically. The hydrodynamic evolution in this version of EPOS is non viscous, but initial fluctuations are smoothed artificially to reproduce some of the effects of shear viscosity. The freezeout temperature is set high, at 166 MeV, but hadrons are then allowed to rescatter. Strings which have higher momentum, or which break near the surface of the hydrodynamic system, are allowed to escape from the system. In the intermediate p_T region, strings which break within the medium take their quarks from the thermal distribution; simulating a coalescence like interaction between minijets and the medium.

3

ALICE Experimental Setup

In the previous chapters, the theory underlying QGP production in heavy-ion collisions has been briefly summarised, and a selection of models which will impact the p_{T} distribution of Λ and K^0_S particles have been put forward. In this chapter, the Large Hadron Collider used to accelerate and collide the lead ions and the ALICE experiment used to detect the Λ and K^0_S particles are described. Focus is placed on the sub-detectors of particular importance for this analysis, and for further information the readers attention is directed to the ALICE Physics Performance Reports [130, 131].

3.1   The Large Hadron Collider

The Large Hadron Collider (LHC) is a particle accelerator and collider based at the CERN laboratories in Switzerland [132]. 27 km in circumference, it is located approximately 100 m underground beneath both Switzerland and France, as shown in Figure 3.1. It is an evolution of earlier accelerators; making use of the pre-existing SPS to act as an injector system, and the tunnels dug for the LEP electron-positron collider.

At full energy, it should be able to collide proton beams at a centre-of-mass energy of 14 TeV, and lead ions at 5.5 TeV per nucleon. However, to date, it has only operated at up to $\sqrt{s} = 8$ TeV for pp collisions. The analysis described in this work is based largely on Pb–Pb collision data collected at a centre-of-mass energy of 2.76 TeV per nucleon. For

comparison, results obtained in pp collisions at $\sqrt{s} = 7$ TeV are also shown, as well as data collected during a short $\sqrt{s} = 2.76$ TeV pp run.
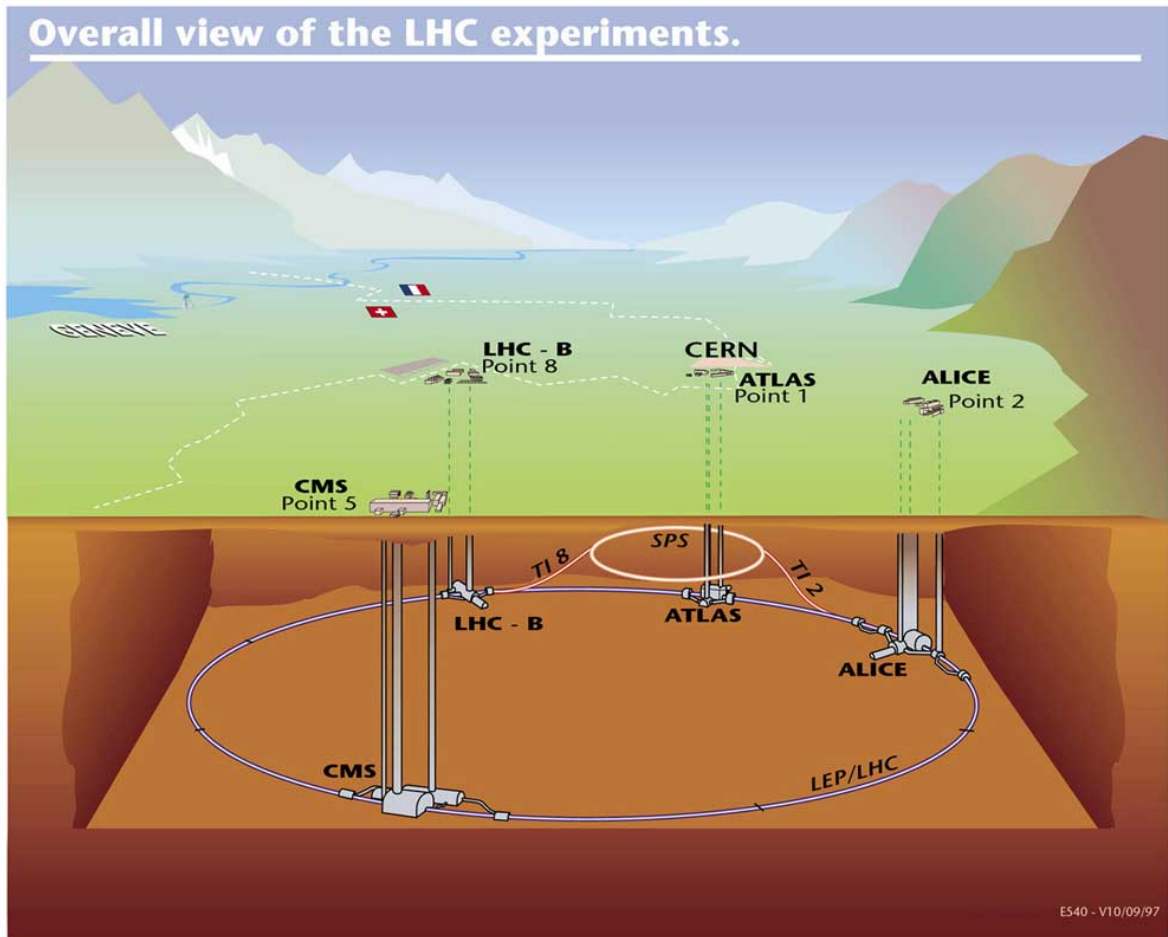
Figure 3.1: Diagram of the LHC - Diagram of the LHC, indicating the four main experiments. [133]

One of the principle design goals for the LHC was the search for the Higgs Boson [134, 135] which requires high luminosity due to the relatively small cross sections for creation. This requirement enforced the design of the machine as a proton-proton collider, rather than the proton-antiproton design of Fermilab's Tevatron [136]. This then led to further design restrictions; while protons and antiprotons can be accelerated in a single beampipe, counter-circulating protons require opposite magnetic fields and so must be separated. The beams are generally carried in separate pipes, although they do share a common superconducting magnet array. At the interaction point, the beams are in a

common vacuum, and steered together by the use of further magnets.

The proton-proton design is clearly of benefit for heavy ion collisions, allowing positively charged ions to be accelerated within the same system. There are some differences in the systems performance under heavy-ion conditions (for instance there is a higher rate of electromagnetic interactions) but overall the LHC has performed very well accelerating and colliding both protons and lead ions. This can be seen in Figure 3.2, which shows the integrated luminosity delivered for pp collisions up until the end of 2013, and the integrated luminosity for Pb–Pb collisions delivered in 2010. In both cases, the luminosity increases strongly as time goes on, and has to date reached 77% of its design luminosity, although only at 57% of its design beam energy [137].
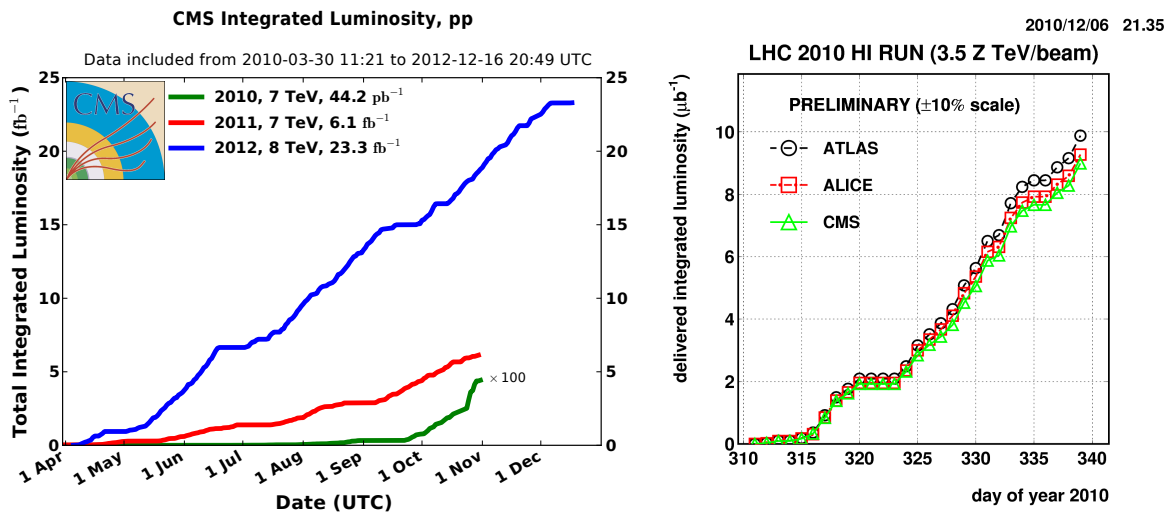
Figure 3.2: Integrated Luminosity at the LHC - Left: integrated luminosity of pp collisions as recorded by the CMS experiment at the LHC for 2010, 2011 and 2012 [138]. A considerable year-on-year increase in the integrated luminosity can be observed. Right: integrated luminosity of Pb–Pb collisions for the 2010 run studied in this work [139]. The luminosity can be seen to increase as the run continues.

The LHC has crossing points for 4 major experiments, indicated in Figure 3.1. Of these, LHCb [140] is designed primarily to study CP violating effects in B mesons, making use of the boost of particles located at large rapidities in pp collisions. Due to this highly asymmetric design, it does not participate in heavy ion collisions, which would produce unacceptably high particle fluxes in the detectors active regions. ATLAS [141] and CMS [142] are general purpose detectors; primarily designed for high-luminosity pp collisions,

but also in operation during Pb–Pb collisions. Their design as near-hermetic high energy particle detectors offer some distinct advantages in heavy ion physics. In particular, as mentioned in Section 2.4.3, they have fine-grained hadronic calorimeters which lend themselves to studies of jets, and a large geometrical acceptance allowing studies of particle correlations over a wide range.

3.2 ALICE

The fourth experiment, ALICE (A Large Ion Collider Experiment), was designed primarily for studying heavy ion collisions. Before describing it in more detail, it is useful to define the coordinate systems used within ALICE.

3.2.1 ALICE Coordinates

ALICE uses a right handed cartesian coordinate system [130], which is consistent with the coordinates used by all LHC experiments. Referring to Figure 3.3, which shows the ALICE detector and all sub-detectors, the z-direction is defined to be parallel to the beam, with positive z pointing away from the muon arm shown on the right hand side of the diagram. x is chosen to be in the horizontal plane, pointing towards the centre of the LHC, with y then fully defined as pointing vertically upwards. The ends of the detector are often labelled A and C for the positive and negative z direction, respectively.

Given the symmetry of the detector, it is often more useful to refer to polar coordinates. Under these, the definition of z remains unchanged, and r would indicate the radial distance from the beamline outwards. θ measures the angle from the z axis, while the azimuthal angle ϕ is defined such that it is zero in the positive x direction, and increases towards the positive y direction at $\phi = \pi/2$. Typically, when a quantity is referred to as 'transverse' or 'parallel', this is in reference to the beam direction, and so the transverse component of a vector is its radial component, and its parallel component the z component. For this analysis, the variations in hadron distribution with azimuthal angle ϕ will not

be discussed although, as mentioned in Section 2.3.1, they can be of importance when measuring elliptic flow.

Rather than using θ, it is conventional in particle physics to use the concept of pseudorapidity. This is defined by

$$\eta = -\ln[\tan\left(\frac{\theta}{2}\right)], \tag{3.1}$$

which is chosen because it approaches the rapidity of the particle (introduced in Section 1.5) from above as the particle approaches ultrarelativistic speeds. In order to study particle production at central rapidity, taking advantage of the central energy plateau, it is useful to have a detector centred around $\eta = 0$.

3.2.2 Design Considerations

As a specialised heavy ion experiment, ALICE has some particular design considerations. It needs to be able to cope with the extreme conditions associated with Pb–Pb collisions at LHC energies; particularly the density of charged particles, which were predicted to potentially reach as high as $dN_{ch}/d\eta \sim 8000$ [131]. When measured, this density was somewhat lower, falling at 1601 ± 50, which is around 400 times as high as that measured in pp collisions [144]. To measure in detail the hadronic spectra, and also photons and leptonic signatures of QGP, it is essential that the detector has excellent spatial resolution and particle identification abilities. In order to cover the central rapidity plateau, the main part of the detector fully covers a region from $-0.9 < \eta < 0.9$ and is mainly azimuthally symmetric although, due to space constraints, certain detectors do not cover the full azimuth. As the thermal distribution of partons produces hadrons at relatively low momenta, while jet quenching is observed in hadrons at much higher momenta, it is necessary that the experiment have good momentum resolution over a wide range of momenta.

Figure 3.3 shows all the subdetectors making up the ALICE experiment. Of these, the TPC, ITS and VZERO detectors are discussed in greater detail below, as they are
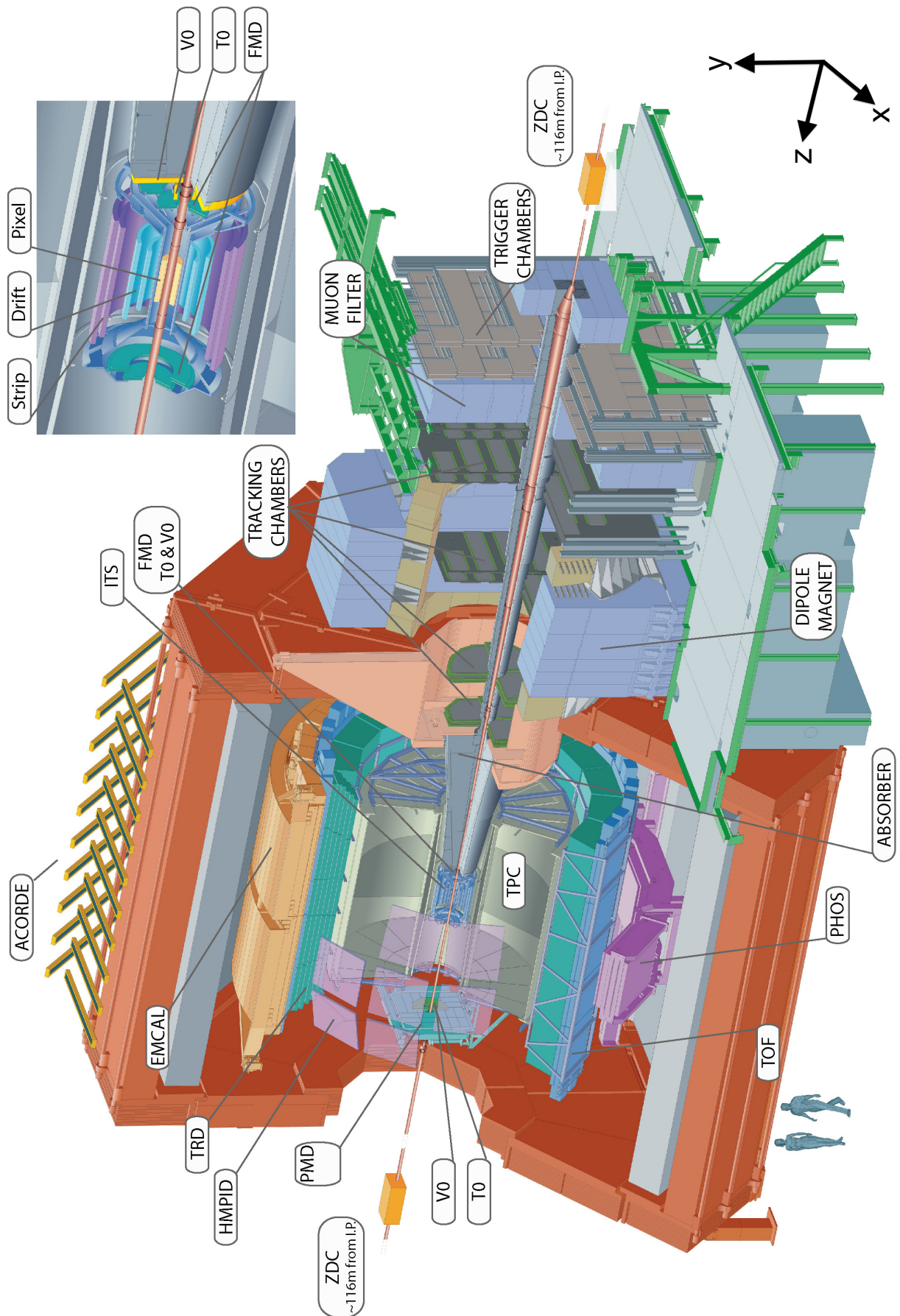
Figure 3.3: 3D ALICE Schematic - ALICE with all detectors labelled, and ITS shown in detail in the inlay [143].

60

of importance in this analysis, and mention the other subdetectors merely in passing. The majority of these are located in the central barrel, within the large L3 magnet which allows measurement of the momentum by the tracking detectors through the curvature of the charged particles' motion. These are tracked by the TPC and the ITS, which offers excellent vertexing to aid particle identification of weakly decaying particles. Further particle identification is offered by energy loss measurements in the TPC, and time-of-flight measurements recorded in the TOF. Electrons and photons can be further identified and categorised by measurements taken in the Electromagnetic Calorimeter (EMCAL), the Photon Spectrometer (PHOS) and the Transition Radiation Detector (TRD). Tau leptons are largely detected by the distinctive 'kink' topology left in the tracking detectors, while muons are detected in the muon arm located at large negative pseudorapidity $(-4.0 < \eta < -2.4)$. The muon arm is not located within the central barrel, partly for space reasons, but also because the boost implied on decaying particles allows identification of quarkonia to low p_{T}. Multiplicity counters, the FMD, T0 and VZERO aid studies of the overall event characterisation, as well as triggering to identify events of interest. Finally, the Zero Degree Calorimeters (ZDC), located at $z = \pm 116$ m assist with determination of the centrality of an event by recording the energy of spectator nucleons.

3.3 Time Projection Chamber

The ALICE Time Projection Chamber (TPC) is the largest detector of its type ever built, with a volume just under 90 m^3 [145]. It is cylindrical in design; covering $-2.5 < z < 2.5$ m, $0.85 < r < 2.5$ m. This allows it to completely reconstruct tracks with $|\eta| < 0.9$, and to reconstruct tracks with $|\eta| < 1.5$ at the cost of reduced track length and momentum resolution. It consists of 2 separate detection volumes, separated by a central high voltage transverse electrode. These detection volumes are filled with 90 m^3 of Ne, CO_2 & N_2 (in 90:10:5 proportions respectively) [146], which is ionised by incoming charged particles and allows them to drift to the endplates under the 400 V cm^{-1} electric field applied uniformly

in the z direction. The endplates consist of multi-wire proportional chambers (a grid of charged wires which cause the electrons to avalanche, and can then resolve the charge as an electronic signal) with cathode pad readouts, where the pads are roughly 5 x 10 mm, dependant on radial position. Overall, this gives a readout area of 32.5 m^2 split into 560,000 pads.

As charged particles pass through the gas, it will ionise along the path of the particles. The electrons released in this process will drift, under the presence of the electric field, to the read-out device at the end of the detector. As the magnetic field used for momentum resolution is also along the z direction, the particles will travel in a slight helix around the field lines, strongly reducing the transverse drift due to diffusion [106]. The position of the electron on the read-out detector immediately gives 2D information about the location of the initial ionisation, and the 3rd dimension can be extrapolated by measuring the time taken for the drifting electron to reach the read-outs. This requires information about the timing of the initial collision, which is known from several of the other subdetectors at ALICE. The granularity of the system is limited by the size of the pads, giving spatial bins, and the frequency of the signal sampling, giving time bins recording the z position of the particle. The TPC analogue to digital converter can sample at a rate of 5 or 10 MHz [145]. Ultimately, however, the spread of the charge due to diffusion limits the maximum useful granularity of the system to 150 ns in time and 1 mm in space.

Tracks are reconstructed from the TPC readout by first of all identifying clusters; roughly gaussian distributions of charge distributed over a few neighbouring space and time bins. A 'Kalman Filter' approach is then used to combine these clusters into tracks; starting from the outer pad row, the clusters are sequentially added to tracks by searching plausible clusters for a signal. The region of 'plausible' clusters is recalculated with each new cluster, adjusting for approximate p_T, scattering and potential energy loss within the TPC.

Having identified tracks, the p_T of a particle is given by the curvature of the track in the 0.5 T magnetic field. Using the TPC alone, ALICE reaches a momentum resolution of

0.7% for momenta around 1 GeV/c, and of 6.5% for momenta around 10 GeV/c. This can be further improved by incorporating information from the silicon inner tracking system, as discussed in the next section.
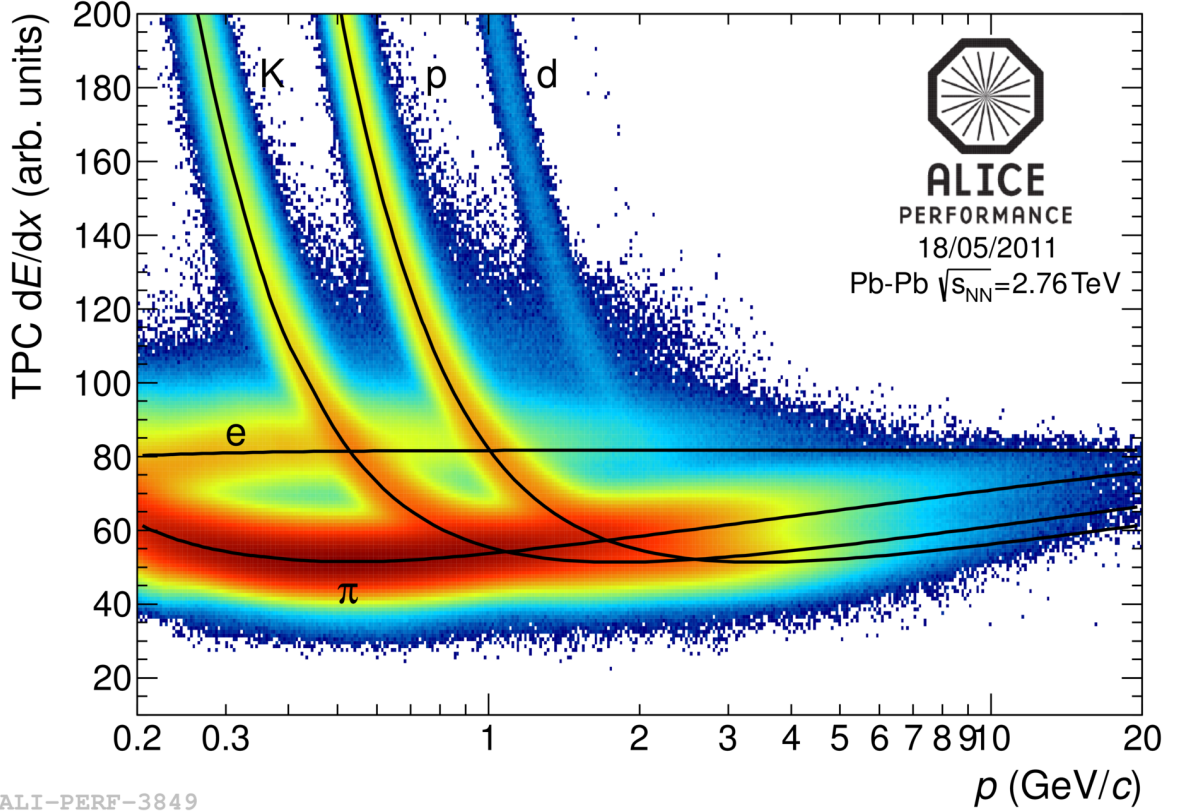
Figure 3.4: Energy Loss in the TPC - Energy Loss vs Momentum as measured in the ALICE TPC in Pb–Pb collisions at $\sqrt{s_{NN}} = 2.76$ TeV [147].

As well as this momentum and position information, the rate of energy loss of a charged particle along the track can give further information about the identity of the particle. The Bethe-Bloch formula [148, 149] is typically used to characterise the rate of energy loss for a charged particle traversing a medium. Using the form given in [106], the rate of energy loss per distance travelled can be written as

$$-\frac{dE}{dx} = \left(\frac{4\pi r_e^2 m_e c^2 N_0 Z z^2}{A\beta^2}\right)\left(\ln\left(\frac{2m_e c^2 \beta^2}{(1-\beta^2)I}\right) - \beta^2\right), \tag{3.2}$$

where β is the speed of the particle as a fraction of the speed of light, c. The material traversed is defined by its atomic number, Z, mass number, A, and its effective ionisation

potential, I, while z gives the charge of the particle in eV. The electron mass, m_e, classical electron radius, $r_e = 2.8$ fm, and Avogadro's Number are constants. As this formula is dependant on velocity rather than momentum, plotting it against momentum can identify the particle by its charge to mass ratio. Unfortunately, this will only work well when the particles momentum is comparable to its mass, although at higher momenta the logarithmic rise can also reveal further information. Figure 3.4 shows the rate of energy loss as measured in the TPC in Pb–Pb collisions plotted against the momentum of the track, and the separation between particle species can be clearly resolved below $\sim$1 GeV/c. ALICE has a resolution of around 6.5% on the energy loss measurements.

3.4   ITS

The Inner Tracking System (ITS) serves to identify the primary vertex of a collision, as well as improving the tracking performance of the TPC and triggering events. It is a series of silicon semiconductor detector layers. These detectors typically consist of a p-n junction with a reverse bias potential applied to create a substantial depletion zone lacking in charge carriers. As a charged particle passes through this region, it will ionise and excite the atoms, creating conduction electrons and holes which can carry the current, and so showing up as an electrical signal. In principle, very small silicon pixels, offering superb position resolution, could be mass produced and so could be used for all position and momentum tracking in ALICE. However, they have a large material budget; the 6 layers of silicon used in ALICE, along with their supporting structures and coolant systems, contribute a material budget of around 7% of a radiation length, compared with 3.5% for the much larger TPC. In addition, silicon detectors are expensive, and so impractical to use at large radii in a cylindrical detector.

In ALICE, 6 cylindrical layers of silicon detector are used, close to the interaction point. These offer full tracking capability for particles with $|\eta| < 0.9$ for collisions falling within 10.6 cm of the nominal detector centre, while the innermost layer covers $|\eta| < 2.0$

to aid overall multiplicity measurements. The main design criteria for the ITS relevant for this analysis are the identification of primary and secondary vertices to within 100 μm and the improvement of TPC momentum measurements.

The innermost 2 layers are situated at $r = 4$ and 7 cm. At this range, the overall particle multiplicity is particularly high (up to 80 particles per cm^2); thus silicon pixel detectors (SPD) are used. The pixels measure 50 x 425 μm, offering excellent spatial resolution to distinguish between neighbouring tracks. Following this, the next two layers are Silicon Drift Detectors (SDD), located at $r = 15$ and 24 cm. At these distances the particle multiplicity has dropped to $\sim$7 particles per cm^2, and so the larger drift detectors with active area 70 x 75 mm are sufficient. These offer particle resolution of 35 μm in the drift ($r\phi$) direction, and 25 μm longitudinally. The outermost 2 layers, at $r = 39$ and 44 cm, are Silicon Strip Detectors (SSD) with a small stereo angle of 35 mrad. This gives them excellent $r\phi$ resolution of around 20 μm, for precision matching of tracks between the ITS and TPC, but a lower z resolution of 820 μm.

Overall, the ITS can reconstruct primary vertices with a resolution of less than 10 μm in the z direction, and around 35 μm in the x-y plane [131]. This excellent resolution works best in the case of Pb–Pb events, where there are potentially thousands of charged primary tracks. In the case of pp events, the resolution can rapidly drop off due to the lower multiplicity, reaching as low as 100 (150) μm for resolution in the z (x-y) direction when there are only 3 tracks in the event. For Λ and K$_S^0$, with an expected lifetime (multiplied by the speed of light) of 7.89 cm and 2.68 cm respectively, these resolutions allow clear separation of the primary and secondary vertices for transverse momentum as low as 50 MeV/c. The momentum resolution of the TPC and ITS together is much improved from the stand-alone TPC resolution at high p_T, only dropping to 3.5% for transverse momenta greater than 100 GeV/c.

3.5 VZERO

The VZERO is a pair of scintillator detectors, situated asymmetrically such that VZERO-A covers $2.8 < \eta < 5.1$ and VZERO-C covers $-3.7 < \eta < -1.7$. When a charged particle traverses the scintillator material, the minimum ionising energy loss of the particle excites atoms of the scintillator, which later release the energy through scintillation photons. These photons are shifted down in frequency by Wavelength Shifting Fibres, to optimise the efficiency of the receiver, then carried through fibre-optic cables to photo-multiplier tubes which can record the intensity of the photons.

The VZERO detectors have relatively crude spatial resolution, only being split into 32 individual counters, but timing resolution of better than 1 ns [4]. This allows the use of the VZERO for fast rejection of beam-gas interactions, as they will not have the characteristic timing difference of interactions occurring at the nominal centre of the detector. Their large pseudorapidity coverage, coupled with a common response to any charged particle, makes them highly suitable for use as a minimum-bias trigger, particularly when combined with the SPD.

The VZERO is designed to give the same response to any charged particle, and so its response is strongly correlated with the multiplicity of an event. As described in Section 2.2.1, the multiplicity of an event would be expected to correlate to the number of nucleons participating in an event, and so events with the highest multiplicity would be the most central collisions. The VZERO response amplitude is fitted with a Monte-Carlo simulation of the Glauber Model, and used to assign every Pb–Pb event to a centrality bin, as shown in Figure 3.5. The Glauber Model can then be used to estimate the typical number of participant nucleons and binary collisions in any given centrality bin. It is worth noting that it is impossible for any particular event to say what the precise number of participants is, as statistical effects will smear the distributions. However, when using wide centrality bins, typically of greater than 5 percentage points in width, the average numbers are well understood [4], and are cross checked using the energy of spectator nucleons deposited in the Zero Degree Calorimeters.
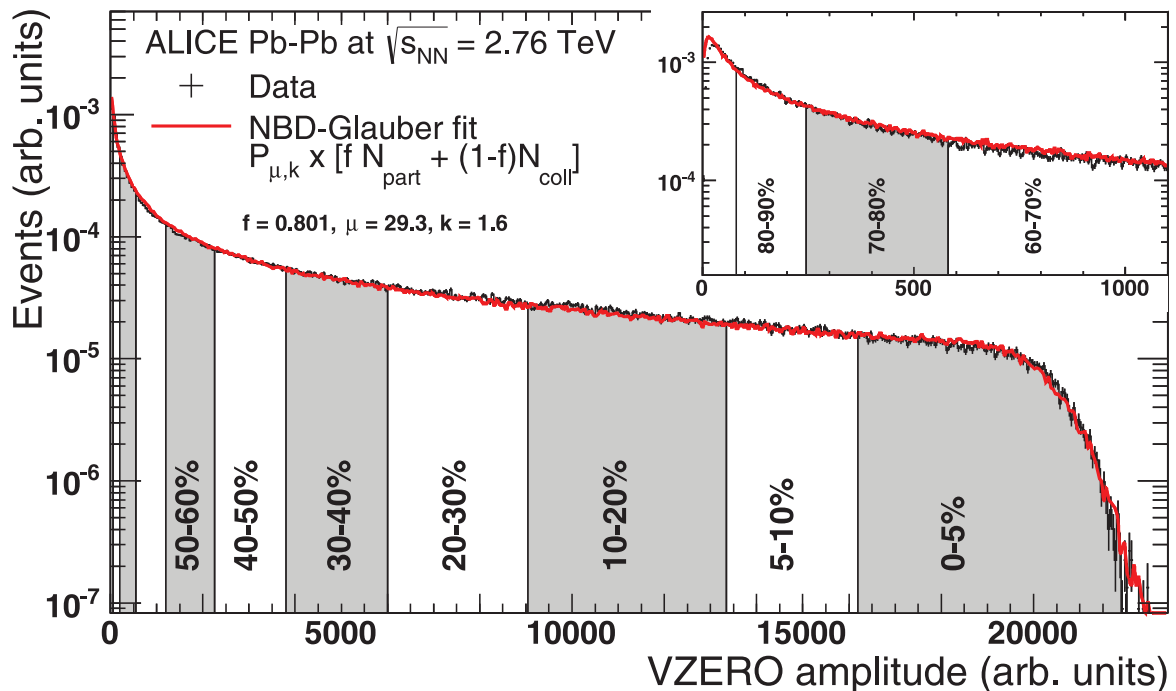
Figure 3.5: Centrality Bins in ALICE - Charged particle multiplicity as measured with the VZERO scintillators in ALICE, compared with a Glauber Model fit [4].

3.6 Run and Event Selection

This analysis uses data gathered during the November 2010 Pb–Pb run at a nucleon-nucleon centre of mass energy $\sqrt{s_{NN}} = 2.76$ TeV, as well as pp data collected during July 2010 at $\sqrt{s} = 7$ TeV and March 2011 at $\sqrt{s} = 2.76$ TeV. A minimum bias trigger was used to select the events, requiring a hit in each of the VZERO detectors and the SPD for Pb–Pb collisions, and a hit in any of the three for pp collisions where the charged particle multiplicity is notably less. This gives a near-perfect trigger efficiency for Pb–Pb events, and around 85% efficiency for pp collisions [150]. Only runs where the detector was considered to be in 'good' condition were used; in particular runs where one or more sub-detectors were not active were removed. This was of particular relevance for the $\sqrt{s}$ = 2.76 TeV pp runs, where including runs without the SDD would have greatly increased the statistics. Given additional time, it would be of interest to include these runs, which should allow the extension in p_T of the results.

In order to optimise the reconstruction capabilities of the detector, the primary vertex

Data Type	Run Period	N_{ev} Initial	N_{ev} $|z| < 10$ cm	N_{ev} No Pileup
Pb–Pb, $\sqrt{s_{NN}} = 2.76$ TeV	LHC10h	2.00×10^7	1.73×10^7	1.73×10^7
pp, $\sqrt{s} = 7$ TeV	LHC10d	1.35×10^8	1.08×10^8	1.07×10^8
pp, $\sqrt{s} = 2.76$ TeV	LHC11a	2.96×10^6	2.39×10^6	2.38×10^6

Table 3.1: Number of data events collected by detector.

of the collision is required to be within 10 cm along the beamline of the optimal centre of the experiment. Further, for pp events, it is necessary to remove pileup events; events where more than one collision happens within the same beam crossing. The SPD is used to resolve vertices, and events with two well separated vertices, each with at least 3 tracks, are rejected. The number of events remaining after each of these stages are shown in Table 3.1. Pb–Pb events were categorised by their centrality using the VZERO signal, as shown in Figure 3.5.

4

Analysis

In order to compare the p_T distributions of Λ and K_S^0 across different colliding systems, an analysis chain was developed to extract a sample of the particles from the recorded data events and use Monte Carlo simulations to estimate the true yield of primary K_S^0 and Λ. This is done by identifying the particles through their characteristic decays, which show up as two oppositely charged tracks in the detector. After the application of appropriate cuts to improve the purity of the sample, the invariant mass of the remaining candidates is calculated, and the number of Λ and K_S^0 extracted by integrating over the invariant mass peak. Monte Carlo simulations using HIJING, PYTHIA and GEANT3 were used to calculate the efficiency of reconstructing the particles in this fashion within ALICE, and also used to estimate the contamination of the sample with secondary particles, particularly Λ produced through the weak decay of multi-strange particles.

In this chapter, the analysis chain is discussed in greater detail, and also the techniques used to estimate the systematic errors on the particle spectra.

4.1   V0 Selection

Λ and K_S^0 each decay dominantly to a pair of oppositely charged particles; $p\pi^-$ and $\pi^+\pi^-$ with branching ratios of 63.9% and 69.2% respectively [23]. These are referred to as 'V0s' due to their distinctive decay topology; as the initial particle is neutral the decay

shows up in most tracking detectors as a V-shaped vertex separated from the primary vertex. An example of this is shown in Figure 4.1.
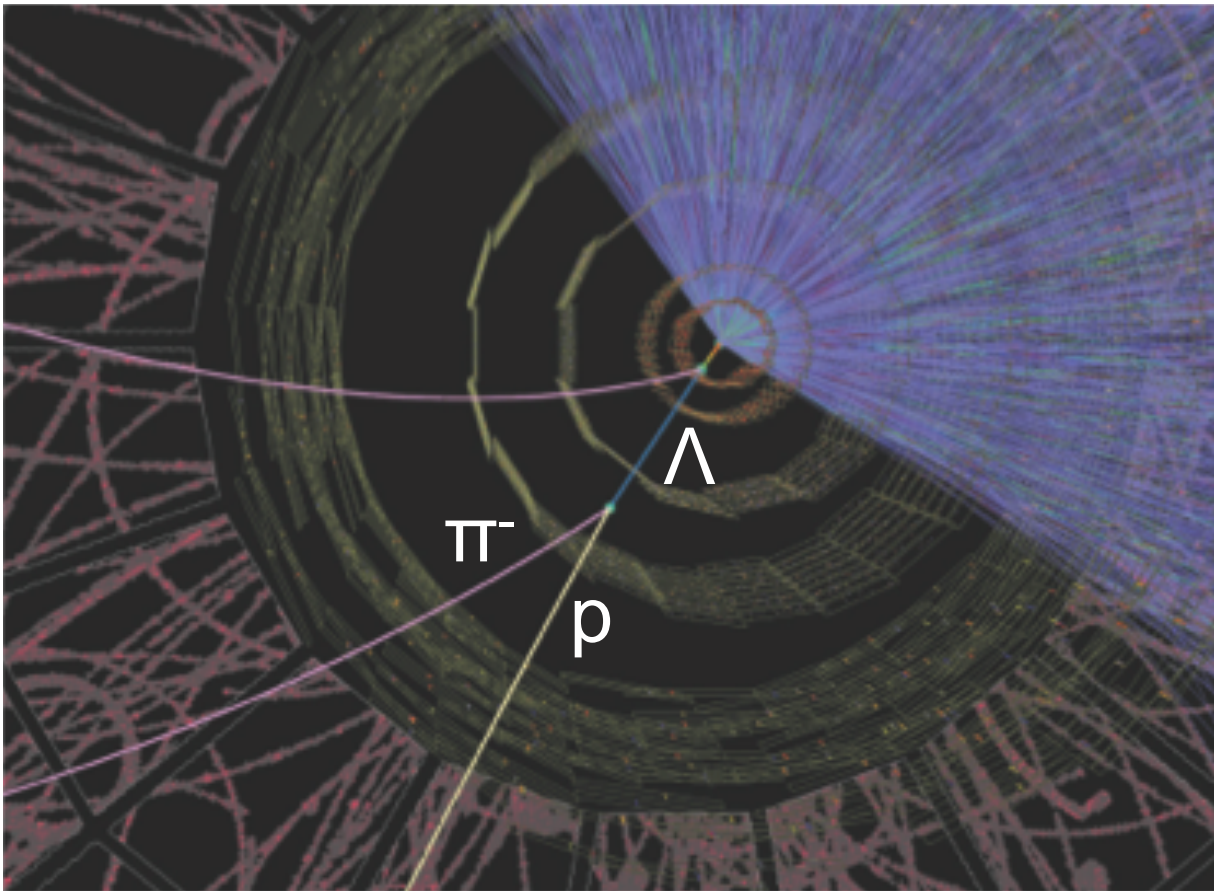
Figure 4.1: Simulated Λ decay in ALICE - Example of a Λ decay from Pb–Pb 5.5 TeV Hijing MC Event. For clarity, not all tracks are shown. [131]

The ALICE V0 finder, described in [131], was first used to identify potential V0s. All possible pairings of oppositely charged tracks with an impact parameter relative to the primary vertex greater than 0.5 mm are initially considered as V0 candidates. They are further required to have a distance of closest approach (DCA) between the two tracks of less than 1.5 times the estimated uncertainty in the tracks position at that point. The V0's momentum is defined as the sum of the momenta of the two tracks (hereafter referred to as daughter tracks), and its position is taken as a point on the DCA line connecting the two daughter tracks (see Figure 4.2), with its position along that line determined by the relative uncertainties of the two reconstructed tracks.

Having identified potential V0s, the simplest way to check for Λ's and K_S^0's among them

is to assume the nature of the daughters, and calculate the invariant mass. This reveals a peak at the mass of the particles which can be used to estimate the relative levels of signal and background. A crude sideband subtraction process was used to estimate the approximate signal/background ratio and significance of the signal, and an iterative approach taken to select kinematic cuts which would optimise these variables. The cuts considered are discussed below, with several shown graphically in Figure 4.2. For Pb–Pb collisions, there was found to be little difference between the optimal cuts for different centrality intervals, and so the same cuts were used throughout. For pp collisions however, the emphasis was on preserving signal rather than reducing background levels, and so a slightly different set of cuts are used.

4.2 Kinematic Cuts

4.2.1 Pseudorapidity

As mentioned in Section 3.2.2, the ALICE detector is optimised for measuring charged particles in the central pseudorapidity region. The central detectors used in this analysis cover a region $|\eta| < 0.9$. For the study of V0s presented here, a cut on η was applied to both of the daughter tracks, and tightened slightly to $|\eta| < 0.8$, to avoid edge effects in the detector.

4.2.2 Rapidity

Pseudorapidity is an approximation to rapidity; as the momentum of the particle increases relative to its mass, pseudorapidity approaches rapidity from above. As mentioned in Section 1.5, the average particle multiplicity per unit rapidity is roughly constant in the central rapidity region, and so particle spectra are typically measured in a small rapidity region and then normalised to unit rapidity. However, a cut on pseudorapidity implies a momentum dependant rapidity cut, changing the normalisation in different p_{T} bins. As such, it is necessary to have a cut on rapidity tighter than the effective cut on

pseudorapidity of the V0s implied by the cuts on the daughter tracks. A cut of $|y| < 0.5$ was found to satisfy this.

4.2.3 Cosine of Pointing Angle

The pointing angle (PA) is defined as the angle between the reconstructed position and momentum vectors of a V0, as indicated in Figure 4.2. Experimentally, it is the cosine of the angle which is reconstructed, through the inner product of the vectors. A value of $\cos(PA) = 1$ would indicate that the V0 points directly back to the primary vertex, while a lower value would indicate that the V0 is possibly a secondary particle or combinatorial background. This was found to be the most powerful differential between signal and background, and so a relatively tight cut of $\cos(PA) > 0.998$ was taken for Pb–Pb collisions. Figure 4.3 clearly shows the peak in Λ candidate distribution at high $\cos(PA)$, indicating that tighter cuts would lead to an improved signal to background ratio. However, earlier studies [151] had indicated that tightening the cut beyond this point could lead to discrepancies between data and the Monte Carlo simulations used to correct the data (Section 4.4), and so the cut was fixed at $\cos(PA) > 0.998$.

For pp collisions, the same cut was used in the region $p_T < 4$ GeV/c, where the combinatorial background is relatively high. At higher p_T however, the final errors were limited more by the signal than the background, and so a looser cut of $\cos(PA) > 0.9$ is used.

4.2.4 DCA to Primary Vertex

The distance of closest approach between each of the daughter tracks and the primary vertex was tightened beyond that used in the ALICE V0 finder. Monte Carlo studies suggest that the majority of the background is combinatorial; random pairings of primary pions and protons which happen to pass close to each other, or cross over. As such, excluding daughter tracks which could have come from the primary vertex was expected to strongly reduce the background. This proved to be the case, and so the cut was
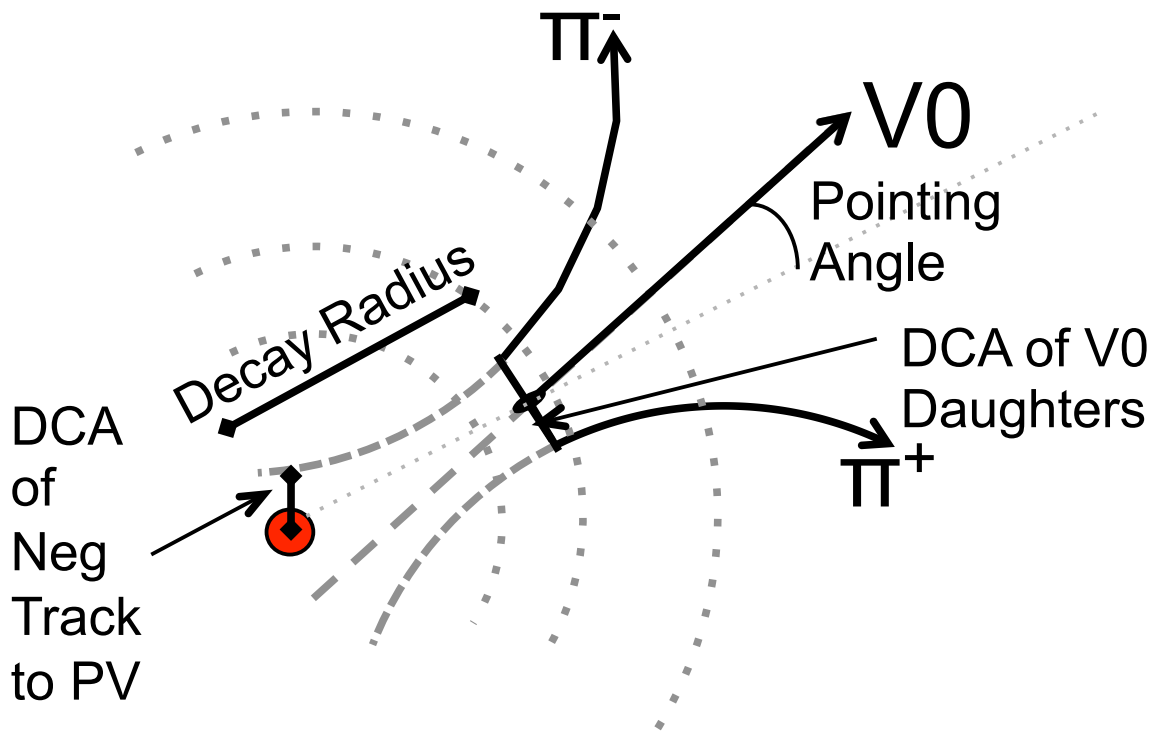
Figure 4.2: Kinematic Cuts - Schematic indicating some kinematic cut variables.
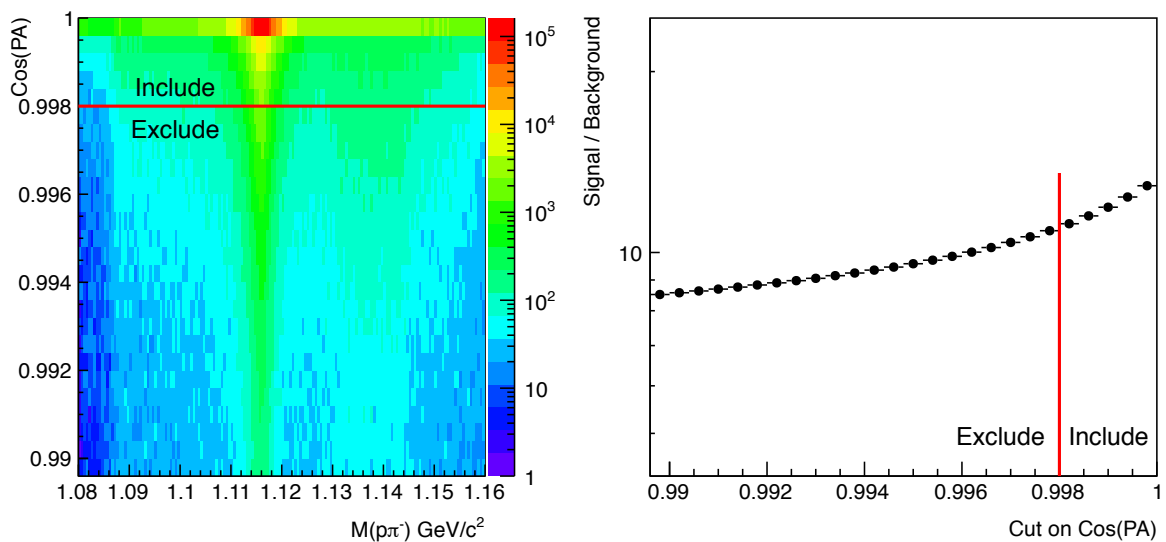
Figure 4.3: Distribution of Λ with Cosine of Pointing Angle in 7 TeV pp - Left: invariant mass of Λ candidates against cosine of pointing angle. Right: estimated signal to background ratio of Λ candidates as a function of the cosine of pointing angle cut chosen.

tightened to $DCA_{PV} > 0.1$ cm for both Pb–Pb and pp collisions. Although tightening the cut further would have improved the signal to background ratio further, the loss of signal lead to increased statistical errors, and so the choice was made to optimise the significance of the signal, seen in Figure 4.4, rather than the signal to background ratio.
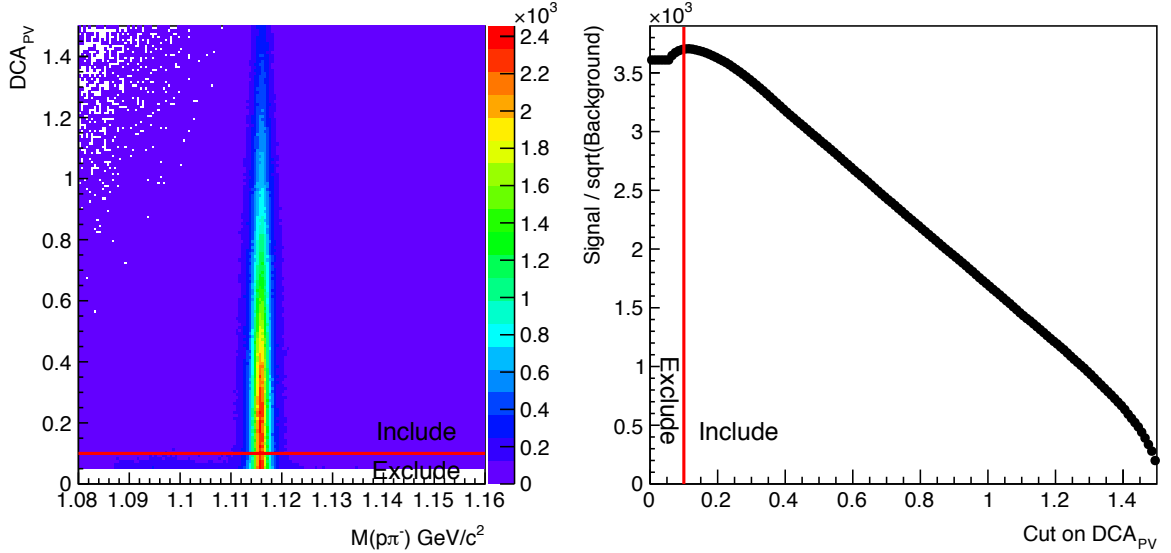
Figure 4.4: Distribution of Λ with DCA to Primary Vertex in 7 TeV pp - Left: invariant mass of Λ candidates against DCA of daughter tracks to primary vertex. Right: estimated significance of Λ candidates above background as a function of the DCA to primary vertex cut chosen.

4.2.5   DCA between Daughter Tracks

The distance of closest approach between the daughter tracks can also be used to preferentially select real V0s. As the detector has a finite track resolution, it is impossible to say definitively that the two tracks originated from a common point, but the smaller the measured distance of closest approach between the two tracks, the greater the likelihood that they did in fact originate from a common decay vertex. For Pb–Pb collisions, restricting this variable to $DCA_{daughters} < 1\sigma$ (where σ is the position resolution of the tracks at the point of closest approach) was effective at reducing the combinatorial background, while for pp collisions this was not further restricted, in order to maximise the signal statistics. As Figure 4.5 shows, the background is spread out over a wide range in this variable, and

so a fairly tight cut would be required to make meaningful gains in the resolution between peak and background. Using the looser cuts described here gave some gains in statistical uncertainty without any major cost in systematic uncertainty.
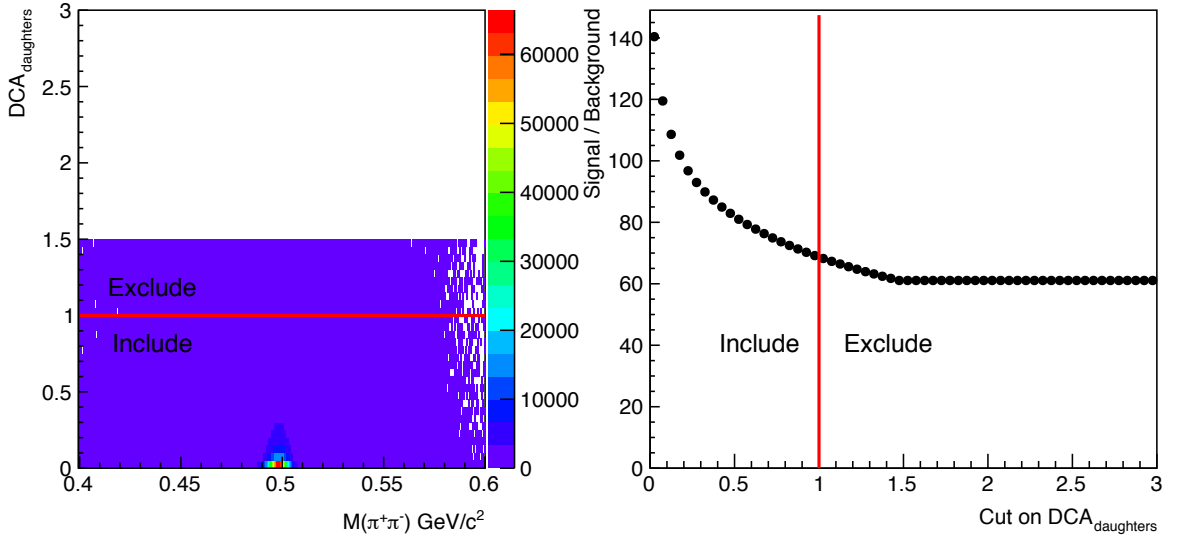
Figure 4.5: Distribution of K_S^0 with DCA between Daughters in 7 TeV pp - Left: invariant mass of K_S^0 candidates against DCA between daughter tracks. Right: estimated signal to background ratio of K_S^0 candidates as a function of the DCA between daughters cut chosen.

4.2.6 Number of TPC Clusters

The quality of the charged track reconstruction in the TPC is related to the number of clusters a track is composed of. In order to reduce contamination from fake tracks, but not be too sensitive to run-by-run changes in the TPC condition, a reasonably loose cut was selected for both pp and Pb–Pb collisions. Although the signal to background ratio (Figure 4.6) could be improved by further tightening of the cut, variations in the TPC operating voltage can affect this signal, leading to discrepancies between data and Monte Carlo, as shown in Figure 4.7. As such, the cut was kept loose, requiring at least 70 clusters deposited in the TPC, from a possible 160 pad rows, which excludes only a small fraction of real V0s.
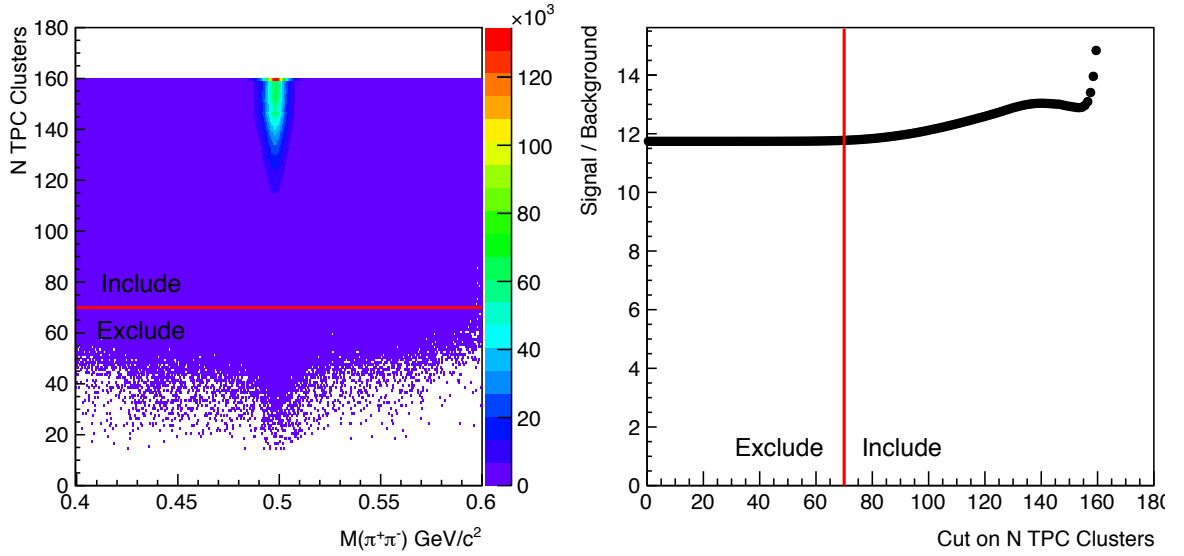
Figure 4.6: Distribution of K_S^0 with Number of TPC Clusters in Pb–Pb - Left: invariant mass of K_S^0 candidates against number of TPC clusters. Right: estimated signal to background ratio of K_S^0 candidates as a function of the TPC cluster cut chosen.
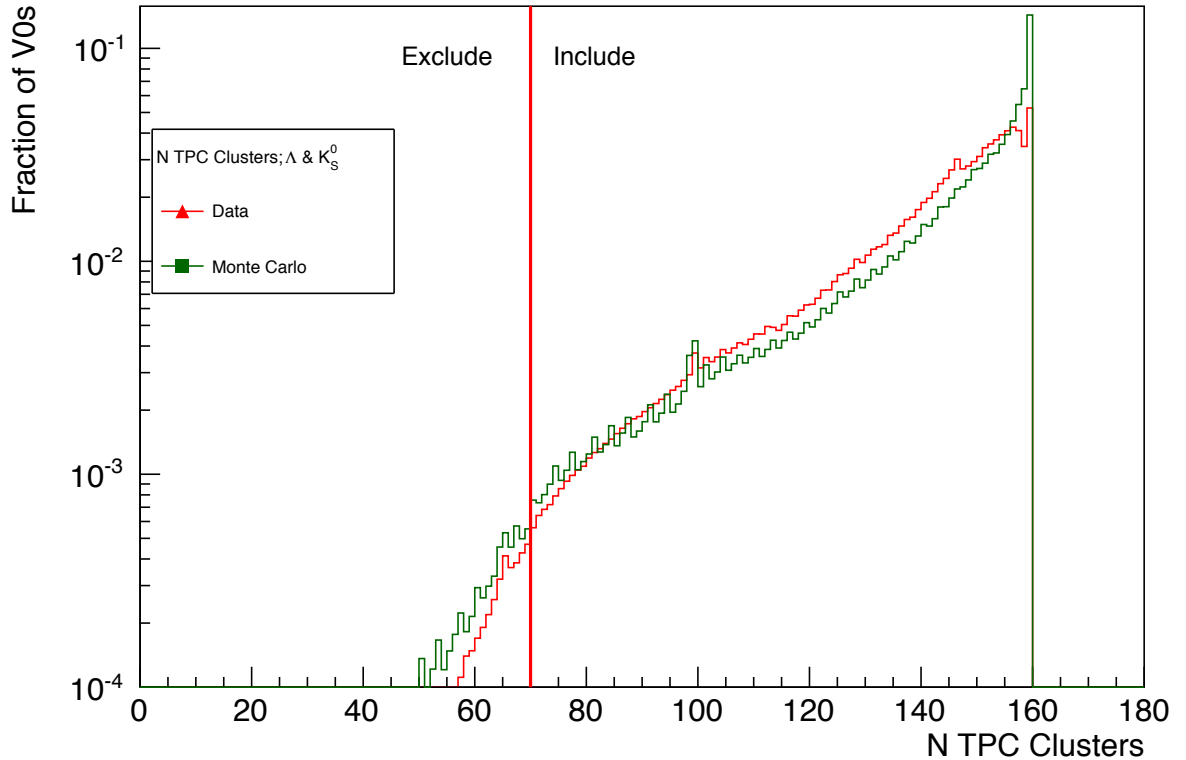
Figure 4.7: Estimated Distribution of K_S^0 and Λ with Number of TPC Clusters in Pb–PbData and Monte Carlo - Comparison of Monte Carlo and Data distributions of Λ and K_S^0 with the number of TPC clusters per daughter track. Sideband subtraction is used to estimate distributions.

4.2.7 χ^2 per TPC Cluster

In the TPC track reconstruction procedure a value of χ^2 is assigned to each TPC cluster, and so the overall χ^2 per TPC Cluster gives an impression of the quality of the fit. However, when used in combination with other TPC cuts, a cut on this variable was found to have little additional effect, and so was not used for the final results.

4.2.8 Ratio of TPC Crossed Rows to Findable Clusters

In order to further reduce dependance on the running condition of the TPC, a cut was proposed on the ratio of the number of TPC pad rows actually crossed by the track to the number of clusters which could potentially be found. A higher value of this ratio would indicate a more reliable track. However, in order to optimise this cut, it was necessary to implement it in a region where Monte Carlo could not accurately reproduce the ratio, leading to significant systematic errors. As a result, this cut is not used in this analysis.

4.2.9 Decay Length

As a Λ or K_S^0 would travel some distance before decaying, the quality of the reconstructed signal in the detector varies with the transverse decay length. Decays which are too close to the primary vertex can be difficult to separate from combinatorial background of primary charged particles, while many later decays can leave no signal in the ITS, or even decay partway through the TPC.

Further, a discrepancy between real data and Monte Carlo was discovered at short transverse decay lengths for the K_S^0 spectra. This required the transverse decay length cut to be tightened so as to exclude the inner layers of the ITS, and as a result, only V0s with decay lengths $5 < r < 100$ cm are accepted. This is thought to be due to imperfections in the Monte Carlo predictions for the rate of fake clusters in the SPD, and will be discussed in detail in Section 4.10.

4.2.10 Lifetime

Having measured a particles decay length, it is possible to reconstruct its rest frame lifetime by assuming the mass of the particle. For a particle of momentum p which travels a distance d before decaying, the proper lifetime is given by

$$c\tau = m\frac{d}{p} = m\frac{r}{p_{\mathrm{T}}}, \tag{4.1}$$

where r and p_{T} are the transverse radius and momentum respectively of the V0 decay vertex. Although the last equality does not exactly hold when the position and momentum vectors of the particle are not entirely parallel, the difference was found to be negligible under the resolution of our detector with the applied cos(PA) cuts. This observed lifetime could be compared with the PDG average values of 7.89 cm and 2.68 cm for Λ and $\mathrm{K}_{\mathrm{S}}^{0}$ respectively. The distributions of real Λ and $\mathrm{K}_{\mathrm{S}}^{0}$ would be expected to drop off exponentially with this lifetime, while combinatorial background will drop off more slowly, with $1/r^2$ and contributions from secondaries and interactions with the detector material tend to be more constant. Thus, by only accepting V0s with lifetimes less than three times the PDG value, it is possible to strongly reduce contributions from secondary particles, while retaining 95% of the signal. The cut is indicated in Figure 4.8, and it can clearly be seen that cutting at this distance maximises the signal to background ratio.

For $\mathrm{K}_{\mathrm{S}}^{0}$, the combination of the $c\tau$ cut with the tightened decay length cut entirely removed the signal from the lowest p_{T} bins. As such, and as the background from secondaries is in any case lower for $\mathrm{K}_{\mathrm{S}}^{0}$, the cut is loosened to four times the PDG value and only applied to $\mathrm{K}_{\mathrm{S}}^{0}$ candidates with decay lengths over 12 cm.

4.2.11 PID

At low p_{T}, it is particularly difficult to distinguish Λ from the combinatorial background. However, at such low p_{T}, there are considerably more pions in the event than other charged particles. By using the TPC dE/dx information to distinguish protons from Λ
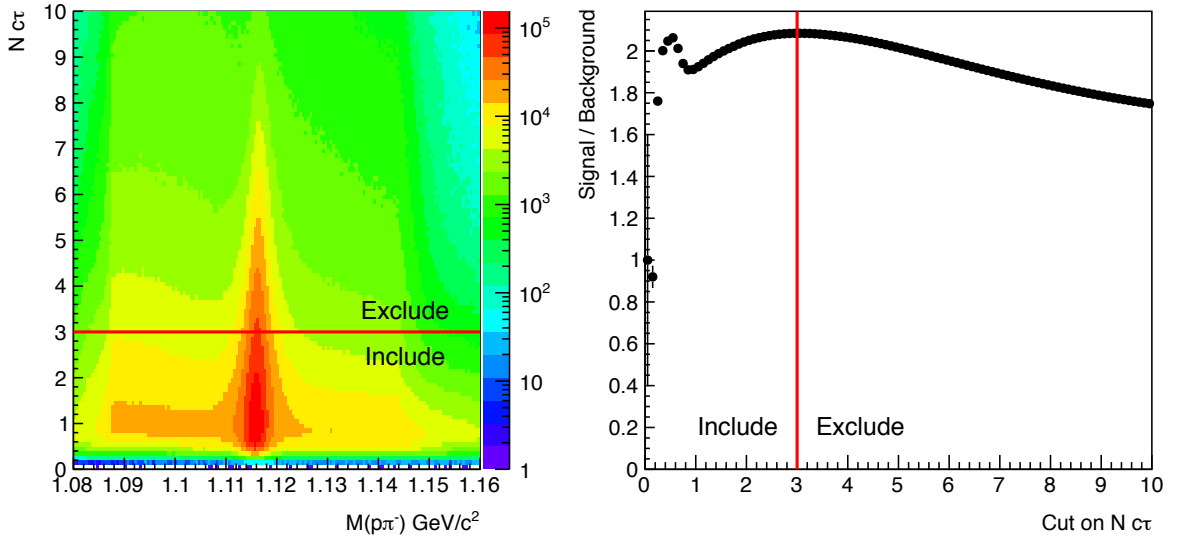
Figure 4.8: Distribution of Λ with Lifetime in Pb–Pb - Left: invariant mass of Λ candidates against lifetime as a multiple of PDG Λ lifetime. Right: estimated signal to background ratio of Λ candidates as a function of the lifetime cut chosen.

decay and combinatorial pions, a significant improvement in the signal/background ratio can be made.

The dE/dx signals in the TPC can be described by a Bethe-Bloch parameterisation (Equation 3.2), which has been tuned to data by the ALICE TPC group. The positive daughter of the Λ candidate is required to fall within 3σ of the parameterisation, which causes no significant loss of signal. This cut is applied to all Λ candidates with p_T of less than 1.2 GeV/c, as this is the region in which the proton and pion dE/dx signals can be differentiated (Figure 3.4). Although this has little effect on the overall signal to background ratio, as seen in Figure 4.9, in the lowest p_T bins, such as Figure 4.10, it has a dramatic effect.

4.2.12 Armenteros-Podolanski Diagram

While estimating the fitting systematics (see Section 4.28), it became apparent that although the signal to background ratio of the $\mathrm{K_S^0}$ was acceptable, the background shape was sufficiently challenging to fit that it was producing large systematic errors of up to 50%. Further studies with Monte Carlo generated data suggested that the source of this
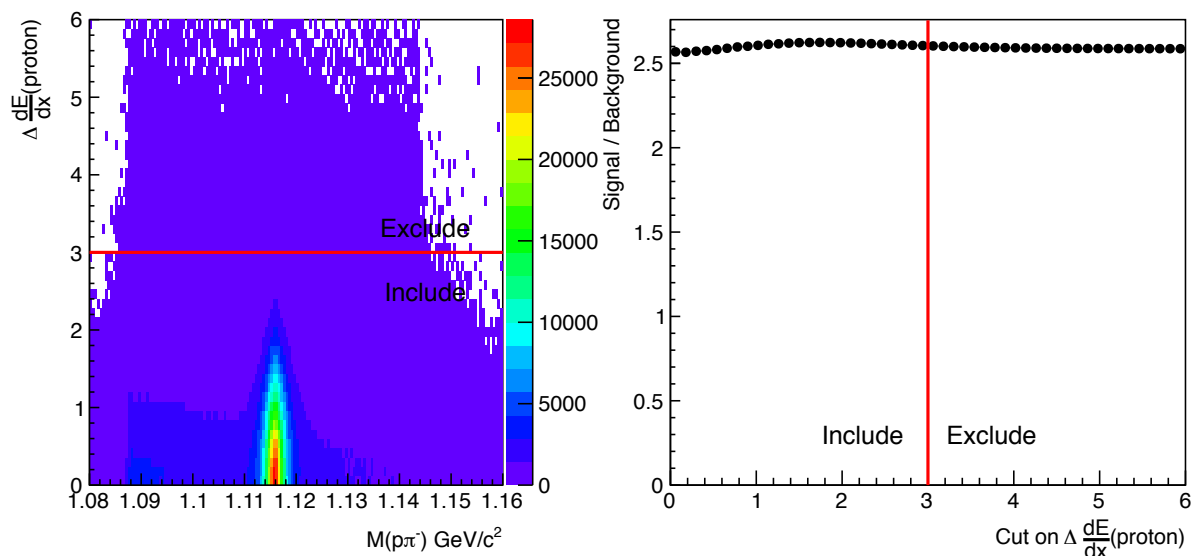
Figure 4.9: Distribution of Λ with TPC PID in Pb–Pb - Left: invariant mass of Λ candidates against $N\sigma$ deviation of the positive daughter from the ideal proton dE/dx signal in the TPC. Right: estimated signal to background ratio of Λ candidates as a function of the PID cut chosen.

ALI-PERF-9086
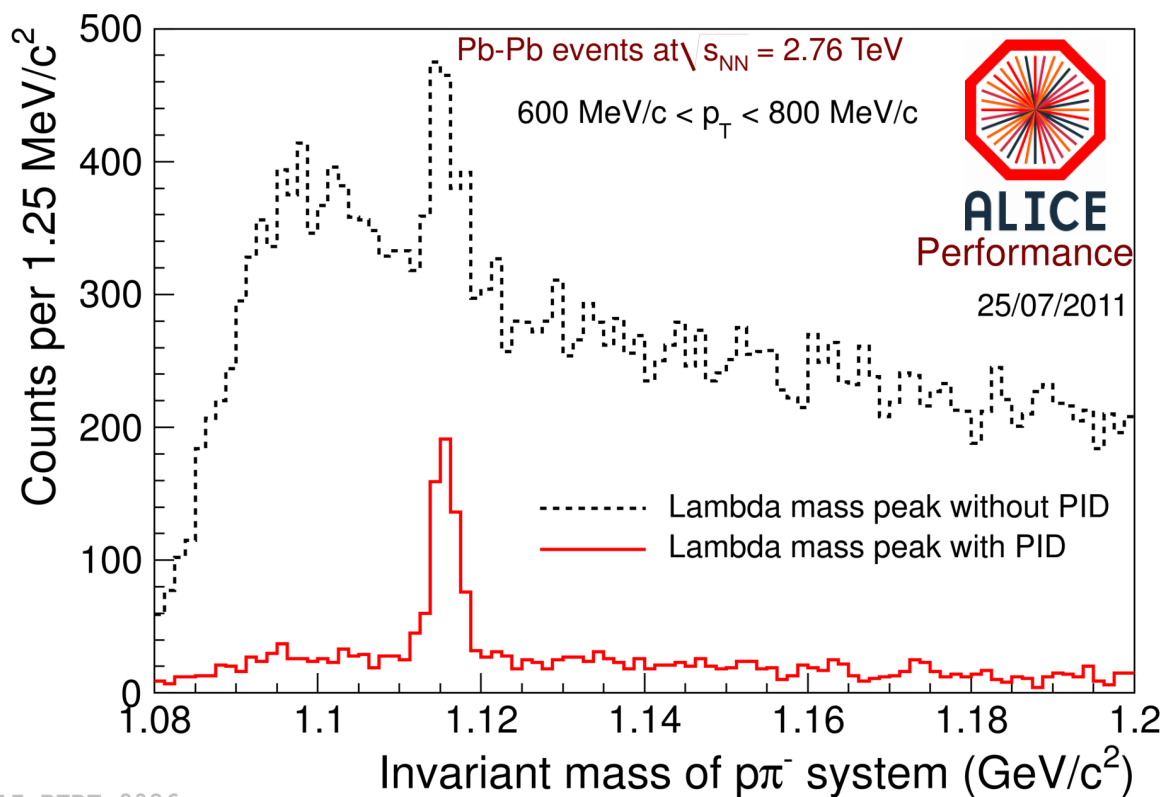
Figure 4.10: Invariant Mass of Λ candidates - Invariant mass of Λ candidates for 0.6 GeV/c < p_{T} < 0.8 GeV/c, with and without PID [152].

80

background feature were Λ and $\overline{\Lambda}$ reconstructed under the K_S^0 mass hypothesis. Attempts were made using PID and $c\tau$ cuts to isolate the Λ and K_S^0 particles, but the most effective method found was to perform a cut on the Armenteros-Podolanski variables.

The Armenteros-Podolanski diagram is effectively an alternative way of visualising the invariant mass plots [153], using the projections of the daughter momenta on that of the V0, as indicated in Figure 4.11. It plots the magnitude of the momentum of the daughter tracks perpendicular to the V0's momentum, p_T^{ARM}, against a construction of the daughter tracks' momenta parallel to the V0's momentum, α, where

$$\alpha = \left(\frac{p_\parallel^+ - p_\parallel^-}{p_\parallel^+ + p_\parallel^-} \right). \tag{4.2}$$

This diagram, shown in Figure 4.12, displays semi-ellipses for the different V0s, with overlap between the Λ and K_S^0 curves. The extent of the overlap varies with p_T, and so the shape and magnitude of the background to the K_S^0 invariant mass peak also varies strongly with p_T.
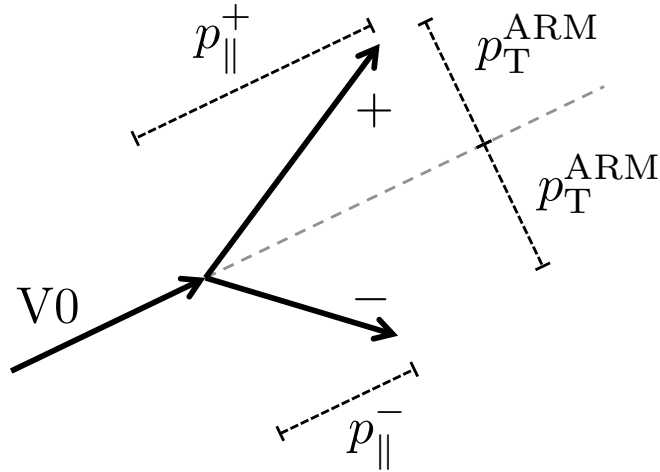
Figure 4.11: Schematic of Momentum Projections Used in Armenteros-Podolanski Diagram - The projection of the positive and negative daughters momentum perpendicular and parallel to the V0's momentum are indicated. The perpendicular components are equal and opposite to satisfy conservation of momentum, and the relative magnitudes of the projections are determined by the Lorentz boost of the V0 and the decay angle relative to the boost in the V0 rest frame.

A linear cut on this diagram was used to exclude Λ and $\overline{\Lambda}$ from the K_S^0 reconstruction.

Care had to be taken not to influence the background shape of the K_S^0 mass peak, for instance by introducing a trough under the K_S^0 peak, and so the cut was chosen to pass approximately perpendicularly through the K_S^0 ellipse. The chosen cut is indicated as a line on Figure 4.12. Studies of Monte Carlo generated data suggested that this choice of cut left the background remarkably smooth, and so it was adopted. The dramatic effect on the signal to background ratio, and the shape of the background removed, can be seen in Figure 4.13.
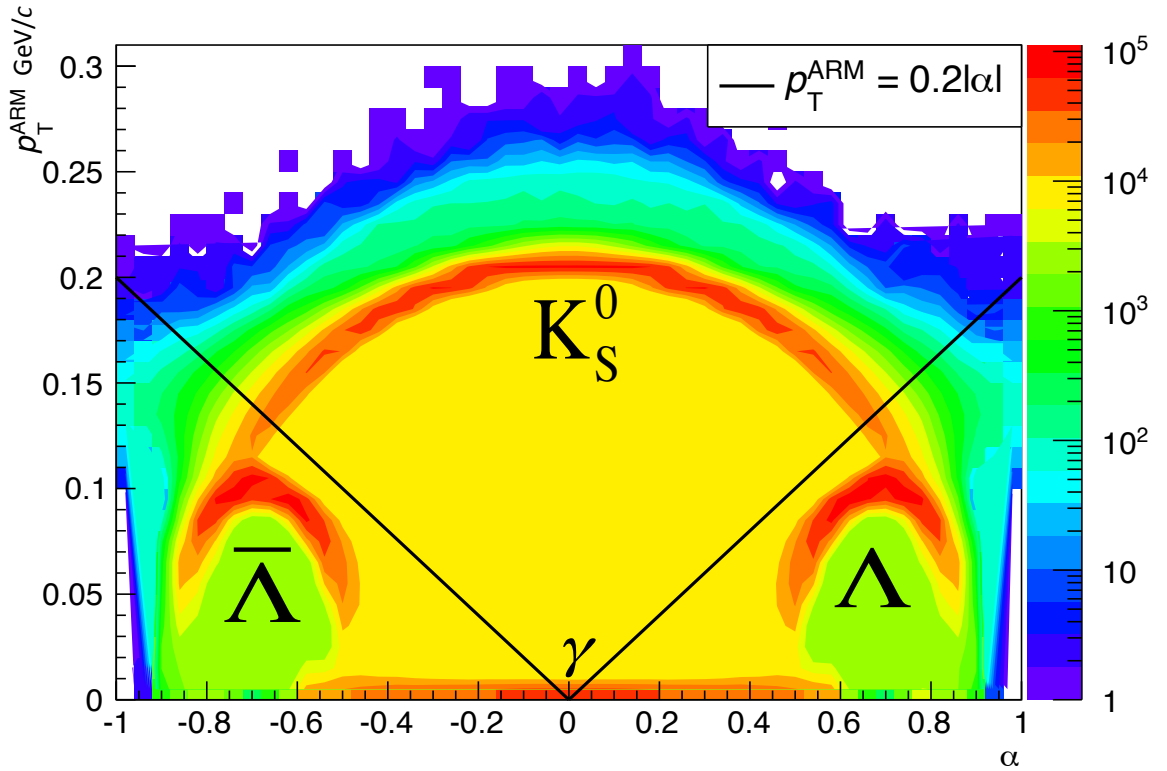
Figure 4.12: Armenteros-Podolanski Diagram for K_S^0 Candidates - Plot of p_T^{ARM} against α for V0s satisfying all other K_S^0 cuts, before any invariant mass selection. The symmetrical central ellipse is the K_S^0, while the Λ and $\overline{\Lambda}$ are off-centre due to the asymmetric mass of their decay products. The peak at very low p_T^{ARM} is due to γ conversions, and does not enter the invariant mass range used for fitting. The line indicates the cut used; all V0s below this line are rejected as K_S^0 candidates.
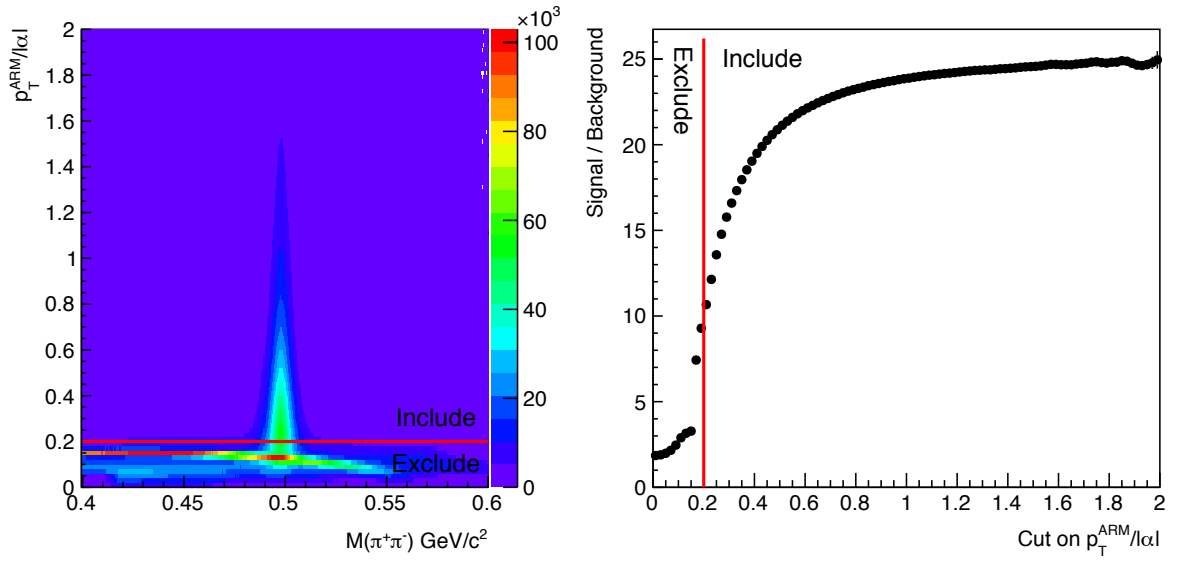
Figure 4.13: Distribution of K_S^0 with Armenteros-Podolanski Variables in Pb–Pb - Left: invariant mass of K_S^0 candidates against $p_T^{ARM}/|\alpha|$. Right: estimated signal to background ratio of K_S^0 candidates as a function of the Armenteros-Podolanski cut chosen.

4.2.13 Cowboys and Sailors

As the daughters of the Λ and K_S^0 decay are curving in the applied magnetic field, there are two possible decay geometries known as 'Cowboys' and 'Sailors' as illustrated in Figure 4.14. However, if a V0 is created from a random crossing of primary particles, it should always have the 'Sailor' topology, as the two particles will have come from a common vertex: the primary vertex. Thus, by selecting only 'Cowboy' decays, it should be possible to remove the majority of the combinatorial background at the cost of half of the signal. Unfortunately, when this was tried it had very little effect on the signal to background ratio, as the curvature of the tracks is generally low, and so this cut was not considered worth the loss of signal.

The final cuts selected are shown in Table 4.1.

4.3 Fitting Routine

In order to estimate the signal and background for the cut iteration procedure sideband regions were identified and subtracted from the peak region, under the assumption that the
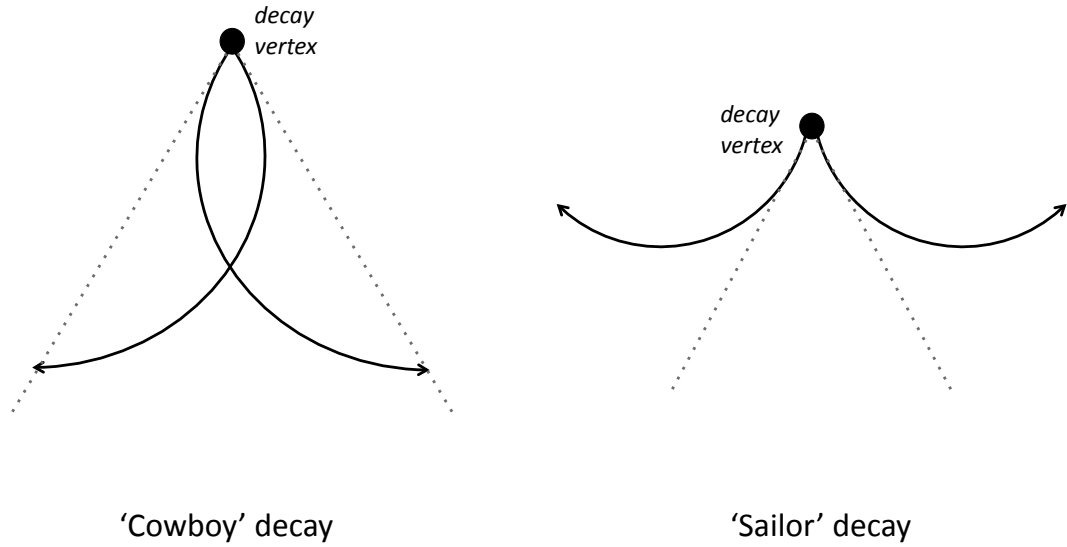
Figure 4.14: Cowboys and Sailors - Possible topologies for decays to pairs of oppositely charged particles in a magnetic field.

Cut Variable	Pb–Pb	pp
Pseudorapidity		$\lvert\eta\rvert < 0.8$
Rapidity		$\lvert y \rvert < 0.5$
Cosine of Pointing Angle	$\cos(\mathrm{PA}) > 0.998$	$p_{\mathrm{T}} < 4 \ \mathrm{GeV}/c : \cos(\mathrm{PA}) > 0.998$
		$p_{\mathrm{T}} > 4 \ \mathrm{GeV}/c : \cos(\mathrm{PA}) > 0.9$
DCA to Primary Vertex		$\mathrm{DCA_{PV}} > 0.1 \ \mathrm{cm}$
DCA between Daughters	$\mathrm{DCA_{daughters}} < 1 \ \sigma$	$\mathrm{DCA_{daughters}} < 1.5 \ \sigma$
Number of TPC Clusters		$\mathrm{N^{TPC}_{clusters}} > 70$
Decay Length		$5.0 < r < 100 \ \mathrm{cm}$
Lifetime		$\Lambda: c\tau < 3c\tau_{PDG}$
		$\mathrm{K^0_S}: c\tau < 4c\tau_{PDG}$ or $r < 12 \ \mathrm{cm}$
PID		$\Lambda: \Delta\frac{\mathrm{d}E}{\mathrm{d}x}(\mathrm{proton}) < 3\sigma$
Armenteros-Podolanski		$\mathrm{K^0_S}: p_{\mathrm{T}}^{\mathrm{ARM}} > 0.2\lvert\alpha\rvert$

Table 4.1: Final cuts used for analysis.

sidebands contain only background which continues smoothly under the peak. However, this relies on the background being approximately linear in order to reach a reasonable estimate, which is not always the case. For example, Figure 4.15 shows the Λ and K_S^0 invariant mass distributions for the most central collisions in the mid-momentum region after the application of all cuts; the Λ background shape is much better described by a quadratic curve than a linear.
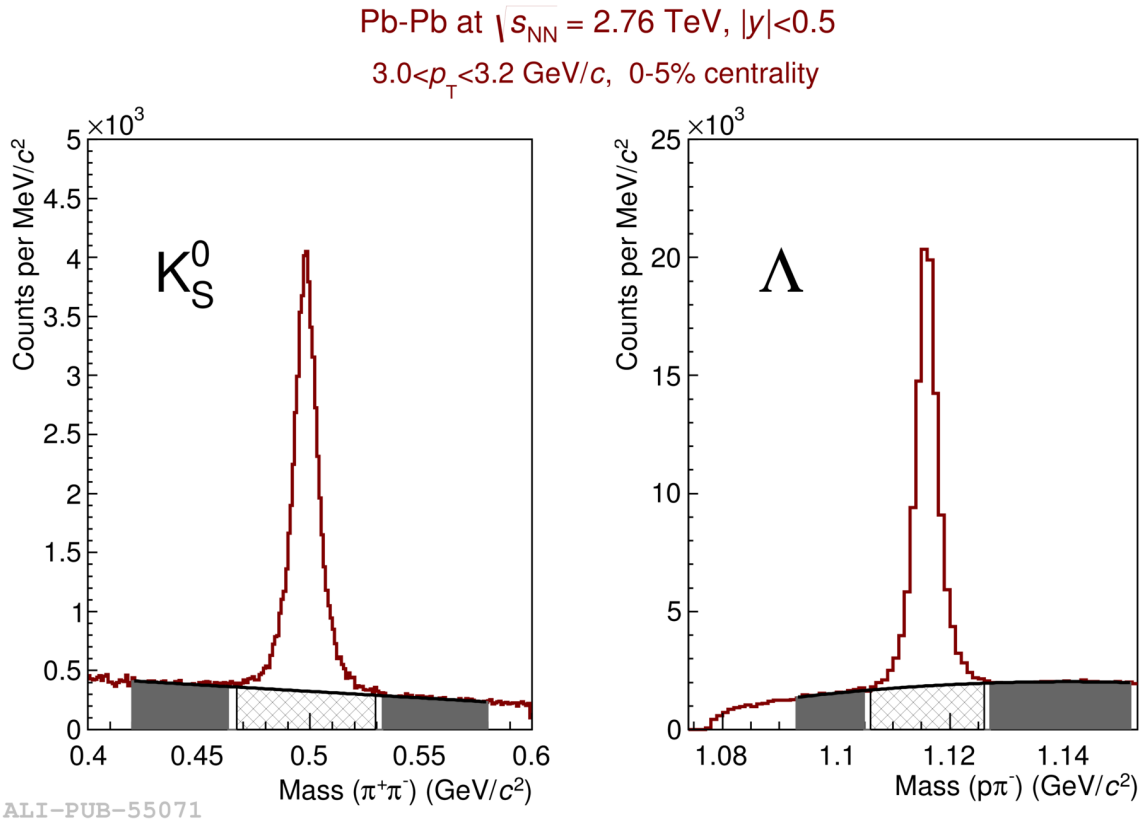
Figure 4.15: Λ and K_S^0 Candidates' Invariant Mass - Distribution of invariant mass for Λ and K_S^0 candidates from Pb–Pb collisions in 0-5% centrality interval, $3.0 < p_T < 3.2$ GeV/c. The region fitted for the background is shaded in grey, and the extrapolated region subtracted from the peak indicated by crosshatching [1].

The fitting routine used to calculate the final yields initially fits with the sum of a Gaussian and second order polynomial, in order to gain a rough description of the distribution. The parameters are very loosely bounded, with the centre and width of the peak initially set by the results of previous fits. The fit range is ideally ± 0.2 GeV/c^2 from the PDG mass, but in practice this has to be adjusted by hand to avoid irregularities in the background, such as the kinematic limit of the Λ, and to ensure a reliable fit.

Having made this initial fit, the centre (m) and width (σ) of the Gaussian are extracted and used to define the peak region. These parameters are shown in Figure 4.16, where it can be seen that the reconstructed mass is close to the PDG value while the width of the peak increases slightly with p_T due to the worsening momentum resolution. The peak region was then excluded from the background fit: a second order polynomial. This curve could then be extrapolated under the peak, and subtracted from the peak region, in order to extract the yield of the particles.
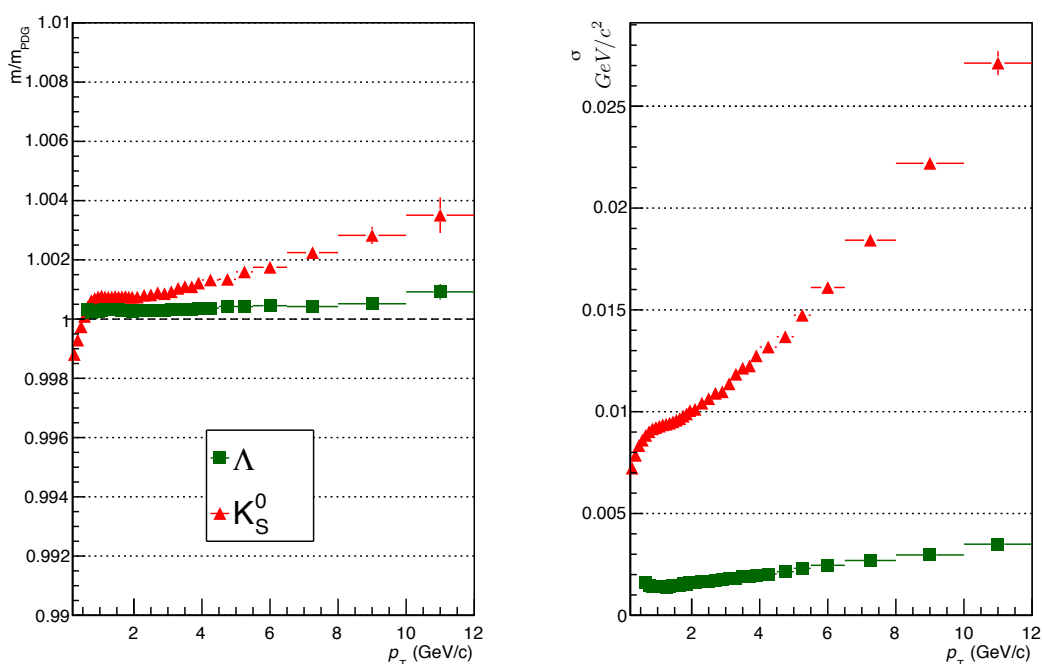
Figure 4.16: Mass and Peak Width from Fitting the Invariant Mass Distributions - Results for the peak centre, m, normalised to PDG mass, and peak width, σ, of the Gaussian fit to the invariant mass distribution in Pb–Pb collisions for 0-90% centrality.

The width of these peak regions was initially set to $\pm 3\sigma$, but had to be extended as the invariant mass distribution of the particles were found to have significant non-gaussian tails, which are treated as background when they lie in the sideband regions. While widening the peak region captured more of the signal, it also reduced the range in which the background fit could be undertaken. This was particularly problematic at high p_T, as the σ of the Gaussian fit was found to increase with p_T, as seen in the right hand plot of

Figure 4.16. A balance between uncertainties introduced by these two issues was found (see Section 4.12.2 for more details), and the peak regions were defined as $\pm 5\sigma$ for K_S^0, and $\pm(3.5\sigma + 2\text{MeV}/c^2)$ for Λ. A further $\pm 0.5\sigma$ was excluded from both the peak region and background fit to reduce the impact of the tails.

4.4 Monte Carlo

In order to correct for the effects of cuts on the Λ and K_S^0 yields, and to account for the acceptance of the detectors, Monte Carlo simulations were used. Pb–Pb collisions were simulated using the HIJING v1.383 generator [77], while pp events were generated using PYTHIA6 (Perugia 0 tune) [154]. In both cases the events were propagated through the detector simulation using GEANT3 v1-11 [155] and the ALICE software framework [156].

The correction was p_T dependant and, to a lesser extent, centrality dependant. Assuming that the Monte Carlo accurately reproduces the detectors' response to the particles,

$$\frac{N_{\text{observed}}}{N_{\text{corrected}}} = \frac{N_{\text{associated}}}{N_{\text{generated}}}, \tag{4.3}$$

where N is the number of particles in a particular p_T and centrality bin, and the subscripts refer to:

- observed - the yield observed in the detector

- corrected - the true yield

- associated - the number detected after passing Monte Carlo simulation through the detector framework

- generated - the number of particles initially generated in the Monte Carlo simulation

The efficiency for a bin may then be defined by

$$\epsilon = \frac{N_{\text{associated}}}{N_{\text{generated}}}, \tag{4.4}$$

and the relationship between the observed and corrected yields may be written as:

$$N_{\text{corrected}} = \frac{N_{\text{observed}}}{\epsilon}. \tag{4.5}$$

In order to ensure that this relationship is valid, it was necessary to check that all the cuts used were reproduced faithfully in Monte Carlo. Unfortunately, the Bethe-Bloch parameterisation of the energy loss measurements in the TPC behaved very differently in Monte Carlo and data. However, it was possible to correct for the effects of this cut separately, as the data response was well described by a Gaussian distribution.

4.5 Generated Spectra

The generated spectra are all Λ and K_S^0 generated in the Monte Carlo event satisfying the following conditions:

- They fall within the same rapidity range as the measured data ($|y| < 0.5$)

- They are a 'Physical Primary' - either a true primary particle, or created by strong or electromagnetic decay from a primary particle.

4.6 Associated Spectra

The associated spectra are formed from Monte Carlo generated particles which have passed through the detector simulation and are, to as great a degree as possible, subject to the same cuts and signal processing as the data. All the cuts used on data are applied to the associated spectra, with the exception of the PID cut. This cut is instead corrected for by assuming a Gaussian distribution of the dE/dx signal in the TPC, as the Monte Carlo did not accurately reproduce this distribution.

As the background levels and distributions of the invariant mass plots are different in the Monte Carlo simulations, it was decided not to pass the associated spectra through

the fitting routine. Instead, background was entirely removed by using the Monte Carlo information to simulate perfect PID. However, as the fitting routine is known to cut off part of the tails of the invariant mass distribution, only associated Λ and K_S^0 within the peak region (taken from the fit to data) are included, and any Λ and K_S^0 falling within the background region are instead subtracted, as would happen in data. As a result, the effects of this erroneous background subtraction are partly corrected for in the efficiency but are also, to be conservative, considered a source of systematic uncertainty.

4.7 Injected and Enhanced Monte Carlo

Producing Monte Carlo events and propagating them through the detector is computationally intensive, particularly for Pb–Pb events. As a result, there is generally a lack of statistics for creating the efficiencies. This problem is exacerbated because the HIJING simulations tend to underestimate the quantity of strangeness found in real events, and at high p_T the yields are naturally very low. In order to boost the statistics of Λ and K_S^0 particles for the efficiency calculation, two different approaches were tried.

For Pb–Pb collisions, additional particles (Λ and K_S^0, but also other strange and charm particles) were added to the Monte Carlo event before propagation through the detector simulation. This is referred to as 'injection' of the strange particles. Three different Monte Carlo samples were used for the Pb–Pb analysis, as described below. All Monte Carlo simulations were calibrated such that the detector condition matched that of the corresponding data samples.

- LHC11a10a_bis - 3M Pb–Pb events, with no injection.

- LHC11a10b_bis - 3M Pb–Pb events, with 1 Λ per event injected with a realistic p_T distribution, and 1 Λ and 1 K_S^0 injected with a flat p_T spectrum up to 10 GeV/c.

- LHC11a10b_plus - 4M Pb–Pb events, with 1 Λ per event injected with a realistic distribution, and 1 Λ and 1 K_S^0 injected with a flat p_T spectrum up to 20 GeV/c.

At low p_T, where the efficiency is rapidly varying, only pure Monte Carlo was used, and the injected particles were included at high p_T, where the statistics necessitated it. The final efficiency 'cocktail' used in the analysis was:

- For $p_T < 1.5$ GeV/c; pure HIJING Monte Carlo only.

- For 1.5 GeV/$c < p_T < 2.0$ GeV/c, Λ only; error-weighted mean of pure and pure plus injected Monte Carlo.

- For $p_T > 1.5$ GeV/c (K_S^0) or 2.0 GeV/c (Λ) ; pure plus injected Monte Carlo.

The efficiencies in the higher p_T region are consistent for both pure and injected samples, and so the injected samples were considered to be safe to use.

For the $\sqrt{s} = 7$ TeV pp sample, the pure Monte Carlo was sufficient. However, for $\sqrt{s} = 2.76$ TeV, it was necessary to increase the statistics in order to push the upper p_T limit to the region required. To do this without introducing the problems associated with injected particles an 'enhanced' Monte Carlo sample was created. For this, the PYTHIA event was sampled before the time-consuming propagation through the detector simulation, and only fully reconstructed if there was a primary Λ or K_S^0 with $p_T > 2$ GeV/c.

The analysis efficiencies created are shown in Figures 4.17 and 4.18. The p_T used for the efficiency calculations is always the true p_T taken from the Monte Carlo, as the sharp jumps in the spectra due to injection and enhancement can otherwise corrupt the efficiency. Although this means that p_T smearing is not corrected for by the efficiency, estimates of the magnitude of smearing for the p_T spectra measured in data are negligible.

4.8 Feeddown Correction

As previously mentioned, the ALICE definition of a physical primary excludes those particles created in weak decays. Thus, feeddown from Ξ and Ω particles must be removed from the Λ spectra. The Monte Carlo efficiency cannot reliably correct for this, as it underestimates the yield of strange particles, and so the efficiency described above is
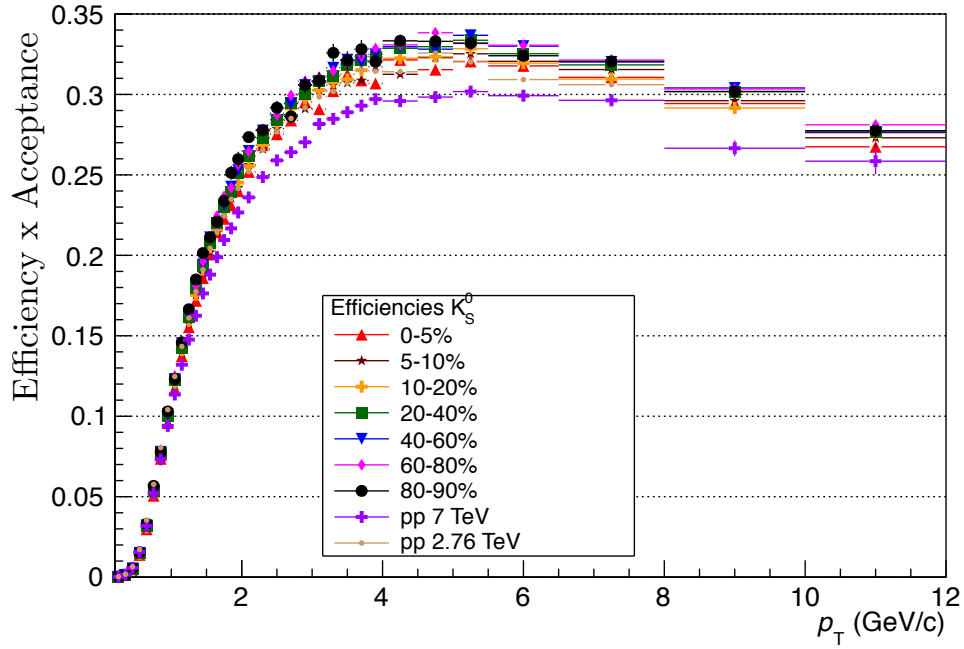
Figure 4.17: K_S^0 **Efficiencies** - Efficiency and Acceptance for reconstructing a K_S^0 in this analysis. Markers indicate different centrality bins and colliding systems, as detailed in the legend.

Figure 4.18: Λ **Efficiencies** - Efficiency and Acceptance for reconstructing a Λ in this analysis. Markers indicate different centrality bins and colliding systems, as detailed in the legend.

91
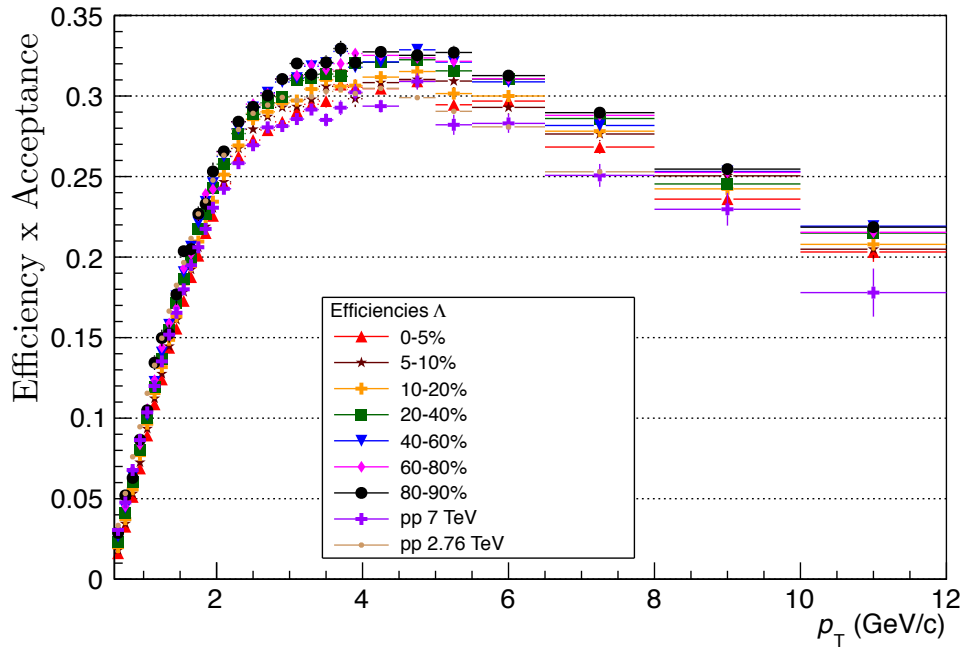
valid only for the physical primaries of interest. The approach used is described below for the Ξ; as the yield of Ω is roughly one twelfth that of the $\Xi^- + \Xi^0$ [50], it falls well within the systematic errors associated with the feeddown subtraction procedure.

A data driven approach was devised. The p_T spectra of Ξ^- measured in data were taken from [50, 157, 158], an example of which is shown in Figure 4.19.
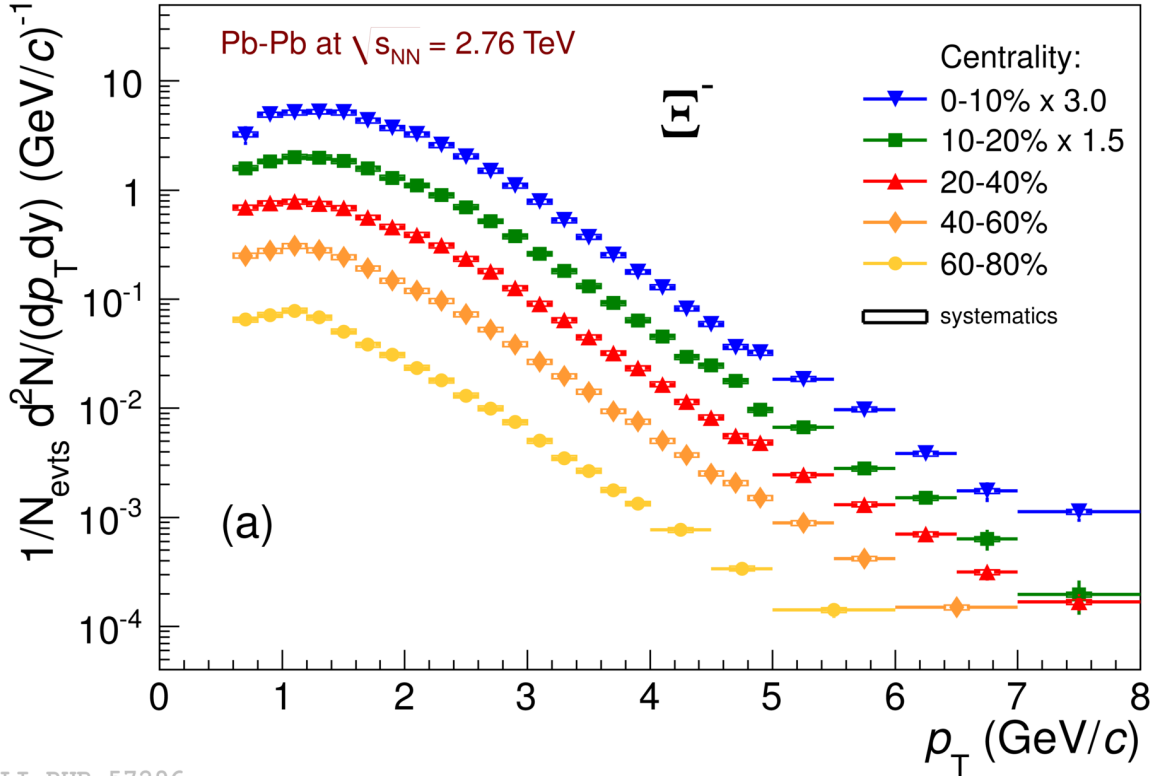
Figure 4.19: Ξ^- **Spectra** - p_T spectra of Ξ^- from $\sqrt{s_{NN}} = 2.76$ TeV Pb–Pb collisions [158].

Monte Carlo simulations were then used to create a feeddown matrix. Using the Monte Carlo truth information, all Λ passing the standard analysis cuts, and additionally having a Ξ^- as a mother, have their p_T and their mother's p_T stored in the matrix. This matrix is divided by the spectra of Ξ^- generated by the Monte Carlo, effectively producing an efficiency for Λ which originate from a Ξ^- decay and appear in our analysis. This matrix is then multiplied by the fully corrected Ξ^- spectrum from data, and projected along the Λ p_T axis to give us the spectra of Λ appearing in our data from Ξ^- decay. The yield of Ξ^- drops off rapidly at high p_T, so the effect of the p_T cut in the matrix is negligible.

The feeddown spectrum is divided by the total spectra of reconstructed Λ, multiplied by 2 to account for decays from Ξ^0, and expressed as a feeddown fraction.
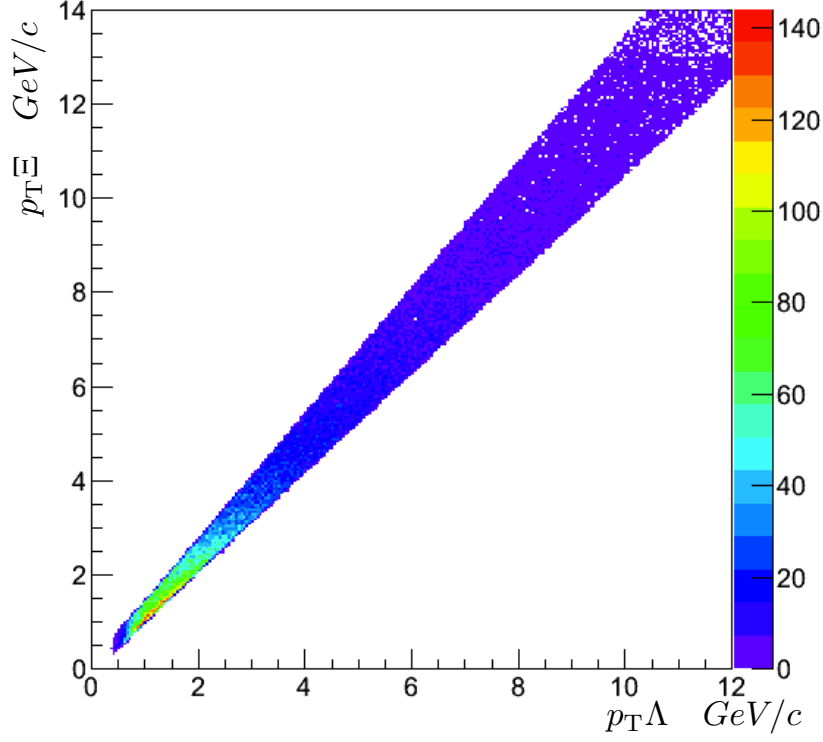
Figure 4.20: Feeddown Matrix - Matrix relating the p_T distribution of Ξ^- to the p_T distribution of their Λ daughters for 0-5% centrality Pb–Pb Monte Carlo simulations.

The typical p_T of a Λ from Ξ^- decay is slightly lower than that of its mother. As the available Ξ^- spectra only cover $p_T < 8$ GeV/c, it was necessary to extrapolate the Ξ^- spectra to higher p_T in order to calculate a feeddown fraction for all p_T. In Pb–Pb, several different fits were used to estimate the Ξ^- spectra; a blastwave fit described the spectra well at low p_T, but would not be expected to extend to higher p_T, where a power law described the trend better. The final feeddown fractions used were given by the blastwave fit for $p_T < 2$ GeV/c, while at higher p_T a smooth function describing the average of all the fits was used, with systematic errors assigned to cover the variation. For the higher p_T part statistical errors were much greater than the variation with centrality, so all centralities were averaged for $p_T > 2$ GeV/c.

For the pp collisions, the situation was simpler as a Tsallis fit (as described in Section 5.6) described the entire p_T range well, and so was used directly to generate the feeddown

fraction. The various feeddown fractions used are shown in Figure 4.21.
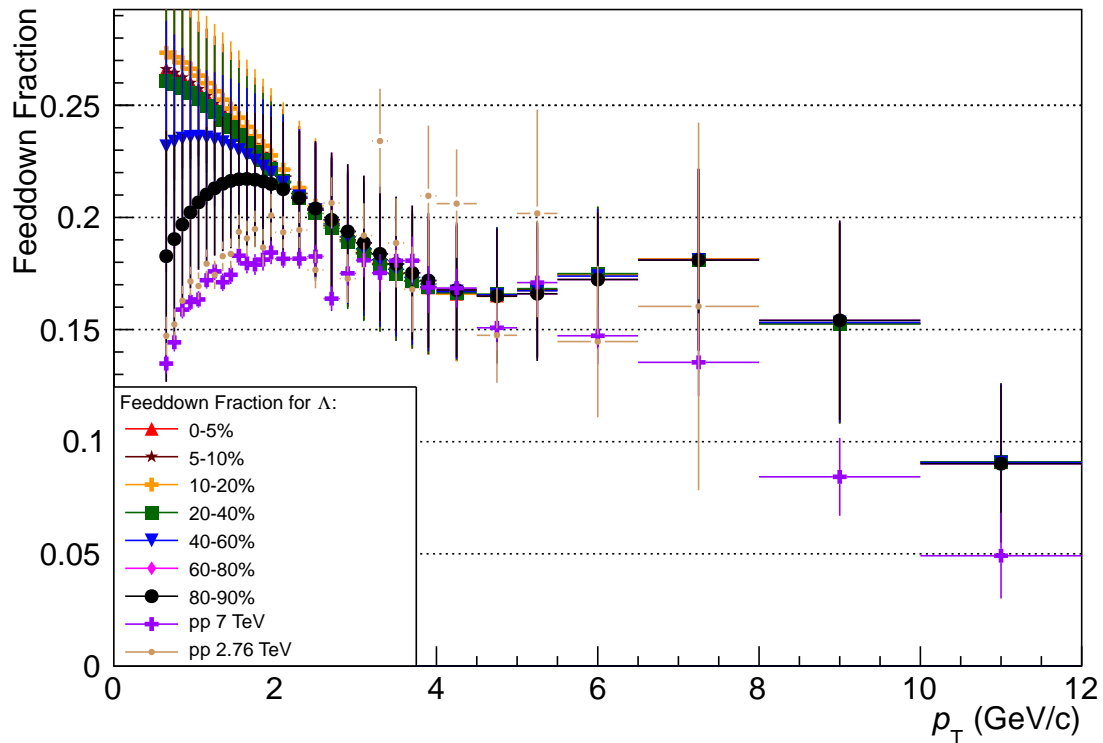
Figure 4.21: Feeddown as a Fraction of Λ Spectra - The estimated fraction of Λ entering our analysis from $\Xi^- + \Xi^0$ decay. Markers indicate different centralities and colliding systems.

4.9 $c\tau$ distributions

As a cross check of the reliability of this analysis, it is instructive to consider the $c\tau$ distribution of the particles. Collectively, the particles must decay (in their own rest frame) with an exponential distribution described by

$$N = N_0 e^{-\lambda \frac{c\tau}{c\tau_0}}, \tag{4.6}$$

where N is the number of particles remaining after proper time τ, N_0 the initial number of particles, and τ_0 the proper lifetime of the particle in its rest frame. The decay constant λ should be equal to 1. As in Section 4.2.10, the particle's lifetime in its rest frame can

be reconstructed using

$$c\tau = m\frac{r}{p_{\mathrm{T}}}, \qquad\qquad (4.7)$$

where the transverse decay length r and momentum p_{T} can be measured, and the mass m is taken to be the PDG value of the particle under consideration. The $c\tau$ distribution for data can be calculated in a manner analogous to the p_{T} distribution; using the invariant mass distribution to estimate the yield observed in the experiment, and correcting for efficiency and acceptance with the Monte Carlo simulations. As the Monte Carlo simulations generate particles with a p_{T} distribution different to that observed in data, it is necessary to reconstruct the $c\tau$ distribution differentially in both r and p_{T} and apply a 2-dimensional efficiency correction. This significantly lowers the statistics per bin, however. Bin widths can be increased somewhat to alleviate this effect, but it was found that large changes to the bin widths reduced the accuracy of correcting with the p_{T}-dependant efficiency too much. Rather than attempting to use the full fitting routine with these low statistics, it was decided to use the sideband subtraction method described in Section 4.3, with the width of the invariant mass peak at a given p_{T} taken from the 1-dimensional fitting process.

A full treatment of the Λ lifetime would similarly require a 2-dimensional feeddown correction. As such, the Λ results presented in this section are not feeddown corrected, and as a result have an apparent lifetime greater than the true value.

The efficiency created using this process is shown in Figure 4.22. It is immediately noticeable that there is a lot of white space on the plot; areas where the efficiency is zero. The empty bins within the distribution are statistical, and could be removed by rebinning, but the large empty areas on the bottom left and top right are more problematic. These are caused by the cuts applied; specifically the lifetime cut in the upper right, and the decay length cut in the lower left. Were the aim of this analysis to measure the $c\tau$ distribution, these cuts would be inappropriate, or at best would restrict us to a $c\tau$ range of 2-4 times the PDG lifetime.

The aim here, however, is to confirm that the $c\tau$ distribution measured in data is
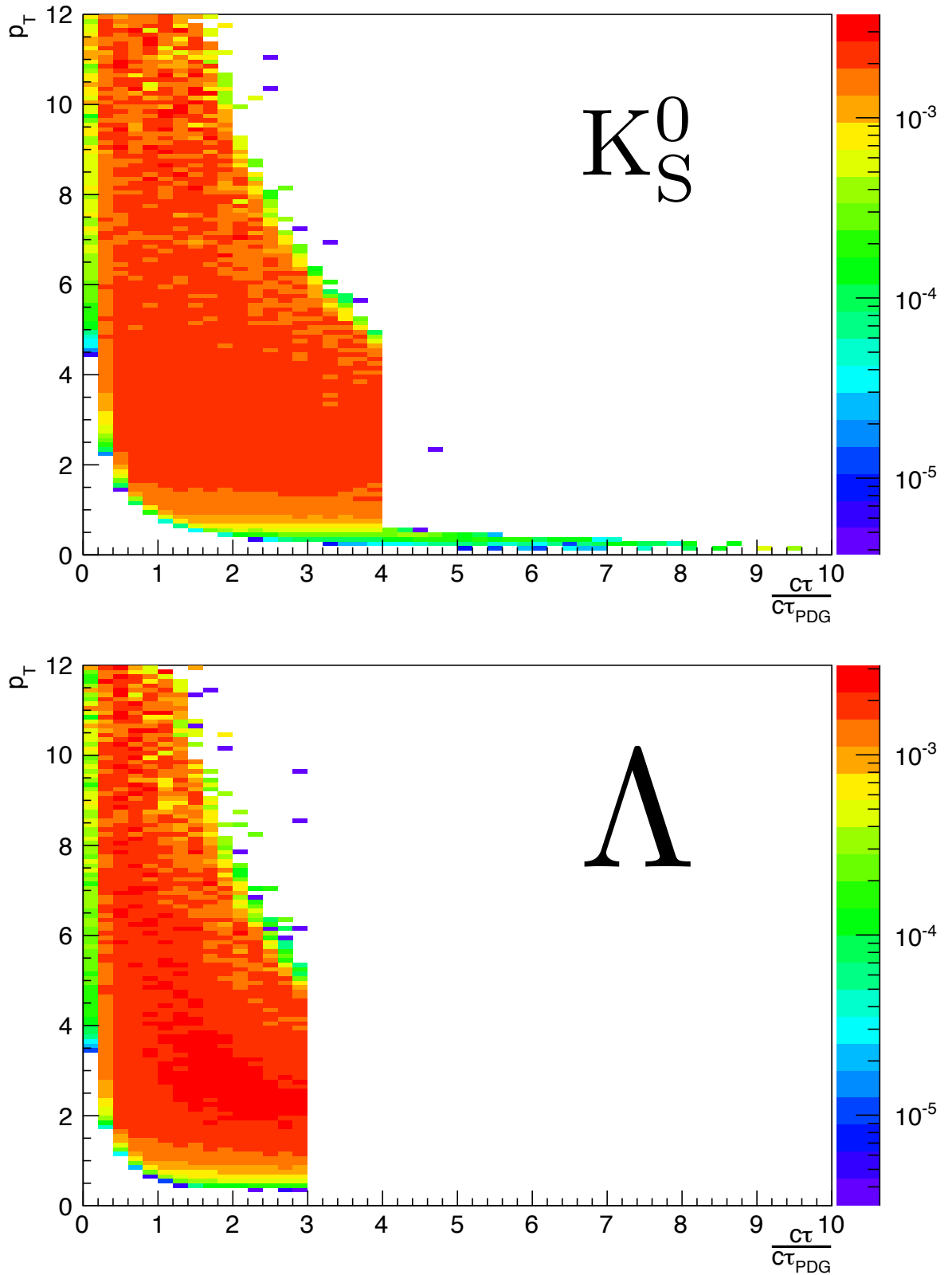
Figure 4.22: Efficiency for Reconstructing a K_S^0 or Λ with a Given $c\tau$ and p_T. - 2D efficiency in $c\tau$ and p_T for K_S^0 (top) or Λ (bottom) in $\sqrt{s} = 2.76$ TeV pp collisions. The large empty region to the right of each plot is due to the lifetime cut, and that in the bottom left is due to the decay length cut.

consistent with the ideal exponential distribution. It is not possible to directly divide the 2-dimensional measured p_T-$c\tau$ distribution by this efficiency to observe the corrected distribution, however the efficiency can be used to consider what the measured distribution would look like for an ideal $c\tau$ distribution and a realistic p_T distribution. An example of these distributions is shown in Figure 4.23 for $\sqrt{s} = 2.76$ TeV pp collisions. The measured data points for K_S^0 are consistent with what one would expect for an ideal initial $c\tau$ distribution, a p_T spectra as measured in this analysis and an efficiency as calculated above. It is not, moreover, compatible with a p_T spectra as generated in the Pythia Monte Carlo sample. For Λ, the measured data points suggest a lifetime longer than the PDG value, as expected, but still follow the data-like curve rather than that for Monte Carlo.

To make this investigation more quantitative, the expected $c\tau$ distribution can be treated as a correction factor. This correction factor is defined by the ratio of an ideal $c\tau$ distribution and the $c\tau$ distribution expected to be observed for an ideal initial $c\tau$ distribution, the measured p_T distribution and the calculated 2d efficiency. This gives us a $c\tau$-differential efficiency for the p_T distribution measured in data. This efficiency is multiplied by the measured $c\tau$ distribution, to gain an estimate of the corrected $c\tau$ distribution as shown in Figure 4.24. Fitting this distribution with an exponential decay gives us a decay constant of 1.024 ± 0.006 for K_S^0, where the ideal would have exactly 1. Although this is not consistent with 1, this contains only statistical errors while systematic errors would comfortably cover this difference. As an estimate of to what extent the distribution is forced towards the ideal, the same process was attempted for different decay constants in the 'ideal' distribution, and the results of the fit varied roughly as one over the 'ideal' decay constant. Overall, for all different centralities and systems, the results were within less than 5% of the ideal decay constant, well within the systematic errors on the p_T spectra, indicating that the results obtained with this analysis are consistent with expectations.

For Λ the result of the fit gives a decay constant of -0.714, or equivalently a lifetime
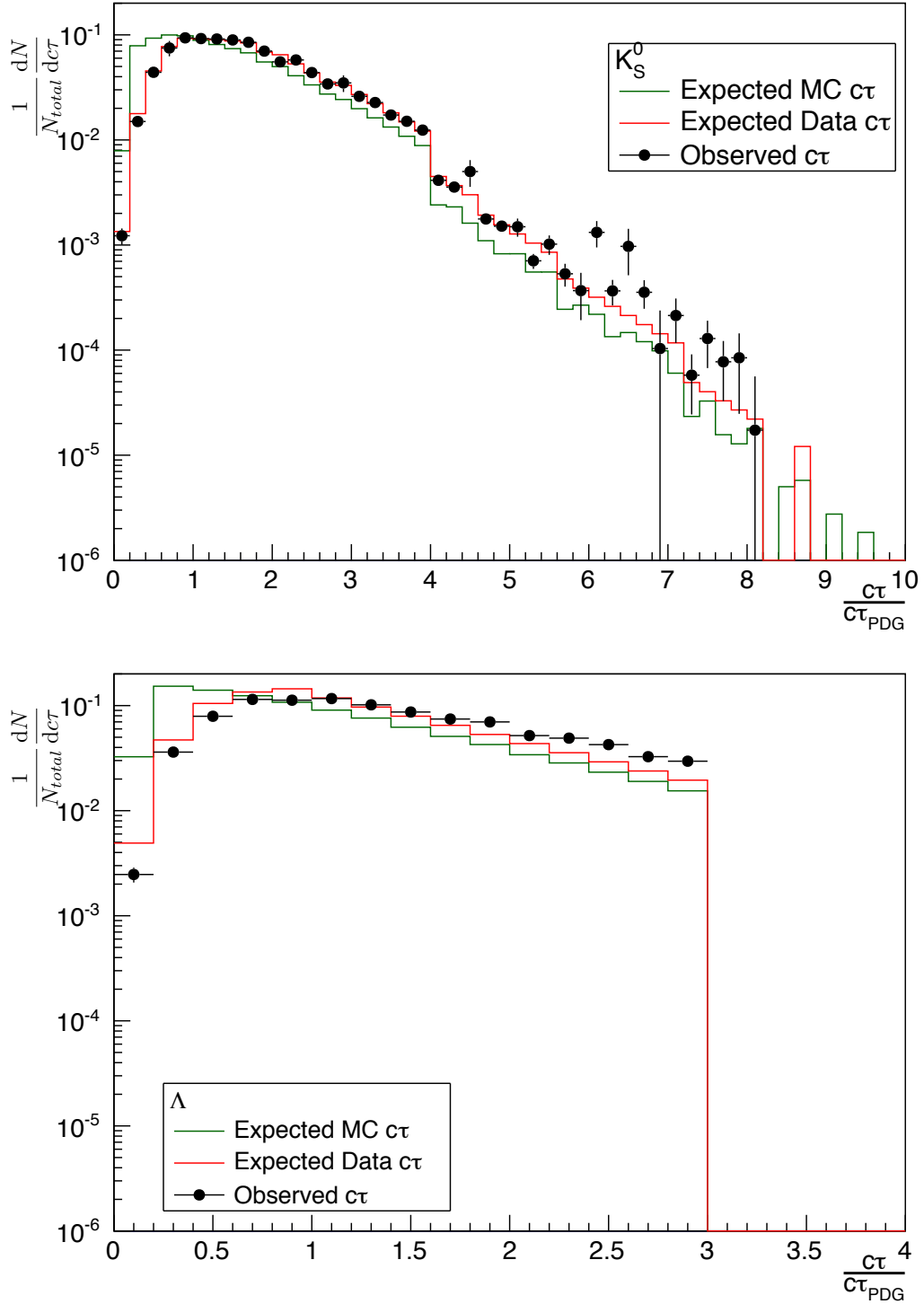
Figure 4.23: Expected Measured $c\tau$ **Distributions for** $\mathrm{K_S^0}$ **and** Λ **in** $\sqrt{s} = 2.76$ TeV pp **Collisions** - The $c\tau$ distribution one would expect to measure for an ideal initial $c\tau$ and a data-like (red) or Monte-Carlo-like (green) p_T distribution. The calculated efficiency has been used to convert the ideal $c\tau$-p_T distribution to an observed distribution. The markers show the measured $c\tau$ distribution which is consistent with the expectation for a data-like p_T distribution. Sharp drops in the distribution are due to applied kinematic cuts. Results for $\mathrm{K_S^0}$ shown in top plot, Λ in bottom plot. Note that Λ results are not feeddown corrected.

of 1.4 times the PDG value. Also shown is an illustration of where a pure Λ sample would be expected to lie, and a crude simulation of the effect of Ξ^- feeddown. For this simulation, there is a flat 18% contamination level from Ξ^-, and the lifetime is considered to be additive, ignoring relativistic effects. However, this simple model does illustrate that the Λ distribution is deviating from the ideal distribution in the expected manner. Were there more time, this simulation could be made more realistic to check the consistency of the lifetime measurements more stringently.

4.10 p_T Limits

The upper p_T limit of the spectra was set by the available statistics; for Pb–Pb this was limited by both data and Monte Carlo availability to 12 GeV/c, while for $\sqrt{s} = 2.76$ TeV pp collisions it was limited to 8 GeV/c by the data available. $\sqrt{s} = 7$ TeV pp was restricted to 12 GeV/c simply for compatibility with the Pb–Pb data. The lower limit however was limited by different factors, as described below.

While creating the $c\tau$ distributions, before the application of the decay length cut, discrepancies were noticed between data and Monte Carlo. Within one narrow p_T bin, the lifetime is given by

$$c\tau = \frac{m}{p_\text{T}} r, \tag{4.8}$$

where the mass and p_T are now approximately constant, so the transverse decay length distribution is proportional to the $c\tau$ distribution. Further, as with the p_T distributions, a relationship between the true and measured lifetimes in data and Monte Carlo can be written:

$$c\tau_\text{corrected} = \frac{c\tau_\text{observed} \cdot c\tau_\text{generated}}{c\tau_\text{associated}}. \tag{4.9}$$

Rearranging, and remembering that the corrected and generated distributions must be
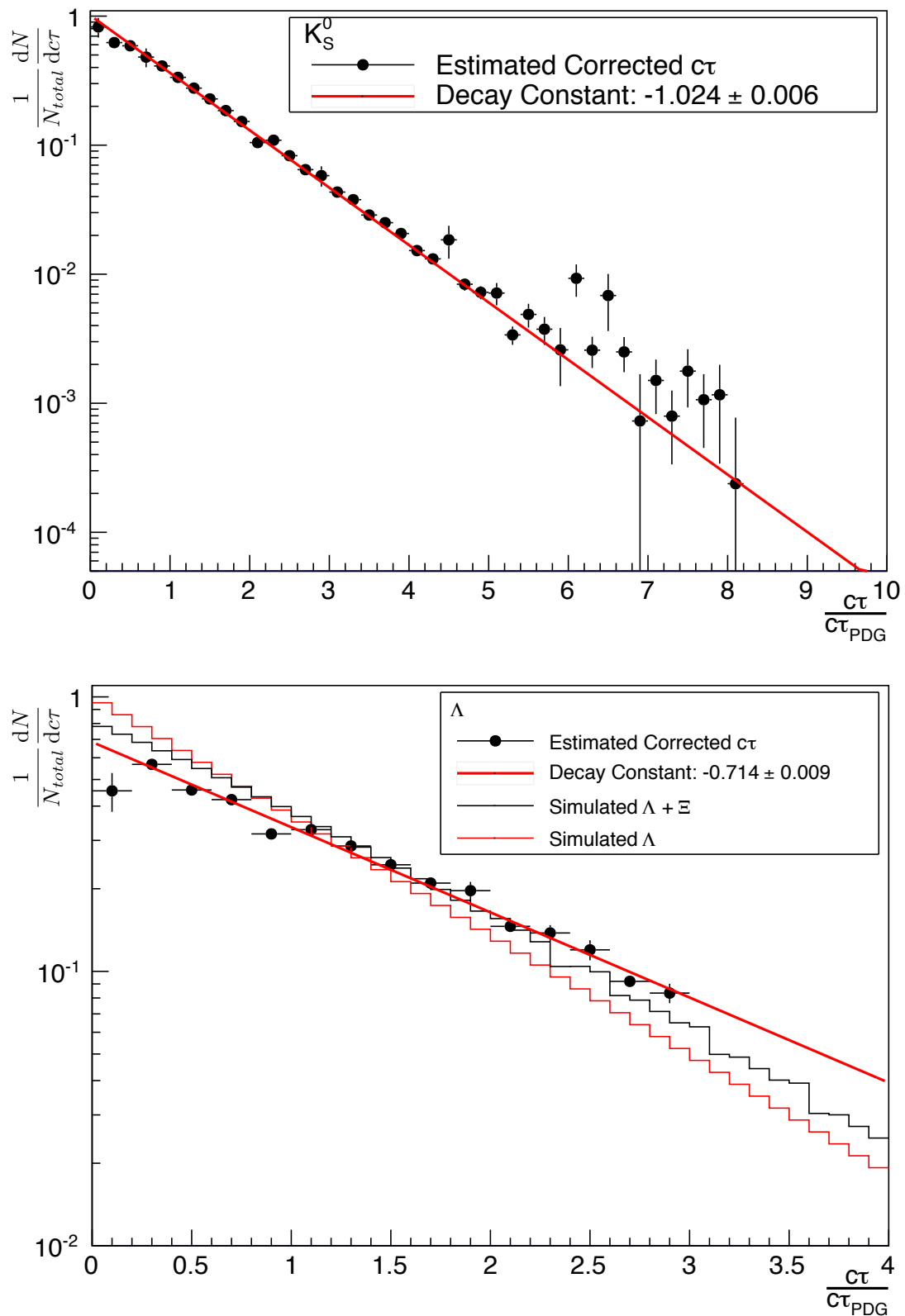
Figure 4.24: Corrected $c\tau$ Distribution for K_S^0 or Λ in $\sqrt{s} = 2.76$ TeV pp collisions - An estimate of the corrected $c\tau$ distribution for K_S^0 (top) or Λ (bottom). The red line is an exponential fit to the data points. Λ is not feeddown corrected, but does show simulations for a pure Λ distribution and a feeddown contaminated Λ distribution.

the ideal distribution (Equation 4.6),

$$\frac{c\tau_{\mathrm{associated}}}{c\tau_{\mathrm{observed}}} = \frac{c\tau_{\mathrm{generated}}}{c\tau_{\mathrm{corrected}}} = \frac{N_{generated}e^{-\lambda\frac{c\tau}{c\tau_0}}}{N_{corrected}e^{-\lambda\frac{c\tau}{c\tau_0}}}. \tag{4.10}$$

Bringing Equations 4.8 and 4.10 together:

$$\frac{r_{\mathrm{associated}}}{r_{\mathrm{observed}}} = K, \tag{4.11}$$

where K is an arbitrary constant. When this was actually plotted, as in Figure 4.25, it was observed that for r < 5 cm, there was a deficit of K_{S}^0 observed in data when compared to Monte Carlo. A similar effect was seen for Λ, although it was less clear cut due to the presence of feeddown. Several studies were undertaken to diagnose this issue, and it appears likely that it is due to a slight discrepancy in the Monte Carlo description of the ITS, possibly the quantity of false clusters. When the V0 selection is limited to those with just 'TPC-only' tracks, the ratio becomes flat, supporting this hypothesis. Unfortunately, this also drastically reduces the available statistics, and it would require the data reconstruction to be entirely rerun to exclude the ITS from the V0 finder. Thus, it was decided instead to exclude V0s with decay length less than 5 cm.
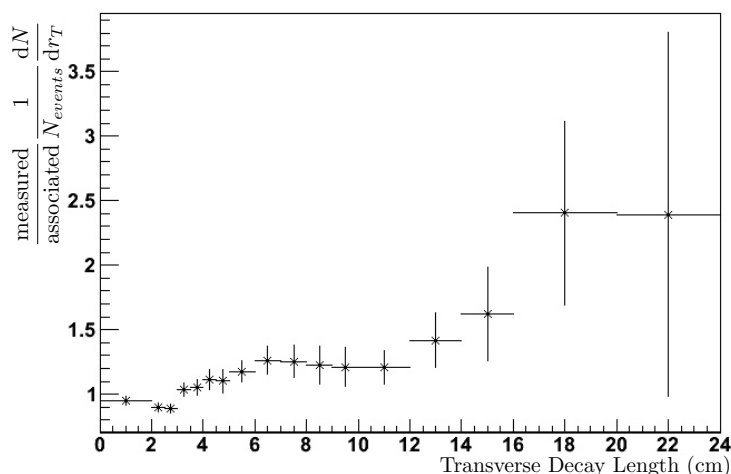
Figure 4.25: Ratio of Measured to Associated Decay Lengths - Ratio of measured to associated transverse decay lengths for K_{S}^0 in 0-5% centrality Pb–Pb collisions for $0.3 <$ $p_{\mathrm{T}} < 0.6$ GeV/c. Excess at higher p_{T} due to contamination from secondaries in material. Deficit for $p_{\mathrm{T}} < 5$ GeV/c less well understood.

	Pb–Pb	pp $\sqrt{s}$ = 2.76 TeV	pp $\sqrt{s}$ = 2.76 TeV
Λ	$0.6 < p_{\mathrm{T}} < 12$ GeV/c	$0.6 < p_{\mathrm{T}} < 8$ GeV/c	$0.6 < p_{\mathrm{T}} < 12$ GeV/c
K$_{\mathrm{S}}^0$	$0.2 < p_{\mathrm{T}} < 12$ GeV/c	$0.2 < p_{\mathrm{T}} < 8$ GeV/c	$0.2 < p_{\mathrm{T}} < 12$ GeV/c

Table 4.2: p_{T} range for different collision systems and particles.

The cut on lifetime, set at 3 times the PDG value for the lifetime $(3c\tau_{PDG})$, can then overlap with this cut. Using Equation 4.8, the 5 cm cut equates to removing all Λ which decay before 1 lifetime has passed at 0.6 GeV/c. However, for K$_{\mathrm{S}}^0$ at the same p_{T}, K$_{\mathrm{S}}^0$ with a measured lifetime less than 1.5 $c\tau_{PDG}$ are removed, and by 0.3 GeV/c all K$_{\mathrm{S}}^0$ are excluded. As the background due to secondaries is reasonably well controlled for K$_{\mathrm{S}}^0$, the $3c\tau_{PDG}$ cut was loosened to $4c\tau_{PDG}$, and applied only for r > 12 cm for K$_{\mathrm{S}}^0$ candidates. With these changes the statistics allowed a good fit of the invariant mass peak down to 0.4 GeV/c for K$_{\mathrm{S}}^0$. It is possible to fit the K$_{\mathrm{S}}^0$ spectra down to 0.2 GeV/c, and these results are included for completeness, but these points do have much higher levels of statistical and systematic errors.

For Λ, the limit was set at 0.6 GeV/c. As described above, the combination of decay length and lifetime cuts in this region are tight, but the statistics are sufficient to fit the invariant mass peak. However, at lower p_{T} the shape of this peak was seen to change, developing a shoulder on the low mass side. It was not possible to reach an understanding of this phenomena, which was not reproduced in the Monte-Carlo samples or in pp collisions, and so it was decided to exclude this p_{T} region.

The final p_{T} ranges used are described in Table 4.2. The fitted mass peaks used to generate these spectra are contained in Appendix B.

4.11 Normalisation to N$_{events}$

For comparison between different data samples, as well as to other experiments and theoretical predictions, it is conventional to normalise the p_{T} spectra to the number of events studied. By convention, this is the number of inelastic collisions in the data sample.

The spectra should give us the number of Λ and K^0_S produced per collision, and so the normalised signal measured is

$$\frac{S_{inelastic}}{N_{inelastic}}, \tag{4.12}$$

where $S_{inelastic}$ is the signal contained in all inelastic collisions recorded, and $N_{inelastic}$ is the number of inelastic collisions recorded. However, the events recorded in the detector are filtered by a trigger, which is not necessarily 100% efficient, and to reliably reconstruct the V0s, a further restriction is applied to collisions with a well defined vertex within 10 cm along the beampipe of the nominal centre (as described in Section 3.6). The efficiency of the trigger, $C_{\frac{inelastic}{triggered}}$, is measured by ALICE [150], and the Monte Carlo efficiency, ϵ, can be used to correct for the number of events outside the 10 cm range. The reproduction of the primary vertex distribution in the z direction is good to better than 1%, and so this method seems reliable. Symbolically, the normalisation procedure may be written:

$$\frac{S_{inelastic}}{N_{inelastic}} = \frac{C_{\frac{inelastic}{triggered}}}{N_{triggered}} \frac{S_{observed}}{\epsilon}. \tag{4.13}$$

This approach works well for pp collisions. The trigger efficiency has been measured [150], the number of triggered events, $N_{triggered}$, is recorded, and both $S_{observed}$ and ϵ are calculated in this analysis.

Unfortunately, in Pb–Pb events, the picture is slightly more complicated. The centrality is only calculated for events with a well defined vertex within 10 cm of the centre of the beampipe. Thus, the number of triggered events is not recorded within any given centrality bin. This is the case for both data and Monte Carlo, and so the efficiency does not correct back to the number of triggered events, merely those within the 10 cm vertex cut. However, as there are so many tracks in a Pb–Pb collision for all the centralities under consideration, the number of triggered events $N_{triggered}$ is equal to the number of events with a good vertex N_{VTX} to within 0.01%. Assuming that the yield per event

within the 10 cm is the same as the yield outside the cut, it is possible to then say

$$\frac{S_{observed}}{\epsilon N_{10cm}} = \frac{S_{10cm}}{N_{10cm}} = \frac{S_{VTX}}{N_{VTX}} = \frac{S_{triggered}}{N_{triggered}} = \frac{S_{inelastic}}{N_{inelastic}}. \tag{4.14}$$

In detail, this is first using the efficiency to correct the signal observed to the signal passing the 10cm vertex cut. The signal observed per bin within the 10cm cut is then the same as the signal per event with a good vertex, and as the vertexing and trigger efficiency are very close to 100% for Pb–Pb events this is then equal to the signal per event for all inelastic collisions.

4.12 Systematic Errors

The fractional statistical errors obtained through this analysis are shown in Figure 4.26, for K_S^0 at the top and Λ underneath. In the intermediate p_T region, essential for studying the baryon anomaly, the statistical errors are generally below 5%, while at high and low p_T the errors rise towards the cutoff. It can be seen that the errors for pp events are significantly higher; there are roughly 100 times more Λ and K_S^0 in Pb–Pb events than in pp events, causing the statistical errors to be significantly higher in pp collisions.

Having established the statistical errors, it is necessary also to look at sources of systematic errors. This was not just a linear process; certain sources of systematic error were initially large, and were reduced by changes to the analysis, often increasing the statistical error slightly. Examples of this would be the fitting of the K_S^0, which was improved by introducing the cut on the Armenteros-Podolanski diagram, and removing the cut on the ratio of crossed rows to findable clusters in the TPC.

Several sources of systematic error were considered, as detailed below. Where an error was found to be 1% or less it was considered negligible and so not included, as this is well below the level of statistical error.
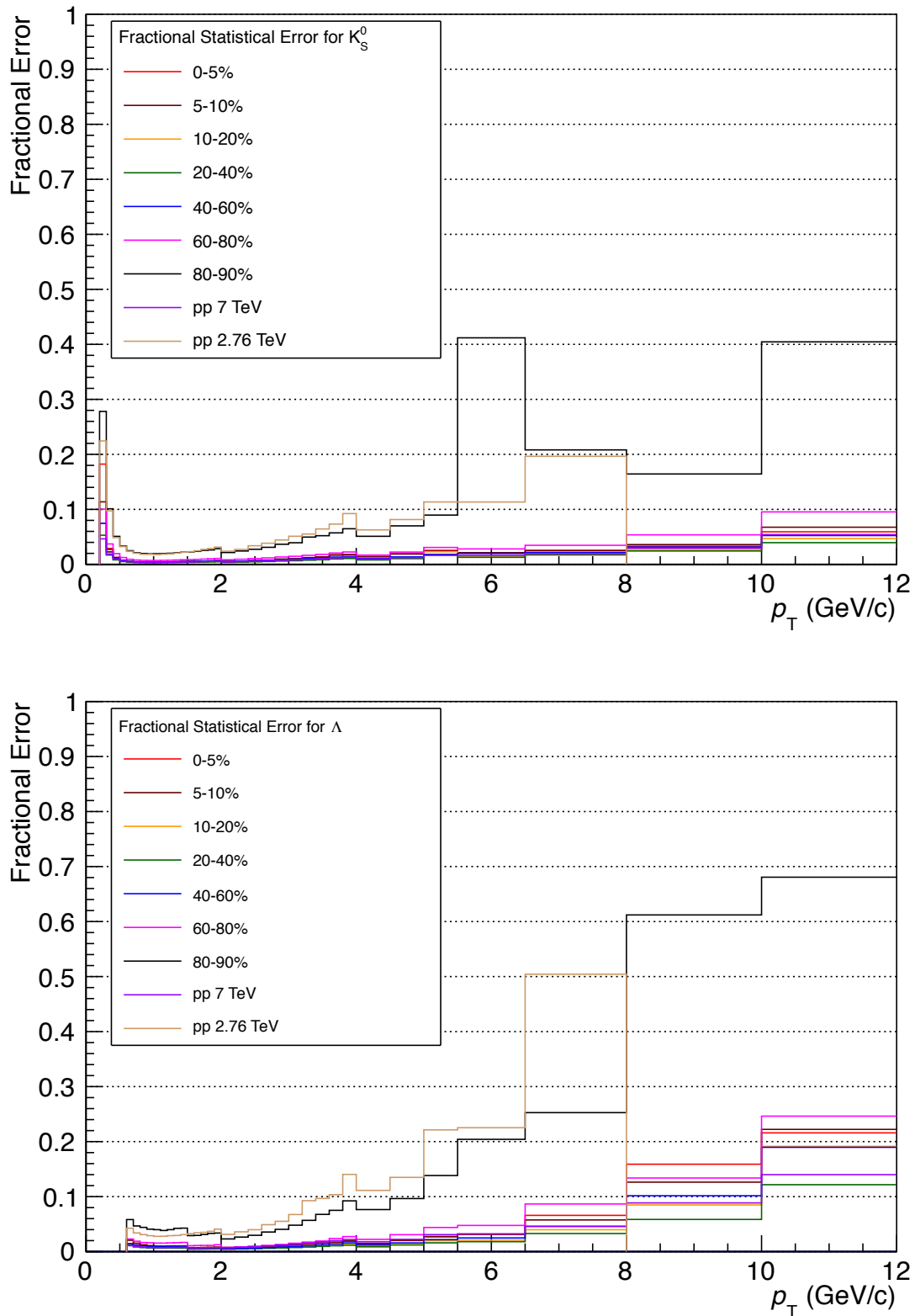
Figure 4.26: Fractional Statistical Errors on Λ and K_S^0 Spectra. - The statistical uncertainties of the corrected K_S^0 (top) and Λ (bottom) spectra, expressed as a fraction of the corrected spectra. Colours indicate different centralities and colliding systems.

4.12.1 Cut Systematics

One of the largest sources of systematic error considered was that due to imperfect Monte Carlo reproduction of the variables cut upon. As such, the corrected yield becomes dependant on exactly where the cut is applied. In order to evaluate the strength of this effect, it was decided to vary each cut such that the uncorrected yield of V0s changed by 10%, and measure the change in corrected yield. An example of these changes for different cuts is shown in Figure 4.27.
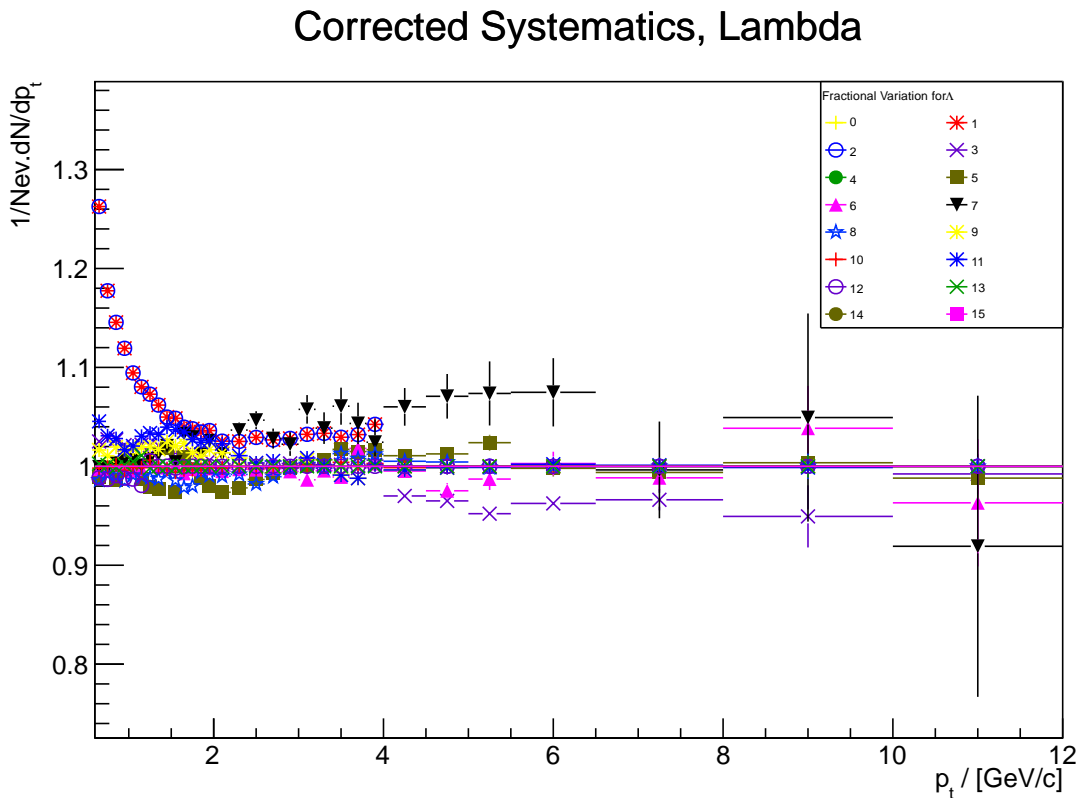
Figure 4.27: Cut Systematics for $\sqrt{s} = 7$ TeV pp - Variation in corrected yield for different cut combinations. See Table 4.3 for legend key.

The systematic error due to cut variation was then taken as the largest variation in each p_T bin. There was one exception which was the Cosine of Pointing Angle cut for the pp collisions. This, when loosened, strongly changed the corrected spectra by as much as 24% at the lowest p_T. Several efforts were made to understand this; as there is very little background in these bins, it does appear to be strongly changing the yield of true Λ and K_S^0 in a way not reproduced in the Monte Carlo simulations. An abundance of

N	$\cos(\text{PA}) <$	$N_{\text{clusters}} >$	$\text{DCA}_{\text{PV}} >$	$c\tau_{PDG} <$	$\Delta\frac{\text{d}E}{\text{d}x}(\text{proton}) <$	$\frac{p_{\text{T}}^{\text{ARM}}}{|\alpha|} >$
0	0.998, 0.9	70	0.1	3	3	0.2
1	0.9	70	0.1	3	3	0.2
2	OFF	70	0.1	3	3	0.2
3	0.996	70	0.1	3	3	0.2
4	0.998, 0.9	OFF	0.1	3	3	0.2
5	0.998, 0.9	115	0.1	3	3	0.2
6	0.998, 0.9	70	OFF	3	3	0.2
7	0.998, 0.9	70	0.3	3	3	0.2
8	0.998, 0.9	70	0.1	2	3	0.2
9	0.998, 0.9	70	0.1	4	3	0.2
10	0.998, 0.9	70	0.1	2.9	3	0.2
11	0.998, 0.9	70	0.1	OFF	3	0.2
12	0.998, 0.9	70	0.1	3	2	0.2
13	0.998, 0.9	70	0.1	3	4	0.2
14	0.998, 0.9	70	0.1	3	3	-999
15	0.998, 0.9	70	0.1	3	3	0.3

Table 4.3: Description of different cut variations used to calculate systematics for $\sqrt{s} = 2.76$ TeV pp collisions. Variations shown for Λ in Figure 4.27.

secondaries in this region could explain this, but crude estimations based on how Monte Carlo predicts the levels of secondaries elsewhere do not seem to support this idea. Were there more time available, it would be desirable to solve this problem, but as it is, the variation due to the Cosine of Pointing Angle is considered separately for pp events, and added in quadrature to the systematic variation associated with the other cuts.

4.12.2 Fitting Systematics

The choices made in fitting the invariant mass peaks can affect the final yield; for instance the σ used to define the peak width, and the order of the polynomial function used to fit the background. The quality of the fit is, to some extent, incorporated into the statistical error as that includes the errors on the fit parameters, but that does not account for errors due to, for instance, fitting the tails of the signal as if they were background.

The systematic error here was split into two categories. Firstly, there is the choice of peak width which dictates how much signal will be treated as though it were background.

Secondly, there is 'unknown' systematic error, which is a rough estimate of how accurate the fitting technique generally is.

The errors were calculated by adjusting by hand levels of signal and background in Monte Carlo until the invariant mass distributions roughly reproduced data. This was then passed through the fitting routine, and the results compared to the true signal. The final choice of peak width was made at this point to minimise the systematics, 5σ for K_S^0 and $3.5\sigma + 2\text{MeV}/c^2$ for Λ. This unusual choice for Λ was made because at low p_T the value of sigma was similar to the binning used for the invariant mass histogram, and increased slowly with p_T (see Figure 4.16). Thus, while sigma gradually increased with p_T, the actual area integrated increased in steps, leading to an irregular pattern in the yield. At high p_T, a choice of, say, 5σ would take the mass peak over the kinematic limit, and so it proved more convenient to have a tight peak widened by 4 bins.

The discrepancy caused by considering outlying V0s as background rather than signal should be well reproduced in Monte Carlo, and so the p_T dependance measured in Monte Carlo was applied to the systematic errors for the data. The unknown part of the systematics, however, was dependant on the precise background shape, which was not perfectly reproduced. Thus, the maximal discrepancy between fitted and true yields was taken as the systematic error for each particle. The two systematic errors were added in quadrature to give a total systematic error associated with the fitting routine. No variation was noted with centrality, and so all these systematic errors were calculated in the 0-90% centrality bin. The errors were, however, recalculated for pp events.

The final fitting systematics are shown in Figure 4.28. It can be seen that the systematic error associated with the fitting routine has been kept below 8% for Λ, and below 3% for K_S^0 where the background is better controlled.

4.12.3   Feeddown Systematics

As mentioned in Section 4.8, the systematic error on the feeddown subtraction is defined by the variation of the feeddown fraction; with centrality (when centralities are not clearly
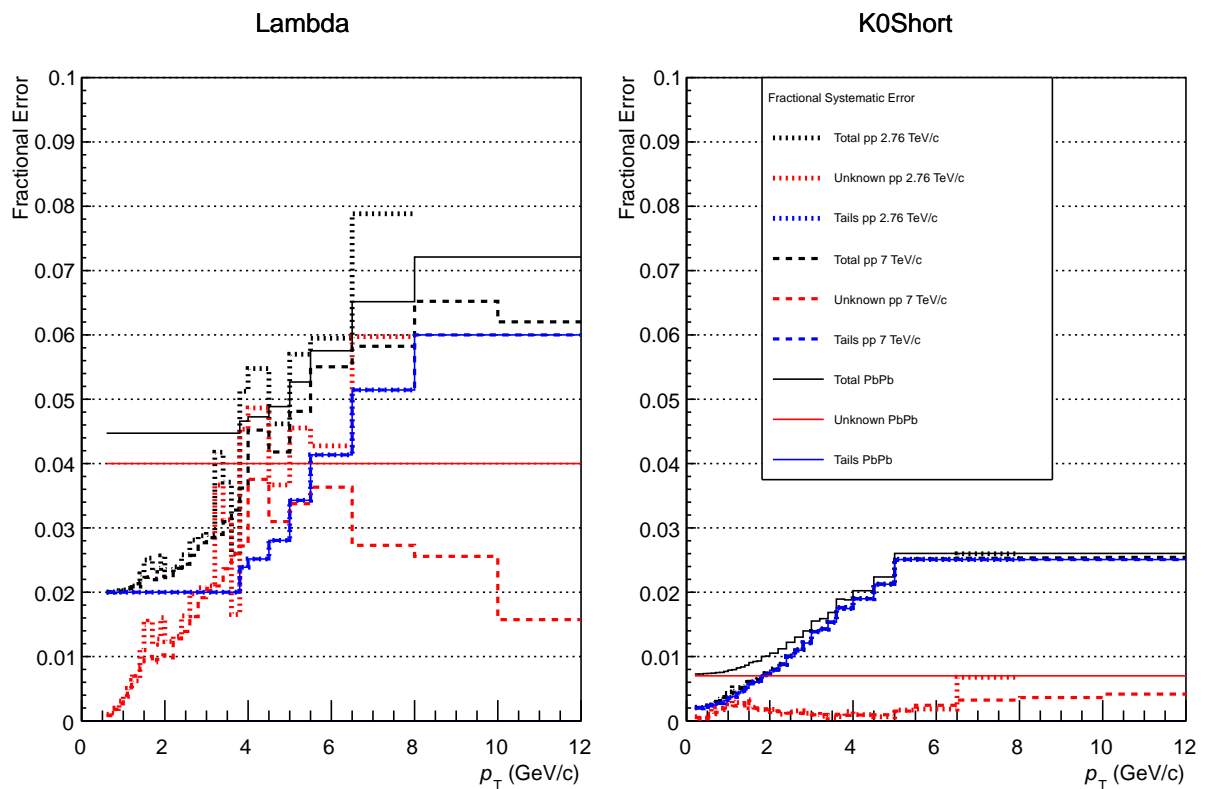
Figure 4.28: Fitting Systematics - Fractional errors associated with the fitting routine; for Λ on the left and K_S^0 on the right. 'Tails' indicates that part of the error associated with signal misidentified as background, and 'Unknown' all other. The 'Total' is the quadratic sum of the two.

separated), with different fit functions and by the magnitude of the statistical error. The overall error is large when compared to the feeddown fraction (variation of around 4 percentage points on a fraction of roughly 18%), and could potentially be reduced when further statistics are available to extend the p_{T} range of the Ξ^- spectra.

4.12.4   Other Systematics

The effect of the cut in the Armenteros-Podolanski diagram is considered separately, as there were concerns that it might introduce misleading background shapes. Applying the cut affected the corrected yield by 1%, so, to be conservative, this was considered as a separate source of systematic error.

The effect of the cut on TPC $\mathrm{d}E/\mathrm{d}x$ is not corrected for by Monte Carlo, but instead by treating the TPC response as a perfect gaussian distribution. This is not quite perfect, and variations on the cut from 2σ to 4σ can change the corrected yield by up to 2%. This is taken as a separate source of systematic error.

The breakdown of the different sources of systematic error is shown in Figure 4.29 for pp collisions at $\sqrt{s} = 7$ TeV, and the total systematic error is shown in Figure 4.30 for all collision systems. As previously mentioned, the problems with the Cosine of Pointing Angle cut in pp collisions leads to the systematic error reaching the 15-30% mark at low p_{T}, but overall the errors are kept below 15%, and below 8% for Pb–Pb collisions.

4.12.5   Systematic Errors on Ratios

Where ratios of spectra are taken, such as Λ to $\mathrm{K}^0_{\mathrm{S}}$ or Pb–Pb to pp, the systematic errors are not added in quadrature, as there will be some correlation between them. The variation on ratios due to altering the cuts is around 50% that of the individual spectra for the $\Lambda/\mathrm{K}^0_{\mathrm{S}}$ ratio, and this is taken as a benchmark for other cases where the errors should be shared by numerator and denominator.
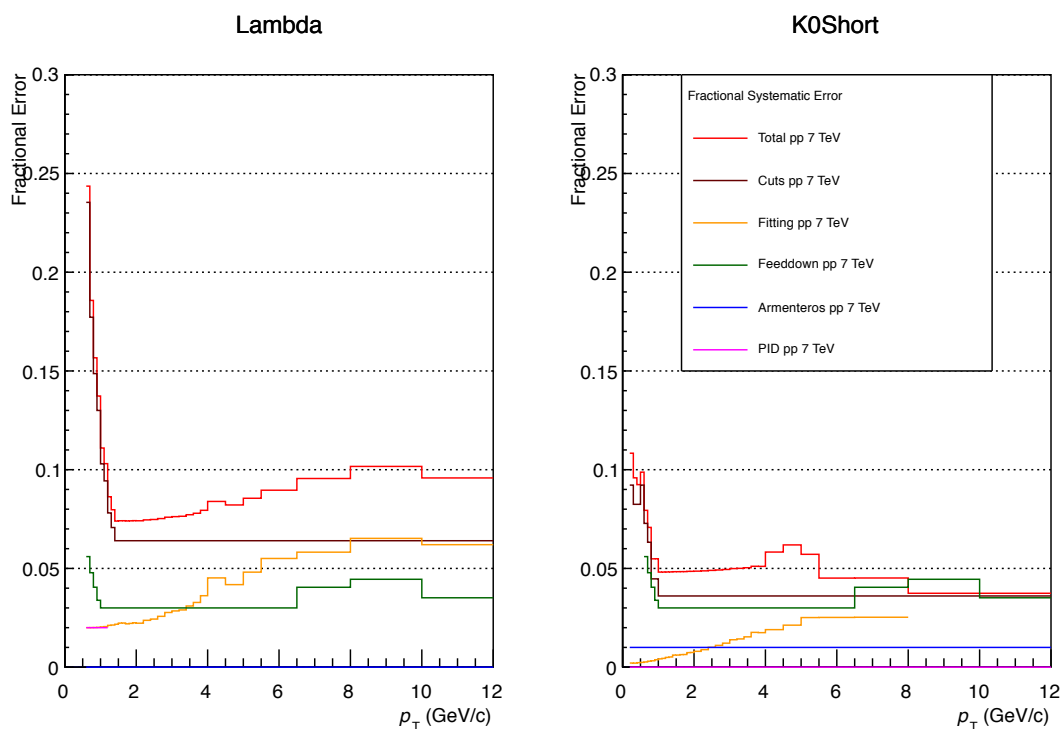
Figure 4.29: Systematic Errors for pp **Collisions at** $\sqrt{s} = 7$ TeV - Breakdown of sources of systematic error for pp collisions at $\sqrt{s} = 7$ TeV.
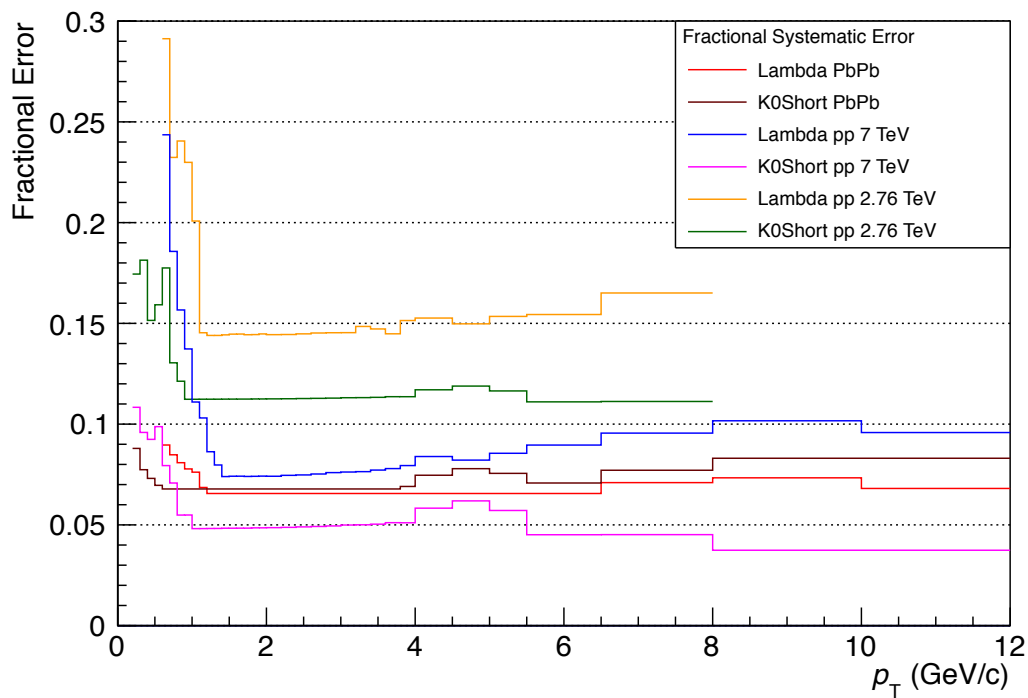
Figure 4.30: Systematic Errors - Total systematic errors for all particles and collision systems.

111

5

Results

The analytical steps taken to calculate the spectra of Λ and K_S^0 in Pb–Pb and pp collisions with ALICE at the LHC have been discussed. Cross checks of the lifetime measurement, and also comparisons to the measured charged kaon spectra [159, 160], give confidence that the spectra are correct within the given statistical and systematic errors.

In this chapter, the results of this analysis will be discussed. The spectra will be directly compared to the theoretical models introduced in Chapter 2, which highlights areas of agreement and disagreement between the models and the data. It is more interesting to investigate ratios of the spectra, which remove some common areas of uncertainty, and allow us to isolate the physics of interest. The p_T-integrated yield will also be evaluated, which allows investigation into the thermal model of hadron production.

5.1 Spectra

The fully corrected spectra of Λ and K_S^0 are shown in Figures 5.1 and 5.2 respectively. The plots are shown both on linear and logarithmic scales, and also with and without a scaling factor which more clearly separates the spectra (but does not change the centrality ordering). The statistical and systematic errors can be seen to be well under control, which allows a clear centrality ordering to be resolved. The yield is higher in more central Pb–Pb events, as expected from considerations of the Glauber Model. The very lowest p_T point
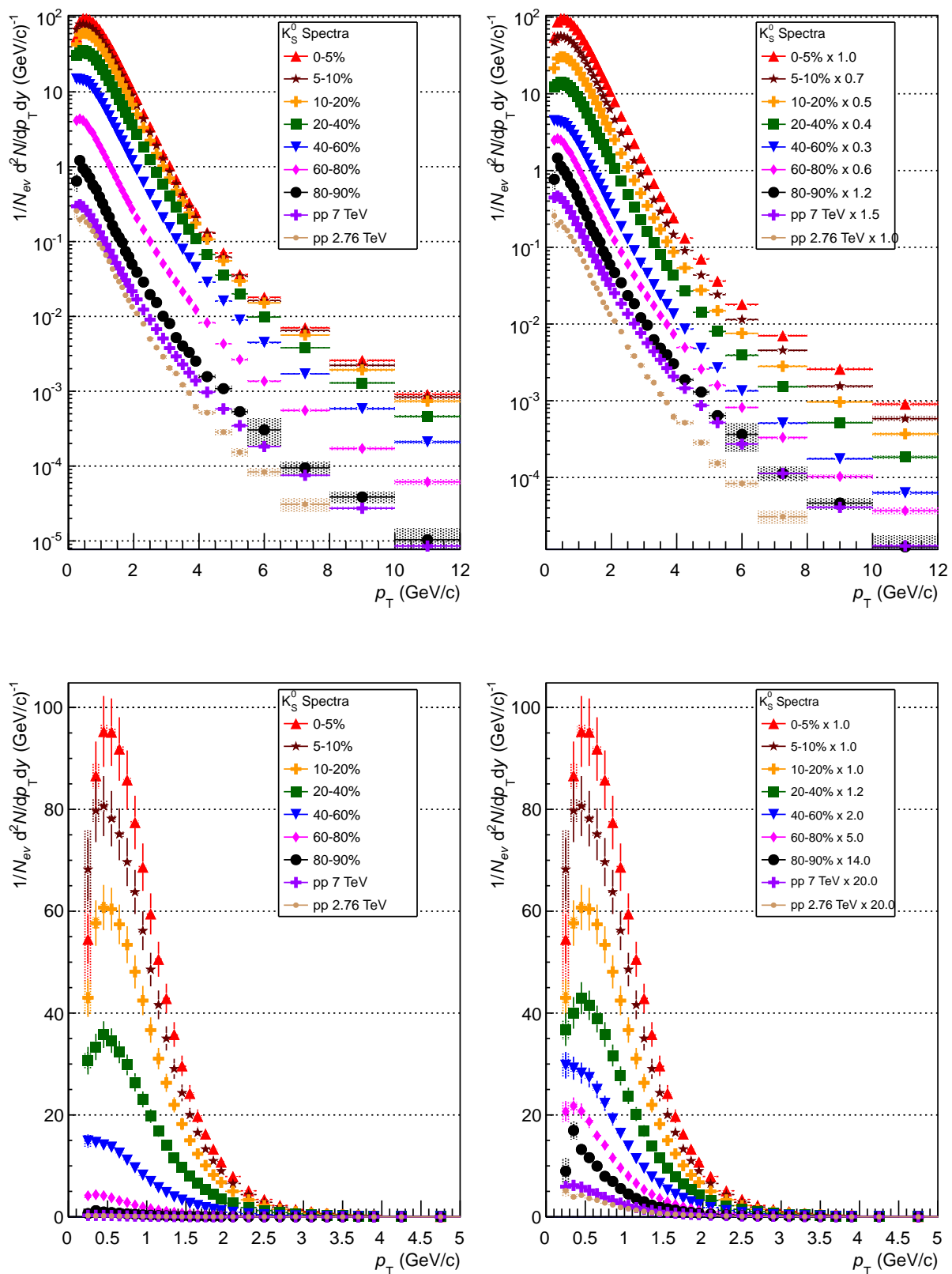
Figure 5.1: K_S^0 **Spectra** - The fully corrected spectra of K_S^0, shown in log scale (top) and linear scale (bottom). The right hand plots have a scaling factor applied, to more clearly separate the spectra while leaving the centrality ordering unchanged.
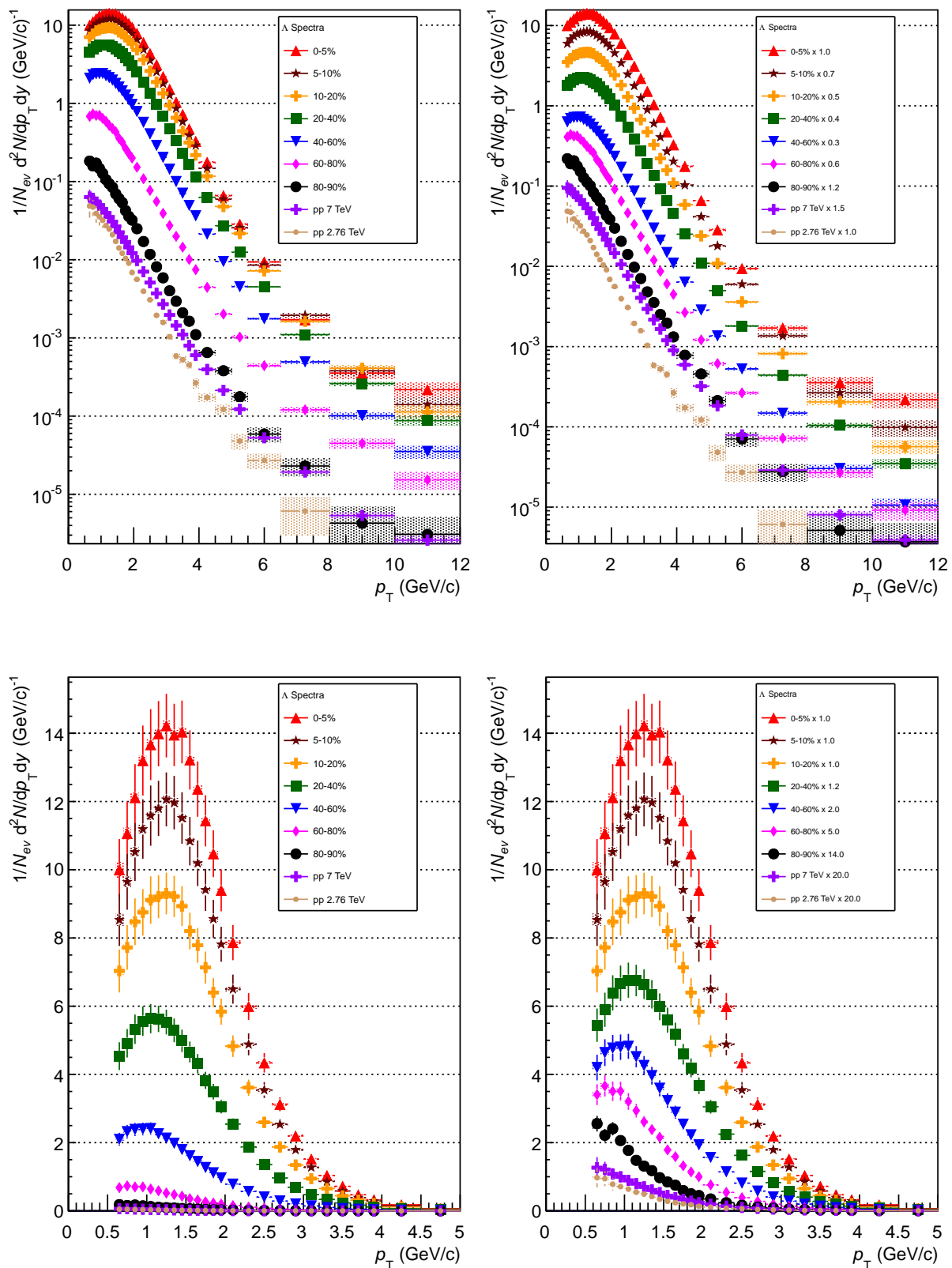
Figure 5.2: Λ **Spectra** - The fully corrected spectra of Λ, shown in log scale (top) and linear scale (bottom). The right hand plots have a scaling factor applied, to more clearly separate the spectra while leaving the centrality ordering unchanged.

of the K_S^0 does not always hold to the centrality ordering as it has large statistical errors from the tight decay length cut. However, this point helps to resolve the turning point of the spectra, particularly for more peripheral samples and also for the pp collisions, and so is included.

The bulk of the particles are at lower p_T, with more than 50% typically falling below 1 GeV/c for K_S^0 and 1.3 GeV/c for Λ. Only around 5% of K_S^0 fall above 4 GeV/c, and around 12% of Λ. Thus, in the intermediate region of p_T between 2-4 GeV/c, of interest for studies of the baryon anomaly, there is approximately 10% of the total yield of K_S^0 and around 30% of the total yield of Λ.

It is possible to see the effect of increased energy between the $\sqrt{s} = 7$ TeV pp collisions, and the 2.76 TeV collisions; approaching higher p_T, the 7 TeV sample drops off more slowly, giving a harder p_T spectrum than the lower energy, as would be expected.

Distinguishing more subtle effects directly from observation of the spectra is more difficult. There does appear to be a change in behaviour between low and high p_T, with a point of inflection on the curves at around 4 GeV/c . This could indicate a change in behaviour from hydrodynamic to vacuum-like fragmentation, but is not clearly defined. It can also be seen that the peak of the curves moves to higher p_T as one moves from pp collisions to peripheral Pb–Pb and on to the most central Pb–Pb collisions. This could be indicative that the system is being pushed to a higher collective velocity for more central events.

5.2   Spectra Comparisons

Comparisons of the spectra to the theoretical models are shown in Figures 5.3 and 5.4. The Vish2+1 model reproduces the shape of the spectra at low p_T, but slightly overestimates the magnitude for both Λ and K_S^0. For p_T above 2 GeV/c , the measured spectra deviate strongly away from the theoretical prediction, indicating that particle production above this p_T is not dominated by hydrodynamics.
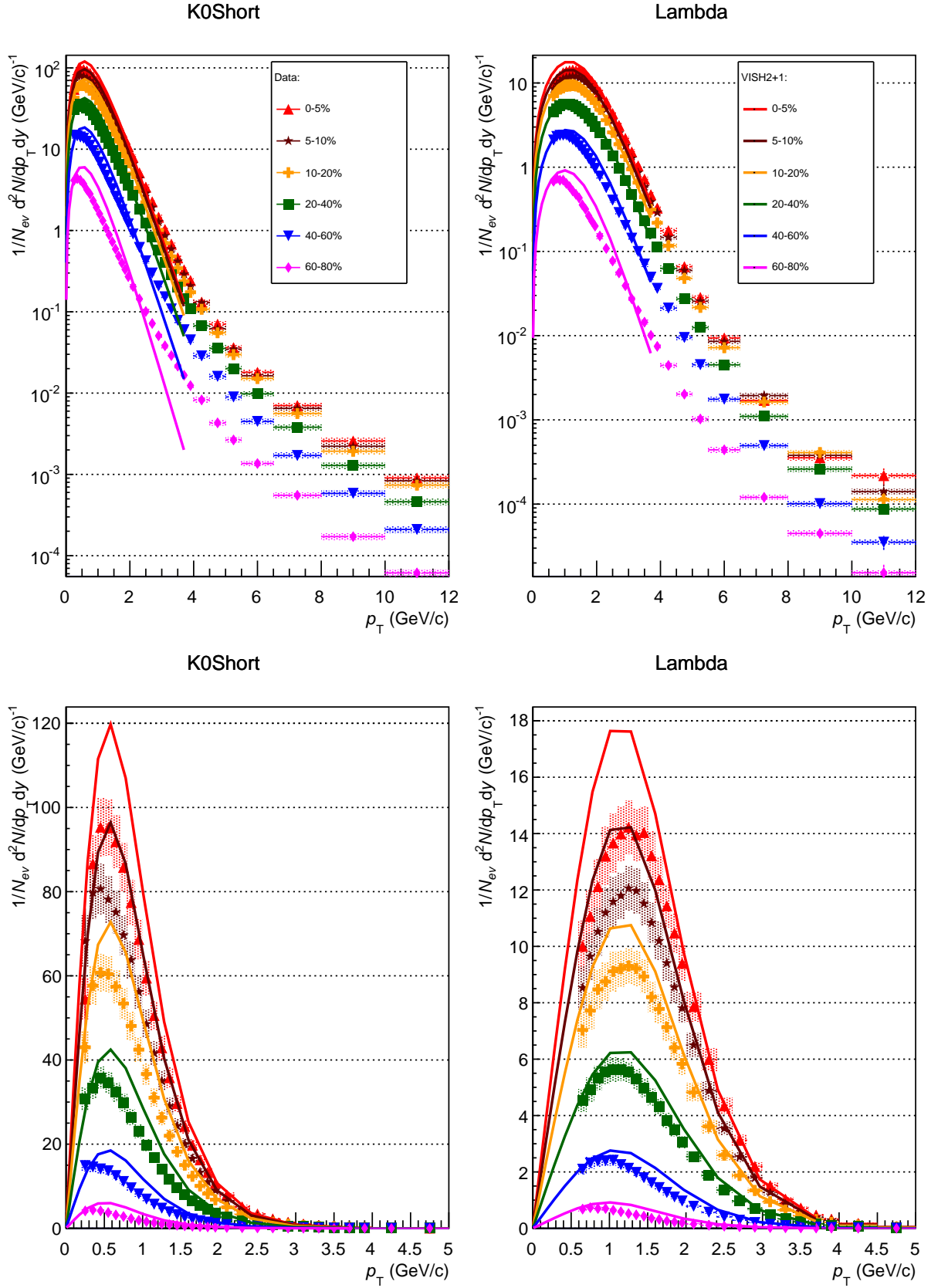
Figure 5.3: Λ **and** K_S^0 **Spectra Compared to Vish2+1 Model** - The fully corrected spectra of K_S^0 (left) and Λ (right), shown in log scale (top) and linear scale (bottom) compared to the Vish2+1 hydrodynamical model.
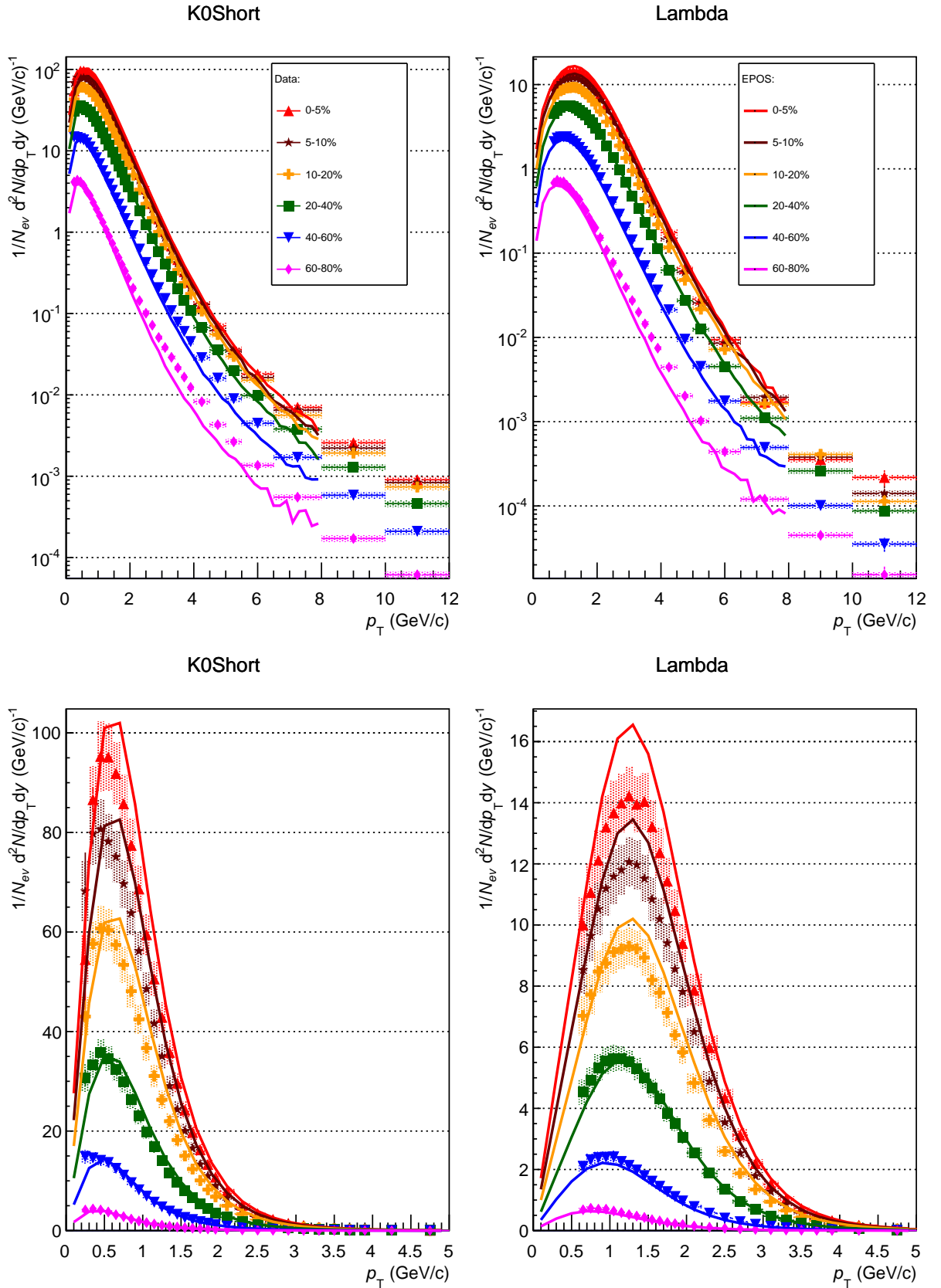
Figure 5.4: **Λ and K$_S^0$ Spectra Compared to EPOS 2.17v3 Model** - The fully corrected spectra of K$_S^0$ (left) and Λ (right), shown in log scale (top) and linear scale (bottom) compared to the EPOS model.

The EPOS model also describes the behaviour of the spectra at low p_T, with a slightly overestimated magnitude for Λ. Similar predictions to the hydrodynamical model are to be expected at low p_T, as EPOS behaves as a hydrodynamical model for low p_T. However, the strength of the model is in the reinteraction of harder particles with the fluid medium, reflected in the overall reproduction of the spectra up to $p_T = 8$ GeV/c .

5.3 Ratio
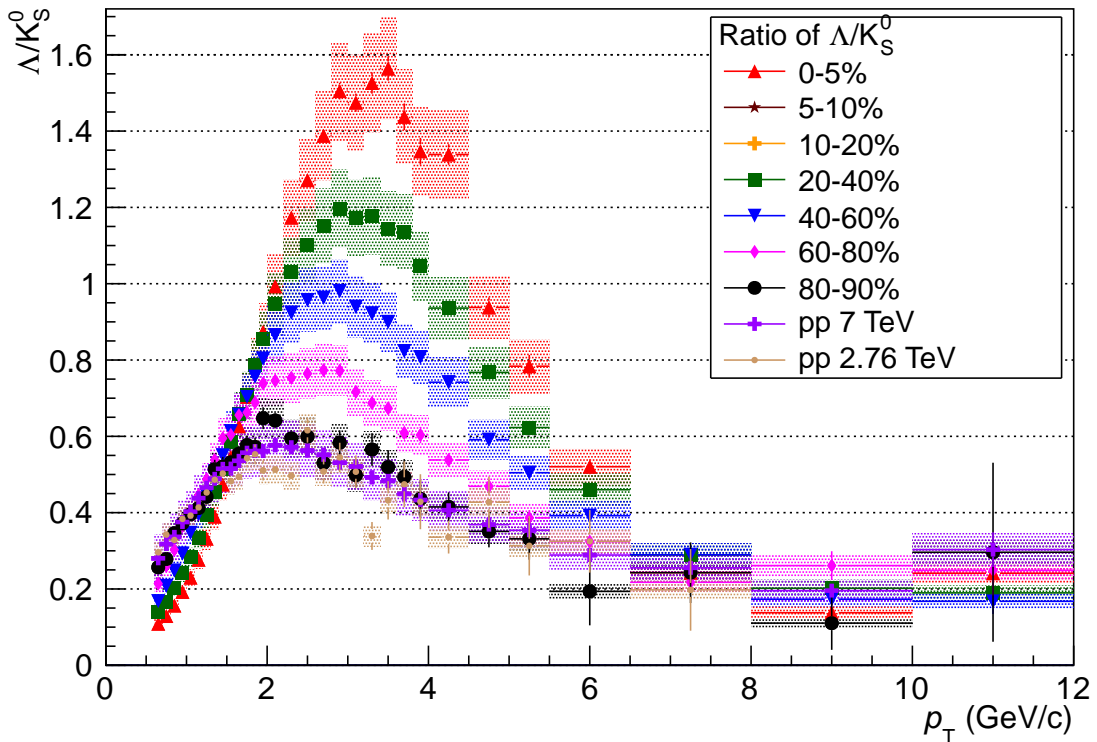
Figure 5.5: Λ/K_S^0 **Ratio** - The Λ/K_S^0 ratio for Pb–Pb and pp collisions. Only selected centralities shown for clarity.

In order to isolate the physics of interest, and particularly to analyse the baryon anomaly, it is instructive to study the ratio of the Λ to K_S^0 p_T spectra. By doing so, the differences between the particles can be highlighted, and more easily compared to other experiments and ratios of other particles where the production cross sections may be considerably lower.

The ratio as measured in this analysis is shown in Figure 5.5 for selected centralities and collision systems. It can be seen that the errors are well under control, giving well defined centrality ordering and clearly showing the shape of each curve.

The ratios for 80-90% centrality Pb–Pb collisions, $\sqrt{s} = 7$ TeV pp collisions and $\sqrt{s} = 2.76$ TeV collisions are all consistent. However, more central collisions show a pronounced increase in the ratio between 2 and 6 GeV/c, with the most central collisions peaking at almost 3 times the value of the most peripheral. All centralities are consistent above approximately 6 GeV/c.

The change in the ratio does not appear to be an energy dependant, as it remains unchanged between the two pp samples, but instead is related to the number of participant nucleons in the collision. Above $p_{\mathrm{T}} = 6$ GeV/c, it appears that relative particle production is vacuum-like for all centralities, and not affected by any medium created; suggesting that any jet quenching effects are not hadrochemistry dependant. Below this momentum, however, the strong enhancement of the ratio indicates a strong increase in Λ production relative to $\mathrm{K_S^0}$.

However, looking in more detail at the low p_{T} region of the ratio, reproduced in Figure 5.6, some evidence for a suppression of the ratio can be seen in this region. With all centralities overlaid, the overlapping systematic errors make it hard to make any conclusive statements. Despite this, by selecting only central and peripheral centralities, it can clearly be resolved that the pp and peripheral Pb–Pb events are once again consistent, with the more central events suppressed; and that the magnitude of the suppression increases for more central events. Recalling that the bulk of particles are contained within this low p_{T} region, this could suggest that the enhancement of the ratio at mid-p_{T} is due to a redistribution of particles from low to higher p_{T}. This possible explanation will be further discussed in Section 6.1.
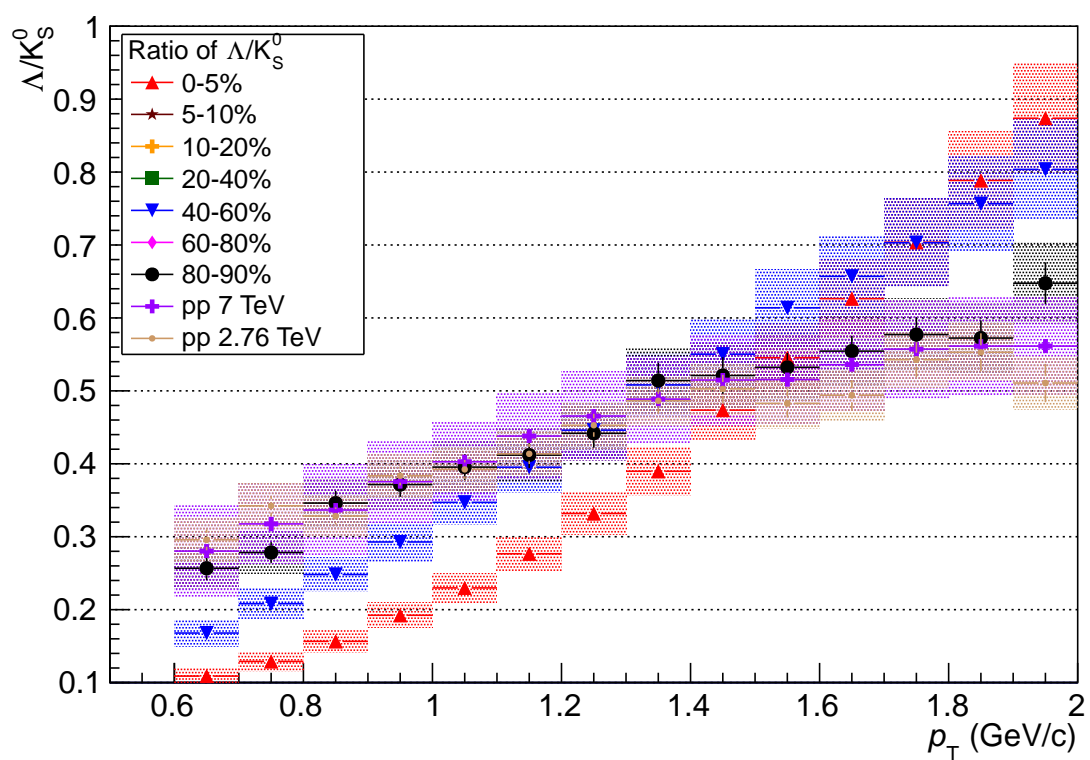
Figure 5.6: Λ/K_S^0 **Ratio at Low** p_T - The low p_T portion of the Λ/K_S^0 ratio for Pb–Pb and pp collisions. Only selected centralities shown for clarity.

5.4   Ratio Comparisons

5.4.1   Theoretical Comparisons

As with the spectra, it is useful to compare the Λ/K^0_S ratio to theoretical predictions. Figure 5.7 gives an overview of the theoretical predictions for the 0-5% centrality bin. In addition to the aforementioned VISH2+1 and EPOS models, this plot also shows a recombination model. This model, received in private communication from R. Fries and discussed in [60, 86], uses the concept of coalescence to allow formation of hadrons from partons nearby in phase space, as discussed in Section 2.5.
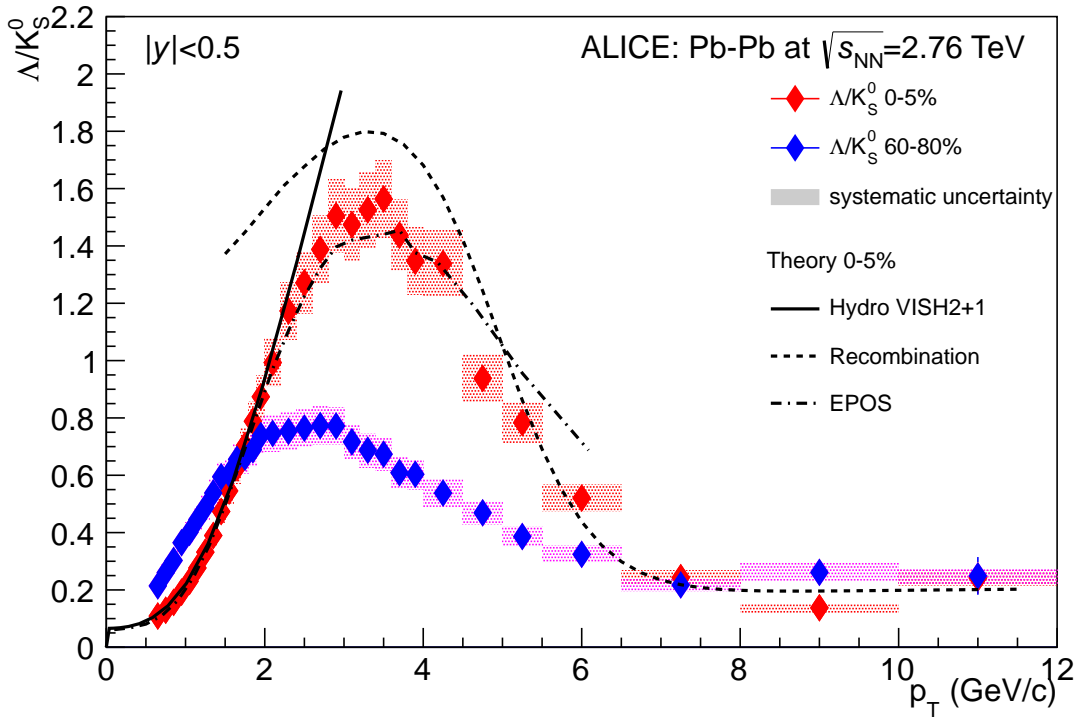
Figure 5.7: Λ/K^0_S **Ratio Compared with Theory** - The Λ/K^0_S ratio, as measured in 0-5% and 60-80% centrality bins, as compared to theoretical predictions for the 0-5% centrality.

From Figure 5.7, it can clearly be seen that the hydrodynamic picture gives a very good representation of the ratio's behaviour at low p_T, below 2 GeV/c. Above this point, however, the VISH2+1 curve appears to tend to infinity, rather than turning over as observed

in data. As hydrodynamic flow creates a collective velocity, this would be expected to translate to a higher momentum for Λ than for K_S^0, as the mass is correspondingly greater. Thus, the Λ/K_S^0 ratio is depleted at low p_T, but increasingly enhanced for higher p_T. However, within a pure hydrodynamical picture, there is no mechanism to return the particle production to vacuum levels, as seen in data.

The coalescence picture is very different. It instead predicts the behaviour of the turnover very well, but does not accurately predict the magnitude of peak of the ratio, or the low-p_T region. It does reproduce the behaviour of the system as it returns to vacuum-like production, indicating perhaps that it is the coalescence mechanism which is dominant over hydrodynamical flow as in the upper limits of the affected p_T range.

The interplay between these mechanisms is better represented with EPOS, which allows partons with higher momentum to completely escape the medium. Further, it allows interaction between medium-momenta partons and the medium, allowing a plausible prediction to be made for the Λ/K_S^0 ratio over the full momentum range. It reproduces the hydrodynamical behaviour at low p_T and accurately describes both the shape and magnitude of the ratio in the crossover region. It would be of interest to see the EPOS prediction continued to higher p_T, as it does appear to deviate slightly at its upper limit. However, as the EPOS model treats high p_T particle formation as vacuum formation, it is likely that it will be consistent with the measured data.

It is worth noting that the EPOS model shown here has been tuned to LHC data, to best represent the π, K and p results. While this should not directly affect the Λ/K_S^0 ratio, it is worth noting that the p/π ratio (shown in Figure 5.11) exhibits similar behaviour to that of Λ/K_S^0 and so has possibly influenced the prediction.

For the VISH2+1 and EPOS models, predictions are also available for other centralities. Figure 5.8 shows the evolution of the ratio with centrality for the VISH2+1 model. Immediately, problems can be seen with this prediction. There is little distinction between the centralities, and the ordering of centralities at higher p_T is different to the measured data. To some extent, this can be attributed to the lack of a turnover mechanism; in the
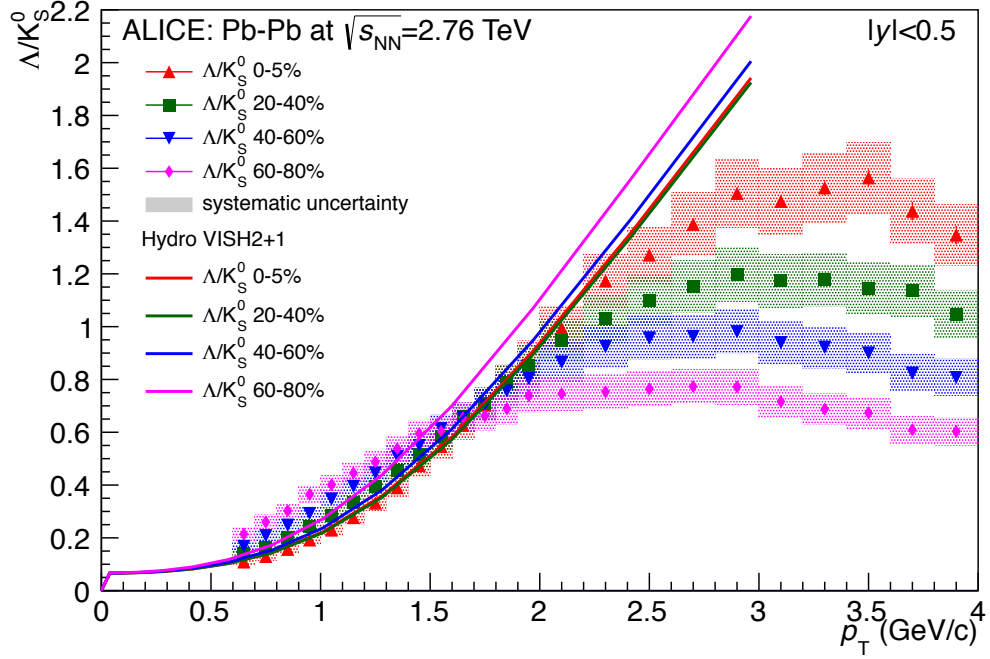
Figure 5.8: Λ/K_S^0 **Ratio Compared with Hydrodynamical Model** - The Λ/K_S^0 ratio for selected centralities, as compared to the predictions from the VISH2+1 model for matching centralities.

measured ratio the different centralities are less separated at low p_T, where the central hydrodynamic prediction is accurate, and without this mechanism it is reasonable to expect this pattern to continue to higher p_T. The data is however better separated in centrality than the prediction, even at low p_T and, further, the prediction shows no return to pp collision behaviour for the more peripheral events. A possible explanation for this could be that the hydrodynamic picture is inappropriate for the more peripheral collisions, or at least is less dominant.

The comparison to the EPOS model, shown in Figure 5.9 is helpful at this point. Recalling that at low p_T the EPOS model also reproduces viscous hydrodynamical behaviour, one would expect to see the same problems as observed in the VISH2+1 predictions. However, EPOS does include a turnover mechanism, and further incorporates a core-corona model. This model treats nucleon-nucleon collisions occurring on the edge of the system as independent events (corona), and only clustered collisions contribute to the medium
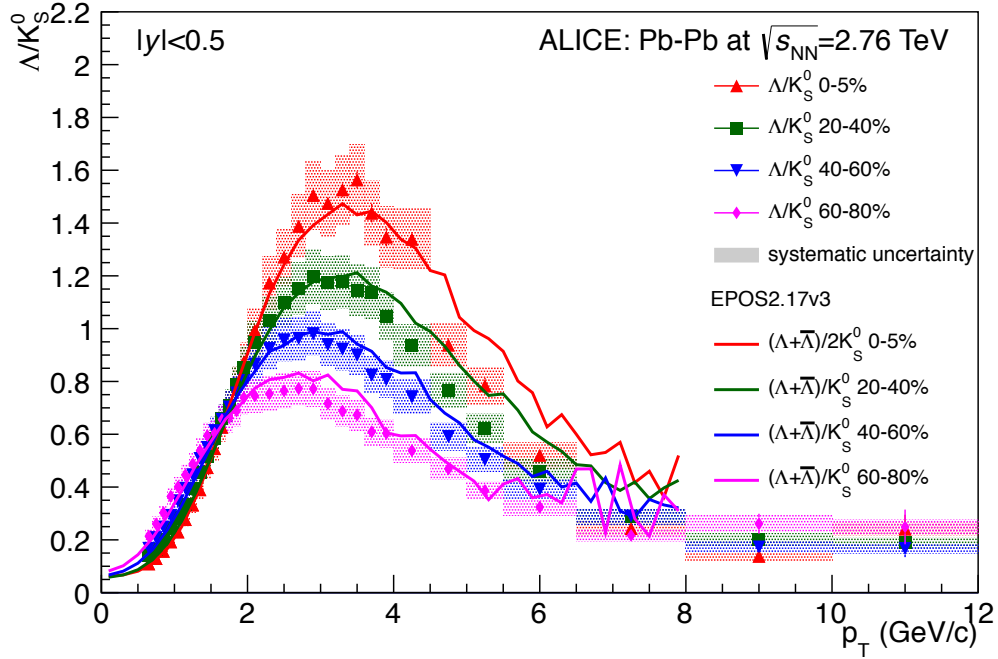
Figure 5.9: Λ/K_S^0 **Ratio Compared with the EPOS Model** - The Λ/K_S^0 ratio for selected centralities, as compared to the predictions from the EPOS model for matching centralities.

(core). This could have the effect of reducing the hydrodynamical behaviour in peripheral collisions, as the corona is proportionally larger compared to the core. Thus, at the lowest p_T, stronger separation of the different centralities is seen, and at mid-momentum the correct centrality ordering is maintained. Overall, the EPOS model does a very good job of reproducing the centrality dependance of the Λ/K_S^0 ratio.

This would suggest that, to first order, the mechanisms present in the EPOS model are responsible for the behaviour of the Λ/K_S^0 ratio. Hydrodynamics is important, most obviously so in the most central events, but its interplay with vacuum-like fragmentation via coalescence is also important. It also emphasises that a collective medium is not formed by the entirety of the colliding system: parton-parton collisions at the edge do not appear to contribute to the thermodynamic behaviour.

5.4.2 Experimental Comparisons

Direct comparisons of the spectra of identified particles between different experiments are difficult because of large underlying dependancies on collision energy and centrality. However, by taking the ratio of two particles, such as $\Lambda/\mathrm{K}_\mathrm{S}^0$, a comparison can be directly made of the differences in particle production between experiments, as many of the underlying dependancies cancel out.

Figure 5.10 shows the $\Lambda/\mathrm{K}_\mathrm{S}^0$ ratio as measured in this experiment alongside that measured in Au–Au collisions at $\sqrt{s_\mathrm{NN}} = 200$ GeV at STAR [161]. The STAR points have statistical and systematic error added in quadrature, and show both the $\Lambda/\mathrm{K}_\mathrm{S}^0$ and $\overline{\Lambda}/\mathrm{K}_\mathrm{S}^0$ ratio, due to the significant difference in these at RHIC energies. The anti baryon to baryon ratio at RHIC is approximately 0.8, while at the LHC it has been measured to be consistent with 1 [48, 49]. Taking this into account, the magnitude of the enhancement of the $\Lambda(\overline{\Lambda})/\mathrm{K}_\mathrm{S}^0$ ratio does not appear to change between the two collision systems and energies. The extent of the enhancement does seem to change slightly however; it begins at approximately $p_\mathrm{T} = 1.5$ GeV/c, and continues only to 5 GeV/c at RHIC energy. Recalling that predictions based on coalescence of neighbouring mini-jets suggested that the enhancement might continue to 10 - 20 GeV/c at LHC energies [121, 124] (see Section 2.5), no evidence for this theory is observed.

Overall, the comparison to STAR results confirm that the enhancement of the baryon to meson ratio is only weakly dependant on the collision energy, but instead appears to be a function only of the multiplicity of the collision.

It is also of interest to compare the $\Lambda/\mathrm{K}_\mathrm{S}^0$ ratio to a similar ratio measured in ALICE, the proton to pion ratio. One would expect the ratios to be broadly similar - as both the K_S^0 and the Λ contain a single (anti-) strange quark, and the proton and pion do not, any effects due to strangeness production could be expected to cancel out in the ratio, at least to first order. On the other hand, the relative masses are somewhat different; the mass of the Λ is around 2.25 times that of the K_S^0, while the proton is more than 6 times the mass of a pion, which could be expected to change the behaviour within the hydrodynamical
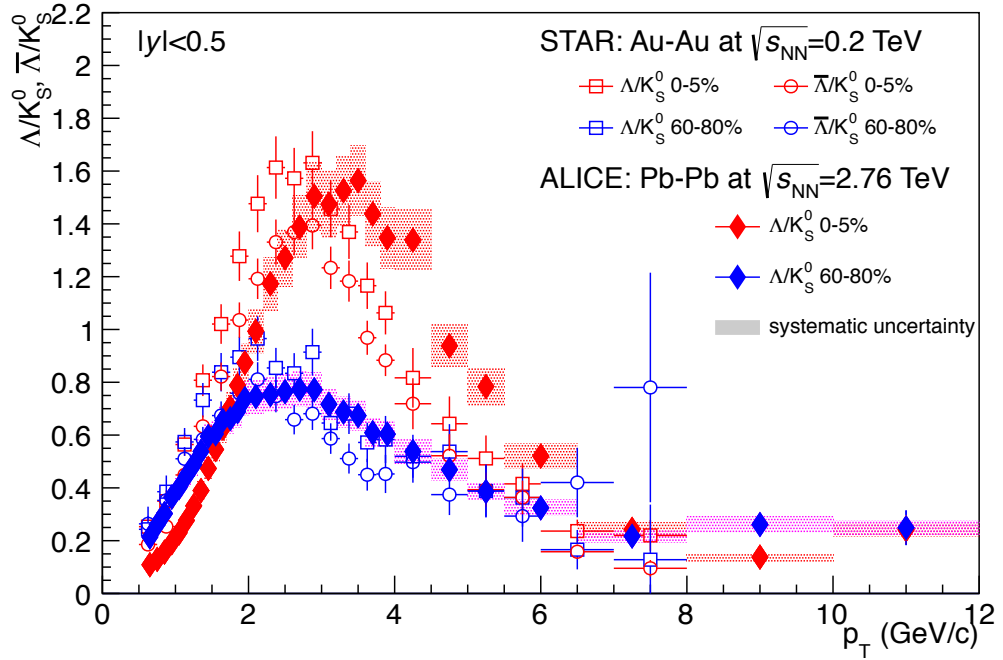
Figure 5.10: Λ/K_S^0 **Ratio Compared with STAR** - Λ/K_S^0 measured in this analysis compared with similar ratios measured at STAR [161].
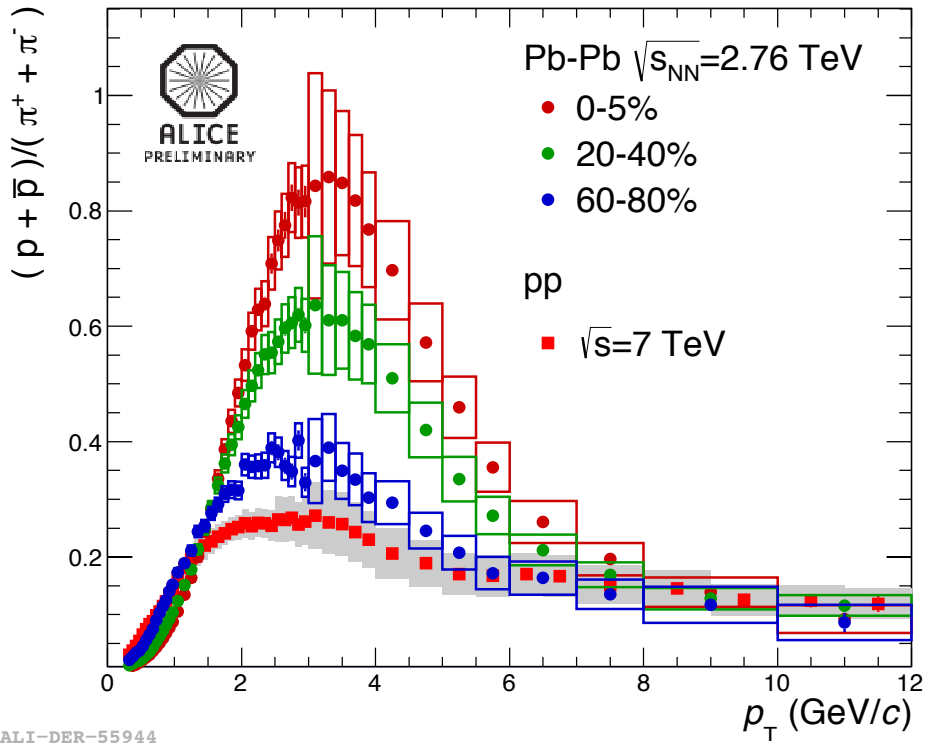
Figure 5.11: p/π **Ratio Measured by ALICE** - The ratio of protons and their antiparticles to charged pions, for selected centralities in Pb–Pb collisions, and pp collisions at $\sqrt{s}$ = 7 TeV[162].

picture.

The p/π ratio measured by ALICE is shown in Figure 5.11, derived from [162]. The overall behaviour is very similar; there is an enhancement in the ratio for more central Pb–Pb collisions when compared to pp events, the ratios are consistent with each other at high p_T, and there is potentially a slight suppression at low p_T. However, looking in more detail, there are slight differences. The overall magnitude is somewhat lower; peaking at around 0.9 rather than 1.5, while the enhancement relative to pp is slightly more - around 4 times rather than 3. In addition, the enhancement seems to start at slightly lower p_T, of around 1.5 GeV/c rather than 2 GeV/c for the Λ/K$_S^0$ ratio. As mentioned earlier, the EPOS model reproducing the Λ/K$_S^0$ ratio is tuned to the proton and pion spectra, so these slight differences in the ratio indicate that the EPOS model is not merely coincidentally tuned to the Λ/K$_S^0$ ratio, and also that they should be explained by physics contained within the EPOS model.

5.5 Nuclear Modification Factor, R_{AA}

Taking the ratio between the spectra of different particle species has allowed us to directly compare Pb–Pb and pp collisions. Similarly, taking the ratio of the spectra measured in Pb–Pb to that measured in pp collisions can allow us to compare the different species. However, in order to understand the evolution of this ratio with centrality, and also to aid instinctive understanding of the ratio, it is conventional to normalise to the equivalent number of pp collisions for each Pb–Pb centrality bin. If the Pb–Pb collision is merely a superposition of independent nucleon-nucleon interactions, this ratio would be flat and consistent with unity. Any deviation from 1 can thus be interpreted as additional physics due to interactions between the nucleon-nucleon collisions; whether this be the formation of Quark-Gluon plasma, cold nuclear effects due to the collisions taking place within the nucleus, or something else altogether.

In order to estimate the equivalent number of pp collisions to a given Pb–Pb centrality,

Centrality Interval	Average Number of Binary Collisions
0-5%	1685
5-10%	1316
10-20%	921.2
20-40%	438.4
40-60%	127.7
60-80%	26.71
80-90%	6.293

Table 5.1: Average number of binary collisions for different centrality intervals in Pb–Pb collisions at $\sqrt{s_{NN}} = 2.76$ TeV [4].

the Glauber model is used, as described in Section 2.2.1. The average number of binary collisions for each centrality bin has been calculated by ALICE (see [4]) and is reproduced in Table 5.1 for the centrality bins used in this analysis.

The ratio of particle spectra between Pb–Pb and pp collisions in a given centrality bin, R_{AA}, is then defined as

$$R_{AA} = \frac{\frac{\mathrm{d}^2 N}{\mathrm{d}y\mathrm{d}p_T}(\text{Pb–Pb})}{N_{\text{coll}}\frac{\mathrm{d}^2 N}{\mathrm{d}y\mathrm{d}p_T}(\text{pp})}, \tag{5.1}$$

where N_{coll} is the average number of binary nucleon-nucleon collisions for the centrality bin of interest.

The R_{AA} of Λ and K_S^0 are reproduced in Figures 5.13 and 5.12 respectively for all centrality intervals considered in this analysis. Unfortunately, both the errors and p_T range of this measurement are significantly limited by the spectra measured in pp at 2.76 TeV, but the overall trends can be discerned. For this analysis, the 2.76 TeV sample was restricted to collisions where the entirety of the detector was active, and so additional statistics may be obtained by considering those events where the SDD was inactive. In addition, the 80-90% centrality bin is not included, as the variation in N_{coll} from the Glauber Model can be as much as 50% in this bin.

For both particles it can be seen that the ratio flattens out when moving to more peripheral bins, but is still not consistent with 1, save for Λ at intermediate transverse momenta. In the more peripheral bins, the R_{AA} for K_S^0 seems consistent with a constant value of around 0.7, while Λ is still displaying p_T-dependant modification between the pp
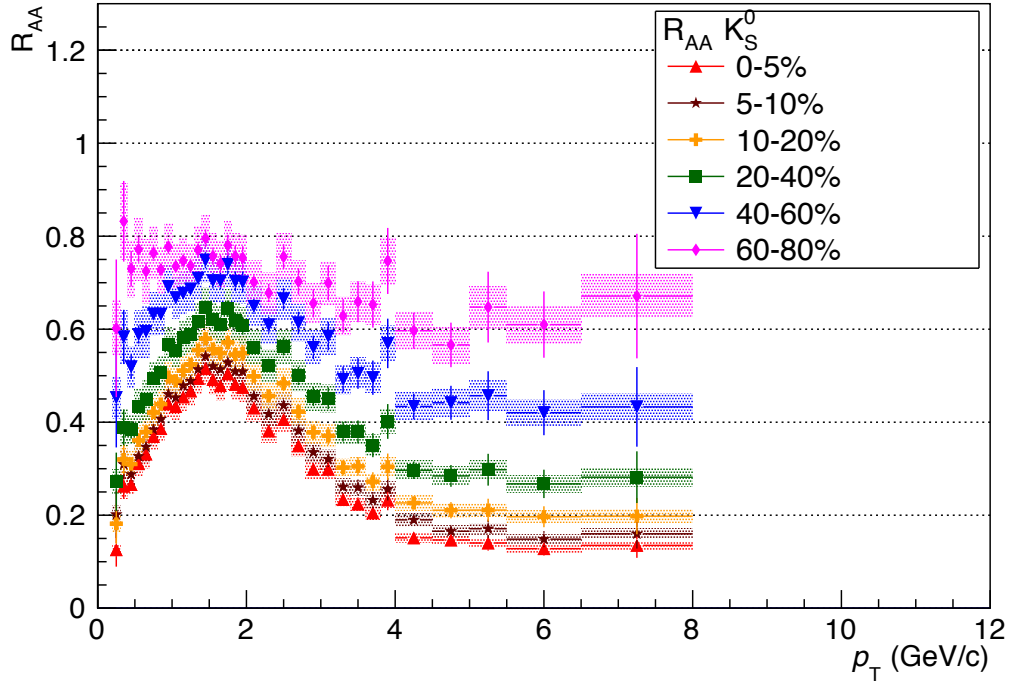
Figure 5.12: K_S^0 R_{AA} - R_{AA} of K_S^0 for all measured centrality bins. Statistical errors are indicated by the lines, while systematic errors are represented by the hatched areas.
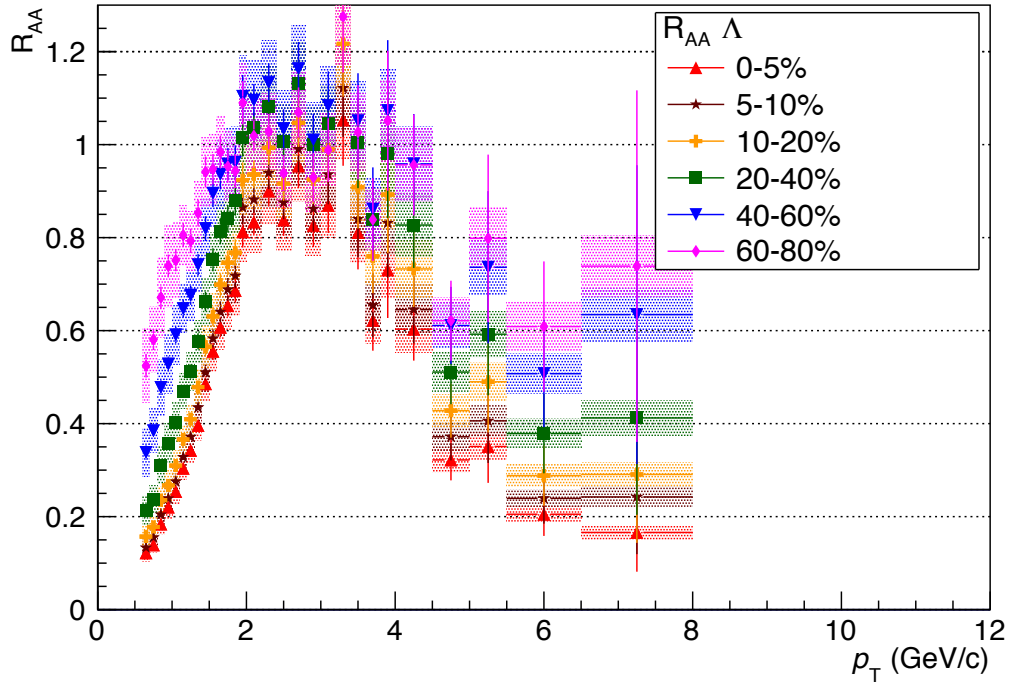
Figure 5.13: Λ R_{AA} - R_{AA} of Λ for all measured centrality bins. Statistical errors are indicated by the lines, while systematic errors are represented by the hatched areas.

and Pb–Pb collisions.

Of more interest is the difference in behaviour between Λ and K_S^0. As mentioned in Section 2.4.5, under some predictions the degree of jet quenching is dependant upon particle species. This might be observed as a difference in the R_{AA} of the two particles at high p_T. At low and intermediate p_T, the baryon anomaly should also be evident as a difference in the R_{AA}.

The R_{AA} of Λ and K_S^0 for the 0-5% centrality bin are shown together in Figure 5.14, along with the R_{AA} for protons and charged pions and kaons, as measured by ALICE and reported in [160]. Also shown are the recent phi meson results, presented at Quark Matter Conference 2014 [163]. It is striking from this plot that, within errors, the baryons seem to follow a common trajectory, as do the mesons. Above $p_T \sim 7$ GeV/c all particles appear to follow a common trajectory, with no distinction between particle mass or composition. This would seem to disfavour the idea of particle-dependant jet suppression, although it is certainly possible that more subtle effects are hidden by the relatively large systematic errors.

At lower p_T evidence of flow can be seen, as the suppression for baryons sets in at higher p_T than for the lighter mesons. The peak in the Λ/K_S^0 plot then comes from the difference in position of these two peaks of the R_{AA}, suggesting once again that the baryon anomaly may come from the redistribution of particles in p_T, rather than an additional production source.

The ϕ results are of particular interest, as this meson has a mass similar to that of the baryons. Although the errors are significant, allowing for the possibility that it falls somewhere between the two trends, it seems to follow the other mesons. This would suggest that the low p_T effects are mostly due to the number of constituent quarks, rather than the mass of the particle; leading naturally to a coalescence image. It would be of interest to see these results extended to lower p_T, where flow effects should be more significant.
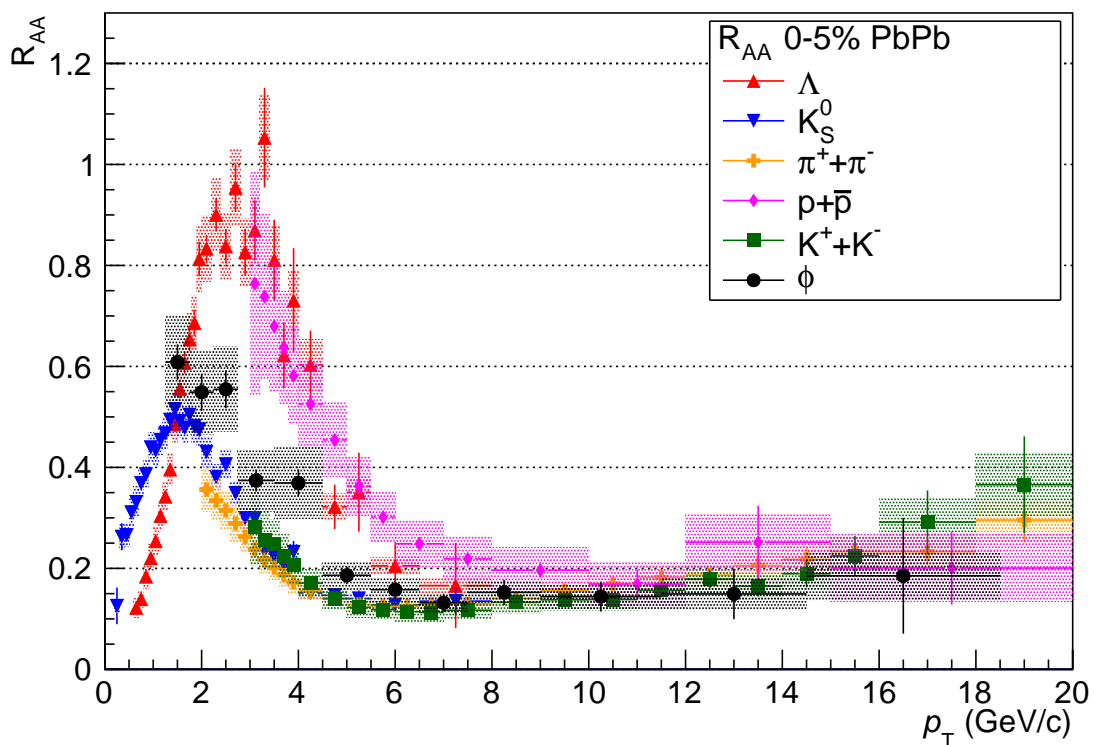
Figure 5.14: R_{AA} of Identified Particles with ALICE - R_{AA} of Λ and K^0_S for the 0-5% centrality bin, with the published ALICE results for the R_{AA} of protons, charged pions and charged kaons [160]. Also shown are results for the phi meson from the Quark Matter 2014 Conference [163]. Statistical errors are indicated by the lines, while systematic errors are represented by the hatched areas.

5.6 Integrated Yields

While the p_T dependant yields and ratios are useful for separating out effects which come into play at low, intermediate and higher transverse momentum, it is also instructive to consider the total yield, integrated over all transverse momenta. This can be used to constrain models for overall particle production, such as the models based on thermal production of particles as discussed in Section 2.1, and can also help determine the question of whether re-distribution or additional production channels are responsible for the baryon anomaly.

In order to calculate the p_T-integrated yield, it is necessary to estimate that part of the yield which falls beyond the p_T limits of the measured spectra. Simple estimates show that the part of the spectra above the highest p_T measured contribute much less than 1% to the yield, and can be neglected. However, the low p_T part is more significant, and requires extrapolation of the measured spectra.

For Pb–Pb collisions, where it is seen that the behaviour is consistent with hydrodynamics at low p_T, the spectra can be well described by a blast wave fit: a thermal distribution with a collective flow superimposed [12]. The parameterisation used for this is

$$\frac{\mathrm{d}N}{\mathrm{d}p_T} \propto \int_0^1 x m_T K_1\left(\frac{m_T \cosh \eta}{T}\right) I_0\left(\frac{p_T \sinh \eta}{T}\right) \mathrm{d}x, \tag{5.2}$$

$$\eta = \tanh(\beta_{\max} x^n),$$

$$m_T = \sqrt{p_T^2 + m^2},$$

where K_1 and I_0 are modified Bessel functions of the second and first kind respectively. $\beta_{\max}$ takes its usual relativistic meaning as a velocity expressed as a fraction of the speed of light, and describes the maximum collective expansion velocity of the medium. The fit parameter n is used to describe the variation in collective flow velocity between the centre, where it is 0 by symmetry, to its maximum at the boundary of the medium. The local temperature of the medium in its rest frame is given by T, while p_T and m are the

transverse momentum and mass of the particle respectively.

For pp collisions, however, where no hydrodynamical behaviour is expected, this parameterisation of the spectra seems inappropriate. Instead, a parameterisation is used based in Tsallis statistics [164], which allows a deformation of a thermal m_T-exponential to a power-law tail suitable for hard scattering. The parameterisation chosen has been used extensively, see for example [165], and takes the form:

$$\frac{\mathrm{d}N}{\mathrm{d}p_T} \propto p_T \frac{(n-1)(n-2)}{nT(nT + m(n-2))} \left(1 + \frac{m_T - m}{nT}\right)^{-n}, \tag{5.3}$$

where n is a fit parameter. Although the parameter T appears as if it were a temperature, its physical significance is unclear for pp collisions, and it is merely used as a free fit parameter. The transverse mass, m_T, is defined as in Equation 5.2 in terms of transverse momentum p_T and particle mass m.

For both functions, the results of the fits are shown in Figure 5.15, and the results for the p_T-integrated yields summarised in Table 5.2. The fits are undertaken only in the low p_T part of the spectra, up to 2.5 GeV/c for Λ, and up to 1.4 GeV/c for K_S^0. The systematic errors on the integrated yield was split into two parts, which were then added in quadrature. Firstly, the spectra were shifted up and down by their systematic errors, and the maximal variation in the integrated yield taken as one source of error. Secondly, the fit function was varied, and the change in the low-p_T portion of the integrated yield, which varied from 10-30% of the total yield, was added in quadrature to the systematic error. In addition the two lowest p_T points of the K_S^0 spectra, where the statistical errors are particularly limiting, were removed to check the effect that their inclusion had on the low-p_T extrapolation. It is worth noting that the blastwave and Tsallis fits are very similar for the more peripheral Pb–Pb collisions and pp collisions, and so potentially choosing the wrong one does not seem to introduce a major source of error.

It is notable that the ratios of the integrated yields are consistent with a constant value of around 0.25. It is difficult to make any conclusive statements due to the large errors,
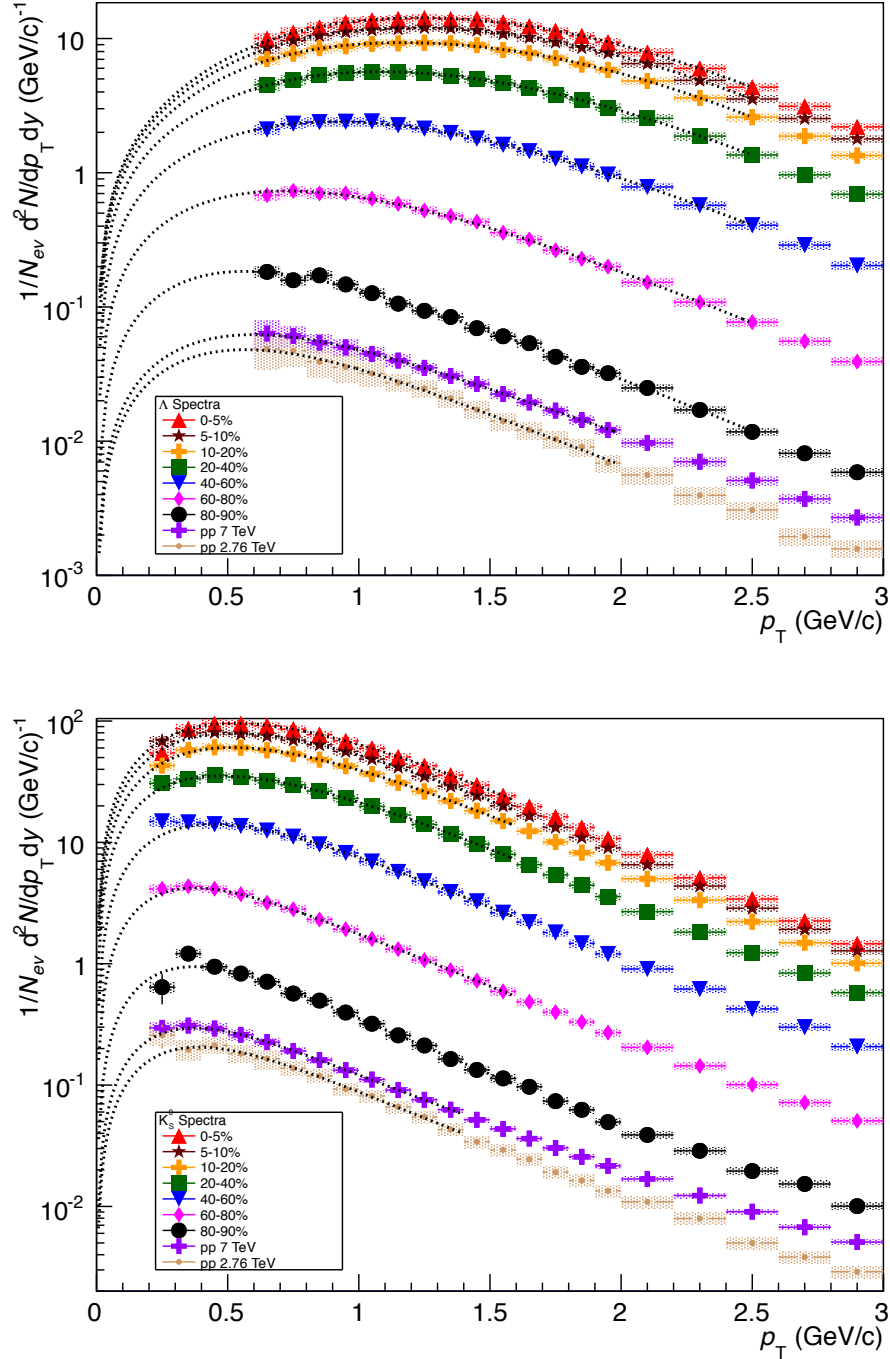
Figure 5.15: Λ and K$_S^0$ Spectra with Low-p_T Fits. - Fully corrected spectra for K$_S^0$ (top)and Λ (bottom), also showing the fits used to extrapolate to low p_T. The fit used is a blastwave function for Pb–Pb events, and a Tsallis function for pp.

Centrality	Λ	K_S^0	Λ/K_S^0
0-5%	25 ± 2	108 ± 8	0.24 ± 0.014
5-10%	21 ± 2	89 ± 7	0.24 ± 0.014
10-20%	16.6 ± 1.4	67 ± 5	0.25 ± 0.015
20-40%	9.8 ± 0.8	39 ± 3	0.25 ± 0.02
40-60%	3.9 ± 0.3	14 ± 1	0.27 ± 0.02
60-80%	1.05 ± 0.09	3.9 ± 0.4	0.27 ± 0.02
80-90%	0.23 ± 0.03	0.83 ± 0.09	0.27 ± 0.03
$\sqrt{s}= 7$ TeV pp	0.081 ± 0.015	0.28 ± 0.03	0.29 ± 0.03
$\sqrt{s}= 2.76$ TeV pp	0.058 ± 0.015	0.19 ± 0.03	0.3 ± 0.05

Table 5.2: dN/dy for Λ and K_S^0 as measured in ALICE. The low p_T part of the spectra have been estimated using blastwave and Tsallis fits.

and it does appear that there is a consistent trend of the central values. Nonetheless, a constant ratio could be interpreted as suggesting that the source of the baryon anomaly is a redistribution of particles in p_T. This will be further discussed in Section 6.1.

The values of the integrated yields for the most central collisions have been incorporated into global thermal fits, as described in Section 2.1. This was performed in [3], and is shown in Figure 5.16. Both Λ and K_S^0 agree very well with the overall fit at T=156 MeV, with deviations of around half the measured errors in each case. This puts additional pressure on the tension between the fit and the measured proton and antiproton yields, both of which lie around 3σ below the fit. Some explanations posited to explain this - for instance high levels of proton-antiproton annihilation [166] - would also affect the Λ yields, and so are challenged by this measurement. It is notable that the temperature extracted, $T = 156$ MeV, fits in well with the plateau in temperature observed at RHIC energies, supporting the interpretation of this as the critical temperature of the QGP phase.
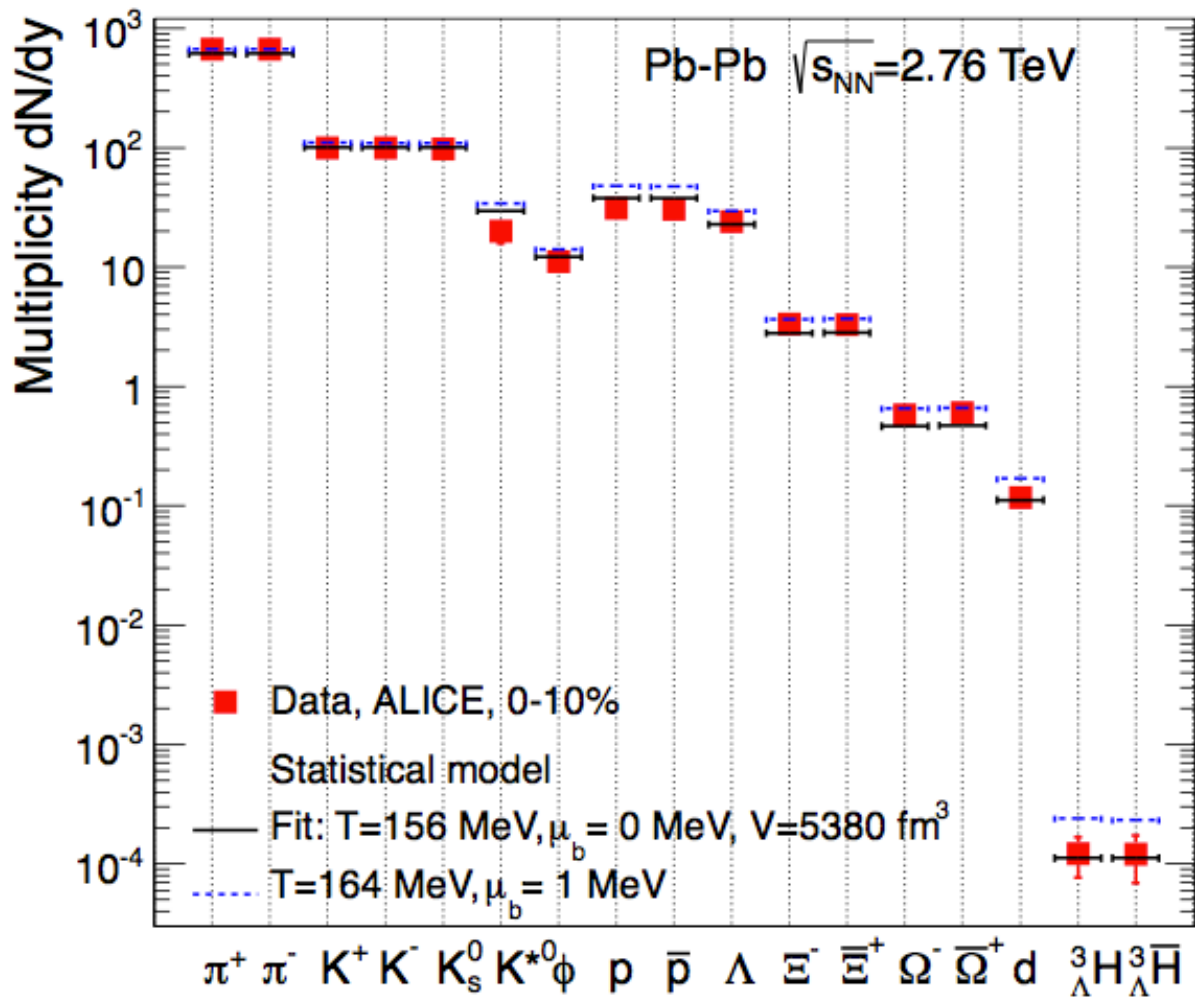
Figure 5.16: Thermal Fit to ALICE 0-10% Data - Thermal fit to central ALICE data, taken from [3]

6

Discussion

In the previous chapter, the main results from this analysis were shown, and such conclusions as could be directly drawn from them discussed. The particle spectra are well described by the EPOS model: a model based upon Lund string breaking which simulates the interaction between p_{T} regions where hydrodynamics, coalescence and vacuum-like fragmentation dominate. The majority of particles are found at low p_{T}, where a hydrodynamical description seems to capture the behaviour of the system. The $\Lambda/\mathrm{K}^0_{\mathrm{S}}$ ratio shows a clear enhancement of Λ over $\mathrm{K}^0_{\mathrm{S}}$ in the intermediate momentum region, and a possible suppression for $p_{\mathrm{T}} < 1.5$ GeV/c. This behaviour is again well reproduced by the EPOS model. Studies of the R_{AA} of the particles suggest that all particles behave similarly above a p_{T} of around 7 GeV/c, with no particle-dependant jet quenching observed. Finally, estimates of the total p_{T}-integrated yields of the particles agree well with an overall thermal model, and give values for the total $\Lambda/\mathrm{K}^0_{\mathrm{S}}$ ratio which are approximately constant with centrality.

Some of these concepts will be brought together in this chapter, to try and establish whether the baryon anomaly is due to redistribution of the particles in p_{T}, or instead requires enhancement or suppression of particle production mechanisms. These results will be compared to those recently shown for p–Pb collisions by the ALICE collaboration, and how this affects the interpretations placed on the Pb–Pb results will be discussed.

Throughout, areas will be illustrated in which further research could benefit our understanding.

6.1 Redistribution and Enhanced Baryon Production

The measured Λ/K_S^0 ratio (Figure 5.5) suggests at first glance that there is enhanced baryon production at intermediate p_T in Pb–Pb collisions or, equivalently, suppressed baryon production in pp collisions. Coalescence models support this idea; in a medium 3 quarks close to each other can easily exchange colour to form a colourless state, while baryon production through fragmentation requires the production of 6 quarks, a baryon and an anti-baryon, in order to conserve baryon number. Thus, if coalescence is a dominant source of particle production in Pb–Pb collisions, an enhancement in baryon production relative to meson should be observed.

An alternative model is that the enhancement at intermediate p_T is caused by a redistribution of particles in p_T; baryons produced at low p_T may be pushed to higher p_T by collective flow. Flow models can generate an excess of baryons at intermediate p_T without any increase in overall baryon production; the impact of the collective flow is greater on the heavier baryons than on the lighter mesons and so the baryons are pushed to higher p_T. Coalescence models incorporate a similar effect; not only are baryons easier to produce through coalescence, their typical momenta is higher than mesons because they take in the total momentum of three quarks rather than two.

In attempting to untangle these competing processes, it is useful to investigate whether the data is consistent with redistribution of particles in p_T, enhanced baryon production, or indeed both. Figure 6.1 shows the ratio of p_T-integrated yields of Λ and K_S^0, taken from Table 5.2. Generally, enhanced production of Λ would lead to an increase in the integrated ratio as for more central collisions, while redistribution of Λ would leave the ratio unchanged.

The measured ratio is consistent with a constant value of 0.25, and so consistent with a
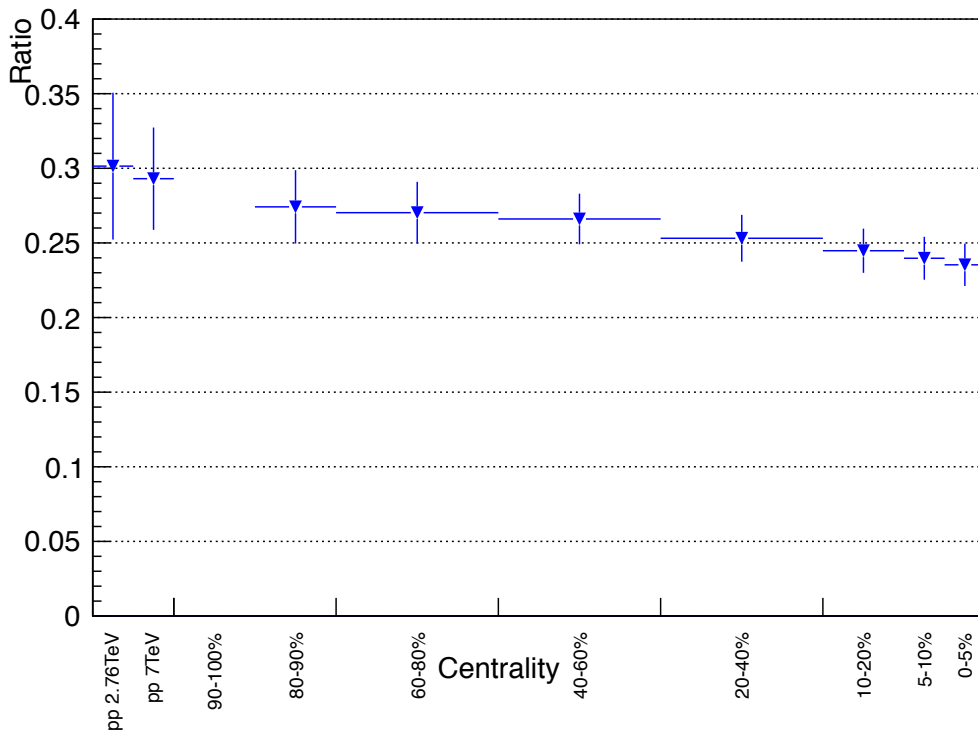
Figure 6.1: Ratio of p_T-integrated Λ/K_S^0 Yields. - Yields of Λ and K_S^0 are integrated from $p_T = 0$ upwards using the blastwave & Tsallis fits discussed in Section 5.6. These integrated yields are then divided to give the total Λ/K_S^0 ratio.

redistribution model. It is striking however that, despite the relatively large errors, there is a clear trend within the points; the ratio gets larger heading to more peripheral events. Rather than supporting a model of enhanced baryon production, this trend would in fact lead to the opposite conclusion: the production of baryons relative to mesons appears to be suppressed in central Pb–Pb collisions. This warrants further investigation, as it does not fit in with the theoretical picture of QGP behaviour. Study of the 2011 Pb–Pb data should offer enough statistics to resolve this point, as well as extending the p_T spectra to lower p_T and so reducing the systematic errors on the integrated yields. In addition, studies of other baryon and meson spectra can help to understand this point. Figure 6.2 shows various particle ratios measured in pp, p–Pb and Pb–Pb collisions with ALICE. The ratios of protons and Ξ^- to pions drop off when moving from the lighter systems to Pb–Pb collisions, suggesting that this baryon suppression could be a general effect, not limited to Λ and K_S^0.
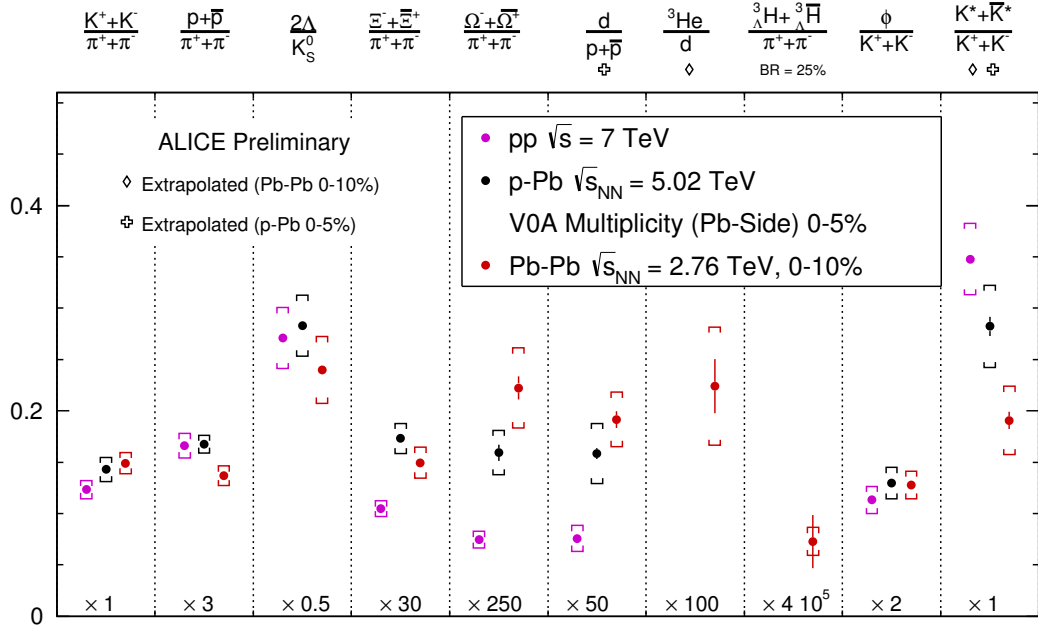
Figure 6.2: Integrated Particle Ratios with ALICE at the LHC - Particle ratios in central p–Pb and Pb–Pb, and all pp collisions. The ratios of protons, Λ and Ξ^- to pions show hints of baryon suppression in Pb–Pb collisions [52]. Scale factors, displayed along the bottom axis, are applied to allow comparison of ratios on a common vertical axis.

6.1.1 Double Ratio of Λ/K_S^0 in Central Pb–Pb to pp Collisions

To investigate this further with the data currently available, the p_T-differential Λ/K_S^0 ratio is used. It was earlier shown, in Figure 5.6, that at very low p_T there is evidence that the Λ/K_S^0 ratio is lowest in the most central events, allowing for the possibility of redistribution. If, for clarity, only the 0-5% centrality bin is discussed, the double ratio of Λ/K_S^0 in Pb–Pb collisions divided by that measured in pp collisions can be studied. In Figure 6.3 this ratio is shown, both for $\sqrt{s} = 2.76$ TeV and also for $\sqrt{s} = 7$ TeV, as the limited statistics available for the lower energy make it harder to resolve the trend. The results of the blastwave and Tsallis fits to the p_T spectra have been used to extend the ratios to $p_T = 0$. This double ratio clearly shows the enhancement at high p_T, but also more prominently reveals the suppression at low p_T. The 2011 data would also allow improvement of the statistics at high p_T; it seems likely that the ratio for $\sqrt{s} = 2.76$ TeV will be consistent with 1, but this cannot be confirmed with the presently analysed data

sample.
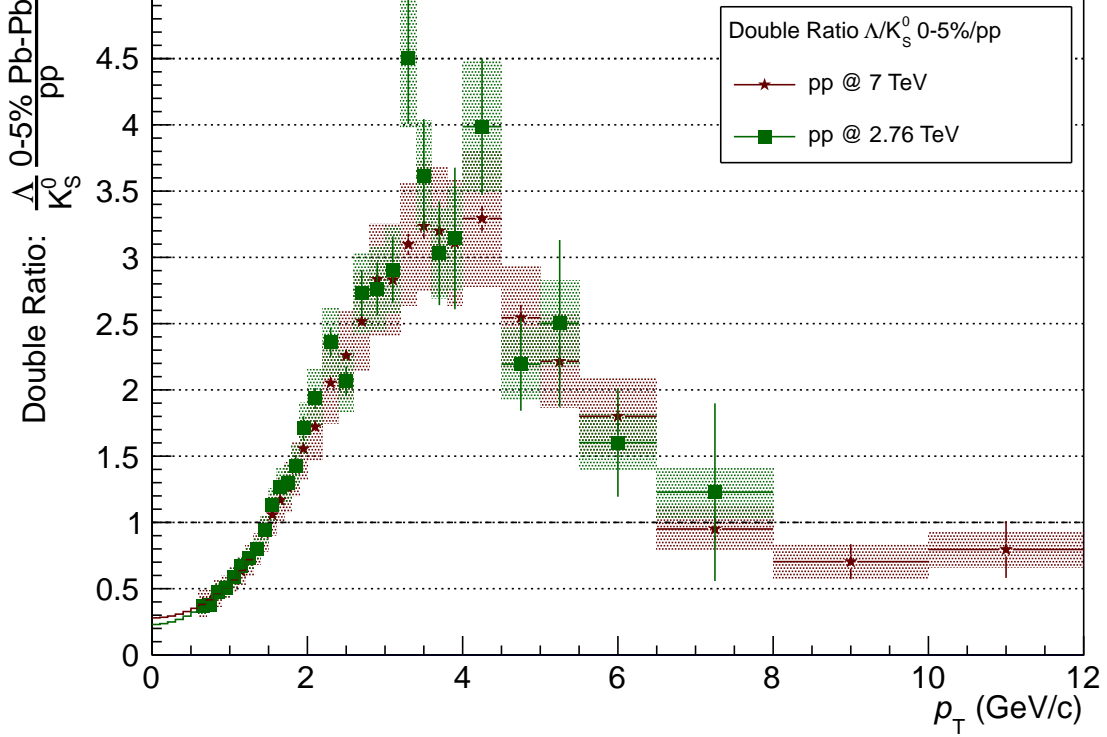
Figure 6.3: Double Ratio of Λ/K^0_S **(0-5% Pb–Pb)/(pp)** - The Λ/K^0_S ratio in 0-5% Pb–Pb collisions is divided by that measured in pp at $\sqrt{s} = 2.76$ TeVand 7 TeV. Statistical uncertainties are indicated by the error bars and systematic uncertainties by the shaded areas. Both a suppression region at low p_T and an enhancement region at intermediate p_T can be clearly resolved.

The suppression at low p_T still looks less significant than the intermediate-p_T enhancement, but the weighting of the spectra towards low p_T could explain this. This region contains around 90% of all K^0_S, and so a relatively small change here could be as significant as, or larger than, the more obvious enhancement at intermediate p_T. Uniquely identifying how the particles are redistributed is challenging, however. The measurements of the R_{AA} (Figure 5.14) clearly show a p_T dependant change in the behaviour of both particles, and so any change in the number of Λ can be compensated for, or increased by a corresponding change in the number of K^0_S in that region. So, for example, the measured data could be explained entirely by an increase in the number of K^0_S at low p_T, and an increase in the number of Λ at intermediate p_T, although this is highly unlikely within

our theoretical framework.

6.1.2 Change in Particle Numbers

As both particle species can be enhanced or redistributed in p_{T} independently, it is not possible to unambiguously determine whether the low p_{T} suppression balances the intermediate p_{T} enhancement. To get a feel for the number of particles associated with each p_{T} region, each particle species can be independently investigated, under the assumption that the other is merely scaled up in moving from pp to Pb–Pb collisions, and that its shape does not change. For instance, by assuming that the p_{T} distribution of $\mathrm{K^0_S}$ is the same in Pb–Pb and pp collisions, it is possible to calculate how many fewer Λ would be needed at low p_{T} when moving from pp to Pb–Pb, and how many more at intermediate p_{T}, in order to reproduce the measured double ratio in Figure 6.3. This can be written as

$$K_{Pb}(p_{\mathrm{T}}) = NK_p(p_{\mathrm{T}}), \tag{6.1}$$

$$\frac{\Lambda_{Pb}(p_{\mathrm{T}})/K_{Pb}(p_{\mathrm{T}})}{\Lambda_p(p_{\mathrm{T}})/K_p(p_{\mathrm{T}})} = f(p_{\mathrm{T}}) \ \text{ by definition}, \tag{6.2}$$

$$\therefore \ \Lambda_{Pb}(p_{\mathrm{T}}) = Nf(p_{\mathrm{T}})\Lambda_p(p_{\mathrm{T}}), \tag{6.3}$$

where the double ratio is defined as $f(p_{\mathrm{T}})$, and the Λ and $\mathrm{K^0_S}$ spectra in a given collision system are represented by their letter and an appropriate subscript. The change in the number of Λ in a given p_{T} bin is then given by

$$\Delta\Lambda(p_{\mathrm{T}}) = \Lambda_{Pb}(p_{\mathrm{T}}) - \Lambda_p(p_{\mathrm{T}}) = (Nf(p_{\mathrm{T}}) - 1)\Lambda_p(p_{\mathrm{T}}). \tag{6.4}$$

A similar process can be performed for the case of Λ remaining constant, and only allowing $\mathrm{K^0_S}$ to change, which gives us a formula for the change in number of $\mathrm{K^0_S}$ in a given p_{T} bin:

$$\Delta K(p_{\mathrm{T}}) = (1 - Nf(p_{\mathrm{T}}))K_p(p_{\mathrm{T}}). \tag{6.5}$$

Rather than explicitly calculating the scaling factor N, the particle distributions are normalised such that there are 1000 Λ in each distribution, to highlight the relative changes in particle number. From the integrated Λ/K_S^0 ratio, this implies approximately 4000 K_S^0. These 'Δ-functions' are plotted in Figure 6.4. Note that, again for clarity, the number of particles in a given bin is not divided by the bin width. It is immediately evident that the low p_T 'suppression' region is a stronger effect than the mid-p_T 'enhancement'. The number of particles in the two regions can be integrated to show the overall change in particle numbers; these are listed in Table 6.1 for the pp $\sqrt{s} = 7$ TeV reference. This suggests that roughly 50% of the total yield of particles move in or out of the low p_T region, while only 10% are added to or removed from the intermediate p_T region.
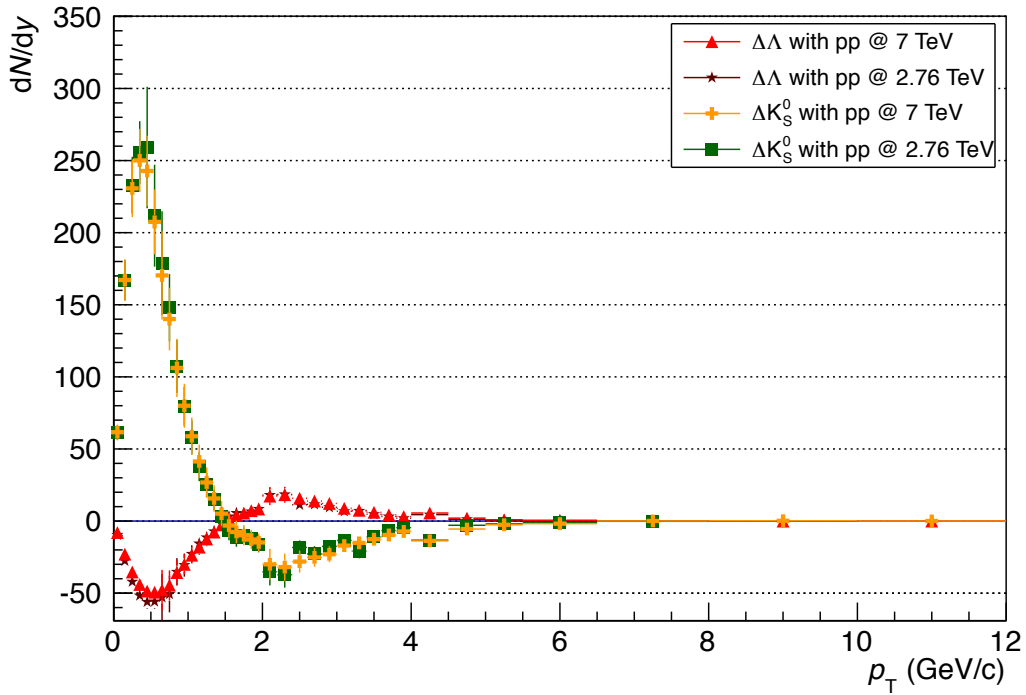
Figure 6.4: $\Delta\Lambda$ and ΔK_S^0 Required to Change pp-like Λ/K_S^0 Ratio to Pb–Pb-like. - $\Delta\Lambda$ and ΔK_S^0 calculated under the assumption that the other particles distribution is unchanged between pp and Pb–Pb, and that there are 1000 Λ particles.

From the table, a conclusion can be made that redistribution of one particle alone is not able to reproduce the Λ/K_S^0 ratio observed in Pb–Pb collisions: for either assumption the low p_T part of the ratio dominates over the intermediate p_T part. Further, enhancement

Particle	$0.0 < p_T < 1.5$ GeV/c	$1.5 < p_T < 5.5$ GeV/c	all p_T
$\Delta\Lambda$	-470 ± 30	128 ± 11	-340 ± 40
ΔK_S^0	1840 ± 80	-260 ± 20	1600 ± 100

Table 6.1: Change in number of particles in a given p_T region required to make the pp-like Λ/K_S^0 ratio Pb–Pb-like, under the assumption that only one particle distribution changes shape. Total number of Λ fixed to 1000.

of one particle alone is insufficient, as there is always suppression in one p_T region under these assumptions; a combination of redistribution and enhancement would be required.

These conclusions will not necessarily hold when both particles are allowed to vary independently. They emphasise only that redistribution of particles is a possibility: the low p_T suppression region in the Λ/K_S^0 ratio is as significant as the more obvious enhancement region.

6.1.3 Redistribution or Enhancement Alone

The above analysis cannot be easily extended to the more general case. Instead, the question can be asked whether the observed change in the Λ/K_S^0 spectra is consistent with a hypothesis of enhancement of baryon production alone or redistribution alone?

Enhancement is straightforward to rule out; if there are 1000 K_S^0 in each system, then at low p_T 130 ± 10 Λ are required for the ratio to be Pb–Pb-like, and 250 ± 50 for the ratio to be pp-like. Thus, under the hypothesis that the change in the baryon-meson ratio at intermediate p_T is entirely due to enhancement, ~ 120 Λ must be lost from lower p_T, when moving from a pp to a Pb–Pb system, which is not consistent with the uncertainties on the measurement.

Pure redistribution is, within errors, consistent with the measured results. Table 6.2 shows the number of Λ and K_S^0 in the different p_T regions for pp and central Pb–Pb collisions at $\sqrt{s_{NN}} = 2.76$ TeV, and also gives the Λ/K_S^0 ratio in these regions. The number of K_S^0 has again been normalised to 1000, for easy comparison between the two samples. Starting with the pp sample, and moving 137 Λ and 119 K_S^0 from low to intermediate p_T, gives a Λ/K_S^0 ratios of 0.15±0.5 and 0.9±0.4 in the two regions respectively, matching those

System	Particle	$0.0 < p_\text{T} < 1.5$ GeV/c	$1.5 < p_\text{T} < 5.5$ GeV/c	all p_T
Pb–Pb	Λ	130 ± 10	105 ± 2	235 ± 21
Pb–Pb	K_S^0	880 ± 30	121 ± 3	1000 ± 70
Pb–Pb	$\Lambda/\text{K}_\text{S}^0$	0.15 ± 0.01	0.86 ± 0.03	0.24 ± 0.01
pp	Λ	250 ± 40	48 ± 2	301 ± 80
pp	K_S^0	900 ± 300	95 ± 3	1000 ± 174
pp	$\Lambda/\text{K}_\text{S}^0$	0.30 ± 0.1	0.51 ± 0.03	0.30 ± 0.05

Table 6.2: Distribution of Λ and K_S^0 between 3 p_T regions in $\sqrt{s} = 2.76$ TeV pp and 0-5% Pb–Pb collisions, and the corresponding $\Lambda/\text{K}_\text{S}^0$ ratios. Normalised to 1000 K_S^0 in total.

measured in Pb–Pb collisions. As indicated by the large errors, there are many similar transfers which would be consistent with the Pb–Pb ratio, or indeed many combinations of redistribution of particles and enhancement of baryon production.

Overall then, it can be stated that the measured ratios are not consistent with baryon enhancement alone, but are consistent with redistribution alone, within errors. More likely, however, is that there is a combination of both: some Λ are pushed to a higher p_T by collective flow, as are some lesser number of K_S^0, and additionally extra Λ are created at intermediate p_T. If the trend in the integrated ratios remains after an improvement of statistics, however, this could only be explained by a reduction in the number of Λ, or an enhancement in the number of K_S^0 larger than that of Λ. These changes could be accommodated in the observed ratios by an appropriate redistribution of the particles in p_T, but would require a new theoretical framework to understand.

6.2 Complementary Measurements

6.2.1 Jets and Bulk

In this work, the inclusive p_T spectra of hadrons have been considered; no distinction has been made based on the rapidity or angular distribution of the particles. Alternative measurements can be made; for example by studying the angular distribution of hadrons, one can measure the elliptic flow (Section 2.3.1), which shows that the measured flow is dependant on the number of valence quarks in the hadron, as predicted by the Coalescence

model [60]. An alternative approach, which is currently being studied at ALICE, is to look for differences in jet-like and bulk-like regions of the collisions. In such analyses, the jet peak is defined by a small geometrical region around a high-p_T trigger particle, while the bulk region is taken at the same azimuthal angle, but separated in pseudorapidity from the trigger particle.

By defining the regions in this way, the bulk region falls in the 'ridge' [167], an extended region in pseudorapidity associated with a jet in heavy-ion collisions where there is an enhanced density of intermediate p_T hadrons. In the coalescence model, this can be understood as the region where the quenched jet's energy has been shared among partons flowing in η, which then coalesce to form hadrons at slightly higher p_T than expected from the global temperature [121]. This picture can be tested by examining the baryon-meson ratio in the bulk and comparing it to that in the jet (with the bulk subtracted as an underlying background).
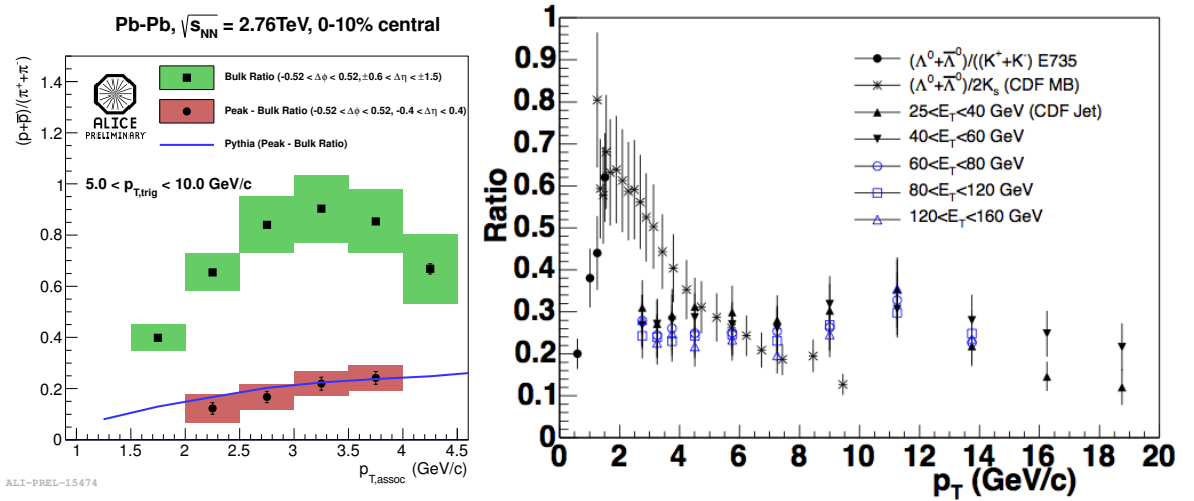
Figure 6.5: Baryon to Meson Ratios Measured in Jet and Bulk - Left: preliminary ALICE results for the p/π ratio measured in the bulk region, and in the jet region with bulk values subtracted. Events require a trigger particle with $5 < p_T < 10$ GeV/c. Also shown is a comparison to Pythia predictions for the peak-bulk ratio. Right: inclusive Λ/K ratios measured by CDF and E735 in p$\bar{\text{p}}$ collisions at the Tevatron, compared to values measured in jets at CDF [168].

While the Λ/K$_S^0$ ratio in jets is not yet available from ALICE, Figure 6.5 (left) shows the preliminary results for the proton to pion ratio measured in jet and bulk regions.

While these results are limited in p_T range, the familiar enhancement at intermediate p_T can be seen in the results for the bulk region. When the bulk particle production is subtracted from the jet region, however, the enhancement disappears, leaving a pp-like baryon-meson ratio. This supports the coalescence picture, and the approach taken in EPOS; baryon production is enhanced for thermal hadrons when compared to those formed through fragmentation. In such a region, the temperature of the medium should be enhanced slightly by jet quenching, and some coalescence should occur between the jet and the bulk, causing the baryon to meson ratio to be enhanced to higher p_T than elsewhere in the medium. Such comparisons are not yet possible with the available data.

Interestingly, Figure 6.5 (right) shows a similar measurement for the lambda to kaon ratio measured in p$\bar{\text{p}}$ collisions at the Tevatron. While the enhancement is not as pronounced or as extended in p_T as that seen in heavy-ion collisions, it does appear to be present in the inclusive measurements of the hadrons, consistent with the inclusive measurement from this work seen in Figure 5.5, and absent within jets. This could point towards coalescence at intermediate p_T in pp or p$\bar{\text{p}}$ collisions, suggesting that the density of partons required for this mechanism to take place is relatively low. As the statistics available at the LHC increase, future results from ALICE should be able to shed more light on this phenomenon.

6.2.2   p–Pb Collisions at ALICE

In addition to the pp and Pb–Pb collisions discussed in this work, the LHC has collided protons with lead ions at $\sqrt{s_{\text{NN}}} = 5.02$ TeV. Traditionally, similar collisions have been used to distinguish initial state 'cold' nuclear effects from the effects due to the hot, dense state of interest. However, at LHC energies, the charged particle multiplicities can be comparable with heavy-ion collisions, making a simple distinction between Pb–Pb and p–Pb collisions less convincing.

Figure 6.6 compares the R_{AA} measurements for charged particles in central and peripheral Pb–Pb collisions with the equivalent measurement, R_{pPb}, taken in p–Pb collisions.
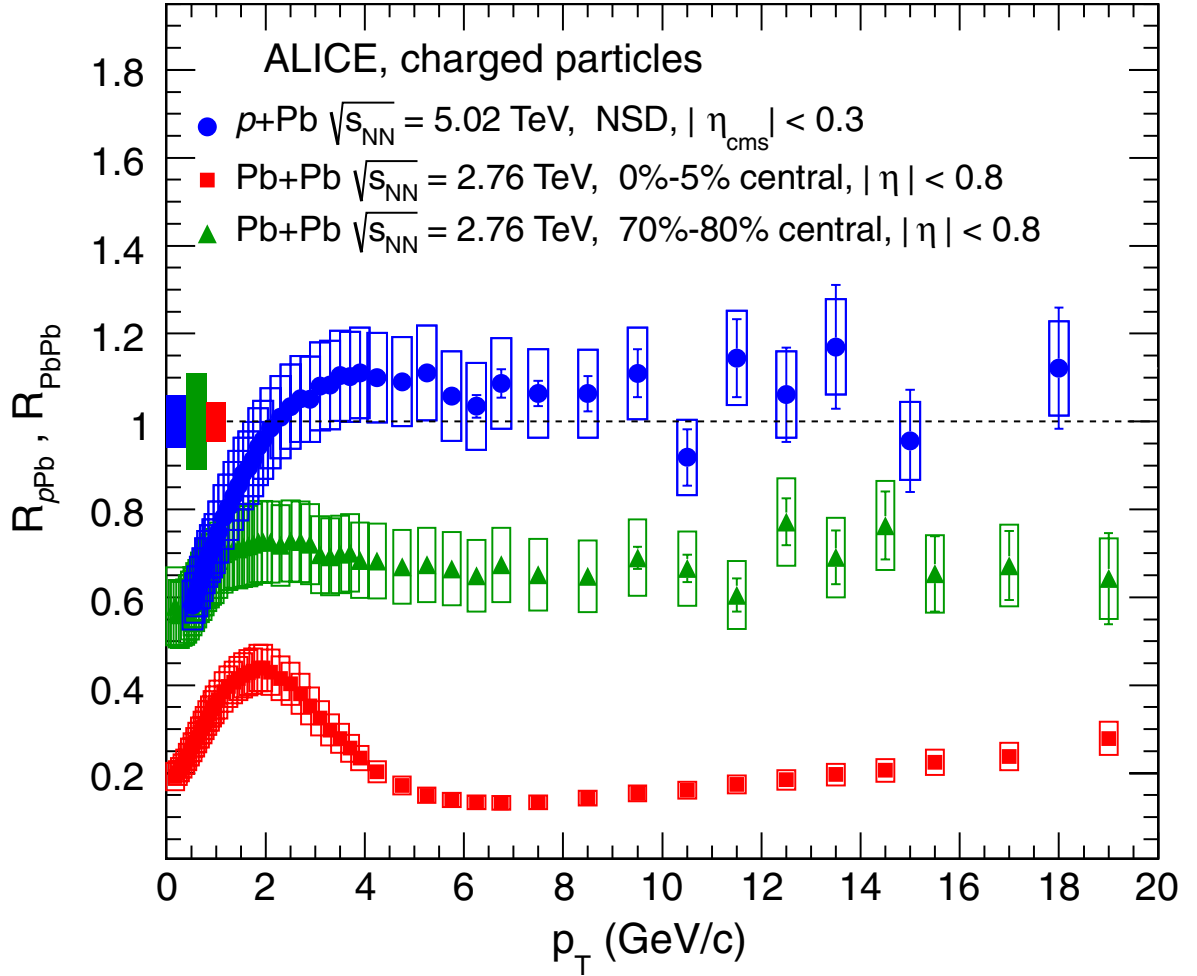
Figure 6.6: R_{pPb} **as Measured in ALICE, Compared to** R_{AA}. - R_{AA} measurements for charged particles at ALICE, compared with the equivalent measurement, R_{pPb}, in p–Pb collisions [169]. Systematic uncertainties are indicated by the boxes.

R_{pPb} is calculated in the same way as R_{AA}(Section 5.5), with the appropriate change to N_{coll}. This clearly demonstrates that the jet quenching in p–Pb collisions is significantly less - if present at all - than in Pb–Pb collisions. At low p_T, it is not consistent with unity, which could be partly due to hydrodynamical behaviour, but could also be wholly explained by low p_T particle production being dominated by processes dependant on N_{part} rather than N_{coll} or on cold nuclear matter effects. This measurement does raise questions over why the measured R_{AA} in Pb–Pb collisions never approaches unity, even for the most peripheral collisions. Hopefully some light will be shed on this when ALICE has gathered the statistics to allow particle differential R_{pPb} measurements, and detailed studies of ultra-peripheral Pb–Pb collisions.

Not all measurements of p–Pb behaviour suggest an absence of behaviour usually associated with QGP production. Measurements of hadronic p_T spectra ([170, 171]) agree well with the hydrodynamically motivated thermal distributions, and show azimuthal anisotropy similar to that associated with elliptic flow [172]. More measurements are needed before a clear picture of the underlying processes in p–Pb collisions can become clear.

Of particular relevance to the analysis described in this work is the measurement of the Λ/K^0_S ratio in p–Pb collisions, reported in [171]. Figure 6.7 (left) shows the results for the p–Pb system, alongside the results from this analysis. It can be seen that, although significantly less prominent than for the Pb–Pb system, there is an enhancement of the Λ/K^0_S ratio in the more central p–Pb collisions when compared to the more peripheral. It is somewhat unclear how significant this result is; the 5% of p–Pb collisions with the highest multiplicity do not obviously compare with the 5% most central Pb–Pb collisions. In particular, it seems possible that the results may be biased towards particularly hard p–Pb collisions. An alternative way of visualising the results is shown in Figure 6.7 (right). Here, the value of the ratio for specific p_T values are plotted against the charged particle multiplicity for pp, p–Pb and Pb–Pb collision systems, at various centre-of-mass energies. To a good degree, all these systems seem to agree on a common parameterisation,

particularly for the peak of the ratio. This would fit well with a coalescence view of the ratio, where the magnitude of coalescence over fragmentation is linked entirely to the parton density, which itself is proportional to the charged particle multiplicity. An argument could be made for this behaviour in a purely hydrodynamic model, where higher particle densities lead to higher pressure gradients. However, the presence of flow in pp collisions would be somewhat surprising, albeit hinted at by some experimental results [173].
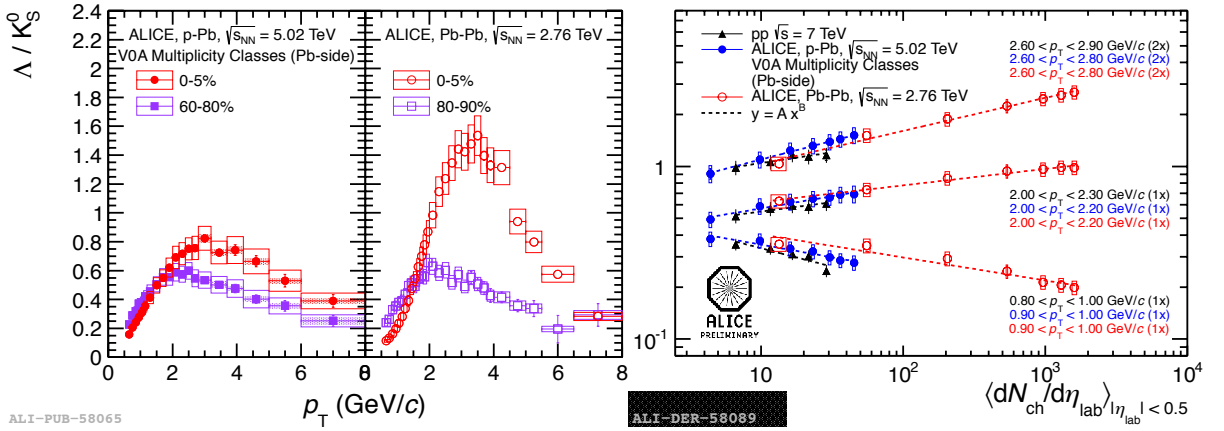
Figure 6.7: Λ/K_S^0 Ratio Results in pp, p–Pb and Pb–Pb Collisions - Left: the Λ/K_S^0 ratio in central and peripheral collisions in p–Pb, $\sqrt{s_{NN}} = 5.02$ TeV, and Pb–Pb collisions at $\sqrt{s_{NN}} = 2.76$ TeV. Right: value of the Λ/K_S^0 ratio at selected p_T for different colliding systems plotted against charged particle multiplicity. [171]

More detailed understanding of the p–Pb system could shed some light onto the precise origins of the enhancement in the Λ/K_S^0 ratio in heavy ion collisions. It is notable that a slightly newer evolution of the EPOS model described in Section 2.6, EPOS3, reproduces the particle p_T distributions well, and in particular can reproduce the Λ/K_S^0 ratio in p–Pb collisions [174]. Within this model, the behaviour of the ratio turns out to be sensitive to the degree of radial flow: without hydrodynamical flow, the EPOS authors were unable to reproduce the baryon enhancement. Future results from the p–Pb system will be interesting; the presence of the baryon anomaly in a region of p_T where jet quenching appears to be non-existent puts tension on the current theoretical interpretations of the Pb–Pb system, and it is to be hoped that more detailed measurements will resolve this.

7

Conclusions

In this work, the yield of Λ and K_S^0 at mid-rapidity have been extracted from Pb–Pb and pp collisions in ALICE at the LHC, at a centre of mass energy $\sqrt{s_{NN}} = 2.76$ TeV. The study of identified hadrons at mid-rapidity in heavy ion collisions is expected to carry the bulk of the information of QGP evolution. In particular, comparing the ratios of Λ to K_S^0 production in Pb–Pb and in pp collisions identifies some areas where heavy ion collisions cannot be explained as a simple superposition of independent nucleon-nucleon collisions.

At low transverse momenta, the particle spectra are described well by a hydrodynamically modified thermal spectrum, and, combined with the other particles identified in ALICE, lend support to an overall picture of hadron production from a thermally equilibrated system. At the highest momentum measured, there are no statistically significant deviations between the production of these strange hadrons and the more common protons and pions, limiting the range of jet quenching models to those without significant hadrochemical dependance. In particular, the formation of pre-colour states from [118] which should lead to a significant difference in nuclear suppression factor for Λ and pions for $p_T > 6$ GeV/c appears to be ruled out by these results.

At intermediate transverse momentum, there is a significant enhancement in Λ production when compared to K_S^0, going from peripheral to more central Pb–Pb collisions. Phenomenologically, this can be understood as a combination of particle flow and coales-

cence, where particles are both redistributed in p_T and baryon production is enhanced, but simple models struggle to reproduce all details of the enhancement. However the EPOS model, which incorporates hydrodynamics and coalescence as consequences of its string breaking phenomenology, gives a good description of the ratio at all p_T. Further, work carried out in the p–Pb system suggests that EPOS is also the most appropriate description of this system, and future results from these collisions should aid understanding of the Pb–Pb system.

Incorporating the 2011 Pb–Pb results, or future results at higher energy, should allow the extension of the measured spectra to both higher and lower p_T, improving the systematic errors and allowing more conclusive measurements of the integrated yield and R_{AA} of the particles. Further, specific measurements of the Λ/K_S^0 ratio in jet and bulk regions should allow further testing of the predictions made in the coalescence model.

References

[1] BETTY ABELEV ET AL. K_S^0 and Λ production in Pb-Pb collisions at $\sqrt{s_{NN}} = 2.76$ TeV. *Phys. Rev. Lett.*, **111**:222301, Nov 2013.

[2] LUKE HANRATTY. K_S^0 and Λ Production in ALICE. *J.Phys.Conf.Ser.*, **509**:012091, 2014.

[3] J STACHEL, A ANDRONIC, P BRAUN-MUNZINGER, AND K REDLICH. Confronting LHC data with the statistical hadronization model. *arXiv:1311.4662*, Nov 2013.

[4] B. ABELEV ET. AL. Centrality determination of Pb-Pb collisions at $\sqrt{s_{NN}} = 2.76$ TeV with ALICE. *Phys. Rev. C*, **88**:044909, Oct 2013.

[5] STEVEN WEINBERG. A Model of Leptons. *Phys. Rev. Lett.*, **19**:1264–1266, Nov 1967.

[6] M. GELL-MANN. A schematic model of baryons and mesons. *Physics Letters*, **8**(3):214 – 215, 1964.

[7] M. BREIDENBACH, J. I. FRIEDMAN, H. W. KENDALL, ET AL. Observed Behavior of Highly Inelastic Electron-Proton Scattering. *Phys. Rev. Lett.*, **23**:935–939, Oct 1969.

[8] H DAVID POLITZER. Asymptotic freedom: An approach to strong interactions. *Physics Reports*, **14**(4):129 – 180, 1974.

[9] http://www.bnl.gov/rhic/ [online, cited 22/04/14].

[10] http://home.web.cern.ch/topics/large-hadron-collider [online, cited 22/04/14].

[11] PROCEEDINGS OF THE 2011 RAL SCHOOL FOR EXPERIMENTAL HIGH ENERGY PHYSICS STUDENTS. http://www.stfc.ac.uk/PPD/23413.aspx [online].

[12] YASUO MIAKE KOHSUKE YAGI, TETSUO HATSUDA. Quark-Gluon Plasma. Cambridge University Press, 2008.

[13] RAYMOND BROCK ET AL. Handbook of perturbative QCD: Version 1.0. *Rev.Mod.Phys.*, **67**:157–248, 1995.

[14] Siegfried Hahn. α_s **determination from event shapes at DELPHI**. *Nuclear Physics B - Proceedings Supplements*, **74**(1–3):12 – 15, 1999. {QCD} 98.

[15] D.E. Soper J.C. Collins and G.F. Sterman. **Factorization of Hard Processes in QCD**. *Adv. Ser. Direct. High Energy Phys.*, **5**:1–91, 1988.

[16] I.J.R. Aitchison and A.J.G. Hey. **Gauge Theories in Particle Physics**. Adam-Hilger, 1989.

[17] A. Chodos, R. L. Jaffe, K. Johnson, C. B. Thorn, and V. F. Weisskopf. **New extended model of hadrons**. *Physical Review D*, **9**(12):3471–3495, June 1974.

[18] Helmut Satz. **The States of Matter in QCD**. *arXiv:0903.2778*, March 2009.

[19] F. Karsch and E. Laermann. **Thermodynamics and In-Medium Hadron Properties from Lattice QCD**. In R. C. Hwa & X.-N. Wang, editor, *Quark-Gluon Plasma*, 2004.

[20] J. D. Bjorken. **Highly relativistic nucleus-nucleus collisions: The central rapidity region**. *Phys. Rev. D*, **27**:140–151, Jan 1983.

[21] Frithjof Karsch. **Deconfinement and chiral symmetry restoration**. *arXiv:hep-lat/9903031*, 1998.

[22] I. R. Kenyon. **Elementary Particle Physics**. Routledge and Kegan Paul, 1987.

[23] J. Beringer et al. **Review of Particle Physics**. *Phys. Rev. D*, **86**:010001, 2012.

[24] P Koch, B Müller, and J Rafelski. **Strangeness in relativistic heavy ion collisions**. *Physics Reports*, **142**(4):167 – 262, 1986.

[25] F.O. Duraes, A.V. Giannini, V.P. Goncalves, and F.S. Navarra. **Baryon stopping in the Color Glass Condensate formalism: A phenomenological study**. *Phys.Rev.*, **C89**:035205, 2014.

[26] CERN. New state of matter created at CERN. **http://press.web.cern.ch/press/PressReleases/Releases2000/ PR01.00EQuarkGluonMatter.html (2000).** [online].

[27] K. Aamodt, B. Abelev, A. Abrahantes Quintana, et al. **Charged-Particle Multiplicity Density at Midrapidity in Central Pb-Pb Collisions at sNN=2.76 TeV**. *Phys. Rev. Lett.*, **105**:252301, Dec 2010.

[28] Fu-Ming Liu and Sheng-Xu Liu. **Quark-gluon plasma formation time and direct photons from heavy ion collisions**. *Phys. Rev. C*, **89**:034906, Mar 2014.

[29] K. Aamodt et al, ALICE COLLABORATION. **Two-pion Bose-Einstein correlations in central Pb-Pb collisions at**. *Physics Letters B*, **696**(4):328 – 337, 2011.

[30] A.K. CHAUDHURI. **Temperature dependence of QGP viscosity over entropy ratio from hydrodynamical analysis of ALICE data in $\sqrt{s_{NN}}$=2.76 TeV Pb+Pb collisions**. *J.Phys.*, **G39**:125102, 2012.

[31] ANDRE MISCHKE. **Overview on heavy flavour measurements in lead-lead collisions at the CERN-LHC**. In *Proceedings for Xth Quark Confinement and the Hadron Spectrum*, 2013.

[32] S. CHATRCHYAN, V. KHACHATRYAN, A. M. SIRUNYAN, ET AL. **Observation of Sequential Υ Suppression in PbPb Collisions**. *Phys. Rev. Lett.*, **109**:222301, Nov 2012.

[33] B. ABELEV, J. ADAM, D. ADAMOVÁ, ET AL. **J/ Suppression at Forward Rapidity in Pb-Pb Collisions at sNN=2.76TeV**. *Phys. Rev. Lett.*, **109**:072301, Aug 2012.

[34] D. D'ENTERRIA AND D. PERESSOUNKO. **Probing the QCD equation of state with thermal photons in nucleus–nucleus collisions at RHIC**. *The European Physical Journal C - Particles and Fields*, **46**(2):451–464, 2006.

[35] FRANK R. BROWN, FRANK P. BUTLER, HONG CHEN, ET AL. **On the existence of a phase transition for QCD with three light quarks**. *Phys. Rev. Lett.*, **65**:2491–2494, Nov 1990.

[36] JOHANN RAFELSKI AND R. HAGEDORN. **From Hadron Gas to Quark Matter II**. *Statistical Mechanics of Quarks and Hadrons*, 1980.

[37] JOHANN RAFELSKI JEAN LETESSIER. **Hadrons and Quark-Gluon Plasma**. Cambridge University Press, 2002.

[38] J RAFELSKI, J LETESSIER, AND A TOUNSI. **Strange Particles for Dense Hadronic Matter**. *ACTA PHYSICA POLONICA B*, **27**:1037–1140, 1996.

[39] T.S. BIRÓ AND J. ZIMÁNYI. **Quarkochemistry in relativistic heavy-ion collisions**. *Physics Letters B*, **113**(1):6 – 10, 1982.

[40] E. SHURYAK. **Two-stage equilibration in high energy heavy ion collisions**. *Phys. Rev. Lett.*, **68**:3270–3272, Jun 1992.

[41] J. RAFELSKI. **Strangeness enhancement**. *The European Physical Journal Special Topics*, **155**(1):139–166, 2008.

[42] W. PAULI. **Zeeman-Effect and the Dependence of Electron-Mass on the Velocity**. *Z. Phys*, **31**:373, 1925.

[43] RUDOLPH C. HWA AND C. B. YANG. **Strangeness enhancement in the parton model**. *Phys. Rev. C*, **66**:064903, Dec 2002.

[44] BERNDT MÜLLER. **Strangeness and the Quark-Gluon Plasma: Thirty Years of Discovery**. *Acta Physica Polonica B*, **43**(4), 2012.

[45] XIANGLEI ZHU. **Recent results on strangeness production at STAR**. *J.Phys.Conf.Ser.*, **509**:012004, 2014.

[46] S.V. AFANASIEV ET AL. **Energy dependence of pion and kaon production in central Pb + Pb collisions**. *Phys.Rev.*, **C66**:054902, 2002.

[47] HANS-JOACHIM DRESCHER, JOERG AICHELIN, AND KLAUS WERNER. **Strangeness suppression in proton proton collisions**. *Phys.Rev.*, **D65**:057501, 2002.

[48] MICHAL BROZ. **Mid-rapidity antibaryon-to-baryon ratios in pp and Pb–Pb collisions measured by the {ALICE} experiment**. *Nuclear Physics A*, **904–905**(0):429c – 432c, 2013. The Quark Matter 2012 Proceedings of the {XXIII} International Conference on Ultrarelativistic NucleusNucleus Collisions.

[49] E. ABBAS, B. ABELEV, J. ADAM, ET AL. **Mid-rapidity anti-baryon to baryon ratios in pp collisions at $\sqrt{s}$ = 0.9, 2.76 and 7 TeV measured by ALICE**. *The European Physical Journal C*, **73**(7):2496, 2013.

[50] B. ABELEV ET. AL. **Multi-strange baryon production at mid-rapidity in Pb–Pb collisions at $\sqrt{s_{NN}}$ = 2.76 TeV**. *Physics Letters B*, **728**(0):216 – 227, 2014.

[51] B. ABELEV, J. ADAM, D. ADAMOVÁ, ET AL. **Pion, Kaon, and Proton Production in Central Pb-Pb Collisions at sNN=2.76 TeV**. *Phys. Rev. Lett.*, **109**:252301, Dec 2012.

[52] XXIV QUARK MATTER DARMSTADT 2014. **https://indico.cern.ch/event/219436/ session/3/contribution/722** [online, cited 27/05/14].

[53] C. ADLER, Z. AHAMMED, C. ALLGOWER, ET AL. **Midrapidity Λ and $\bar{\Lambda}$ Production in Au+Au Collisions at sqrt(sNN)=130 GeV**. *Phys. Rev. Lett.*, **89**:092301, Aug 2002.

[54] K. ADCOX ET AL. **Centrality dependence of pi+ / pi-, K+ / K-, p and anti-p production from sqrt(s(NN)) = 130 GeV Au+Au collisions at RHIC**. *Phys.Rev.Lett.*, **88**:242301, 2002.

[55] PETER F. KOLB AND RALF RAPP. **Transverse flow and hadrochemistry in Au+Au collisions at sNN=200 GeV**. *Phys. Rev. C*, **67**:044903, Apr 2003.

[56] K. ADCOX, S. S. ADLER, N. N. AJITANAND, ET AL. **Single identified hadron spectra from sNN=130 GeV Au+Au collisions**. *Phys. Rev. C*, **69**:024904, Feb 2004.

[57] John Adams et al. **Measurements of identified particles at intermediate transverse momentum in the STAR experiment from Au + Au collisions at sqrt(s(NN)) =200 GeV**. *arXiv:nucl-ex/0601042*, 2006.

[58] Matthew A.C. Lamont. **Recent Results on Strangeness Production at RHIC**. *J.Phys.Conf.Ser.*, **50**:192–200, 2006.

[59] P. Lévai, G. Papp, G. Fai, et al. **Discovery of jet quenching at {RHIC} and the opacity of the produced gluon plasma**. *Nuclear Physics A*, **698**(1–4):631 – 634, 2002. 15th Int. Conf. on Ultra-Relativistic Nucleus-Nucleus Collisions (Quark Matter 2001).

[60] Rainer Fries, Vincenzo Greco, and Paul Sorensen. **Coalescence Models for Hadron Formation from Quark-Gluon Plasma**. *Annual Review of Nuclear and Particle Science*, **58**(1):177–205, 2008.

[61] A. Andronic, P. Braun-Munzinger, and J. Stachel. **Hadron production in central nucleus–nucleus collisions at chemical freeze-out**. *Nuclear Physics A*, **772**(3–4):167 – 199, 2006.

[62] Ulrich Heinz. **Primordial hadrosynthesis in the little bang**. *Nuclear Physics A*, **661**(1–4):140 – 149, 1999.

[63] M. Floris and ALICE Collaboration. **Identified particles in pp and Pb-Pb collisions at LHC energies with the ALICE detector**. *Journal of Physics G Nuclear Physics*, **38**(12):124025, December 2011.

[64] J. Cleymans and K. Redlich. **Chemical and thermal freezeout parameters from 1-A/GeV to 200-A/GeV**. *Phys.Rev.*, **C60**:054908, 1999.

[65] Michael L. Miller, Klaus Reygers, Stephen J. Sanders, and Peter Steinberg. **Glauber Modeling in High-Energy Nuclear Collisions**. *Annual Review of Nuclear and Particle Science*, **57**(1):205–243, 2007.

[66] Per Jespersen. **Stopping in pp collisions at RHIC**. *Masters Thesis; Niels Bohr Institute, Faculty of Science – University of Copenhagen*, 2008.

[67] Aage Bohr and Ben R Mottelson. **Nuclear Structure**, **1**. World Scientific, 1998.

[68] H. De Vries, C.W. De Jager, and C. De Vries. **Nuclear charge-density-distribution parameters from elastic electron scattering**. *Atomic Data and Nuclear Data Tables*, **36**(3):495 – 536, 1987.

[69] J. E. Elias, W. Busza, C. Halliwell, et al. **Projectile Dependence of Multiparticle Production in Hadron-Nucleus Interactions at 100 GeV/c**. *Phys. Rev. Lett.*, **41**:285–287, Jul 1978.

[70] W. Busza, J. E. Elias, D. F. Jacobs, et al. **Charged-Particle Multiplicity in π^--Nucleus Interactions at 100 and 175 GeV/c**. *Phys. Rev. Lett.*, **34**:836–839, Mar 1975.

[71] J. F. Owens. **Large-momentum-transfer production of direct photons, jets, and particles**. *Rev. Mod. Phys.*, **59**:465–503, Apr 1987.

[72] S. S. Adler, S. Afanasiev, C. Aidala, et al. **Centrality Dependence of Direct Photon Production in SNN=200 GeV Au+Au Collisions**. *Phys. Rev. Lett.*, **94**:232301, Jun 2005.

[73] J. W. Cronin, H. J. Frisch, M. J. Shochet, et al. **Production of hadrons at large transverse momentum at 200, 300, and 400 GeV**. *Phys. Rev. D*, **11**:3105–3123, Jun 1975.

[74] K. Geiger. **Space-time description of ultra-relativistic nuclear collisions in the {QCD} parton picture**. *Physics Reports*, **258**(4–5):237 – 376, 1995.

[75] Dinesh Kumar Srivastava. **Production and thermal equilibration of partons in relativistic heavy ion collisions: S**(1/2) = 20-A/GeV versus 200-A/GeV**. *Eur.Phys.J.C*, 1999.

[76] K.J Eskola, K Kajantie, and J Lindfors. **Quark and gluon production in high energy nucleus-nucleus collisions**. *Nuclear Physics B*, **323**(1):37 – 52, 1989.

[77] Miklos Gyulassy and Xin-Nian Wang. **HIJING 1.0: A Monte Carlo program for parton and particle production in high-energy hadronic and nuclear collisions**. *Comp. Phys. Comm.*, **83**:307, 1994.

[78] Julian Schwinger. **On Gauge Invariance and Vacuum Polarization**. *Phys. Rev.*, **82**:664–679, Jun 1951.

[79] T. Matsui. **Dynamical evolution of the quark-gluon plasma and phenomenology**. *Nuclear Physics A*, **461**(1–2):27 – 48, 1987.

[80] E.G. Ferreiro, C. Pajares, and D. Sousa. **String fusion model results on Pb–Pb central collisions at {SPS} energies**. *Physics Letters B*, **422**(1–4):314 – 318, 1998.

[81] Kunihiro Nagano. **Gluon distribution function xg (x , Q 2) and the strong coupling constant s (M 2 Z) from the analysis of structure functions**. *Journal of Physics G: Nuclear and Particle Physics*, **28**(5):737, 2002.

[82] A.H. Mueller and Jianwei Qiu. **Gluon recombination and shadowing at small values of x**. *Nuclear Physics B*, **268**(2):427 – 452, 1986.

[83] Edmond Iancu and Raju Venugopalan. **The color glass condensate and high energy scattering in QCD**, chapter 5, pages 249–363. World Scientific, 2003.

[84] Pasi Huovinen. **Hydrodynamics at RHIC and LHC: What have we learned?** *Int.J.Mod.Phys.*, **E22**:1330029, 2013.

[85] Miklos Gyulassy. **The QGP discovered at RHIC**. *arXiv:nucl-th/0403032*, pages 159–182, 2004.

[86] Bolek Wyslouch Berndt Muller, Jurgen Schukraft. **First Results from Pb+Pb collisions at the LHC**. *arXiv:1202.3233*, 2012.

[87] Barbara V. Jacak and Berndt Müller. **The Exploration of Hot Nuclear Matter**. *Science*, **337**(6092):310–314, 2012.

[88] Huichao Song. **Hydrodynamic Modeling for Relativistic Heavy Ion Collisions at RHIC and the LHC**. *arXiv:1401.0079*, 2013.

[89] Jean-Yves Ollitrault. **Anisotropy as a signature of transverse collective flow**. *Phys. Rev. D*, **46**:229–245, Jul 1992.

[90] J. Barrette et al. **Observation of anisotropic event shapes and transverse flow in Au + Au collisions at AGS energy**. *Phys.Rev.Lett.*, **73**:2532–2535, 1994.

[91] C. Alt et al. **Directed and elliptic flow of charged pions and protons in Pb + Pb collisions at 40-A-GeV and 158-A-GeV**. *Phys.Rev.*, **C68**:034903, 2003.

[92] K.H. Ackermann et al. **Elliptic flow in Au + Au collisions at (S(NN))**(1/2) = 130 GeV**. *Phys.Rev.Lett.*, **86**:402–407, 2001.

[93] K. Aamodt, B. Abelev, A. Abrahantes Quintana, et al. **Elliptic Flow of Charged Particles in Pb-Pb Collisions at sNN=2.76 TeV**. *Phys. Rev. Lett.*, **105**:252302, Dec 2010.

[94] SergeiA. Voloshin, ArthurM. Poskanzer, and Raimond Snellings. **Collective Phenomena in Non-Central Nuclear Collisions**, pages 293–333. Springer Berlin Heidelberg, 2010.

[95] S. Voloshin and Y. Zhang. **Flow study in relativistic nuclear collisions by Fourier expansion of Azimuthal particle distributions**. *Z.Phys.*, **C70**:665–672, 1996.

[96] Nicolas Borghini, Phuong Mai Dinh, and Jean-Yves Ollitrault. **Flow analysis from multiparticle azimuthal correlations**. *Phys.Rev.*, **C64**:054901, 2001.

[97] Ulrich Heinz, Chun Shen, and Huichao Song. **The viscosity of quark-gluon plasma at RHIC and the LHC**. *AIP Conference Proceedings*, **1441**(1):766–770, 2012.

[98] U. Heinz. **The Little Bang: searching for quark–gluon matter in relativistic heavy-ion collisions**. *Nuclear Physics A*, **685**(1–4):414 – 431, 2001. Nucleus-Nucleus Collisions 2000.

[99] R. J. Fries, B. Müller, C. Nonaka, and S. A. Bass. **Hadron production in heavy ion collisions: Fragmentation and recombination from a dense parton phase**. *Phys. Rev. C*, **68**:044902, Oct 2003.

[100] U. A. Wiedemann. **Jet Quenching in Heavy Ion Collisions**. *Landolt Börnstein*, **23**:521, 2010.

[101] Ringaile Placakyte. **Parton Distribution Functions**. *Proceedings, 31st International Conference on Physics in collisions (PIC 2011)*, 2011.

[102] DESY. **http://www-h1.desy.de/** [online, cited 10/04/14].

[103] Bo Andersson, G. Gustafson, G. Ingelman, and T. Sjostrand. **Parton Fragmentation and String Dynamics**. *Phys.Rept.*, **97**:31–145, 1983.

[104] Gregory Soyez. **Recent progress in defining jets**. *Nucl.Phys.Proc.Suppl.*, **191**:131–140, 2009.

[105] J.D. Bjorken. **Energy Loss of Energetic Partons in Quark - Gluon Plasma: Possible Extinction of High p(t) Jets in Hadron - Hadron Collisions**. *FERMILAB-PUB-82-059-THY*, 1982.

[106] Konrad Kleinknecht. **Detectors for Particle Radiation**. Cambridge University Press, 2 edition, 1998.

[107] Miklos Gyulassy and Michael Plümer. **Jet quenching in dense matter**. *Physics Letters B*, **243**(4):432 – 438, 1990.

[108] R. Baier, Yuri L. Dokshitzer, Alfred H. Mueller, S. Peigne, and D. Schiff. **Radiative energy loss of high-energy quarks and gluons in a finite volume quark - gluon plasma**. *Nucl.Phys.*, **B483**:291–320, 1997.

[109] R. Baier, Yuri L. Dokshitzer, Alfred H. Mueller, S. Peigne, and D. Schiff. **Radiative energy loss and p(T) broadening of high-energy partons in nuclei**. *Nucl.Phys.*, **B484**:265–282, 1997.

[110] J. Adams, M. M. Aggarwal, Z. Ahammed, et al. **Direct Observation of Dijets in Central Au–Au Collisions at $\sqrt{s_{\mathrm{NN}}} = 200$ GeV**. *Phys. Rev. Lett.*, **97**:162301, Oct 2006.

[111] K. Aamodt, B. Abelev, A. Abrahantes Quintana, et al. **Particle-Yield Modification in Jetlike Azimuthal Dihadron Correlations in Pb-Pb Collisions at $\sqrt{s_{\mathrm{NN}}} = 2.76$ TeV**. *Phys. Rev. Lett.*, **108**:092301, Mar 2012.

[112] AAD, G. ET AL, ATLAS COLLABORATION. **Observation of a Centrality-Dependent Dijet Asymmetry in Lead-Lead Collisions at $\sqrt{s_{NN}} = 2.76$ TeV with the ATLAS Detector at the LHC**. *Phys. Rev. Lett.*, **105**:252303, Dec 2010.

[113] SERGUEI CHATRCHYAN ET AL. **Observation and studies of jet quenching in PbPb collisions at nucleon-nucleon center-of-mass energy = 2.76 TeV**. *Phys.Rev.*, **C84**:024906, 2011.

[114] ANDREAS MORSCH. **Jet-like near-side peak shapes in Pb–Pb collisions at with {ALICE}**. *Nuclear Physics A*, **910–911**(0):281 – 284, 2013. Hard Probes 2012 5th International Conference on Hard and Electromagnetic Probes of High-Energy Nuclear Collisions.

[115] S. SAPETA AND U.A. WIEDEMANN. **Jet hadrochemistry as a characteristic of jet quenching**. *The European Physical Journal C*, **55**(2):293–302, 2008.

[116] K.J. ESKOLA, V.J. KOLHINEN, AND C.A. SALGADO. **The scale dependent nuclear effects in parton distributions for practical applications**. *The European Physical Journal C - Particles and Fields*, **9**(1):61–68, 1999.

[117] SERGUEI CHATRCHYAN ET AL. **Study of high-pT charged particle suppression in PbPb compared to pp collisions at $\sqrt{s_{NN}} = 2.76$ TeV**. *Eur.Phys.J.*, **C72**:1945, 2012.

[118] R. BELLWIED AND C. MARKERT. **In-medium hadronization in the deconfined matter at RHIC and LHC**. *Phys.Lett.*, **B691**:208–213, 2010.

[119] P. AURENCHE AND B.G. ZAKHAROV. **Jet color chemistry and anomalous baryon production in AA-collisions**. *The European Physical Journal C*, **71**(12):1–12, 2011.

[120] V. GRECO, C.M. KO, AND P. LEVAI. **Parton coalescence at RHIC**. *Phys.Rev.*, **C68**:034904, 2003.

[121] R.C.HWA. **Physics Revealed at Intermediate p_T**. *J.Phys.G.*, **35**:104017, 2008.

[122] L. RAVAGLI AND R. RAPP. **Quark Coalescence based on a Transport Equation**. *Phys.Lett.*, **B655**:126–131, 2007.

[123] A. ADARE ET AL. **Scaling properties of azimuthal anisotropy in Au+Au and Cu+Cu collisions at s(NN) = 200-GeV**. *Phys.Rev.Lett.*, **98**:162301, 2007.

[124] RUDOLPH C. HWA AND C.B. YANG. **Recombination of shower partons at high p_T in heavy ion collisions**. *Phys. Rev. C*, **70**:024905, 2004.

[125] HUICHAO SONG AND ULRICH W. HEINZ. **Suppression of elliptic flow in a minimally viscous quark-gluon plasma**. *Phys. Lett. B*, **658**:279–283, 2008.

[126] Huichao Song and Ulrich W. Heinz. **Causal viscous hydrodynamics in 2+1 dimensions for relativistic heavy-ion collisions**. *Phys. Rev. C*, **77**:064901, 2008.

[127] Huichao Song and Ulrich W. Heinz. **Multiplicity scaling in ideal and viscous hydrodynamics**. *Phys. Rev. C*, **78**:024902, 2008.

[128] K. Werner, Iu. Karpenko, M. Bleicher, T. Pierog, and S. Porteboeuf-Houssais. **Jets, Bulk Matter, and their Interaction in Heavy Ion Collisions at Several TeV**. *Phys. Rev. C*, **85**:064907, 2012.

[129] K. Werner. **Lambda-to-Kaon Ratio Enhancement in Heavy Ion Collisions at Several TeV**. *Phys. Rev. Lett.*, **109**:102301, Sep 2012.

[130] ALICE Collaboration, F Carminati, P Foka, et al. **ALICE: Physics Performance Report, Volume I**. *Journal of Physics G: Nuclear and Particle Physics*, **30**(11):1517, 2004.

[131] ALICE Collaboration, B Alessandro, F Antinori, et al. **ALICE: Physics Performance Report, Volume II**. *Journal of Physics G: Nuclear and Particle Physics*, **32**(10):1295, 2006.

[132] Lyndon Evans and Philip Bryant. **LHC Machine**. *Journal of Instrumentation*, **3**(08):S08001, 2008.

[133] **http://www.atlas.ch/photos/lhc.html** [online, cited 22/04/14].

[134] Georges Aad et al. **Observation of a new particle in the search for the Standard Model Higgs boson with the ATLAS detector at the LHC**. *Physics Letters B*, **716**:1–29, 2012.

[135] S. Chatrchyan, V. Khachatryan, A.M. Sirunyan, et al. **Observation of a new boson at a mass of 125 GeV with the CMS experiment at the LHC**. *Physics Letters B*, **716**(1):30 – 61, 2012.

[136] **http://www.fnal.gov/pub/tevatron/** [online, cited 22/04/14].

[137] M Lamont. **The First Years of LHC Operation for Luminosity Production**. In *Proceedings of IPAC2013, Shanghai, China*, pages 6–10, 2013.

[138] CMS Luminosity. **https://twiki.cern.ch/twiki/bin/view/CMSPublic/LumiPublicResults** [online].

[139] LHC Programme Coordination. **http://lpc.web.cern.ch/lpc/** [online].

[140] **https://lhcb.web.cern.ch/lhcb/** [online, cited 22/04/14].

[141] ATLAS. **http://atlas.ch/** [online, cited 22/04/14].

[142] CMS. **http://cms.web.cern.ch/** [online, cited 22/04/14].

[143] K. Aamodt et al. **The ALICE experiment at the CERN LHC**. *JINST*, **3**:S08002, 2008.

[144] K. Aamodt, A. Abrahantes Quintana, D. Adamová, et al. **Centrality Dependence of the Charged-Particle Multiplicity Density at Midrapidity in Pb-Pb Collisions at sNN=2.76 TeV**. *Phys. Rev. Lett.*, **106**:032301, Jan 2011.

[145] Hans Rudolf Schmidt and the Alice Experiment. **The ALICE TPC: Status and perspectives**. *Journal of Physics: Conference Series*, **230**(1):012023, 2010.

[146] K. Aamodt et al (ALICE Collaboration). **The ALICE experiment at the CERN LHC**. *JINST*, **3**, 2008.

[147] Betty Bezverkhny Abelev et al. **Performance of the ALICE Experiment at the CERN LHC**. *arXiv:1402.4476*, 2014.

[148] H. Bethe. **Zur Theorie des Durchgangs schneller Korpuskularstrahlen durch Materie**. *Annalen der Physik*, **397**(3):325–400, 1930.

[149] F. Bloch. **Zur Bremsung rasch bewegter Teilchen beim Durchgang durch Materie**. *Annalen der Physik*, **408**(3):285–320, 1933.

[150] B. Abelev et. al. **Measurement of inelastic, single- and double-diffraction cross sections in proton–proton collisions at the LHC with ALICE**. *The European Physical Journal C*, **73**(6):1–20, 2013.

[151] K. Aamodt et al, ALICE collaboration. **Strange particle production in proton-proton collisions at $\sqrt{s} = 0.9$ TeV with ALICE at the LHC**. *The European Physical Journal C - Particles and Fields*, **71**:1–24, 2011. 10.1140/epjc/s10052-011-1594-5.

[152] Presentation by L. Hanratty at Strangeness in Quark Matter 2013, Birmingham UK. **http://indico.cern.ch/event/204432/session/11/contribution/74** [online, cited 26/08/14].

[153] J. Podolanski and R. Armenteros. **III. Analysis of V-events**. *Philosophical Magazine Series 7*, **45**(360):13–30, 1954.

[154] Torbjorn Sjostrand, Stephen Mrenna, and Peter Z. Skands. **PYTHIA 6.4 Physics and Manual**. *JHEP*, **0605**:026, 2006.

[155] Rene Brun, Federico Carminati, and Simone Giani. **GEANT Detector Description and Simulation Tool**. CERN Program Library Long Writeup W5013, 1994.

[156] ALICE Collaboration. **Technical Design Report: AliRoot, ALICE Offline Simulation, Reconstruction, and Analysis Framework**. *CERN/LHCC*, **2005-18**, 2005.

[157] B. Abelev et. al. **Multi-strange baryon production in** pp **collisions at** $\sqrt{s} = \mathbf{7}$ TeV **with ALICE**. *Physics Letters B*, **712**(4-5):309–318, 2012.

[158] Domenico Colella. **Multi-strange baryon production in Pb–Pb and** pp **collisions at** $\sqrt{s_{\mathrm{NN}}} = \mathbf{2.76}$ TeV **with ALICE**. In *Strangeness in Quark Matter*, 2013.

[159] Betty Abelev et al. **Pion, Kaon, and Proton Production in Central Pb-Pb Collisions at** $\sqrt{s_{\mathrm{NN}}}$=2.76 TeV. *Phys. Rev. Lett.*, **109**:252301, Dec 2012.

[160] ALICE Collaboration. **Production of charged pions, kaons and protons at large transverse momenta in** pp **and Pb–Pb collisions at** $\sqrt{s_{\mathrm{NN}}} = \mathbf{2.76}$ TeV. *arXiv:1401.1250*, Jan 2014.

[161] G. Agakishiev et al. **Strangeness Enhancement in Cu+Cu and Au+Au Collisions at** $\sqrt{s_{NN}} = 200$ **GeV**. *Phys. Rev. Lett.*, **108**:072301, 2012.

[162] Antonio Ortiz Velasquez. **Production of pions, kaons and protons at high in Pb–Pb collisions**. *Nuclear Physics A*, **904–905**(0):763c – 766c, 2013. The Quark Matter 2012 Proceedings of the {XXIII} International Conference on Ultrarelativistic NucleusNucleus Collisions.

[163] XXIV Quark Matter Darmstadt 2014. **https://indico.cern.ch/event/219436/ session/18/contribution/216** [online, cited 27/05/14].

[164] Constantino Tsallis. **Possible Generalization of Boltzmann-Gibbs Statistics**. *J. Stat. Phys. 52 479*, **52**(1/2):479, 1988.

[165] B. I. Abelev, J. Adams, M. M. Aggarwal, et al. **Strange particle production in p+p collisions at** $\sqrt{s}=$ **200** GeV. *Phys. Rev. C*, **75**:064901, Jun 2007.

[166] Jan Steinheimer, Jörg Aichelin, and Marcus Bleicher. **Nonthermal p/pi Ratio at LHC as a Consequence of Hadronic Final State Interactions**. *Phys. Rev. Lett.*, **110**:042501, Jan 2013.

[167] Jörn Putschke and the STAR Collaboration. **Intra-jet correlations of high- p t hadrons from STAR**. *Journal of Physics G: Nuclear and Particle Physics*, **34**(8):S679, 2007.

[168] T. Aaltonen et al. **Production of kshort, kstar(892)and phi(1020) in minimum bias events and kshort and lambda in jets in pbar p collisions at sqrt(s)=1.96 TeV**. *Phys.Rev.*, **D88**:092005, 2013.

[169] B. Abelev, J. Adam, D. Adamová, et al. **Transverse Momentum Distribution and Nuclear Modification Factor of Charged Particles in p–Pb Collisions at** $\sqrt{s_{\mathrm{NN}}} = \mathbf{5.02}$ TeV. *Phys. Rev. Lett.*, **110**:082302, Feb 2013.

[170] Serguei Chatrchyan et al. **Study of the production of charged pions, kaons, and protons in pPb collisions at $\sqrt{s_{NN}} = 5.02$ TeV.** *arXiv:1307.3442*, July 2013.

[171] Betty Bezverkhny Abelev et al. **Multiplicity Dependence of Pion, Kaon, Proton and Lambda Production in p-Pb Collisions at $\sqrt{(s_N N)} = 5.02$ TeV.** *Phys.Lett.*, **B728**:25–38, 2014.

[172] K. Werner, M. Bleicher, B. Guiot, Iu. Karpenko, and T. Pierog. **Evidence for flow in pPb collisions at 5 TeV from v2 mass splitting.** *arXiv:1307.4379*, July 2013.

[173] Vardan Khachatryan et al. **Observation of Long-Range Near-Side Angular Correlations in Proton-Proton Collisions at the LHC.** *JHEP*, **1009**:091, 2010.

[174] K. Werner. **Flow in proton-nucleus collisions.** *PoS*, **EPS-HEP2013**:201, 2014.

Appendix A

K_S^0 and Λ Production in Pb–Pb Collisions at $\sqrt{s_{\mathrm{NN}}} = 2.76$ TeV [1]

K^0_S and Λ Production in Pb-Pb Collisions at $\sqrt{s_{NN}}$ = 2.76 TeV

B. Abelev *et al.*[*]

(ALICE Collaboration)

The ALICE measurement of K^0_S and Λ production at midrapidity in Pb-Pb collisions at $\sqrt{s_{NN}}$ = 2.76 TeV is presented. The transverse momentum (p_T) spectra are shown for several collision centrality intervals and in the p_T range from 0.4 GeV/c (0.6 GeV/c for Λ) to 12 GeV/c. The p_T dependence of the Λ/K^0_S ratios exhibits maxima in the vicinity of 3 GeV/c, and the positions of the maxima shift towards higher p_T with increasing collision centrality. The magnitude of these maxima increases by almost a factor of three between most peripheral and most central Pb-Pb collisions. This baryon excess at intermediate p_T is not observed in pp interactions at $\sqrt{s}$ = 0.9 TeV and at $\sqrt{s}$ = 7 TeV. Qualitatively, the baryon enhancement in heavy-ion collisions is expected from radial flow. However, the measured p_T spectra above 2 GeV/c progressively decouple from hydrodynamical-model calculations. For higher values of p_T, models that incorporate the influence of the medium on the fragmentation and hadronization processes describe qualitatively the p_T dependence of the Λ/K^0_S ratio.

Collisions of heavy nuclei at ultrarelativistic energies are used to investigate a deconfined high temperature and density state of nuclear matter, the quark-gluon plasma. It was observed at the Relativistic Heavy Ion Collider (RHIC) [1,2], that the Λ/K^0_S and p/π ratios at intermediate p_T (2–6 GeV/c) are markedly enhanced in central heavy-ion collisions when compared with peripheral or pp results. A similar observation was also made at the Super Proton Synchrotron [3]. These observations led to a revival and further development of models based on the premise that deconfinement opens an additional mechanism for hadronization by allowing two or three soft quarks from the bulk to combine forming a meson or a baryon [4,5]. If the (anti-)quarks generated by (mini)jet fragmentation are also involved in recombination [6], the baryon enhancement could even extend up to 10–20 GeV/c [7].

The relative contribution of different hadronization mechanisms changes with hadron momentum. While at intermediate p_T recombination might be dominating, hydrodynamical radial flow contributes to the baryon enhancement at lower p_T, and fragmentation could take over at higher p_T. For this reason, it is important to identify baryons and mesons in a wide momentum range, which can be achieved by the topological decay reconstruction of K^0_S and Λ particles.

In this Letter we present the K^0_S and Λ p_T spectra and the Λ/K^0_S ratios from Pb-Pb collisions at $\sqrt{s_{NN}}$ = 2.76 TeV recorded by the ALICE Collaboration [8] in November

2010. The p_T dependence of the Λ/K^0_S ratios is compared with pp results obtained at $\sqrt{s}$ = 0.9 and 7 TeV, that bracket the Pb-Pb measurements in energy.

For the analysis presented here, we used the time projection chamber (TPC) and the inner tracking system to reconstruct charged particle tracks within the pseudorapidity interval of $|\eta| < 0.9$. For the offline analysis, we accepted only events with the primary vertex position within ± 10 cm of the detector center and with at least one particle hit in each of the trigger detectors (Silicon Pixel Detector, VZERO-A and VZERO-C). The events were classified by the collision centrality, based on the amplitude distribution in the VZERO counters fitted with a Glauber model description as discussed in Ref. [9]. The final data sample contained 1.6×10^7 events in the 0%–90% centrality range, corresponding to an integrated luminosity of 2.3 ± 0.1 μb^{-1}.

The weakly decaying K^0_S and Λ were reconstructed using their distinctive V-shaped decay topology in the channels (and branching ratios) $K^0_S \to \pi^+ \pi^-$ (69.2%) and $\Lambda \to p\pi^-$ (63.9%) [10]. The reconstruction method forms so-called V0 decay candidates and the details are described in Ref. [11]. Because of the large combinatorial background in Pb-Pb collisions, a number of topological selections had to be more restrictive than those used in the pp analysis [11]. In addition, we retained only the V0 candidates reconstructed in a rapidity window of $|y| < 0.5$, with their decay-product tracks within the acceptance window $|\eta| < 0.8$. To further suppress the background, we kept only V0 candidates satisfying the cut on the proper decay length $l_T m/p_T < 3c\tau(4c\tau)$, where l_T and m are the V0 transverse decay length and nominal Λ (K^0_S) mass [10], and $c\tau$ is 7.89 cm (2.68 cm) for Λ (K^0_S) [10]. For the Λ candidates with $p_T < 1.2$ GeV/c, a three-standard-deviation particle-identification cut on the difference

between the specific energy loss (dE/dx) measured in the TPC and that defined by a momentum-dependent parametrization of the Bethe-Bloch curve was applied for the proton decay-product tracks. To reduce the contamination of Λ reconstructed as K_S^0, an additional selection was applied in the Armenteros-Podolanski variables [12] of K_S^0 candidates, rejecting candidates with $p_T^{\mathrm{arm}} < 0.2 \times |\alpha^{\mathrm{arm}}|$. Here, p_T^{arm} is the projection of the positively (or negatively) charged decay-product momentum on the plane perpendicular to the V0 momentum. The decay asymmetry parameter α^{arm} is defined as $\alpha^{\mathrm{arm}} = (p_{\parallel}^+ - p_{\parallel}^-)/(p_{\parallel}^+ + p_{\parallel}^-)$, where $p_{\parallel}^+ (p_{\parallel}^-)$ is the projection of the positively (negatively) charged decay-product momentum on the momentum of the V0. The minimal radius of the fiducial volume of the secondary vertex reconstruction was chosen to be 5 cm to minimize systematic effects introduced by efficiency corrections. It was verified that the decay-length distributions reconstructed within this volume were exponential and agreed with the $c\tau$ values given in the literature [10].

The raw yield in each p_T bin was extracted from the invariant-mass distribution obtained for this momentum bin. The raw yield was calculated by subtracting a fit to the background from the total number of V0 candidates in the peak region. This region was $\pm 5\sigma$ for K_S^0, and $\pm(3.5\sigma + 2 \text{ MeV}/c^2)$ (to better account for tails in the mass distribution at low p_T) for Λ. The σ was obtained by a Gaussian fit to the mass peaks. The background was determined by fitting polynomials of first or second order to sideband regions left and right of the peak region.

The overall reconstruction efficiency was extracted from a procedure based on HIJING events [13] and the GEANT3 [14] transport Monte Carlo simulation package, followed by detector simulations and reconstruction done with the ALICE software framework [15]. The efficiency included the geometrical acceptance of the detectors, track reconstruction efficiency, the efficiency of the applied topological selection cuts, and the branching ratios for the V0 decays. The typical efficiencies for both particles were about 30% for $p_T > 4 \text{ GeV}/c$, dropping to 0 at $p_T \sim 0.3 \text{ GeV}/c$. The efficiencies did not change with the event centrality for p_T above a few GeV/c. However, at lower p_T, they were found to be dependent on the event centrality. For Λ at $p_T < 0.9 \text{ GeV}/c$ the difference was about a factor 2 between the 0%–5% and 80%–90% centrality intervals. The final momentum spectra were corrected in each centrality bin separately.

The spectra of Λ were in addition corrected for the feed-down contribution coming from the weak decays of Ξ^- and Ξ^0. A two-dimensional response matrix, correlating the p_T of the detected decay Λ with the p_T of the decayed Ξ, was generated from Monte-Carlo simulations. By normalizing this matrix to the measured Ξ^- spectra [16], the distributions of the feed-down Λ were determined and subtracted from the inclusive Λ spectra. The phase space

distributions and total yields for the Ξ^0 were assumed to be the same as for the Ξ^-. The feed-down correction was found to be a smooth function of p_T with a maximum of about 23% at $p_T \sim 1 \text{ GeV}/c$ and monotonically decreasing to 0% at $p_T > 12 \text{ GeV}/c$. As a function of centrality, this correction changed by only a few percent.

Since the ratio Ω^-/Ξ^- in Pb-Pb collisions of different centralities at $\sqrt{s_{NN}} = 2.76$ TeV does not exceed 0.18 [16], and taking into account that the branching ratio $\Omega^- \to \Lambda K^-$ is 67.8% [10], the feed-down contribution from decays of Ω^- baryons is less than 1.5%, which is negligible compared with other sources of uncertainty (see below). We did not correct the Λ spectra for the feed-down from non-weak decays of Σ^0 and the $\Sigma(1385)$ family.

The fraction of Λ's produced in hadronic interactions with the detector material was estimated using the Monte Carlo simulations mentioned above, found to be less than 1%, and was neglected.

The following main sources of systematic uncertainty were considered: raw yield extraction, feed-down, efficiency corrections, and the uncertainty on the amount of crossed material. These were added in quadrature to yield the overall systematic uncertainty on the p_T spectra for all centralities.

The systematic uncertainties on the raw yields were estimated by using different functional shapes for the background and by varying the fitting range. Over the considered momentum range, the obtained raw yields varied within 3% for K_S^0 and 4%–7% for Λ.

As a measure for the systematic uncertainty of the feed-down correction, we used the spread of the values determined for different centrality ranges with respect to the feed-down correction estimated for minimum bias events. This deviation was found to be about 5% relative to the overall Λ yield.

The systematic uncertainty associated with the efficiency correction was evaluated by varying one-by-one the topological, track selection, and particle-identification cuts. The cut variations were chosen such that the extracted uncorrected yield of the K_S^0 and Λ would change by 10%. To measure the systematic uncertainty related to each cut, we used as a reference the corrected spectrum obtained with the nominal cut values. For Λ, the feed-down correction was reevaluated and taken into account for every variation of the cut on the cosine of the pointing angle. The overall p_T-dependent systematic uncertainty associated with the efficiency correction was then estimated by choosing the maximal (over all cut variations) deviation between varied and nominal spectra values obtained in each momentum bin. For the momentum range considered, this systematic uncertainty was determined to be 4%–6% for both K_S^0 and Λ.

The systematic uncertainty introduced because of possible imperfections in the description of detector material in the simulations was estimated in Ref. [11] and amounted to 1.1%–1.4% for K_S^0 and 1.6%–3.4% for Λ.
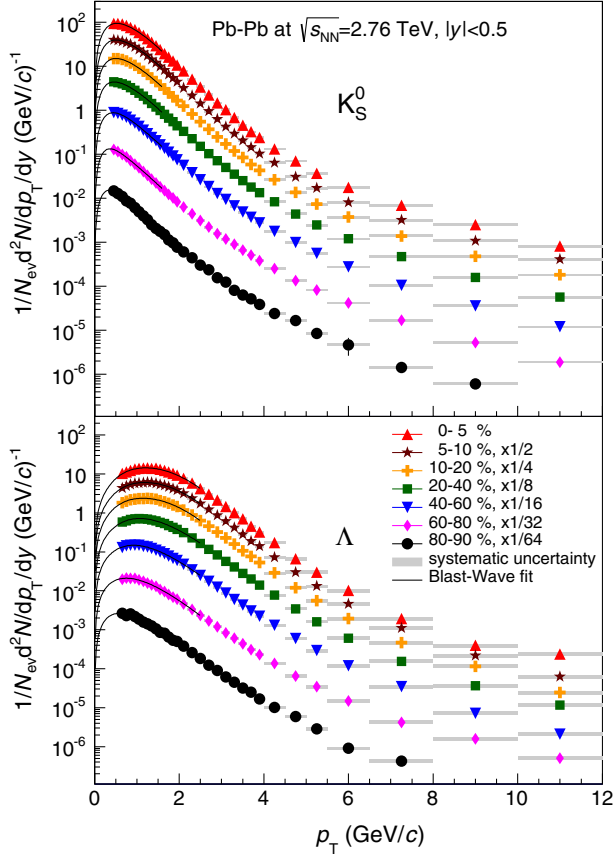
FIG. 1 (color online). K_S^0 and Λ p_T spectra for different event centrality intervals. The curves represent results of blast-wave fits [17].

Since the systematic uncertainties related to the efficiency correction are correlated for the Λ and K_S^0 spectra, they partially cancel in the Λ/K_S^0 ratios. These uncertainties were evaluated by dividing Λ and K_S^0 spectra obtained with the same cut variations and found to be half the size of those that would be obtained if the uncertainties of the Λ and K_S^0 spectra were assumed to be uncorrelated. Altogether, over the considered momentum range, the maximal systematic uncertainty for the measured Λ/K_S^0 ratios was found to be about 10%.

The corrected p_T spectra, fitted using the blast-wave parameterization described in Ref. [17], are shown in Fig. 1. The fit range in p_T was from the lowest measured point up to 2.5 GeV/c (1.6 GeV/c) for Λ (K_S^0). The fitting functions were used to extrapolate the spectra to zero p_T to extract integrated yields dN/dy. The results are given in Table I. The systematic uncertainties of the integrated yields were determined by shifting the data points of the spectra simultaneously within their individual systematic uncertainties and reapplying the fitting and integration procedure. In addition, an extrapolation uncertainty was estimated, by using alternative (polynomial, exponential, and Lévy-Tsallis [18,19]) functions fitted to the low-momentum part of the spectrum, and the corresponding difference in obtained values was added in quadrature.

The p_T dependence of the Λ/K_S^0 ratios is presented in Fig. 2 (left). The Λ/K_S^0 ratios observed in pp events at $\sqrt{s} = 0.9$ [11] and 7 TeV [20] agree within uncertainties over the presented p_T range, and they bound in energy the Pb-Pb results reported here. The ratio measured in the most peripheral Pb-Pb collisions is compatible with the pp measurement, where there is a maximum of about 0.55 at $p_T \sim 2$ GeV/c. As the centrality of the Pb-Pb collisions increases, the maximum value of the ratio also increases and its position shifts towards higher momenta. The ratio peaks at a value of about 1.6 at $p_T \sim 3.2$ GeV/c for the most central Pb-Pb collisions. This observation may be contrasted to the ratio of the integrated Λ and K_S^0 yields which does not change with centrality (Table I). At momenta above $p_T \sim 7$ GeV/c, the Λ/K_S^0 ratio is independent of collision centrality and p_T, within the uncertainties, and compatible with that measured in pp events.

A comparison with similar measurements performed by the STAR Collaboration in Au-Au collisions at $\sqrt{s_{NN}} = 200$ GeV is shown in Fig. 2 (right). Since the antibaryon-to-baryon ratio at the LHC is consistent with unity for all p_T [21,22], the Λ/K_S^0 and $\bar{\Lambda}/K_S^0$ ratios are identical and we show only the former. The STAR Λ/K_S^0 and $\bar{\Lambda}/K_S^0$ ratios shown are constructed by dividing the corresponding p_T spectra taken from Ref. [23]. The quoted 15% p_T-independent feed-down contribution was subtracted from the Λ and $\bar{\Lambda}$ spectra. The shape of the distributions

TABLE I. Integrated yields, dN/dy, for Λ and K_S^0 with uncertainties which are dominantly systematic. A blast-wave fit is used to extrapolate to zero p_T. Fractions of extrapolated yield are specified. Ratios of integrated yields, Λ/K_S^0, for each centrality bin with the total uncertainty, mainly from systematic sources, are shown.

		0%–5%	5%–10%	10%–20%	20%–40%	40%–60%	60%–80%	80%–90%
Λ	dN/dy	26 ± 3	22 ± 2	17 ± 2	10 ± 1	3.8 ± 0.4	1.0 ± 0.1	0.21 ± 0.03
	$p_T < 0.6$ GeV/c frac.	10%	11%	12%	14%	18%	24%	32%
K_S^0	dN/dy	110 ± 10	90 ± 6	68 ± 5	39 ± 3	14 ± 1	3.9 ± 0.2	0.85 ± 0.09
	$p_T < 0.4$ GeV/c frac.	20%	21%	21%	23%	25%	31%	33%
	Ratio dN/dy Λ/K_S^0	0.24 ± 0.02	0.24 ± 0.02	0.25 ± 0.02	0.25 ± 0.02	0.26 ± 0.03	0.25 ± 0.02	0.25 ± 0.02
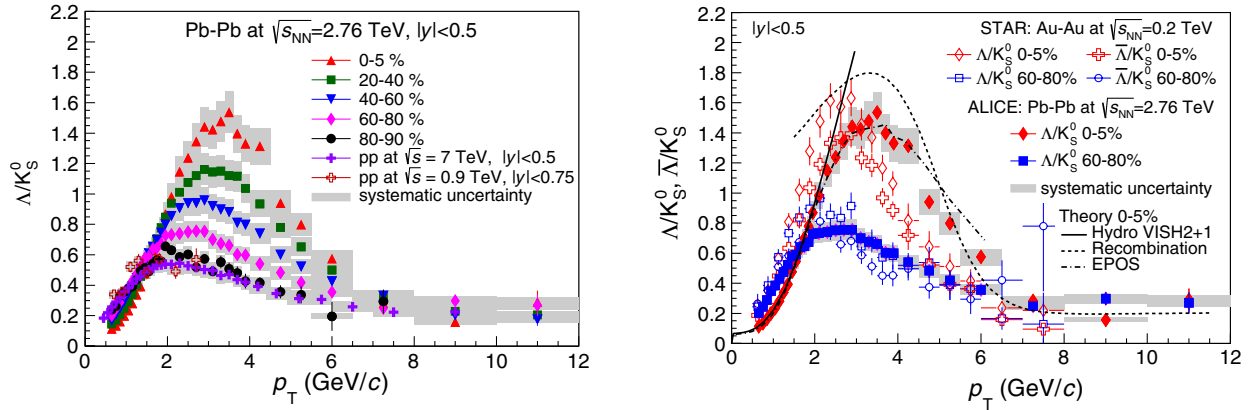
FIG. 2 (color online). Left: Λ/K_S^0 ratios as a function of p_T for different event centrality intervals in Pb-Pb collisions at $\sqrt{s_{NN}} =$ 2.76 TeV and pp collisions at $\sqrt{s} = 0.9$ [11] and 7 TeV [20]. Right: selected Λ/K_S^0 ratios as a function of p_T compared with Λ/K_S^0 and $\bar{\Lambda}/K_S^0$ ratios measured in Au-Au collisions at $\sqrt{s_{NN}} = 200$ GeV [23]. The solid, dashed, and dot-dashed lines show the corresponding ratios from a hydrodynamical model [24–26], a recombination model [28] and the EPOS model [29], respectively.

of Λ/K_S^0 and $\bar{\Lambda}/K_S^0$ are the same but they are offset by about 20% and have peak values around 10% higher, and, respectively, lower, than the ALICE data. This comparison between LHC and RHIC data shows that the position of the maximum shifts towards higher p_T as the beam energy increases. It is also seen that the baryon enhancement in central nucleus-nucleus collisions at the LHC decreases less rapidly with p_T, and, at $p_T \sim 6$ GeV/c, it is a factor of 2 higher compared with that at RHIC.

Also shown in the right panel of Fig. 2 is a hydro-dynamical model calculation [24–26] for most central collisions, which describes the Λ/K_S^0 ratio up to p_T about 2 GeV/c rather well, but for higher p_T progressively deviates from the data. Such decoupling between the calculations and measurements is already seen in the comparison with p_T spectra [27]. The agreement for other charged particles is improved when the hydrodynamical calculations are coupled to a final-state rescattering model [28]. Therefore, it would be interesting to compare these data and their centrality evolution with such treatment. For higher p_T, a recombination model calculation [5] is presented (Fig. 2, right). It approximately reproduces the shape, but overestimates the baryon enhancement by about 15%. We also show a comparison of the EPOS model calculations [29] with the current data. This model takes into account the interaction between jets and the hydro-dynamically expanding medium and arrives at a good description of the data.

In conclusion, we note that the excess of baryons at intermediate p_T, exhibiting such a strong centrality dependence in Pb-Pb collisions at $\sqrt{s_{NN}} = 2.76$ TeV, does not reveal itself in pp collisions at the center-of-mass energy up to $\sqrt{s} = 7$ TeV. For $p_T > 7$ GeV/c, the measured Λ/K_S^0 ratios become constant within our uncertainties for all centralities and equal to that of the previously reported pp data. This agreement between collision systems suggests that the ratio of fragmentation into Λ and K_S^0

at high p_T, even in central collisions, is not modified by the medium.

As the collision energy and centrality increase, the maximum of the $\Lambda(\bar{\Lambda})/K_S^0$ ratio shifts towards higher p_T, which is in qualitative agreement with the effect of increased radial flow, as predicted in Ref. [4]. The ratio of integrated Λ and K_S^0 yields does not, within uncertainties, change with centrality and is equal to that measured in pp collisions at 0.9 and 7 TeV. This suggests that the baryon enhancement at intermediate p_T is predominantly due to a redistribution of baryons and mesons over the momentum range rather than due to an additional baryon production channel progressively opening up in more central heavy-ion collisions.

The width of the baryon enhancement peak increases with the beam energy. However, contrary to expectations [7], the effect at the LHC is still restricted to an intermediate-momentum range and is not observed at high p_T. This puts constraints on parameters of particle production models involving coalescence of quarks generated in hard parton interactions [30].

Qualitatively, the baryon enhancement presented here as p_T dependence of Λ/K_S^0 ratios, is described in the low-p_T region (below 2 GeV/c) by collective hydrodynamical radial flow. In the high-p_T region (above 7–8 GeV/c), it is very similar to pp results, indicating that there it is dominated by hard processes and fragmentation. Our data provide evidence for the need to include the effect of the hydrodynamical expansion of the medium formed in Pb-Pb collisions in the mechanisms of hadronization.

[1] S. S. Adler *et al.* (PHENIX Collaboration), Phys. Rev. Lett. **91**, 172301 (2003).

[2] J. Adams *et al.* (STAR Collaboration), arXiv:nucl-ex/0601042.

[3] T. Schuster *et al.* (NA49 Collaboration), J. Phys. G **32**, S479 (2006).

[4] R. Fries and B. Müller, Eur. Phys. J. C **34**, S279 (2004).

[5] R. J. Fries, V. Greco, and P. Sorensen, Annu. Rev. Nucl. Part. Sci. **58**, 177 (2008).

[6] R. C. Hwa and C. B. Yang, Phys. Rev. C **70**, 024905 (2004).

[7] R. C. Hwa, J. Phys. G **35**, 104017 (2008).

[8] K. Aamodt *et al.* (ALICE Collaboration), JINST **3**, S08002 (2008).

[9] B. Abelev *et al.* (ALICE Collaboration), arXiv:1301.4361.

[10] J. Beringer *et al.* (Particle Data Group), Phys. Rev. D **86**, 010001 (2012).

[11] K. Aamodt *et al.* (ALICE Collaboration), Eur. Phys. J. C **71**, 1594 (2011).

[12] J. Podolanski and R. Armenteros, Philos. Mag. **45**, 13 (1954).

[13] M. Gyulassy and X.-N. Wang, Comput. Phys. Commun. **83**, 307 (1994).

[14] R. Brun, F. Carminati, and S. Giani, "CERN Program Library Long Writeup," 1994.

[15] ALICE Collaboration, CERN/LHCC 2005-18, "Technical Design Report: AliRoot, ALICE Offline Simulation, Reconstruction, and Analysis Framework," 2005.

[16] B. Abelev *et al.* (ALICE Collaboration) arXiv:1307.5543.

[17] E. Schnedermann, J. Sollfrank, and U. W. Heinz, Phys. Rev. C **48**, 2462 (1993).

[18] C. Tsallis, J. Stat. Phys. **52**, 479 (1988).

[19] B. Abelev *et al.* (STAR Collaboration), Phys. Rev. C **75**, 064901 (2007).

[20] B. Abelev *et al.* (ALICE Collaboration) (unpublished).

[21] K. Aamodt *et al.* (ALICE Collaboration), Phys. Rev. Lett. **105**, 072002 (2010).

[22] B. Abelev *et al.* (ALICE Collaboration), Phys. Rev. Lett. **109**, 252301 (2012).

[23] G. Agakishiev *et al.* (STAR Collaboration), Phys. Rev. Lett. **108**, 072301 (2012).

[24] H. Song and U. W. Heinz, Phys. Lett. B **658**, 279 (2008).

[25] H. Song and U. W. Heinz, Phys. Rev. C **77**, 064901 (2008).

[26] H. Song and U. W. Heinz, Phys. Rev. C **78**, 024902 (2008).

[27] B. Abelev *et al.* (ALICE Collaboration), arXiv:1303.0737.

[28] H. Song, S. A. Bass, and U. Heinz, Phys. Rev. C **83**, 054912 (2011).

[29] K. Werner, Phys. Rev. Lett. **109**, 102301 (2012).

[30] R. C. Hwa and L. Zhu, arXiv:1202.2091.

B. Abelev,[1] J. Adam,[2] D. Adamová,[3] A. M. Adare,[4] M. M. Aggarwal,[5] G. Aglieri Rinella,[6] M. Agnello,[7,8] A. G. Agocs,[9] A. Agostinelli,[10] Z. Ahammed,[11] N. Ahmad,[12] A. Ahmad Masoodi,[12] I. Ahmed,[13] S. U. Ahn,[14] S. A. Ahn,[14] I. Aimo,[8,7] S. Aiola,[4] M. Ajaz,[13] A. Akindinov,[15] D. Aleksandrov,[16] B. Alessandro,[8] D. Alexandre,[17] A. Alici,[18,19] A. Alkin,[20] J. Alme,[21] T. Alt,[22] V. Altini,[23] S. Altinpinar,[24] I. Altsybeev,[25] C. Alves Garcia Prado,[26]

C. Andrei,[27] A. Andronic,[28] V. Anguelov,[29] J. Anielski,[30] T. Antičić,[31] F. Antinori,[32] P. Antonioli,[19] L. Aphecetche,[33] H. Appelshäuser,[34] N. Arbor,[35] S. Arcelli,[10] N. Armesto,[36] R. Arnaldi,[8] T. Aronsson,[4] I. C. Arsene,[28] M. Arslandok,[34] A. Augustinus,[6] R. Averbeck,[28] T. C. Awes,[37] M. D. Azmi,[38] M. Bach,[22] A. Badalà,[39] Y. W. Baek,[40,41] R. Bailhache,[34] V. Bairathi,[42] R. Bala,[8,43] A. Baldisseri,[44] F. Baltasar Dos Santos Pedrosa,[6] J. Bán,[45] R. C. Baral,[46] R. Barbera,[47] F. Barile,[23] G. G. Barnaföldi,[9] L. S. Barnby,[17] V. Barret,[40] J. Bartke,[48] M. Basile,[10] N. Bastid,[40] S. Basu,[11] B. Bathen,[30] G. Batigne,[33] B. Batyunya,[49] P. C. Batzing,[50] C. Baumann,[34] I. G. Bearden,[51] H. Beck,[34] N. K. Behera,[52] I. Belikov,[53] F. Bellini,[10] R. Bellwied,[54] E. Belmont-Moreno,[55] G. Bencedi,[9] S. Beole,[56] I. Berceanu,[27] A. Bercuci,[27] Y. Berdnikov,[57] D. Berenyi,[9] A. A. E. Bergognon,[33] R. A. Bertens,[58] D. Berzano,[56] L. Betev,[6] A. Bhasin,[43] A. K. Bhati,[5] J. Bhom,[59] L. Bianchi,[56] N. Bianchi,[60] J. Bielčík,[2] J. Bielčíková,[3] A. Bilandzic,[51] S. Bjelogrlic,[58] F. Blanco,[61] F. Blanco,[54] D. Blau,[16] C. Blume,[34] F. Bock,[62,29] A. Bogdanov,[63] H. Bøggild,[51] M. Bogolyubsky,[64] L. Boldizsár,[9] M. Bombara,[65] J. Book,[34] H. Borel,[44] A. Borissov,[66] J. Bornschein,[22] M. Botje,[67] E. Botta,[56] S. Böttger,[68] P. Braun-Munzinger,[28] M. Bregant,[33] T. Breitner,[68] T. A. Broker,[34] T. A. Browning,[69] M. Broz,[70] R. Brun,[6] E. Bruna,[8] G. E. Bruno,[23] D. Budnikov,[71] H. Buesching,[34] S. Bufalino,[8] P. Buncic,[6] O. Busch,[29] Z. Buthelezi,[72] D. Caffarri,[73] X. Cai,[74] H. Caines,[4] A. Caliva,[58] E. Calvo Villar,[75] P. Camerini,[76] V. Canoa Roman,[77,6] G. Cara Romeo,[19] F. Carena,[6] W. Carena,[6] F. Carminati,[6] A. Casanova Díaz,[60] J. Castillo Castellanos,[44] E. A. R. Casula,[78] V. Catanescu,[27] C. Cavicchioli,[6] C. Ceballos Sanchez,[79] J. Cepila,[2] P. Cerello,[8] B. Chang,[80] S. Chapeland,[6] J. L. Charvet,[44] S. Chattopadhyay,[11] S. Chattopadhyay,[81] M. Cherney,[82] C. Cheshkov,[83] B. Cheynis,[83] V. Chibante Barroso,[6] D. D. Chinellato,[54] P. Chochula,[6] M. Chojnacki,[51] S. Choudhury,[11] P. Christakoglou,[67] C. H. Christensen,[51] P. Christiansen,[84] T. Chujo,[59] S. U. Chung,[85] C. Cicalo,[86] L. Cifarelli,[18,10] F. Cindolo,[19] J. Cleymans,[38] F. Colamaria,[23] D. Colella,[23] A. Collu,[78] M. Colocci,[10] G. Conesa Balbastre,[35] Z. Conesa del Valle,[87,6] M. E. Connors,[4] G. Contin,[76] J. G. Contreras,[77] T. M. Cormier,[66] Y. Corrales Morales,[56] P. Cortese,[88] I. Cortés Maldonado,[89] M. R. Cosentino,[62] F. Costa,[6] P. Crochet,[40] R. Cruz Albino,[77] E. Cuautle,[90] L. Cunqueiro,[60] A. Dainese,[32] R. Dang,[74] A. Danu,[91] K. Das,[81] D. Das,[81] I. Das,[87] A. Dash,[92] S. Dash,[52] S. De,[11] H. Delagrange,[33] A. Deloff,[93] E. Dénes,[9] A. Deppman,[26] G. D'Erasmo,[23] G. O. V. de Barros,[26] A. De Caro,[18,94] G. de Cataldo,[95] J. de Cuveland,[22] A. De Falco,[78] D. De Gruttola,[94,18] N. De Marco,[8] S. De Pasquale,[94] R. de Rooij,[58] M. A. Diaz Corchero,[61] T. Dietel,[30] R. Divià,[6] D. Di Bari,[23] C. Di Giglio,[23] S. Di Liberto,[96] A. Di Mauro,[6] P. Di Nezza,[60] Ø. Djuvsland,[24] A. Dobrin,[58,66] T. Dobrowolski,[93] B. Dönigus,[28,34] O. Dordic,[50] A. K. Dubey,[11] A. Dubla,[58] L. Ducroux,[83] P. Dupieux,[40] A. K. Dutta Majumdar,[81] D. Elia,[95] D. Emschermann,[30] H. Engel,[68] B. Erazmus,[6,33] H. A. Erdal,[21] D. Eschweiler,[22] B. Espagnon,[87] M. Estienne,[33] S. Esumi,[59] D. Evans,[17] S. Evdokimov,[64] G. Eyyubova,[50] D. Fabris,[32] J. Faivre,[35] D. Falchieri,[10] A. Fantoni,[60] M. Fasel,[29] D. Fehlker,[24] L. Feldkamp,[30] D. Felea,[91] A. Feliciello,[8] G. Feofilov,[25] J. Ferencei,[3] A. Fernández Téllez,[89] E. G. Ferreiro,[36] A. Ferretti,[56] A. Festanti,[73] J. Figiel,[48] M. A. S. Figueredo,[26] S. Filchagin,[71] D. Finogeev,[97] F. M. Fionda,[23] E. M. Fiore,[23] E. Floratos,[98] M. Floris,[6] S. Foertsch,[72] P. Foka,[28] S. Fokin,[16] E. Fragiacomo,[99] A. Francescon,[73,6] U. Frankenfeld,[28] U. Fuchs,[6] C. Furget,[35] M. Fusco Girard,[94] J. J. Gaardhøje,[51] M. Gagliardi,[56] A. Gago,[75] M. Gallio,[56] D. R. Gangadharan,[100] P. Ganoti,[37] C. Garabatos,[28] E. Garcia-Solis,[101] C. Gargiulo,[6] I. Garishvili,[1] J. Gerhard,[22] M. Germain,[33] A. Gheata,[6] M. Gheata,[6,91] B. Ghidini,[23] P. Ghosh,[11] P. Gianotti,[60] P. Giubellino,[6] E. Gladysz-Dziadus,[48] P. Glässel,[29] L. Goerlich,[48] R. Gomez,[77,102] P. González-Zamora,[61] S. Gorbunov,[22] S. Gotovac,[103] L. K. Graczykowski,[104] R. Grajcarek,[29] A. Grelli,[58] C. Grigoras,[6] A. Grigoras,[6] V. Grigoriev,[63] A. Grigoryan,[105] S. Grigoryan,[49] B. Grinyov,[20] N. Grion,[99] J. F. Grosse-Oetringhaus,[6] J.-Y. Grossiord,[83] R. Grosso,[6] F. Guber,[97] R. Guernane,[35] B. Guerzoni,[10] M. Guilbaud,[83] K. Gulbrandsen,[51] H. Gulkanyan,[105] T. Gunji,[106] A. Gupta,[43] R. Gupta,[43] K. H. Khan,[13] R. Haake,[30] Ø. Haaland,[24] C. Hadjidakis,[87] M. Haiduc,[91] H. Hamagaki,[106] G. Hamar,[9] L. D. Hanratty,[17] A. Hansen,[51] J. W. Harris,[4] H. Hartmann,[22] A. Harton,[101] D. Hatzifotiadou,[19] S. Hayashi,[106] A. Hayrapetyan,[6,105] S. T. Heckel,[34] M. Heide,[30] H. Helstrup,[21] A. Herghelegiu,[27] G. Herrera Corral,[77] N. Herrmann,[29] B. A. Hess,[107] K. F. Hetland,[21] B. Hicks,[4] B. Hippolyte,[53] Y. Hori,[106] P. Hristov,[6] I. Hřivnáčová,[87] M. Huang,[24] T. J. Humanic,[100] D. Hutter,[22] D. S. Hwang,[108] R. Ilkaev,[71] I. Ilkiv,[93] M. Inaba,[59] E. Incani,[78] G. M. Innocenti,[56] C. Ionita,[6] M. Ippolitov,[16] M. Irfan,[12] M. Ivanov,[28] V. Ivanov,[57] O. Ivanytskyi,[20] A. Jachołkowski,[47] C. Jahnke,[26] H. J. Jang,[14] M. A. Janik,[104] P. H. S. Y. Jayarathna,[54] S. Jena,[52,54] R. T. Jimenez Bustamante,[90] P. G. Jones,[17] H. Jung,[41] A. Jusko,[17] S. Kalcher,[22] P. Kaliňák,[45] A. Kalweit,[6] J. H. Kang,[109] V. Kaplin,[63] S. Kar,[11] A. Karasu Uysal,[110] O. Karavichev,[97] T. Karavicheva,[97] E. Karpechev,[97] A. Kazantsev,[16] U. Kebschull,[68] R. Keidel,[111] B. Ketzer,[34] M. M. Khan,[12] P. Khan,[81] S. A. Khan,[11] A. Khanzadeev,[57] Y. Kharlov,[64] B. Kileng,[21] T. Kim,[109] B. Kim,[109] D. J. Kim,[80] D. W. Kim,[41,14] J. S. Kim,[41] M. Kim,[41] M. Kim,[109]

S. Kim,[108] S. Kirsch,[22] I. Kisel,[22] S. Kiselev,[15] A. Kisiel,[104] G. Kiss,[9] J. L. Klay,[112] J. Klein,[29] C. Klein-Bösing,[30]
A. Kluge,[6] M. L. Knichel,[28] A. G. Knospe,[113] C. Kobdaj,[6,114] M. K. Köhler,[28] T. Kollegger,[22] A. Kolojvari,[25]
V. Kondratiev,[25] N. Kondratyeva,[63] A. Konevskikh,[97] V. Kovalenko,[25] M. Kowalski,[48] S. Kox,[35]
G. Koyithatta Meethaleveedu,[52] J. Kral,[80] I. Králik,[45] F. Kramer,[34] A. Kravčáková,[65] M. Krelina,[2] M. Kretz,[22]
M. Krivda,[45,17] F. Krizek,[2,3,115] M. Krus,[2] E. Kryshen,[57] M. Krzewicki,[28] V. Kucera,[3] Y. Kucheriaev,[16]
T. Kugathasan,[6] C. Kuhn,[53] P. G. Kuijer,[67] I. Kulakov,[34] J. Kumar,[52] P. Kurashvili,[93] A. B. Kurepin,[97] A. Kurepin,[97]
A. Kuryakin,[71] V. Kushpil,[3] S. Kushpil,[3] M. J. Kweon,[29] Y. Kwon,[109] P. Ladrón de Guevara,[90]
C. Lagana Fernandes,[26] I. Lakomov,[87] R. Langoy,[116] C. Lara,[68] A. Lardeux,[33] A. Lattuca,[56] S. L. La Pointe,[58]
P. La Rocca,[47] R. Lea,[76] M. Lechman,[6] S. C. Lee,[41] G. R. Lee,[17] I. Legrand,[6] J. Lehnert,[34] R. C. Lemmon,[117]
M. Lenhardt,[28] V. Lenti,[95] M. Leoncino,[56] I. León Monzón,[102] P. Lévai,[9] S. Li,[40,74] J. Lien,[116,24] R. Lietava,[17]
S. Lindal,[50] V. Lindenstruth,[22] C. Lippmann,[28] M. A. Lisa,[100] H. M. Ljunggren,[84] D. F. Lodato,[58] P. I. Loenne,[24]
V. R. Loggins,[66] V. Loginov,[63] D. Lohner,[29] C. Loizides,[62] X. Lopez,[40] E. López Torres,[79] G. Løvhøiden,[50]
X.-G. Lu,[29] P. Luettig,[34] M. Lunardon,[73] J. Luo,[74] G. Luparello,[58] C. Luzzi,[6] P. M. Jacobs,[62] R. Ma,[4]
A. Maevskaya,[97] M. Mager,[6] D. P. Mahapatra,[46] A. Maire,[29] M. Malaev,[57] I. Maldonado Cervantes,[90]
L. Malinina,[49,118] D. Mal'Kevich,[15] P. Malzacher,[28] A. Mamonov,[71] L. Manceau,[8] V. Manko,[16] F. Manso,[40]
V. Manzari,[95,6] M. Marchisone,[40,56] J. Mareš,[119] G. V. Margagliotti,[76] A. Margotti,[19] A. Marín,[28] C. Markert,[6,113]
M. Marquard,[34] I. Martashvili,[120] N. A. Martin,[28] P. Martinengo,[6] M. I. Martínez,[89] G. Martínez García,[33]
J. Martin Blanco,[33] Y. Martynov,[20] A. Mas,[33] S. Masciocchi,[28] M. Masera,[56] A. Masoni,[86] L. Massacrier,[33]
A. Mastroserio,[23] A. Matyja,[48] J. Mazer,[120] R. Mazumder,[121] M. A. Mazzoni,[96] F. Meddi,[122] A. Menchaca-Rocha,[55]
J. Mercado Pérez,[29] M. Meres,[70] Y. Miake,[59] K. Mikhaylov,[15,49] L. Milano,[56,6] J. Milosevic,[50,123] A. Mischke,[58]
A. N. Mishra,[121] D. Miśkowiec,[28] C. Mitu,[91] J. Mlynarz,[66] B. Mohanty,[124,11] L. Molnar,[53,9] L. Montaño Zetina,[77]
M. Monteno,[8] E. Montes,[61] M. Morando,[73] D. A. Moreira De Godoy,[26] S. Moretto,[73] A. Morreale,[80] A. Morsch,[6]
V. Muccifora,[60] E. Mudnic,[103] S. Muhuri,[11] M. Mukherjee,[11] H. Müller,[6] M. G. Munhoz,[26] S. Murray,[72] L. Musa,[6]
B. K. Nandi,[52] R. Nania,[19] E. Nappi,[95] C. Nattrass,[120] T. K. Nayak,[11] S. Nazarenko,[71] A. Nedosekin,[15]
M. Nicassio,[28,23] M. Niculescu,[6,91] B. S. Nielsen,[51] S. Nikolaev,[16] S. Nikulin,[16] V. Nikulin,[57] B. S. Nilsen,[82]
M. S. Nilsson,[50] F. Noferini,[18,19] P. Nomokonov,[49] G. Nooren,[58] A. Nyanin,[16] A. Nyatha,[52] J. Nystrand,[24]
H. Oeschler,[29,125] S. K. Oh,[41,126] S. Oh,[4] L. Olah,[9] J. Oleniacz,[104] A. C. Oliveira Da Silva,[26] J. Onderwaater,[28]
C. Oppedisano,[8] A. Ortiz Velasquez,[84] A. Oskarsson,[84] J. Otwinowski,[28] K. Oyama,[29] Y. Pachmayer,[29] M. Pachr,[2]
P. Pagano,[94] G. Paić,[90] F. Painke,[22] C. Pajares,[36] S. K. Pal,[11] A. Palaha,[17] A. Palmeri,[39] V. Papikyan,[105]
G. S. Pappalardo,[39] W. J. Park,[28] A. Passfeld,[30] D. I. Patalakha,[64] V. Paticchio,[95] B. Paul,[81] T. Pawlak,[104]
T. Peitzmann,[58] H. Pereira Da Costa,[44] E. Pereira De Oliveira Filho,[26] D. Peresunko,[16] C. E. Pérez Lara,[67]
D. Perrino,[23] W. Peryt,[104,*] A. Pesci,[19] Y. Pestov,[127] V. Petráček,[2] M. Petran,[2] M. Petris,[27] P. Petrov,[17] M. Petrovici,[27]
C. Petta,[47] S. Piano,[99] M. Pikna,[70] P. Pillot,[33] O. Pinazza,[6,19] L. Pinsky,[54] N. Pitz,[34] D. B. Piyarathna,[54] M. Planinic,[31]
M. Płoskoń,[62] J. Pluta,[104] S. Pochybova,[9] P. L. M. Podesta-Lerma,[102] M. G. Poghosyan,[6] B. Polichtchouk,[64] A. Pop,[27]
S. Porteboeuf-Houssais,[40] V. Pospíšil,[2] B. Potukuchi,[43] S. K. Prasad,[66] R. Preghenella,[18,19] F. Prino,[8] C. A. Pruneau,[66]
I. Pshenichnov,[97] G. Puddu,[78] V. Punin,[71] J. Putschke,[66] H. Qvigstad,[50] A. Rachevski,[99] A. Rademakers,[6] J. Rak,[80]
A. Rakotozafindrabe,[44] L. Ramello,[88] S. Raniwala,[42] R. Raniwala,[42] S. S. Räsänen,[115] B. T. Rascanu,[34] D. Rathee,[5]
W. Rauch,[6] A. W. Rauf,[13] V. Razazi,[78] K. F. Read,[120] J. S. Real,[35] K. Redlich,[93,128] R. J. Reed,[4] A. Rehman,[24]
P. Reichelt,[34] M. Reicher,[58] F. Reidt,[6,29] R. Renfordt,[34] A. R. Reolon,[60] A. Reshetin,[97] F. Rettig,[22] J.-P. Revol,[6]
K. Reygers,[29] L. Riccati,[8] R. A. Ricci,[129] T. Richert,[84] M. Richter,[50] P. Riedler,[6] W. Riegler,[6] F. Riggi,[47] A. Rivetti,[8]
M. Rodríguez Cahuantzi,[89] A. Rodriguez Manso,[67] K. Røed,[24,50] E. Rogochaya,[49] S. Rohni,[43] D. Rohr,[22]
D. Röhrich,[24] R. Romita,[117,28] F. Ronchetti,[60] P. Rosnet,[40] A. Rossegger,[6] A. Rossi,[6] P. Roy,[81] C. Roy,[53]
A. J. Rubio Montero,[61] R. Rui,[76] R. Russo,[56] E. Ryabinkin,[16] A. Rybicki,[48] S. Sadovsky,[64] K. Šafařík,[6] R. Sahoo,[121]
P. K. Sahu,[46] J. Saini,[11] H. Sakaguchi,[130] S. Sakai,[62,60] D. Sakata,[59] C. A. Salgado,[36] J. Salzwedel,[100] S. Sambyal,[43]
V. Samsonov,[57] X. Sanchez Castro,[90,53] L. Šándor,[45] A. Sandoval,[55] M. Sano,[59] G. Santagati,[47] R. Santoro,[18,6]
D. Sarkar,[11] E. Scapparone,[19] F. Scarlassara,[73] R. P. Scharenberg,[69] C. Schiaua,[27] R. Schicker,[29] C. Schmidt,[28]
H. R. Schmidt,[107] S. Schuchmann,[34] J. Schukraft,[6] M. Schulc,[2] T. Schuster,[4] Y. Schutz,[6,33] K. Schwarz,[28]
K. Schweda,[28] G. Scioli,[10] E. Scomparin,[8] R. Scott,[120] P. A. Scott,[17] G. Segato,[73] I. Selyuzhenkov,[28] J. Seo,[85]
S. Serci,[78] E. Serradilla,[61,55] A. Sevcenco,[91] A. Shabetai,[33] G. Shabratova,[49] R. Shahoyan,[6] S. Sharma,[43]
N. Sharma,[120] K. Shigaki,[130] K. Shtejer,[79] Y. Sibiriak,[16] S. Siddhanta,[86] T. Siemiarczuk,[93] D. Silvermyr,[37]
C. Silvestre,[35] G. Simatovic,[31] R. Singaraju,[11] R. Singh,[43] S. Singha,[11] V. Singhal,[11] B. C. Sinha,[11] T. Sinha,[81]

B. Sitar,[70] M. Sitta,[88] T. B. Skaali,[50] K. Skjerdal,[24] R. Smakal,[2] N. Smirnov,[4] R. J. M. Snellings,[58] R. Soltz,[1]
M. Song,[109] J. Song,[85] C. Soos,[6] F. Soramel,[73] M. Spacek,[2] I. Sputowska,[48] M. Spyropoulou-Stassinaki,[98]
B. K. Srivastava,[69] J. Stachel,[29] I. Stan,[91] G. Stefanek,[93] M. Steinpreis,[100] E. Stenlund,[84] G. Steyn,[72] J. H. Stiller,[29]
D. Stocco,[33] M. Stolpovskiy,[64] P. Strmen,[70] A. A. P. Suaide,[26] M. A. Subieta Vásquez,[56] T. Sugitate,[130] C. Suire,[87]
M. Suleymanov,[13] R. Sultanov,[15] M. Šumbera,[3] T. Susa,[31] T. J. M. Symons,[62] A. Szanto de Toledo,[26] I. Szarka,[70]
A. Szczepankiewicz,[6] M. Szymański,[104] J. Takahashi,[92] M. A. Tangaro,[23] J. D. Tapia Takaki,[87] A. Tarantola Peloni,[34]
A. Tarazona Martinez,[6] A. Tauro,[6] G. Tejeda Muñoz,[89] A. Telesca,[6] C. Terrevoli,[23] A. Ter Minasyan,[16,63] J. Thäder,[28]
D. Thomas,[58] R. Tieulent,[83] A. R. Timmins,[54] A. Toia,[32] H. Torii,[106] V. Trubnikov,[20] W. H. Trzaska,[80] T. Tsuji,[106]
A. Tumkin,[71] R. Turrisi,[32] T. S. Tveter,[50] J. Ulery,[34] K. Ullaland,[24] J. Ulrich,[68] A. Uras,[83] G. M. Urciuoli,[96]
G. L. Usai,[78] M. Vajzer,[3] M. Vala,[45,49] L. Valencia Palomo,[87] P. Vande Vyvre,[6] L. Vannucci,[129] J. W. Van Hoorne,[6]
M. van Leeuwen,[58] A. Vargas,[89] R. Varma,[52] M. Vasileiou,[98] A. Vasiliev,[16] V. Vechernin,[25] M. Veldhoen,[58]
M. Venaruzzo,[76] E. Vercellin,[56] S. Vergara,[89] R. Vernet,[131] M. Verweij,[66,58] L. Vickovic,[103] G. Viesti,[73]
J. Viinikainen,[80] Z. Vilakazi,[72] O. Villalobos Baillie,[17] A. Vinogradov,[16] L. Vinogradov,[25] Y. Vinogradov,[71]
T. Virgili,[94] Y. P. Viyogi,[11] A. Vodopyanov,[49] M. A. Völkl,[29] S. Voloshin,[66] K. Voloshin,[15] G. Volpe,[6] B. von Haller,[6]
I. Vorobyev,[25] D. Vranic,[6,28] J. Vrláková,[65] B. Vulpescu,[40] A. Vyushin,[71] B. Wagner,[24] V. Wagner,[2] J. Wagner,[28]
Y. Wang,[29] Y. Wang,[74] M. Wang,[74] D. Watanabe,[59] K. Watanabe,[59] M. Weber,[54] J. P. Wessels,[30] U. Westerhoff,[30]
J. Wiechula,[107] J. Wikne,[50] M. Wilde,[30] G. Wilk,[93] J. Wilkinson,[29] M. C. S. Williams,[19] B. Windelband,[29] M. Winn,[29]
C. Xiang,[74] C. G. Yaldo,[66] Y. Yamaguchi,[106] H. Yang,[44,58] P. Yang,[74] S. Yang,[24] S. Yano,[130] S. Yasnopolskiy,[16]
J. Yi,[85] Z. Yin,[74] I.-K. Yoo,[85] I. Yushmanov,[16] V. Zaccolo,[51] C. Zach,[2] C. Zampolli,[19] S. Zaporozhets,[49]
A. Zarochentsev,[25] P. Závada,[119] N. Zaviyalov,[71] H. Zbroszczyk,[104] P. Zelnicek,[68] I. S. Zgura,[91] M. Zhalov,[57]
F. Zhang,[74] Y. Zhang,[74] H. Zhang,[74] X. Zhang,[62,40,74] D. Zhou,[74] Y. Zhou,[58] F. Zhou,[74] X. Zhu,[74] J. Zhu,[74] J. Zhu,[74]
H. Zhu,[74] A. Zichichi,[18,10] M. B. Zimmermann,[30,6] A. Zimmermann,[29] G. Zinovjev,[20] Y. Zoccarato,[83]
M. Zynovyev,[20] and M. Zyzak[34]

(ALICE Collaboration)

[1]*Lawrence Livermore National Laboratory, Livermore, California, USA*
[2]*Faculty of Nuclear Sciences and Physical Engineering, Czech Technical University in Prague, Prague, Czech Republic*
[3]*Nuclear Physics Institute, Academy of Sciences of the Czech Republic, Řež u Prahy, Czech Republic*
[4]*Yale University, New Haven, Connecticut, USA*
[5]*Physics Department, Panjab University, Chandigarh, India*
[6]*European Organization for Nuclear Research (CERN), Geneva, Switzerland*
[7]*Politecnico di Torino, Turin, Italy*
[8]*Sezione INFN, Turin, Italy*
[9]*Wigner Research Centre for Physics, Hungarian Academy of Sciences, Budapest, Hungary*
[10]*Dipartimento di Fisica e Astronomia dell'Università and Sezione INFN, Bologna, Italy*
[11]*Variable Energy Cyclotron Centre, Kolkata, India*
[12]*Department of Physics Aligarh Muslim University, Aligarh, India*
[13]*COMSATS Institute of Information Technology (CIIT), Islamabad, Pakistan*
[14]*Korea Institute of Science and Technology Information, Daejeon, South Korea*
[15]*Institute for Theoretical and Experimental Physics, Moscow, Russia*
[16]*Russian Research Centre Kurchatov Institute, Moscow, Russia*
[17]*School of Physics and Astronomy, University of Birmingham, Birmingham, United Kingdom*
[18]*Centro Fermi-Museo Storico della Fisica e Centro Studi e Ricerche "Enrico Fermi", Rome, Italy*
[19]*Sezione INFN, Bologna, Italy*
[20]*Bogolyubov Institute for Theoretical Physics, Kiev, Ukraine*
[21]*Faculty of Engineering, Bergen University College, Bergen, Norway*
[22]*Frankfurt Institute for Advanced Studies, Johann Wolfgang Goethe-Universität Frankfurt, Frankfurt, Germany*
[23]*Dipartimento Interateneo di Fisica "M. Merlin" and Sezione INFN, Bari, Italy*
[24]*Department of Physics and Technology, University of Bergen, Bergen, Norway*
[25]*V. Fock Institute for Physics, St. Petersburg State University, St. Petersburg, Russia*
[26]*Universidade de São Paulo (USP), São Paulo, Brazil*
[27]*National Institute for Physics and Nuclear Engineering, Bucharest, Romania*
[28]*Research Division and ExtreMe Matter Institute EMMI, GSI Helmholtzzentrum für Schwerionenforschung, Darmstadt, Germany*
[29]*Physikalisches Institut, Ruprecht-Karls-Universität Heidelberg, Heidelberg, Germany*
[30]*Institut für Kernphysik, Westfälische Wilhelms-Universität Münster, Münster, Germany*

[31]*Rudjer Bošković Institute, Zagreb, Croatia*
[32]*Sezione INFN, Padova, Italy*
[33]*SUBATECH, Ecole des Mines de Nantes, Université de Nantes, CNRS-IN2P3, Nantes, France*
[34]*Institut für Kernphysik, Johann Wolfgang Goethe-Universität Frankfurt, Frankfurt, Germany*
[35]*Laboratoire de Physique Subatomique et de Cosmologie (LPSC), Université Joseph Fourier,
CNRS-IN2P3, Institut Polytechnique de Grenoble, Grenoble, France*
[36]*Departamento de Física de Partículas and IGFAE, Universidad de Santiago de Compostela, Santiago de Compostela, Spain*
[37]*Oak Ridge National Laboratory, Oak Ridge, Tennessee, USA*
[38]*Physics Department, University of Cape Town, Cape Town, South Africa*
[39]*Sezione INFN, Catania, Italy*
[40]*Laboratoire de Physique Corpusculaire (LPC), Clermont Université, Université Blaise Pascal,
CNRS-IN2P3, Clermont-Ferrand, France*
[41]*Gangneung-Wonju National University, Gangneung, South Korea*
[42]*Physics Department, University of Rajasthan, Jaipur, India*
[43]*Physics Department, University of Jammu, Jammu, India*
[44]*Commissariat à l'Energie Atomique, IRFU, Saclay, France*
[45]*Institute of Experimental Physics, Slovak Academy of Sciences, Košice, Slovakia*
[46]*Institute of Physics, Bhubaneswar, India*
[47]*Dipartimento di Fisica e Astronomia dell'Università and Sezione INFN, Catania, Italy*
[48]*The Henryk Niewodniczanski Institute of Nuclear Physics, Polish Academy of Sciences, Cracow, Poland*
[49]*Joint Institute for Nuclear Research (JINR), Dubna, Russia*
[50]*Department of Physics, University of Oslo, Oslo, Norway*
[51]*Niels Bohr Institute, University of Copenhagen, Copenhagen, Denmark*
[52]*Indian Institute of Technology Bombay (IIT), Mumbai, India*
[53]*Institut Pluridisciplinaire Hubert Curien (IPHC), Université de Strasbourg, CNRS-IN2P3, Strasbourg, France*
[54]*University of Houston, Houston, Texas, USA*
[55]*Instituto de Física, Universidad Nacional Autónoma de México, Mexico City, Mexico*
[56]*Dipartimento di Fisica dell'Università and Sezione INFN, Turin, Italy*
[57]*Petersburg Nuclear Physics Institute, Gatchina, Russia*
[58]*Institute for Subatomic Physics of Utrecht University, Utrecht, Netherlands*
[59]*University of Tsukuba, Tsukuba, Japan*
[60]*Laboratori Nazionali di Frascati, INFN, Frascati, Italy*
[61]*Centro de Investigaciones Energéticas Medioambientales y Tecnológicas (CIEMAT), Madrid, Spain*
[62]*Lawrence Berkeley National Laboratory, Berkeley, California, USA*
[63]*Moscow Engineering Physics Institute, Moscow, Russia*
[64]*Institute for High Energy Physics, Protvino, Russia*
[65]*Faculty of Science, P.J. Šafárik University, Košice, Slovakia*
[66]*Wayne State University, Detroit, Michigan, USA*
[67]*Nikhef, National Institute for Subatomic Physics, Amsterdam, Netherlands*
[68]*Institut für Informatik, Johann Wolfgang Goethe-Universität Frankfurt, Frankfurt, Germany*
[69]*Purdue University, West Lafayette, Indiana, USA*
[70]*Faculty of Mathematics, Physics and Informatics, Comenius University, Bratislava, Slovakia*
[71]*Russian Federal Nuclear Center (VNIIEF), Sarov, Russia*
[72]*iThemba LABS, National Research Foundation, Somerset West, South Africa*
[73]*Dipartimento di Fisica e Astronomia dell'Università and Sezione INFN, Padova, Italy*
[74]*Central China Normal University, Wuhan, China*
[75]*Sección Física, Departamento de Ciencias, Pontificia Universidad Católica del Perú, Lima, Peru*
[76]*Dipartimento di Fisica dell'Università and Sezione INFN, Trieste, Italy*
[77]*Centro de Investigación y de Estudios Avanzados (CINVESTAV), Mexico City and Mérida, Mexico*
[78]*Dipartimento di Fisica dell'Università and Sezione INFN, Cagliari, Italy*
[79]*Centro de Aplicaciones Tecnológicas y Desarrollo Nuclear (CEADEN), Havana, Cuba*
[80]*University of Jyväskylä, Jyväskylä, Finland*
[81]*Saha Institute of Nuclear Physics, Kolkata, India*
[82]*Physics Department, Creighton University, Omaha, Nebraska, USA*
[83]*Université de Lyon, Université Lyon 1, CNRS/IN2P3, IPN-Lyon, Villeurbanne, France*
[84]*Division of Experimental High Energy Physics, University of Lund, Lund, Sweden*
[85]*Pusan National University, Pusan, South Korea*
[86]*Sezione INFN, Cagliari, Italy*
[87]*Institut de Physique Nucléaire d'Orsay (IPNO), Université Paris-Sud, CNRS-IN2P3, Orsay, France*
[88]*Dipartimento di Scienze e Innovazione Tecnologica dell'Università del Piemonte Orientale and Gruppo Collegato INFN,
Alessandria, Italy*

[89]Benemérita Universidad Autónoma de Puebla, Puebla, Mexico

[90]Instituto de Ciencias Nucleares, Universidad Nacional Autónoma de México, Mexico City, Mexico

[91]Institute of Space Science (ISS), Bucharest, Romania

[92]Universidade Estadual de Campinas (UNICAMP), Campinas, Brazil

[93]National Centre for Nuclear Studies, Warsaw, Poland

[94]Dipartimento di Fisica "E.R. Caianiello" dell'Università and Gruppo Collegato INFN, Salerno, Italy

[95]Sezione INFN, Bari, Italy

[96]Sezione INFN, Rome, Italy

[97]Institute for Nuclear Research, Academy of Sciences, Moscow, Russia

[98]Physics Department, University of Athens, Athens, Greece

[99]Sezione INFN, Trieste, Italy

[100]Department of Physics, Ohio State University, Columbus, Ohio, USA

[101]Chicago State University, Chicago, USA

[102]Universidad Autónoma de Sinaloa, Culiacán, Mexico

[103]Technical University of Split FESB, Split, Croatia

[104]Warsaw University of Technology, Warsaw, Poland

[105]A.I. Alikhanyan National Science Laboratory (Yerevan Physics Institute) Foundation, Yerevan, Armenia

[106]University of Tokyo, Tokyo, Japan

[107]Eberhard Karls Universität Tübingen, Tübingen, Germany

[108]Department of Physics, Sejong University, Seoul, South Korea

[109]Yonsei University, Seoul, South Korea

[110]KTO Karatay University, Konya, Turkey

[111]Zentrum für Technologietransfer und Telekommunikation (ZTT), Fachhochschule Worms, Worms, Germany

[112]California Polytechnic State University, San Luis Obispo, California, USA

[113]The University of Texas at Austin, Physics Department, Austin, Texas, USA

[114]Suranaree University of Technology, Nakhon Ratchasima, Thailand

[115]Helsinki Institute of Physics (HIP), Helsinki, Finland

[116]Vestfold University College, Tonsberg, Norway

[117]Nuclear Physics Group, STFC Daresbury Laboratory, Daresbury, United Kingdom

[118]M.V. Lomonosov Moscow State University, D.V. Skobeltsyn Institute of Nuclear Physics, Moscow, Russia

[119]Institute of Physics, Academy of Sciences of the Czech Republic, Prague, Czech Republic

[120]University of Tennessee, Knoxville, Tennessee, USA

[121]Indian Institute of Technology, Indore, India (IITI)

[122]Dipartimento di Fisica dell'Università "La Sapienza" and Sezione INFN, Rome, Italy

[123]University of Belgrade, Faculty of Physics and "Vinča" Institute of Nuclear Sciences, Belgrade, Serbia

[124]National Institute of Science Education and Research, Bhubaneswar, India

[125]Institut für Kernphysik, Technische Universität Darmstadt, Darmstadt, Germany

[126]Konkuk University, Seoul, Korea

[127]Budker Institute for Nuclear Physics, Novosibirsk, Russia

[128]Institute of Theoretical Physics, University of Wroclaw, Wroclaw, Poland

[129]Laboratori Nazionali di Legnaro, INFN, Legnaro, Italy

[130]Hiroshima University, Hiroshima, Japan

[131]Centre de Calcul de l'IN2P3, Villeurbanne, France

*Deceased.

Appendix B

Fitted Mass Peaks for K_S^0 and Λ.
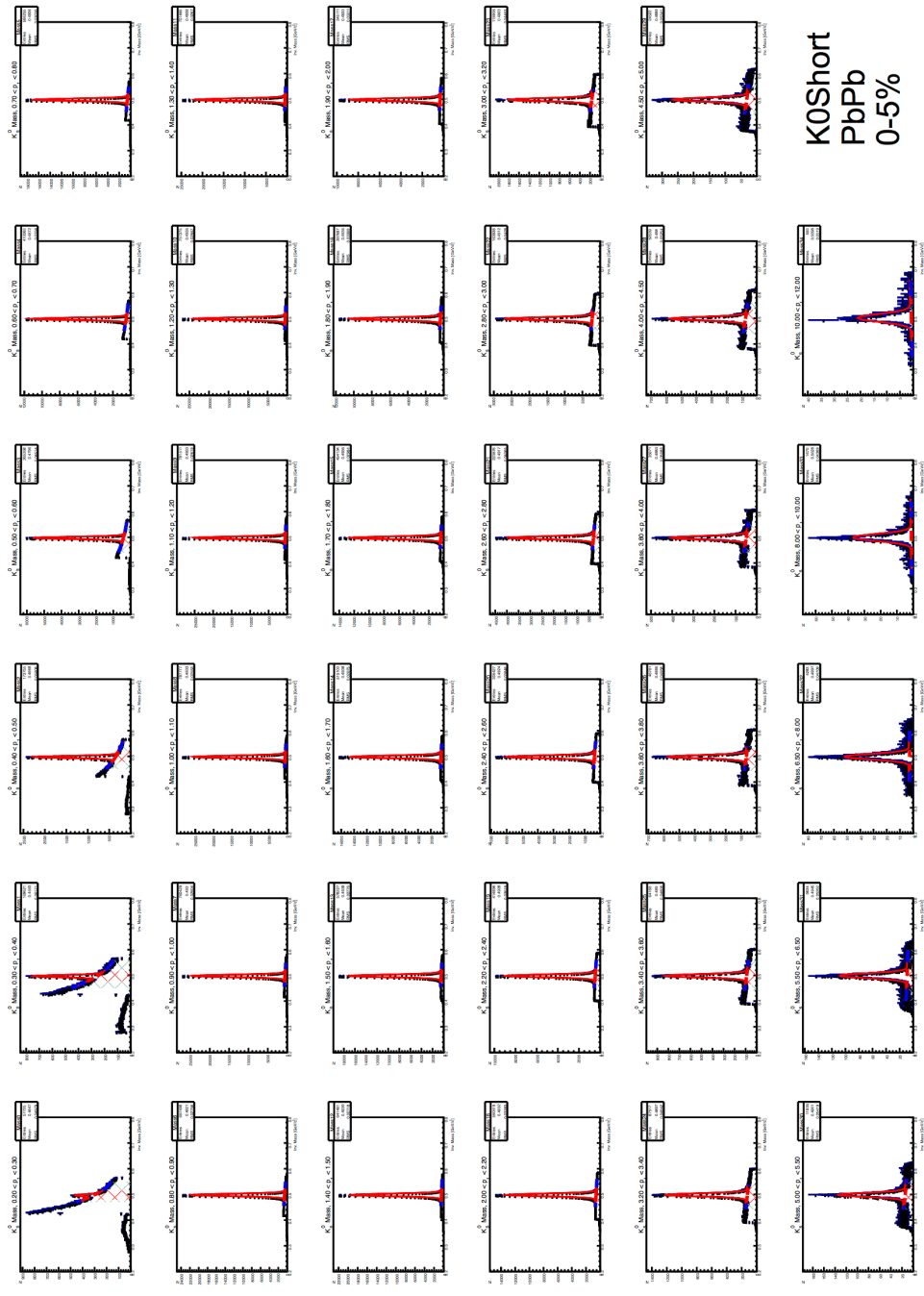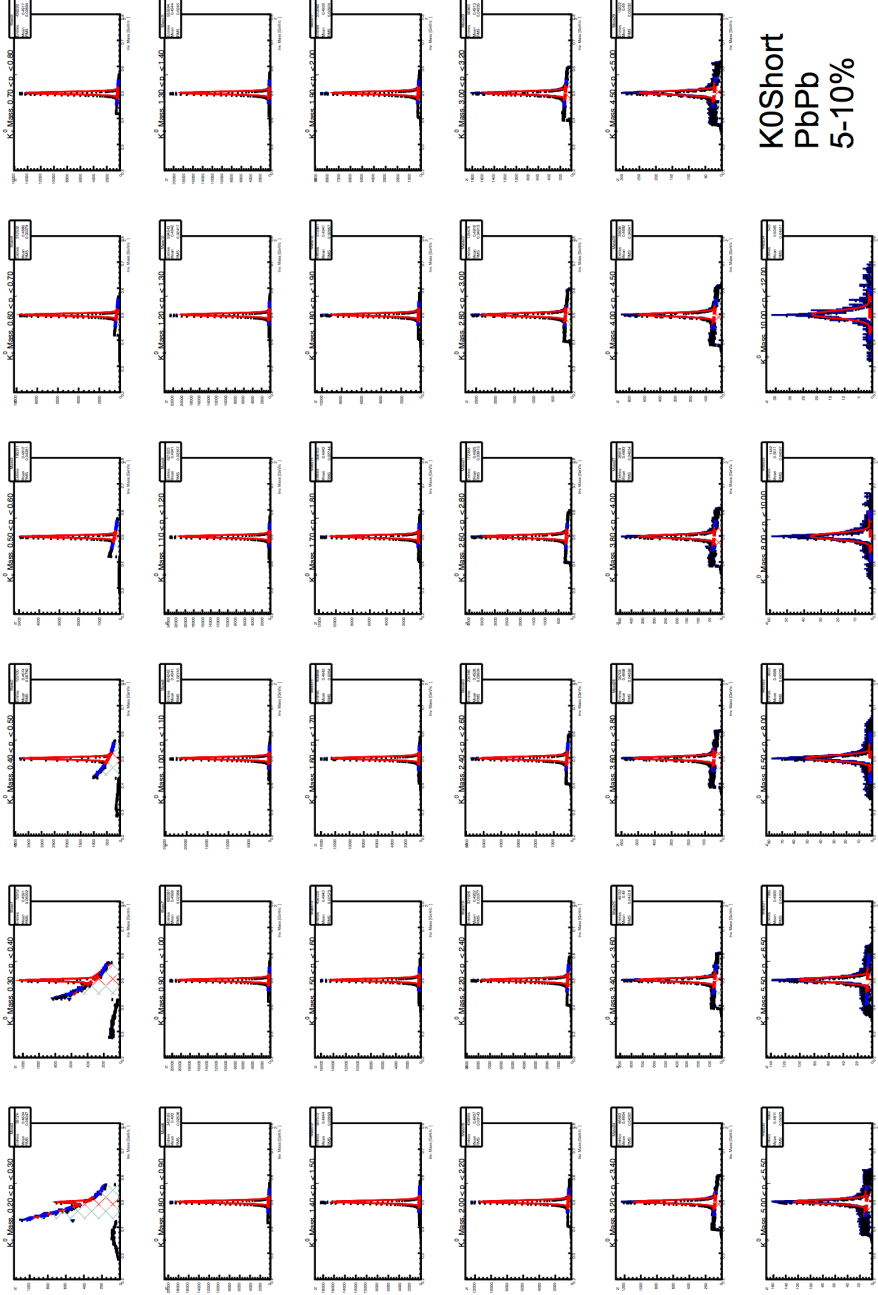
K0Short
PbPb
0-5%

K0Short
PbPb
5-10%
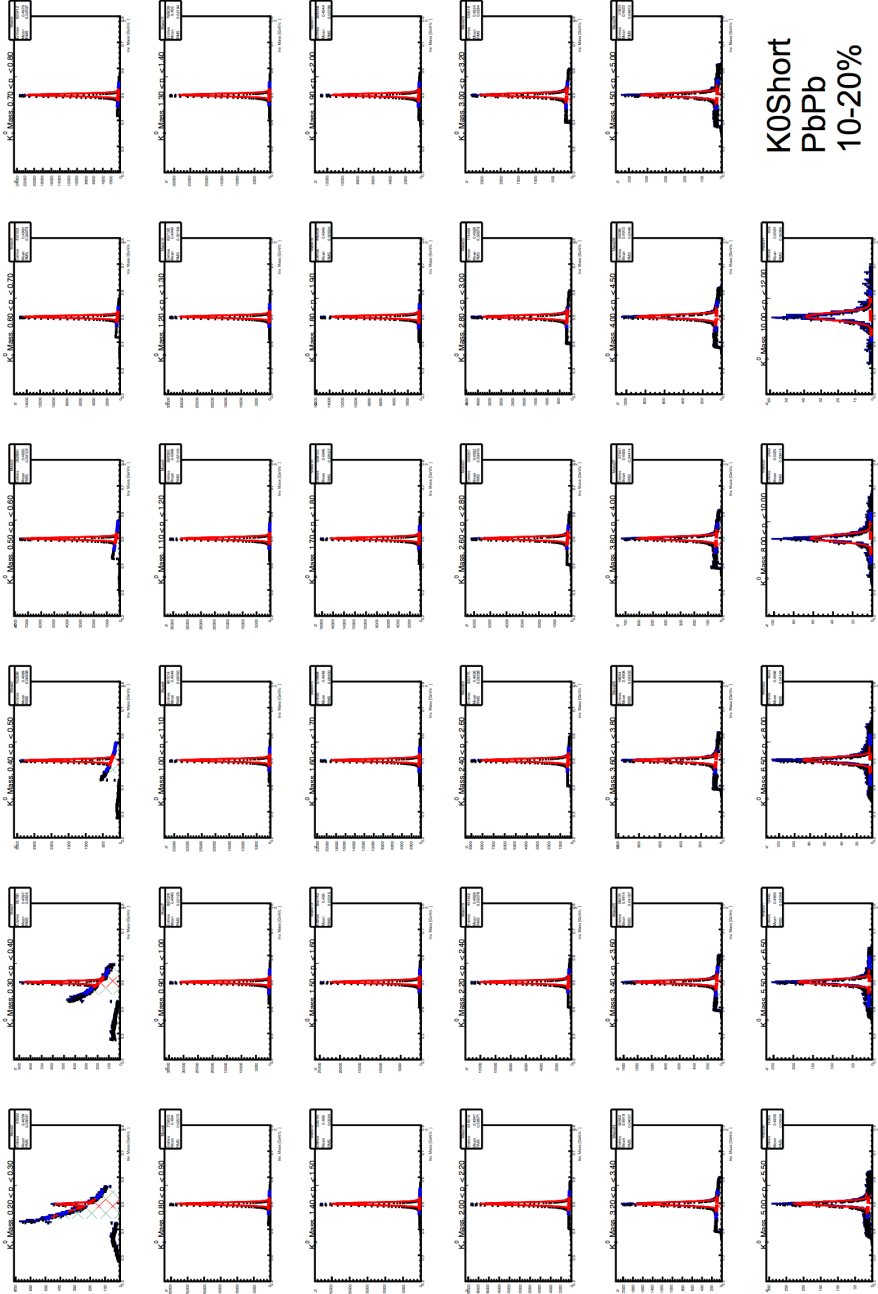
K0Short
PbPb
10-20%
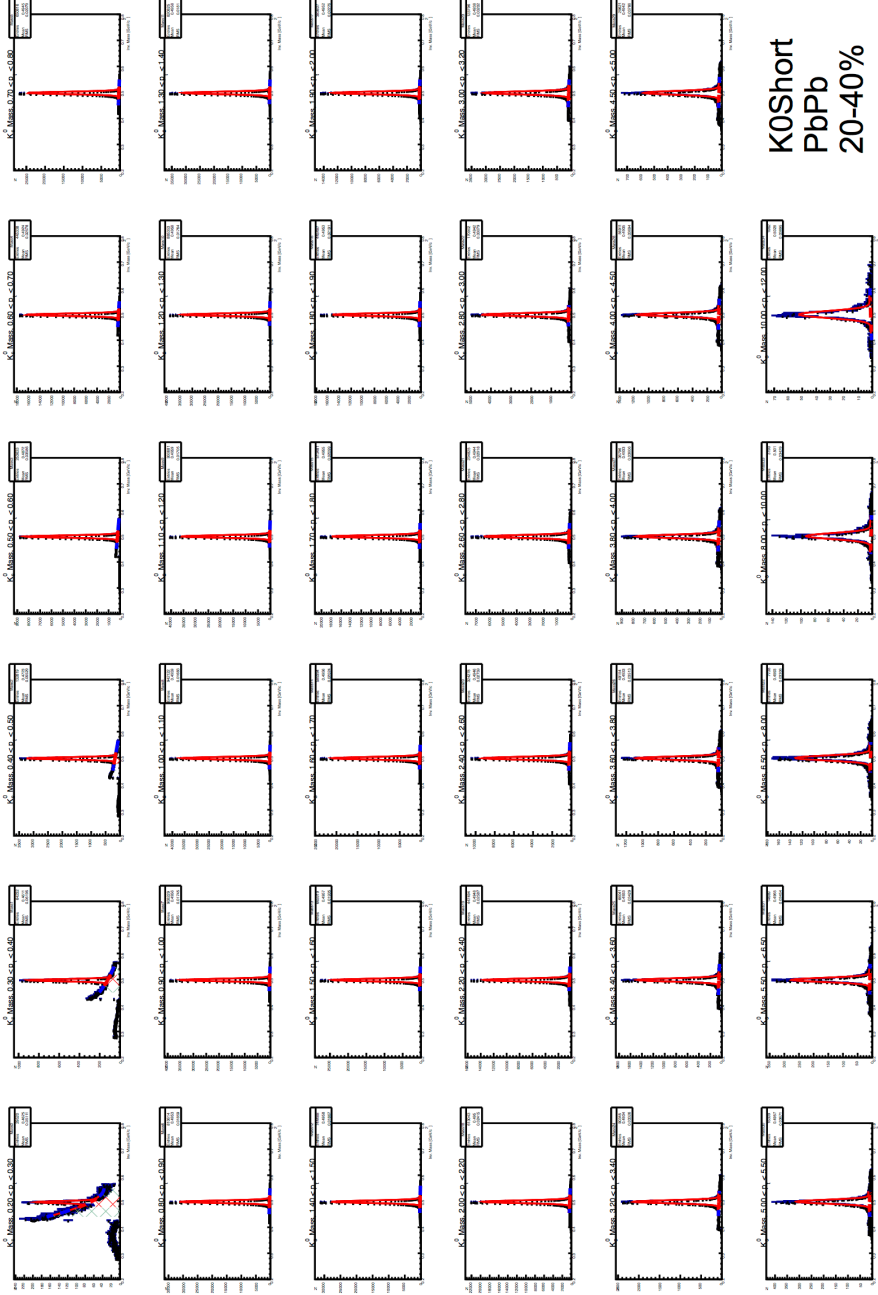
K0Short
PbPb
20-40%
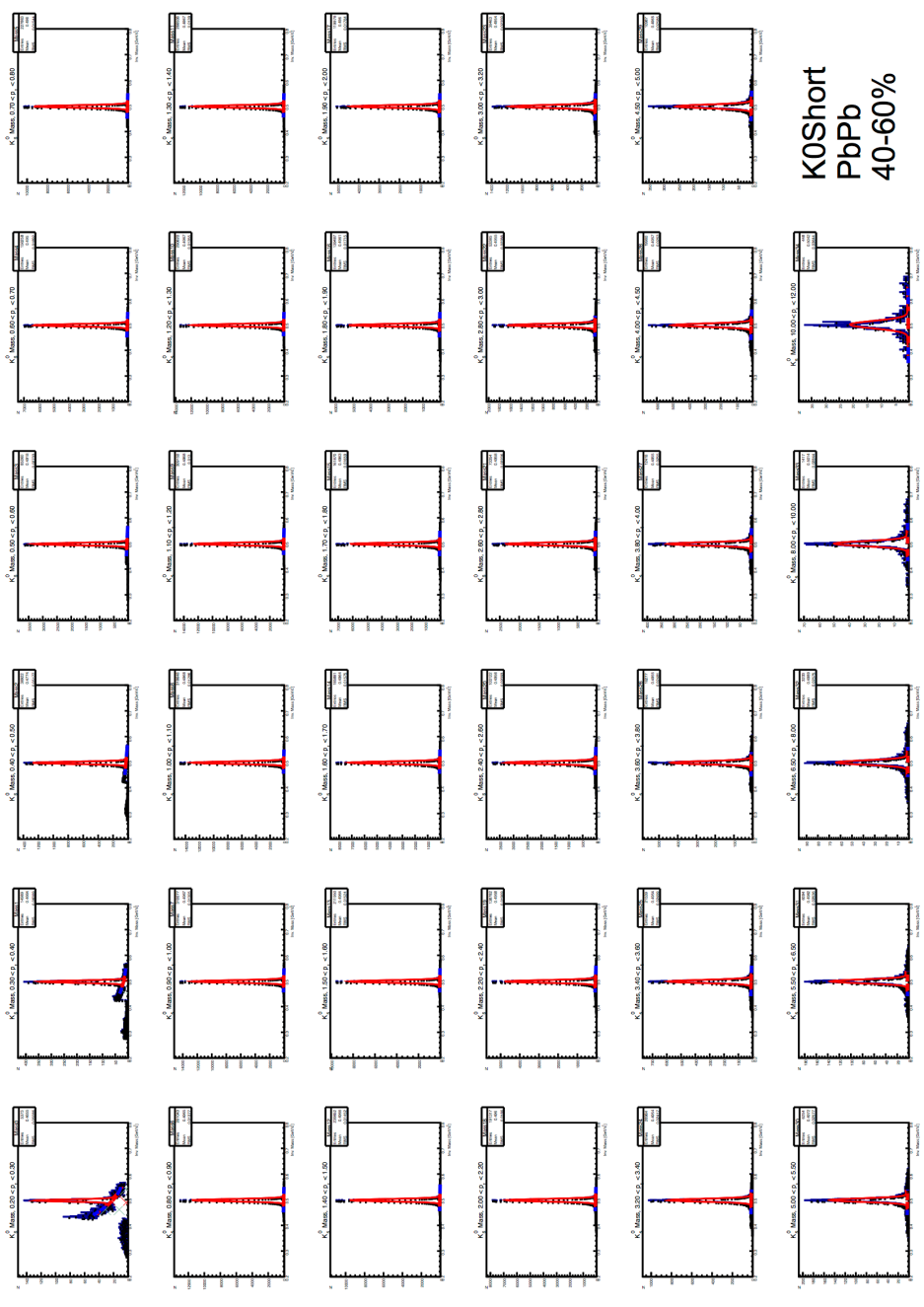
K0Short
PbPb
40-60%
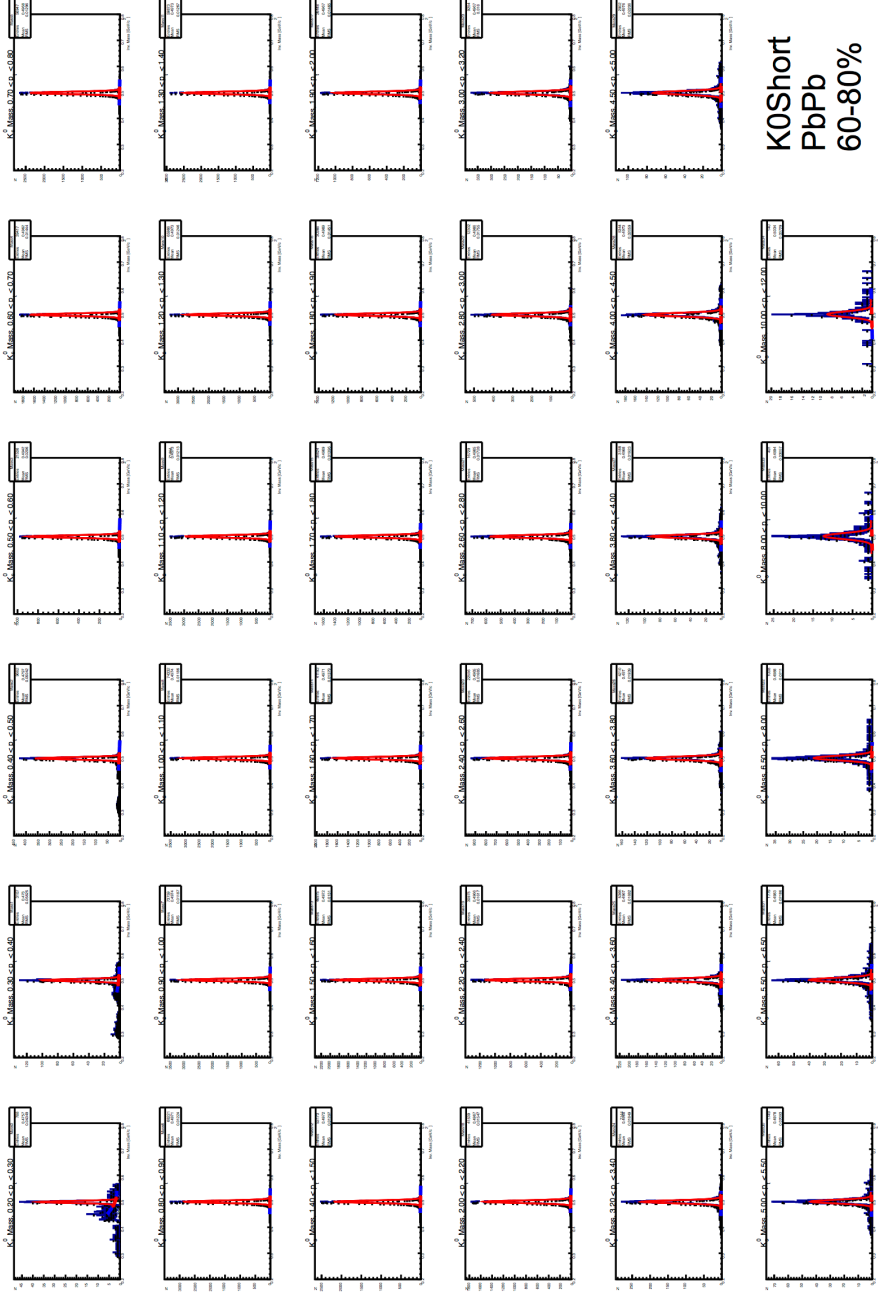
K0Short
PbPb
60-80%
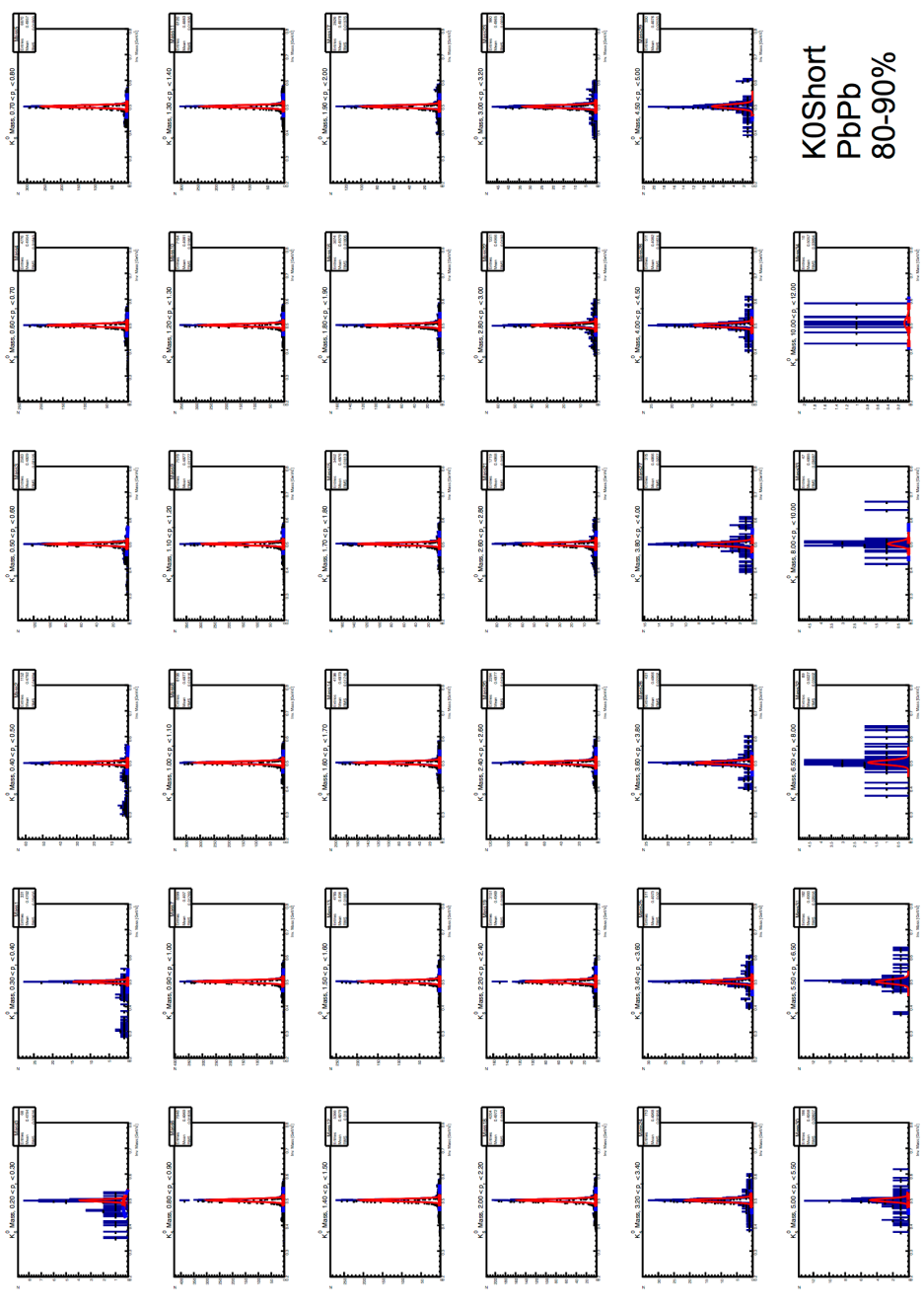
K0Short
PbPb
80-90%
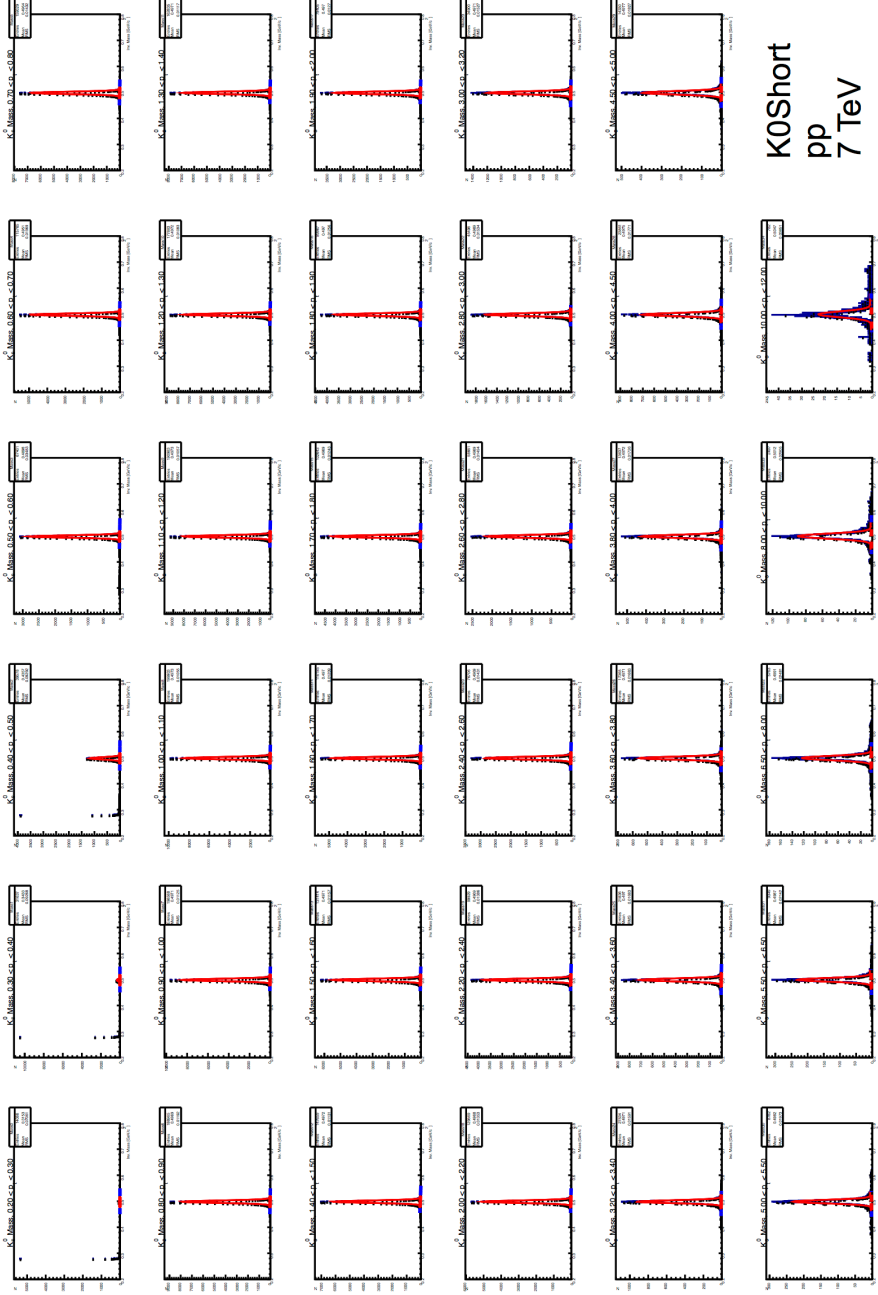
K0Short
pp
7 TeV
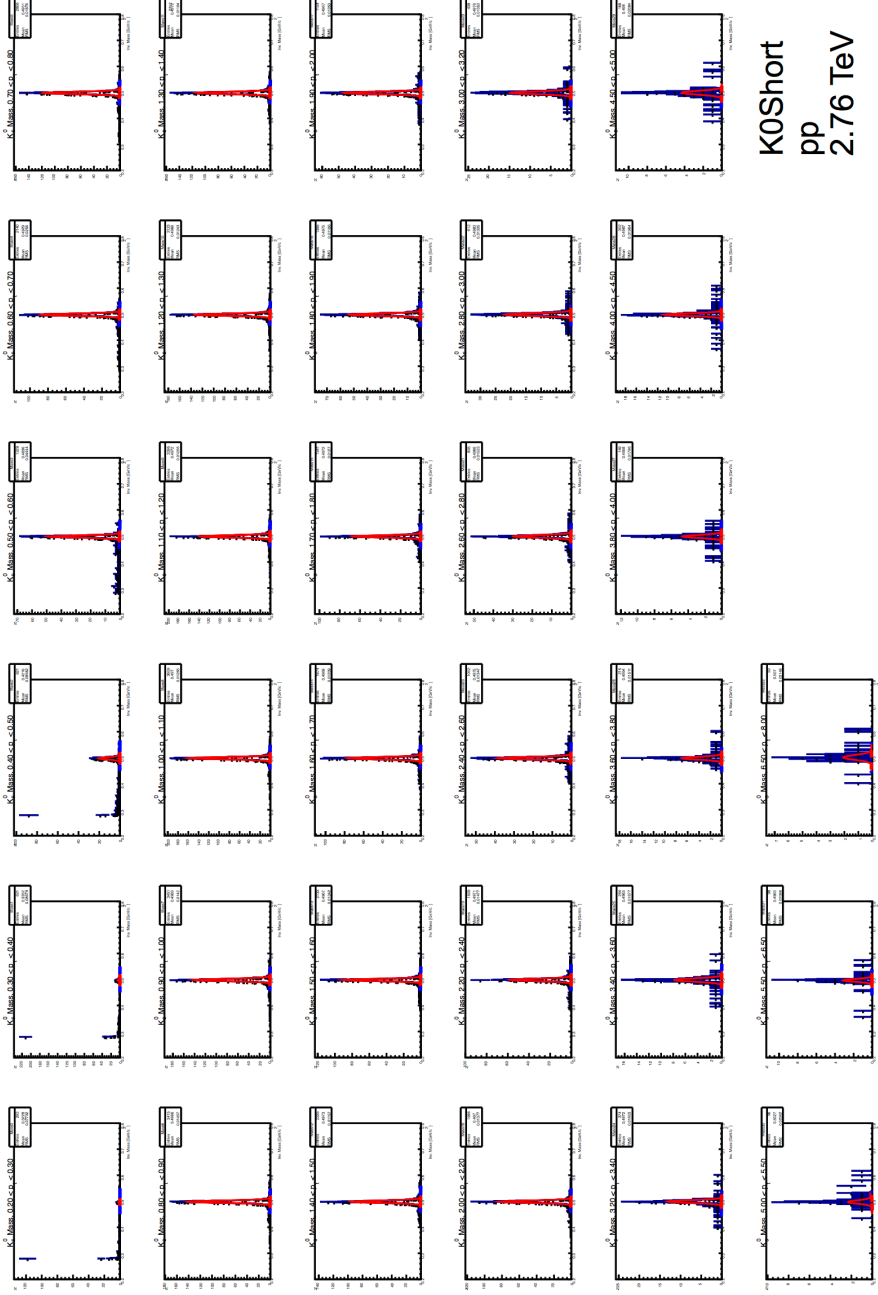
K0Short
pp
2.76 TeV
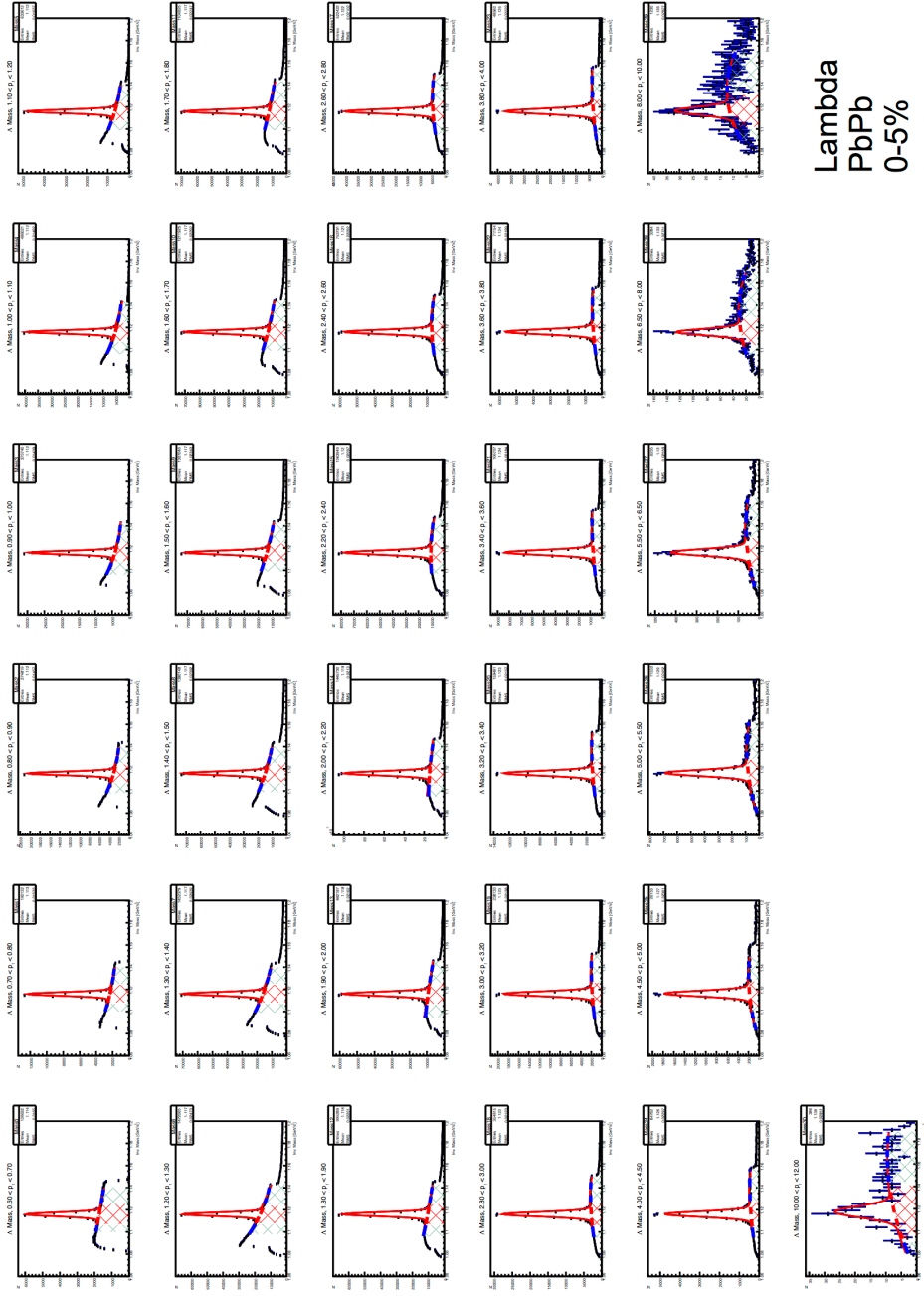
Lambda
PbPb
0-5%
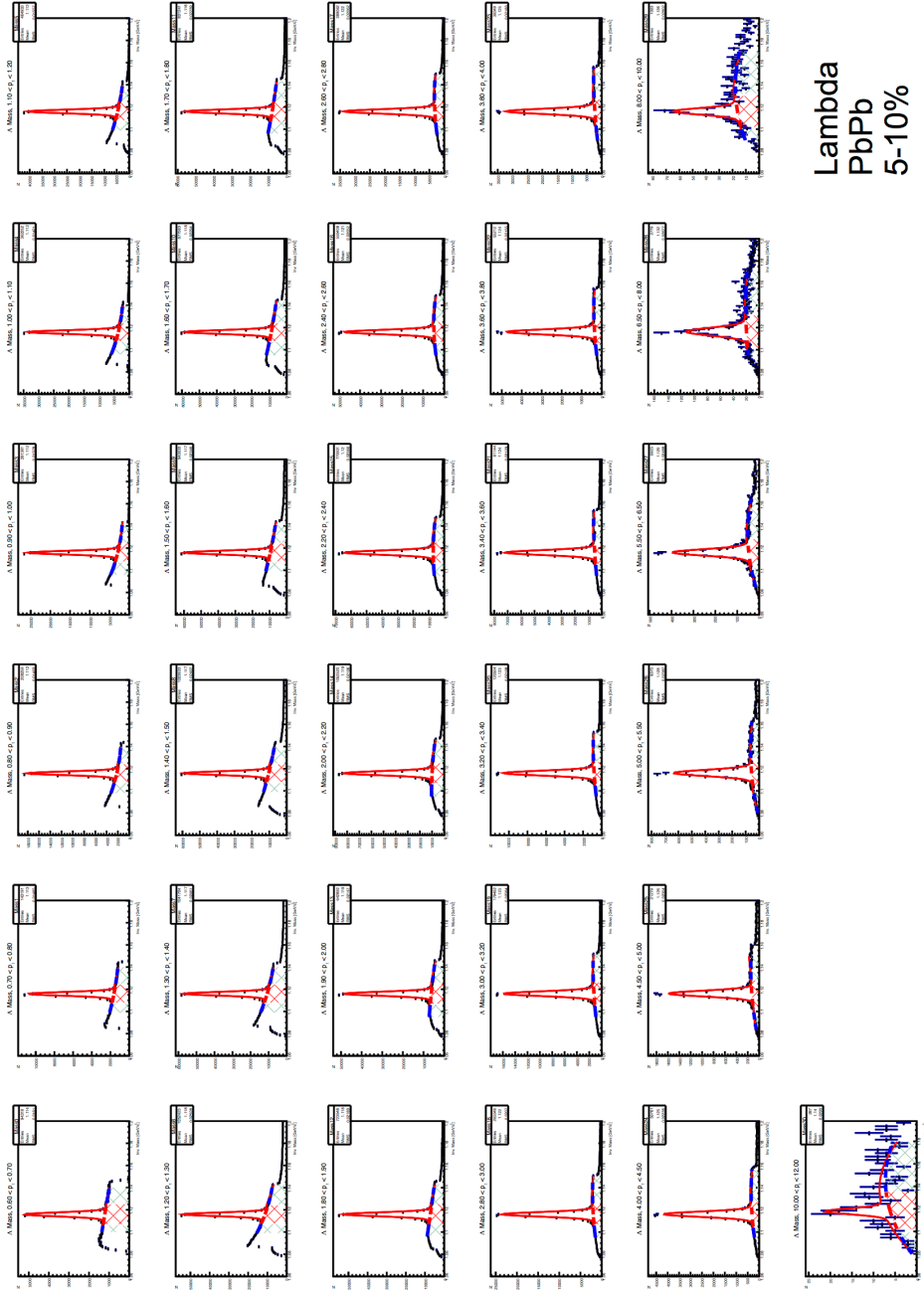
Lambda
PbPb
5-10%

Lambda
PbPb
10-20%

Λ Mass, 0.60 < p <0.70   Λ Mass, 0.70 < p <0.80   Λ Mass, 0.80 < p <0.90   Λ Mass, 0.90 < p <1.00   Λ Mass, 1.00 < p <1.10   Λ Mass, 1.10 < p <1.20

Λ Mass, 1.20 < p <1.30   Λ Mass, 1.30 < p <1.40   Λ Mass, 1.40 < p <1.50   Λ Mass, 1.50 < p <1.60   Λ Mass, 1.60 < p <1.70   Λ Mass, 1.70 < p <1.80

Λ Mass, 1.80 < p <1.90   Λ Mass, 1.90 < p <2.00   Λ Mass, 2.00 < p <2.20   Λ Mass, 2.20 < p <2.40   Λ Mass, 2.40 < p <2.60   Λ Mass, 2.60 < p <2.80

Λ Mass, 2.80 < p <3.00   Λ Mass, 3.00 < p <3.20   Λ Mass, 3.20 < p <3.40   Λ Mass, 3.40 < p <3.60   Λ Mass, 3.60 < p <3.80   Λ Mass, 3.80 < p <4.00

Λ Mass, 4.00 < p <4.50   Λ Mass, 4.50 < p <5.00   Λ Mass, 5.00 < p <5.50   Λ Mass, 5.50 < p <6.50   Λ Mass, 6.50 < p <8.00   Λ Mass, 8.00 < p <10.00

Λ Mass, 10.00 < p <12.00

Lambda
PbPb
20-40%

Lambda
PbPb
40-60%

Λ Mass, 0.60 < p < 0.70
Λ Mass, 0.70 < p < 0.80
Λ Mass, 0.80 < p < 0.90
Λ Mass, 0.90 < p < 1.00
Λ Mass, 1.00 < p < 1.10
Λ Mass, 1.10 < p < 1.20

Λ Mass, 1.20 < p < 1.30
Λ Mass, 1.30 < p < 1.40
Λ Mass, 1.40 < p < 1.50
Λ Mass, 1.50 < p < 1.60
Λ Mass, 1.60 < p < 1.70
Λ Mass, 1.70 < p < 1.80

Λ Mass, 1.80 < p < 1.90
Λ Mass, 1.90 < p < 2.00
Λ Mass, 2.00 < p < 2.20
Λ Mass, 2.20 < p < 2.40
Λ Mass, 2.40 < p < 2.60
Λ Mass, 2.60 < p < 2.80

Λ Mass, 2.80 < p < 3.00
Λ Mass, 3.00 < p < 3.20
Λ Mass, 3.20 < p < 3.40
Λ Mass, 3.40 < p < 3.60
Λ Mass, 3.60 < p < 3.80
Λ Mass, 3.80 < p < 4.00

Λ Mass, 4.00 < p < 4.50
Λ Mass, 4.50 < p < 5.00
Λ Mass, 5.00 < p < 5.50
Λ Mass, 5.50 < p < 6.50
Λ Mass, 6.50 < p < 8.00
Λ Mass, 8.00 < p < 10.00

Λ Mass, 10.00 < p < 12.00

Lambda
PbPb
60-80%

Lambda
PbPb
80-90%
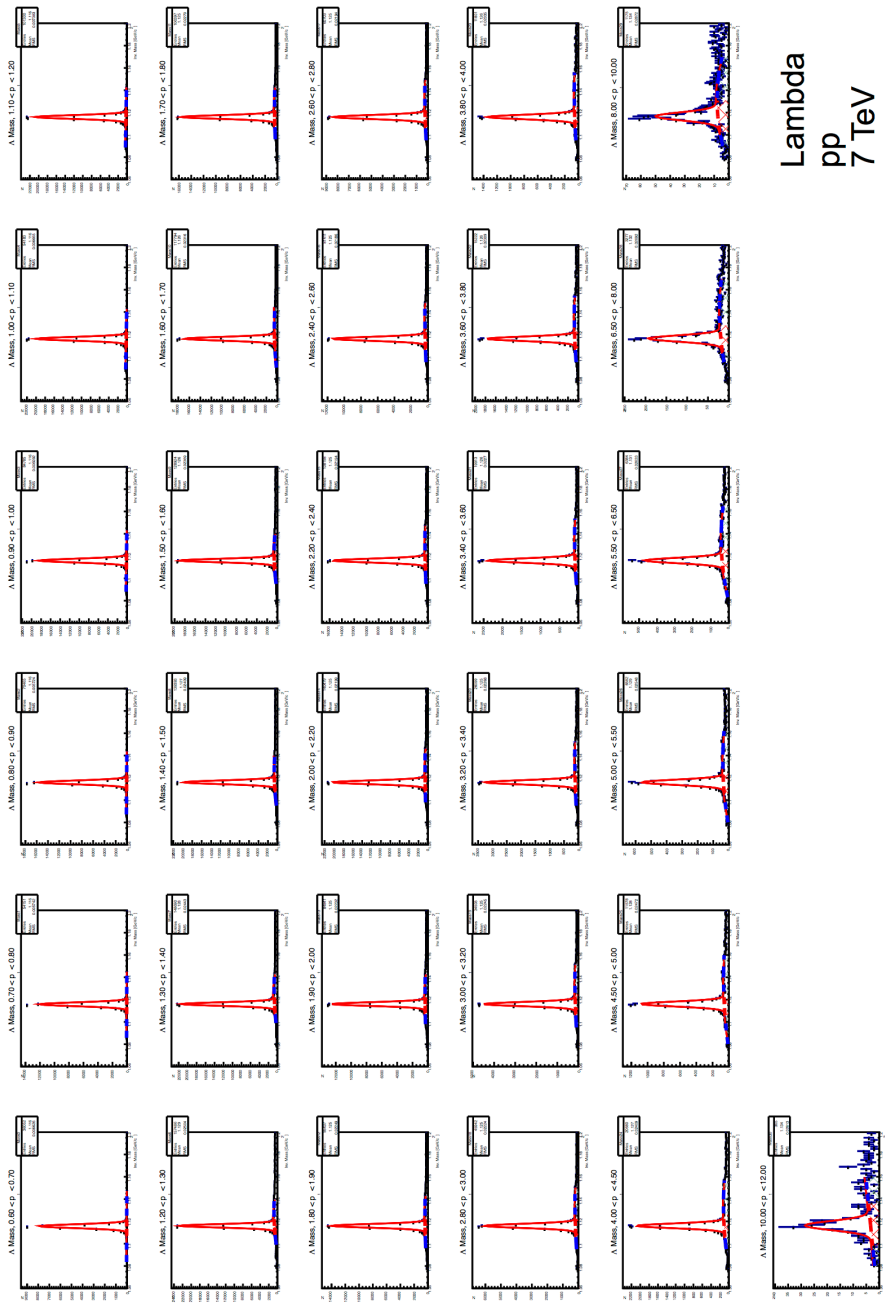
Lambda
pp
7 TeV

Lambda
pp
2.76 TeV